Development and Some Studies on High Frequency Power Inverter Using Power Electronics Components for Ohmic Heating of Liquid Conductor

Thesis Submitted by

Subrata Mandal

Doctor of Philosophy (Engineering)

Electrical Engineering Department,
Faculty Council of Engineering & Technology
Jadavpur University
Kolkata, India
2025

Subrata Mandal
26/11/2025

26.11.25

Associate Professor
Electrical Engg. Dept.
Jadavpur University
Kolkata - 700 032

Jadavpur University

Faculty of Engineering and Technology

INDEX NO. - 275/18/E

1. Title of the Thesis:

Development and Some Studies on High Frequency Power Inverter Using Power Electronics Components for Ohmic Heating of Liquid Conductor

2. Name, Designation & Institution of the Supervisors:

Dr. Madhab Roy
Associate Professor
Electrical Engineering Department
Jadavpur University

3. List of Publications:

Journal:

I. **Subrata Mandal, Madhab Roy** "*Design a High Frequency Power Inverter Using Ferrite-Core Transformer for Ohmic Heating of Liquid Conducting System*" J. Inst. Eng. India Ser. B (2024) https://doi.org/10.1007/s40031-023-00974-0 (Published online: 22 January 2024)

Book Chapters:

None

Conferences:

I. **Subrata Mandal, Madhab Roy** "*Development and Implementation of a Solid State High Frequency Square Wave Inverter for Ohmic Heating of Liquid Beverages*", July 2024. 2024 IEEE International Conference on Smart Power Control and Renewable Energy (ICSPCRE). DOI:10.1109/ICSPCRE62303.2024.10674970

II. **Subrata Mandal, Madhab Roy** "*Ferrite Core Transformer Implementation in a Variable High Frequency Inverter for a Liquid Conductor Load*", December 2024. 2024 IEEE Calcutta Conference (CALCON). DOI:10.1109/CALCON63337.2024.10914213

Subrata Mandal
26/11/2025

M Roy
26.11.25

Associate Professor
Electrical Engg. Dept.
Jadavpur University
Kolkata - 700 032

List of Patents:

None

List of Presentations in National/International/Conferences/ Workshops:

I. **Subrata Mandal, Madhab Roy** "*Development and Implementation of a Solid State High Frequency Square Wave Inverter for Ohmic Heating of Liquid Beverages*", July 2024. 1st IEEE International Conference on Smart Power Control and Renewable Energy (ICSPCRE-2024)' organized by Department of Electrical Engineering, NIT Rourkela, 19-21 July 2024.

II. **Subrata Mandal, Madhab Roy** "*Ferrite Core Transformer Implementation in a Variable High Frequency Inverter for a Liquid Conductor Load*", December 2024. 2024 IEEE Calcutta Conference (CALCON) was organized by the IEEE Kolkata Section. It was held at Jadavpur University Campus, Jadavpur, on December 14-15, 2024.

Subrata Mandal
26/11/2025

Madhab Roy
26.11.25

Associate Professor
Electrical Engg. Dept.
Jadavpur University
Kolkata - 700 032

Statement of Originality

I, **Subrata Mandal,** registered on 22/05/2018 do hereby declare that this thesis entitled ***"Development and Some Studies on High Frequency Power Inverter Using Power Electronics Components for Ohmic Heating of Liquid Conductor***" contains literature survey and original research work done by the undersigned candidate as part of Doctoral studies.

All information in this thesis have been obtained and presented in accordance with existing academic rules and ethical conduct. I declare that, as required by these rules and conduct, I have fully cited and referred all materials and results that are not original to this work.

I also declare that I have checked this thesis as per the "Policy on Anti Plagiarism, Jadavpur University, 2019", and the level of similarity as checked by iThenticate software is 1%.

Signature of Candidate: Subrata Mandal

Date: 26/11/2025

Certified by Supervisor:

(Signature with date, seal)

Madhab Roy 26.11.25

.....

(Dr. Madhab Roy)

Associate Professor
Electrical Engg. Dept.
Jadavpur University
Kolkata - 700 032

CERTIFICATE FROM THE SUPERVISOR

This is to certify that the thesis entitled ***"Development and Some Studies on High Frequency Power Inverter Using Power Electronics Components for Ohmic Heating of Liquid Conductor"*** submitted by Shri **Subrata Mandal**, who got his name registered on 22/05/2018 for the award of **Ph. D. (Engineering)** degree of Jadavpur University is absolutely based upon his own work under the supervision of **Dr. Madhab Roy** and that neither his thesis nor any part of the thesis has been submitted for any degree/diploma or any other academic award anywhere before.

Madhab Roy
26.11.25

(Dr. Madhab Roy)

Signature of the Supervisor

and date with Office Seal

Associate Professor
Electrical Engg. Dept.
Jadavpur University
Kolkata - 700 032

ACKNOWLEDGEMENT

The work presented in this thesis would not have been possible without my close association with many people. I take this opportunity to extend my sincere gratitude and appreciation to all those who have been instrumental in the successful completion of this thesis.

First and foremost, I would like to extend my sincere gratitude to my research guide **Dr. Madhab Roy, Associate Professor, Electrical Engineering Department, Jadavpur University**, for giving me opportunity to work in UHT laboratory, his dedicated help, advice, inspiration, encouragement and continuous support throughout my course work. His enthusiasm, integral view on research and his mission for providing high-quality work have made a deep impression on me.

I am also thankful to **Prof. Palash Kundu, Electrical Engineering Department, Jadavpur University** for providing his profound knowledge and guidance. I am also very much thankful to **Prof. Sanjib Bhattacharya** associated with University of North Bengal for his sincere co-ordination and Support.

I would like to pay my special thanks to the **HOD, Electrical Engineering Department, Jadavpur University** for the cooperation during the research. I am grateful for her constant support and help. I would also like to thank all the members of my **thesis committee** for their encouragement and insightful comments. I gratefully acknowledge all the **faculty members of Electrical Engineering Department of Jadavpur University**.

Finally, I express my sincere gratitude to my parents, my wife, my daughter, and all my family members for their unwavering love, support, and encouragement throughout this journey. Their presence has been my greatest strength.

I offer my regards and blessings to all those who supported me in any respect during the completion of my research.

Subrata Mandal.

Subrata Mandal

26/11/2025

Preface

There are large amount of salts or organic acids are present as electrolyte in liquid food conducting materials. If the electric current passes through these liquid foods, electrical energy will be changed into heating energy by using the electrical conductivity of liquid food conducting materials, which is called ohmic heating. Ohmic heating overcomes the deficiency of traditional heating as it realizes material heating without temperature gradient, and the purpose of uniform heating throughout is achieved directly. It has advantages of rapid heating; no heating surface is required, easy control and environment friendly. It can achieve high temperature sterilization rapidly for liquid-solid mixing foods containing particles. So, the ohmic heating technology is considered to be one of the most potential heat treatment technologies in food processing, but it has serious problem associated with electrode corrosion and contamination into the processed liquid food conducting material under power frequency alternating current (50/60 Hz) heating.

In the literature review, an ohmic heating experiment using a continuous ohmic heating device to heat skim milk was also discovered. The results showed that while pollution and corrosion on electrode surfaces were not significantly reduced when liquid flow rate was increased, they were reduced when power frequency was high. Therefore, it has been determined that using high frequency alternating current the corrosion problem can eliminate in ohmic heating process. Hence to minimize this corrosion of electrodes a high frequency power source instead of 50 or 60 Hz is being proposed here. The variable high frequency power source is not readily available in market; also it is not established at what frequency is required to stop the electrode corrosion, so a research in this field is needed. In view of this, a novel high frequency square wave inverter (H-bridge and Push-pull using ferrite core transformer) with a variable frequency provision has been developed using solid state components and power switches such as MOSFETs for heating a liquid non-linear load-resistance (R) of liquid-food conductor (Green Coconut water, orange juice, sugar cane juice etc.). Finally the simulated liquid food is being heated by this high frequency ohmic heater and it has been found increasing the frequency reduces the electrode corrosion.

Scanning electron microscopy (SEM) and energy dispersive X-ray spectroscopy (EDX) analysis were used to look at deposits that developed on the electrode surface and metal ion migration into the heating solution. Inverter driver finally was modified with a microcontroller (Arduino Uno) to generate precise Pulse Width Modulation (PWM) signals for controlling the power switches. The inverter’s design and implementation process

typically follows a two-phase approach: software simulation of driver circuit and hardware realization. This ensures that the circuit functions optimally before physically constructing the system. The primary objective of the simulation phase is to verify the feasibility of the inverter's operation under different conditions. When preparing food using ohmic heating, electrical conductivity can be utilized to track significant changes in the product. The electrical conductivities of a few chosen liquids and fruit juices—apple, orange, and sugar cane were measured while they were being heated. A wide range of processing temperatures, from 20 to 50°C, was used to measure the various characteristic of different food samples reported here. Experimental analysis has been done that how the electrical parameters of various food materials change with the supply frequency. Mathematical model and simulation of the push-pull inverter developed using a ferrite core transformer, have also been carried out for the system to compare simulation results with the practical output.

Contents

Preface.....i

Contents iii

List of Figures viii

List of Tables xv

List of abbreviations xvi

1. INTRODUCTION

1.1 General introduction.....1

1.2 Objectives of the work 2

1.3 Contribution of the thesis 3

1.4 Thesis organization 3

2. REVIEW AND DEVELOPMENT OF HIGH-FREQUENCY INVERTER OHMIC HEATING SYSTEM IN LABORATORY

2.1 Introduction 5

2.2 Single-phase half-bridge inverter (VSI).....6

2.3 Design of driver circuit for half bridge inverter.....7

2.3.1 Choice of switching device.....8

2.3.2 MOSFET.....10

2.3.3 Switching losses.....13

2.3.4 Driving the inverter.....14

2.3.5 Principle of PWM 14

2.3.6 Pulse Width Modulation (PWM) generator.....14

2.3.7 Half bridge driver.....15

2.4 Details of driver circuits parameters 18

2.4.1 Pulse Width Modulator IC LM3524.....18

2.4.2 Optocoupler IC 6N136.....21

2.4.3 NE555 Timer 22

2.5 Experimental output of the H-bridge driver circuit.....24

2.5.1 Driver output voltage at various frequency and duty cycle 27

2.6 Block diagram of high frequency square wave H-bridge inverter.....29

2.7 High frequency inverter along with components 30

2.7.1 Auto transformer.....30

2.7.2 Isolation transformer 31
2.7.3 Diode rectifier 31
2.7.4 DC link capacitor 32
2.7.5 Selection of DC link capacitor 33
2.7.6 Calculation of the capacitance value 34
2.8 Power switches 35
2.8.1 Different types of MOSFET used in this work 35
2.9 Snubber circuit 38
2.9.1 RCD snubber design 39
2.10 Development and observation on high frequency inverter 40
2.10.1 Experiment on half bridge inverter 40
2.10.2 Thermal performance of Half-bridge inverter using IRF840 MOSFET 41
2.10.2.1 Inverter output voltage wave across the tungsten filament bulb load at 5 kHz 42
2.10.2.2 Inverter output voltage wave across the tungsten filament bulb load at 10 kHz 45
2.10.3 Thermal performance of Half-bridge inverter using 2SK727 MOSFET 47
2.11 Summary 49

3. DESIGN AND DEVELOPMENT OF HIGH FREQUENCY PUSH-PULL INVERTER USING FERRITE CORE TRANSFORMER FOR OHMIC HEATING AND EXPERIMENTS ON LIQUID CONDUCTORS-FOODS

3.1 Introduction 50
3.2 Push-pull inverter 50
3.3 Requirements of high frequency ferrite core transformer 52
3.3.1 Ferrite core transformer in push-pull inverter 52
3.3.2 Design of ferrite-core transformer 52
3.4 Driver circuit using totem pole 56
3.4.1 Design and calculation of gate current (Ig) for turning on the MOSFETs 56
3.4.2 Module and components used for the gate driver 59
3.4.3 Frequency & duty cycle control of the driver 60
3.5 Driver output voltage using totem pole at various frequency and duty cycle 60
3.6 Driver output voltage with MOSFET connection 63
3.7 Experiment on push-pull inverter 66
3.7.1 Thermal performance of Push-pull inverter using IRF840 MOSFET 66

3.7.1.1 Thermal analysis of the IRF840 MOSFET in inverter operation at 10.5 kHz 66

3.7.1.2 Inverter output voltage wave across the tungsten filament bulb load at 10.5 kHz 67

3.7.1.3 Thermal analysis of the IRF840 MOSFET in inverter operation at 7.5 kHz 69

3.7.1.4 Thermal analysis of the IRF840 MOSFET in inverter operation at 15 & 5 kHz 70

3.7.2 Thermal performance of push-pull inverter using 2SK727 MOSFET 71

3.7.2.1 Thermal analysis of the 2SK727 MOSFET in inverter operation at 15 & 7.5 kHz 71

3.7.2.2 Inverter output voltage wave across the tungsten filament bulb load at 15 kHz 72

3.7.2.3 Thermal analysis of the 2SK727 MOSFET in inverter operation at 15 & 10 kHz 73

3.7.2.4 Thermal analysis of the 2SK727 MOSFET in inverter operation at 7.5 & 20 kHz 74

3.7.2.5 Inverter output voltage wave across the tungsten filament bulb load at 20 kHz 75

3.8 Study on ohmic heating's impact on liquid food materials 75

3.8.1 Electrode details 76

3.8.2 Analysis of electrode corrosion induced by ohmic heating at 50 Hz AC supply 77

3.8.3 SEM-EDX analysis of ohmic heating effects 78

3.8.3.1 EDX information on electrodes prior to ohmic heating treatment 78

3.8.3.2 Graphical presentation of SEM-EDX results for electrodes after heat treatment 81

3.8.3.3 Results of the 0.5% NaCl solution's EDX (SS 304) after heating 82

3.8.3.4 Results of the 0.5% NaCl solution's EDX (SS 316) after heating 83

3.8.3.5 EDX result of the 0.5% NaCl solution's rough surface (unclean electrode) 84

3.8.3.6 EDX result of 0.5% NaCl solution's flat surface (SS 304) 85

3.8.3.7 EDX result of 0.1% NaCl solution for gold plated electrode after heating 86

3.8.3.8 EDX result of 0.1% NaCl solution for gold titanium electrode after heating 87

3.9 Liquid sample heating using push-pull inverter 89

3.9.1 Ohmic heating of 1% & 2% NaCl solution at 1kHz, 5kHz & 10 kHz frequency 91

3.9.2 Corrosion of electrodes made of stainless steel (SS 316) for different frequency (50 Hz- 5kHz- 10kHz) after ohmic heating treatment 92

3.9.3 Voltage across NaCl solution during heating at 20 kHz 93

3.9.4 Corrosion of electrodes made of stainless steel (SS 316) for different frequency (50Hz-20 kHz) after ohmic heating treatment 94

3.9.5 Voltage across coconut water during heating treatment at 10.36 kHz 94

3.10 Summary 94

4. DESIGN AND DEVELOPMENT AND SOME STUDIES ON HIGH FREQUENCY POWER INVERTER USING ARDUINO MICROCONTROLLER

4.1 Introduction 95

4.2 Simulation and testing of microcontroller based driver using software 95

4.2.1 Technical specifications 96

4.2.2 Driver output voltage pulses in simulation at different frequency (1kHz, 3kHz, 5kHz, 10kHz, 12.5kHz and 16kHz) 99

4.3 Hardware design and implementation of driver output voltage pulses 105

4.4 Testing and performance evaluation 109

4.4.1 Microcontroller based inverter output voltage in loaded condition at 10.40 kHz 130

4.5 Summary 131

5. EXPERIMENTAL INVESTIGATIONS ON ACTIVATION ENERGIES AND ELECTRICAL CONDUCTIVITY IN VARIOUS FRUIT JUICES-LIQUIDS

5.1 Introduction 132

5.2 Materials and methods 133

5.3 Results and discussion 137

5.3.1 DC conductivity measurement 138

5.3.1.1 Variation of DC conductivity of different liquids with temperature 138

5.3.1.2 Activation Energies (Ea) for different compositions 139

5.3.2 AC conductivity measurement 140

5.3.2.1 Cole-Cole plot of different food samples 142

5.3.2.2 Frequency dependent ac conductivity of different liquid compositions 143

5.3.3 Graphical presentation of SEM-EDX results for green coconut water, electrodes after heat treatment 150
5.3.3.1 EDX result of green coconut water (Titanium electrode)..... 151
5.3.3.2 EDX result of green coconut water (Flat portion, Titanium electrode) 152
5.3.3.3 Chemical composition of green coconut water..... 153
5.3.3.4 Element Line Scan (ELS) experiment on green coconut water..... 154
5.4 Summary 156

6. DESIGN AND MODELING-SIMULATIONS OF THE HIGH FREQUENCY PUSH-PULL INVERTER SYSTEM

6.1 Introduction 157
6.2 Materials and methods 158
6.2.1 Variation of flux linkages with respect to current 160
6.2.2 Modeling design of the system 160
6.3 Results and discussion..... 161
6.4 Summary 167

7. CONCLUSIONS AND FUTURE SCOPE OF WORK

7.1 Conclusion..... 168
7.2 Scope of future work..... 170

REFERENCES..... 172

List of Figures

Figure 2.1: Half Bridge MOSFET-Inverter circuit.

Figure 2.2: MOSFET and IGBT turn off behavior.

Figure 2.3: Structure of a vertical n-channel enhancement-type MOSFET and circuit symbol.

Figure 2.4: Approximate equivalent input circuit of a MOSFET gate.

Figure 2.5: Pulse Width Modulation (PWM) generator.

Figure 2.6: Output of PWM Generator.

Figure 2.7: Block diagram of the driver circuit for MOSFET-Inverter

Figure 2.8: Driver circuit for half bridge Inverter.

Figure 2.9: Block diagram of IC LM3524

Figure 2.10: Pin diagram of IC LM3524

Figure 2.11: IC LM3524

Figure 2.12: (a) IC 6N136 (b) Pin diagram of Optocoupler IC 6N136.

Figure 2.13: Pin diagram of 555 timers IC

Figure 2.14: hardware setup of the H-bridge inverter driver.

Figure 2.15: Output of inverting driving chip goes to MOSFET gate with controlled duty.

Figure 2.16 (a, b): Arrangement of duty cycle control of IC LM3524

Figure 2.17: H-bridge driver output at 5 kHz with 43% duty cycle.

Figure 2.18: H-bridge driver output at 7.5 kHz with 43% duty cycle.

Figure 2.19: H-bridge driver output at 10 kHz with 43% duty cycle.

Figure 2.20: H-bridge driver output at 15 kHz with 43% duty cycle.

Figure 2.21: H-bridge driver output at 20 kHz with 43% duty cycle.

Figure 2.22: Block diagram for high frequency square wave inverter.

Figure 2.23: (a) Winding diagram of auto transformer (b) Practical Auto transformer.

Figure 2.24: Isolation transformer.

Figure 2.25: (a) Bridge Rectifier circuit (b) Pulsating DC output of rectifier.

Figure 2.26: Practical diode bridge rectifier.

Figure 2.27: Diode bridge rectifier circuit with bus rectified and filtered output.

Figure 2.28: Screw terminal aluminum electrolytic DC link capacitor.

Figure 2.29: (a) Equivalent circuit schematic (b) Packaging of 2SK727 MOSFET.

Figure 2.30: Symbol and packaging of MOSFET IRF840.

Figure 2.31: Packaging and terminals of MOSFET IRFP460.

Figure 2.32: Voltage and current waveforms of the switch during turn-on and turn-off.
Figure 2.33: RCD snubber.
Figure 2.34: Half Bridge Inverter setup.
Figure 2.35: Tungsten filament bulb load.
Figure 2.36: Temperature rise versus time of two MOSFETs (SW1 and SW2) of H-bridge inverter at 5 kHz operation.
Figure 2.37: Inverter output wave across the tungsten filament bulb load for Table 2.3.
Figure 2.38: Temperature rise versus time of two MOSFETs (SW1 and SW2) of H-bridge inverter at 8 kHz operation.
Figure 2.39: Temperature rise versus time of two MOSFETs (SW1 and SW2) of H-bridge inverter at 5.9 kHz operation.
Figure 2.40: Temperature rise versus time of two MOSFETs (SW1 and SW2) of H-bridge inverter at 10 kHz operation.
Figure 2.41: Inverter output wave across the tungsten filament bulb load for Table 2.5.
Figure 2.42: Rising part of the driver circuit output during loading condition for Table 2.5.
Figure 2.43: Falling part of the driver circuit output during loading condition for Table 2.5.
Figure 2.44: Temperature rise versus time of two MOSFETs (SW1 and SW2) of H-bridge inverter at 10 kHz operation.
Figure 2.45: Inverter output wave across the tungsten filament bulb load for Table 2.6.
Figure 2.46: Temperature rise versus time of two MOSFETs (SW1 and SW2) of H-bridge inverter at 10 kHz operation.
Figure 2.47: Inverter output wave across the tungsten filament bulb load for Table 2.7.
Figure 3.1: Push-pull inverter circuit.
Figure 3.2: Dimension of ferrite core transformer.
Figure 3.3: Block diagram of the driver circuit using totem pole.
Figure 3.4: Driver circuit using totem pole for inverter-MOSFETs.
Figure 3.5: Hardware setup of the driver circuit using totem pole.
Figure 3.6: Driver output using totem pole at frequency 5 kHz with 40% duty cycle.
Figure 3.7: Driver output using totem pole at frequency 10 kHz with 37.2% duty cycle.
Figure 3.8: Driver output using totem pole at frequency 15 kHz with 37.5% duty cycle.
Figure 3.9: Driver output using totem pole at frequency 20 kHz with 36.7% duty cycle.
Figure 3.10: Driver output at frequency 5 kHz when gate-source terminal is connected.
Figure 3.11: Driver output at frequency 10 kHz when gate-source terminal is connected.
Figure 3.12: Driver output at frequency 15 kHz when gate-source terminal is connected.

Figure 3.13: Driver output at frequency 20 kHz when gate-source terminal is connected.
Figure 3.14: Driver output pulses across gate-source while MOSFETs are conducting (on) at 10 kHz.
Figure 3.15: Driver output pulses across gate-source while MOSFETs are conducting (on) at 20 kHz.
Figure 3.16: Push-pull Inverter setup with ferrite core transformer.
Figure 3.17: Temperature rise versus time of two MOSFETs (SW1 and SW2) at 10.5 kHz operation.
Figure 3.18: Inverter output wave across the tungsten filament bulb load for Table 3.6 (1000W).
Figure 3.19: Temperature rise versus time of two MOSFETs (SW1 and SW2) at 10.5 kHz operation.
Figure 3.20: Inverter output wave across the tungsten filament bulb load for Table 3.7.
Figure 3.21: Temperature rise versus time of two MOSFETs (SW1 and SW2) at 7.5 kHz operation.
Figure 3.22: Inverter output wave across the tungsten filament bulb load for Table 3.8.
Figure 3.23: Temperature rise versus time of two MOSFETs (SW1 and SW2) at 15 kHz operation.
Figure 3.24: Temperature rise versus time of two MOSFETs (SW1 and SW2) at 5 kHz operation.
Figure 3.25: Temperature rise versus time of two MOSFETs (SW1 and SW2) at 15 kHz operation
Figure 3.26: Temperature rise versus time of two MOSFETs (SW1 and SW2) at 7.5 kHz operation.
Figure 3.27: Inverter output wave across the tungsten filament bulb load for Table 3.10(15 kHz frequency).
Figure 3.28: Temperature rise versus time of two MOSFETs (SW1 and SW2) at 15 kHz operation.
Figure 3.29: Temperature rise versus time of two MOSFETs (SW1 and SW2) at 10 kHz operation.
Figure 3.30: Temperature rise versus time of two MOSFETs (SW1 and SW2) at 7.5 kHz operation.
Figure 3.31: Temperature rise versus time of two MOSFETs (SW1 and SW2) at 20 kHz operation.

Figure 3.32: Inverter output wave across the tungsten filament bulb load for Table 3.12(20 kHz frequency).
Figure 3.33: Stainless steel electrodes (SS 304, 316).
Figure 3.34: Gold plated Electrode.
Figure 3.35: Stainless Steel 304 Electrode EDX Graph (Control)
Figure 3.36: Stainless Steel 316 Electrode EDX Graph (Control)
Figure 3.37: Titanium Electrode EDX Graph of (Control)
Figure 3.38: Gold plated Electrode EDX Graph of (Control)
Figure 3.39: SEM image of a 0.5% NaCl solution.
Figure 3.40: SEM image of a 0.5% NaCl solution.
Figure 3.41: 0.5% NaCl solution's EDX (SS 304).
Figure 3.42: 0.5% NaCl solution's EDX (SS 316 electrode).
Figure 3.43: 0.5% NaCl solution's rough surface (unclean electrode).
Figure 3.44: 0.5% NaCl solution's flat surface (SS 304).
Figure 3.45: 0.1% NaCl solution for gold plated electrode.
Figure 3.46: 0.1% NaCl solution for gold titanium electrode.
Figure 3.47: SEM image of a 1% NaCl solution
Figure 3.48: SEM image of a 1% NaCl solution.
Figure 3.49: Parallel plate electrode setup
Figure 3.50: Output voltage wave across NaCl solution for 10 kHz.
Figure 3.51: Corrosion of electrodes made of stainless steel for different frequency (50 Hz- 5 kHz- 10 kHz).
Figure 3.52: (a,b,c): System Current vs. Time & Temperature of liquid (1% NaCl solution) vs. Time for variable operating frequency
Figure 3.53: (a,b,c): System Current vs. Time & Temperature of liquid (2% NaCl solution) vs. Time for variable operating frequency
Figure 3.54: Output voltage wave across NaCl solution for 20 kHz.
Figure 3.55: Corrosion of electrodes made of stainless steel for different frequency (50 Hz- 20 kHz).
Figure 3.56: Output voltage wave across coconut water at 10.36 kHz frequency.
Figure 4.1: Pin descriptions of ATmega328P IC.
Figure 4.2: Driver Circuit design in Proteus software.
Figure 4.3: 1 kHz frequency alternate pulses before the optocoupler (yellow and blue) and after the optocoupler (red and green).

Figure 4.4: 3 kHz frequency alternate pulses before the optocoupler (yellow and blue) and after the optocoupler (red and green).
Figure 4.5: 5 kHz frequency alternate pulses before the optocoupler (yellow and blue) and after the optocoupler (red and green).
Figure 4.6: 10 kHz frequency alternate pulses before the optocoupler (yellow and blue) and after the optocoupler (red and green).
Figure 4.7: 12.5 kHz frequency alternate pulses before the optocoupler (yellow and blue) and after the optocoupler (red and green).
Figure 4.8: 16 kHz frequency alternate pulses before the optocoupler (yellow and blue) and after the optocoupler (red and green).
Figure 4.9: Testing of driver circuit using Arduino Uno.
Figure 4.10: 1 kHz frequency alternate pulses from ATmega328P microcontroller IC.
Figure 4.11: 2 kHz frequency alternate pulses from ATmega328P microcontroller IC.
Figure 4.12: 3 kHz frequency alternate pulses from ATmega328P microcontroller IC.
Figure 4.13: 5 kHz frequency alternate pulses from ATmega328P microcontroller IC.
Figure 4.14: 10 kHz frequency alternate pulses from ATmega328P microcontroller IC.
Figure 4.15: 12 kHz frequency alternate pulses from ATmega328P microcontroller IC.
Figure 4.16: 16 kHz frequency alternate pulses from ATmega328P microcontroller IC.
Figure 4.17: Push-pull inverter setup with microcontroller based driver.
Figure 4.18 (a, b,c): 1.2 kHz output pulses from secondary side of optocoupler 6N136.
Figure 4.19 (a, b, c): 2 kHz output pulses from secondary side of optocoupler 6N136.
Figure 4.20 (a, b, c): 3 kHz output pulses from secondary side of optocoupler 6N136.
Figure 4.21 (a, b, c): 5 kHz output pulses from secondary side of optocoupler 6N136.
Figure 4.22 (a, b, c): 10.3 kHz output pulses from secondary side of optocoupler 6N136.
Figure 4.23 (a, b, c): 12 kHz output pulses from secondary side of optocoupler 6N136.
Figure 4.24 (a, b, c): 16.3 kHz output pulses from secondary side of optocoupler 6N136.
Figure 4.25: Delay pulses from optocoupler output.
Figure 4.26: 1 kHz alternate pulses across Gate-Source of MOSFET-inverter without applying drain voltage.
Figure 4.27: 2 kHz alternate pulses across Gate-Source of MOSFET-inverter without applying drain voltage.
Figure 4.28: 3.17 kHz alternate pulses across Gate-Source of MOSFET-inverter without applying drain voltage.
Figure 4.29: 5 kHz alternate pulses across Gate-Source of MOSFET-inverter without

applying drain voltage.
Figure 4.30: 10 kHz alternate pulses across Gate-Source of MOSFET-inverter without applying drain voltage.
Figure 4.31: 12 kHz alternate pulses across Gate-source of MOSFET-inverter without applying drain voltage.
Figure 4.32: 16.1 kHz alternate pulses across Gate-Source of MOSFET-inverter without applying drain voltage.
Figure 4.33 (a, b, c): Driver output pulses across Gate-Source while MOSFETs are conducting (On) in inverter operation at 2 kHz.
Figure 4.34 (a, b, c): Inverter output for 2 kHz frequency at no load condition.
Figure 4.35 (a, b): Driver output pulses across Gate-Source while MOSFETs are conducting (On) in inverter operation at 10.11 kHz.
Figure 4.36 (a, b, c): Inverter output for 10 kHz frequency at no load condition.
Figure 4.37: Inverter output in loaded condition at 3 kHz.
Figure 4.38: Inverter output in loaded condition at 10.40 kHz.
Figure 4.39: Driver output pulses across Gate-Source while MOSFETs are not in proper function.
Figure 5.1: Weighing scale machine.
Figure 5.2: Digital conductivity meter.
Figure 5.3: LCR Meter Bridge with experimental setup.
Figure 5.4: Furnace chamber and digital conductivity meter.
Figure 5.5: Temperature dependence of DC electrical conductivity.
Figure 5.6: DC Conductivity and Activation Energy for different compositions.
Figure 5.7: Cole-Cole plot of different food samples.
Figure 5.8(a, b): Frequency dependent ac conductivity of 0.1% KCl solution with distilled water.
Figure 5.9(a, b): Frequency dependent ac conductivity of 1% NaCl solution with distilled water.
Figure 5.10(a, b): Frequency dependent ac conductivity of 2% NaCl solution with distilled water.
Figure 5.11(a, b): Frequency dependent ac conductivity of coconut water.
Figure 5.12(a, b): Frequency dependent ac conductivity of orange juice.
Figure 5.13(a, b): Frequency dependent ac conductivity of sugar cane juice.
Figure 5.14: AC conductivity (σ_{ac}) for low, medium, and high frequencies for all

compositions.
Figure 5.15(a, b, c): SEM micrograph of green coconut water.
Figure 5.16: EDX result of green coconut water (Titanium electrode)
Figure 5.17: EDX result of green coconut water (Flat portion, Titanium electrode)
Figure 5.18: Identified elements deposited on the above-mentioned electrode surfaces
Fig 5.19(a, b, c, d, e, f, g, h, i, j, k): Elemental Line Scan of green coconut water (Titanium Electrode).
Figure 6.1: Equivalent circuit of push pull type MOSFET-Inverter.
Figure 6.2: Variation of flux linkages with respect to current passing through the coil.
Figure 6.3: Modeling design of the system.
Figure 6.4: Square wave AC (VS) at 5 kHz frequency.
Figure 6.5: Secondary side voltage of the transformer at 5 kHz frequency.
Figure 6.6: Square wave AC (VS) at 10 kHz frequency.
Figure 6.7: Secondary side voltage of the transformer at 10 kHz frequency.
Figure 6.8: Square wave AC (VS) at 20 kHz frequency.
Figure 6.9: Secondary side voltage of the transformer at 20 kHz frequency.
Figure 6.10: Square wave AC (VS) at 25 kHz frequency.
Figure 6.11: Secondary side voltage of the transformer at 25 kHz frequency.
Figure 6.12: Square wave AC (VS) at 50 kHz frequency.
Figure 6.13: Secondary side voltage of the transformer at 50 kHz frequency.
Figure 6.14: Square wave AC (VS) at 100 kHz frequency.
Figure 6.15: Secondary side voltage of the transformer at 100 kHz frequency.
Figure 6.16(a, b): Secondary side voltage of the real transformer.

List of Tables

Table 2.1: Comparison of different type semiconductor switches.
Table 2.2: Absolute maximum rating of 2SK727 MOSFET.
Table 2.3: Thermal analysis of an inverter MOSFET operating at 5 kHz using IRF840 as the switching device.
Table 2.4: Thermal analysis of an inverter MOSFET operating at 8 and 5.9 kHz using IRF840 as the switching device.
Table 2.5: Thermal analysis of an inverter MOSFET operating at 10 kHz using IRF840 as the switching device.
Table 2.6: Thermal analysis of an inverter MOSFET operating at 10 kHz using IRF840 as the switching device.
Table 2.7: Thermal Study of Inverter MOSFET (2SK727) at 10 kHz.
Table 3.1: Thermal Study of Inverter MOSFET (IRF840) at 10.5 kHz.
Table 3.2: Thermal Study of Inverter MOSFET (IRF840) at 10.5 kHz.
Table 3.3: Thermal Study of Inverter MOSFET (IRF840) at 7.5 kHz.
Table 3.4: Thermal Study of Inverter MOSFET (IRF840) at 15 and 5 kHz.
Table 3.5: Thermal Study of Inverter MOSFET (2SK727) at 15 and 7.5 kHz.
Table 3.6: Thermal Study of Inverter MOSFET (2SK727) at 15 and 10 kHz.
Table 3.7: Thermal Study of Inverter MOSFET (2SK727) at 7.5 and 20 kHz.
Table 3.8: 304-grade stainless steel electrode (control)
Table 3.9: 316-grade stainless steel electrode (control)
Table 3.10: Titanium Electrode (Control)
Table 3.11: Gold plated Electrode (Control)
Table 3.12: Results of the 0.5% NaCl solution's EDX (SS 304).
Table 3.13: Results of the 0.5% NaCl solution's EDX (SS 316 electrode).
Table 3.14: EDX result of the 0.5% NaCl solution's rough surface (unclean electrode).
Table 3.15: EDX result of 0.5% NaCl solution's flat surface (SS 304).
Table 3.16: EDX result of 0.1% NaCl solution for gold plated electrode.
Table 3.17: EDX result of 0.1% NaCl solution for gold titanium electrode.
Table 3.18: Results for 1% & 2% Nacl solution at different frequencies.
Table 5.1: Variation of DC conductivity with temperature.
Table 5.2: Activation Energies (Ea) for Different Compositions.
Table 5.3: EDX result of green coconut water (Titanium electrode)
Table 5.4: EDX result of green coconut water (Flat portion, Titanium electrode)
Table 5.5: Chemical Composition of green coconut water (Pradesh et al., 2012)

LIST OF ABBREVIATIONS

AC	: Alternating Current
BJT	: Bipolar Junction Transistor
CSI	: Current Source Inverter
CFI	: Current Fed Inverter
DC	: Direct Current
EDX	: Energy Dispersive X-ray Spectroscopy
ELS	: Element Line Scan
GTO	: Gate Turn-Off thyristor
IC	: Integrated Circuit
IGBT	: Insulated Gate Bipolar Transistor
KCL	: Potassium Chloride
kHz	: Kilohertz
MCT	: MOS Controlled Thyristor
MHz	Megahertz
MOSFET	: Metal Oxide Semiconductor Field Effect Transistor
PWM	: Pulse Width Modulation
PCB	: Printed Circuit Board
SCR	: Sillcon Controlled Rectifier
SIT	: Static Induction Transistor
SITH	: Static Induction Thyristor
SEM	: Scanning electron microscopy
VSI	: Voltage Source Inverter
VFI	: Voltage Fed Inverter

Chapter-1

INTRODUCTION

1.1 General introduction

Ohmic heating, in which liquid food is heated using electrical energy, is essentially a form of resistive heating. If R is the resistance of the food solution or liquid beverages, then electrical power dissipated in the beverage is-

$$P_{electrical} = I^2R \quad (1.1)$$

Where, I= Electrical current passing through liquid food material.

Heat balance equation is as given below:

$$I^2Rt = mS(\theta_2-\theta_1) \quad (1.2)$$

Where,

m= Mass of the food or liquid beverages

S=Specific heat

θ_1=Initial temperature of the beverages

θ_2= Final temperature of the beverages

t= Time period of heating

The presence of salts and acids in liquid food products enhances electrical conductivity, enabling efficient ohmic heating [1]-[7]. However, electrode corrosion is a challenge, particularly with low-frequency AC currents. Research suggests that:

a) Higher frequencies reduce corrosion.

b) AC-induced electrolysis contributes to corrosion.

c) Voltage frequency and amplitude impact corrosion behavior.

Understanding these factors is crucial in designing effective and safe ohmic heating systems for food processing exploring electrode materials, frequency optimization or corrosion mitigation strategies which aids further to this work.

Ohmic heating is an innovative technique gaining momentum, especially in food processing technique. Its potential benefits include:

i) Rapid heating

ii) Uniform temperature distribution

iii) Energy efficiency

The significance of frequency is in ohmic heating performance, particularly regarding electrolysis and gas evolution. Researching optimal frequency range could enhance the effectiveness of the technique and safety prospects to explore applications, benefits or challenges of ohmic heating further. Therefore, research regarding how frequency affects ohmic heating performance must be prioritized. The effectiveness of the technique depends on factors like electrical conductivity, which varies with salt content in juices. This work aims to develop an electrical power supply for ohmic heating, which could largely benefit the food industry by a study to design considerations, applications or potential challenges in implementing ohmic heating for liquid beverages [8]-[16].

Latest studies have emphasized system scale-up operation at higher frequencies (in the kHz range), the development of corrosion-resistant electrode materials, and the use of predictive computational tools to support continuous industrial-scale processes. Despite these advances, electrode degradation and the risk of metal leaching remain the major challenges preventing broad commercial adoption in this sphere [17]-[35]. Even though low frequency ohmic heater is common and easier to design, the use of heavy transformers and expensive inert electrodes are required in order to prevent electrolysis to happen. On the other hand, the high frequency ohmic heater allows the use of much more light weight magnetic devices and cheaper electrodes. In this study, it has been discovered that increasing the frequency minimizes the corrosion in the process of ohmic heating of liquid conducting system for a particular electrode.

1.2 Objectives of the work

This study and design considerations, applications and potential challenges in implementing ohmic heating for liquid beverages needs the following-

- Study and design considerations, applying a higher frequency greater than 50Hz power inverter is suggested here for experimenting in ohmic heating to reduce electrode corrosion and the size of power supply.
- Study and design considerations, application of different driver circuit for experiment in switching operation of MOSFET-inverter at various frequencies for stable operations.

- Study and design considerations, applications and experiment to find out the frequency where the corrosion of electrodes in ohmic heating for liquid beverages is totally eliminated.

1.3 Contribution of the thesis

The following works have been performed under this thesis:

1. Different variable high frequency gate drivers has been designed and developed with various integrated circuits (IC) and solid-state components for inverter.

2. Two different types of power inverters having variable frequency ; one is half bridge (H-bridge) and another is push-pull inverter using ferrite core have been designed and developed with various integrated circuits (IC) and solid-state components.

3. Designed and experimented Arduino Uno based driver using microcontroller ATmega328P, 8-bit AVR (Advanced Virtual RISC) for push-pull inverter which offers significant advantages including higher precision, faster switching speeds, lower power consumption and better noise immunity.
4. The study of electrical conductivity in different liquid samples, including fruit juices: Conductivity measurement is done and analytical method is adopted to understand the ionization and conductivity properties of different liquids which are necessary for ohmic heating process using developed high frequency inverter supply.
5. A mathematical model of push-pull inverter is designed and developed using a ferrite core transformer used in high-frequency applications. This non linear model has been implemented in MATLAB (Matrix Laboratory) and results and analysis are computed for different frequencies to find solutions of experimental difficulties.

1.4 Thesis organization

The thesis is organized as follows and the research work outline is divided into seven distinct chapters.

Chapter 1: The procedure of ohmic heating liquid beverages has been briefly described. Ohmic heating is thoroughly reviewed in the literature, covering both contemporary and conventional control techniques as well as heuristic approaches. The goal of the dissertation (Design a high frequency power inverter having variable frequency provision), the rationale

behind the current endeavor, and the extent of the thesis' organization are all covered in this introductory chapter.

Chapter 2: The objective of this chapter is to explain different approaches associated with designing inverter driver circuits to control the MOSFETs. A variable high frequency gate driver has been designed and developed with various integrated circuits (IC) and solid-state components. The salient components and features of this driver circuit developed are discussed in this chapter. Power inverter (H-bridge) is proposed here.

Chapter 3: The design of high frequency power inverter having variable frequency provision has been developed applying the gate driver signal. This power supply unit is designed along with the copy of the data sheet style. Power inverter push-pull type using ferrite core is proposed in this chapter. Details of the design calculations and experimental results are also discussed in this chapter.

Chapter 4: The objective of this chapter is to design digital driver using microcontroller for push-pull inverter which offer significant advantages including higher precision, faster switching speeds, lower power consumptions and better noise immunity. Their ease of integration with modern digital systems and reduced component complexity make them the preferred choice for efficient and reliable circuit design.

Chapter 5: The study of electrical conductivity in different liquid samples, including fruit juices is a significant tool across multiple fields. Conductivity measurement is a non-destructive, quick and cost-effective analytical method making it widely applicable in laboratory research and industrial applications discuss in this chapter. It is also an essential tool in scientific experiments, where understanding the ionization and conductivity properties of different liquids is necessary for ohmic heating processes using high frequency inverter supply.

Chapter 6: The objective of this chapter is to design, develop and model a push-pull inverter using a ferrite core transformer as this type of inverter is used in high-frequency applications. The modeling results and analysis at different frequencies are presented in this chapter.

Chapter 7: This chapter concludes with a summary of the thesis's overall effort and also makes recommendations for the extent of future research on numerous facets of ohmic heating using high frequency supply.

Chapter-2

REVIEW AND DEVELOPMENT OF HIGH-FREQUENCY INVERTER OHMIC HEATING SYSTEM IN LABORATORY

2.1 Introduction

The design of ohmic heaters can be approached in two ways:

i) Low-frequency ohmic heaters: Easier to design, but requires heavy transformers and expensive inert electrodes to prevent electrolysis.

ii) High-frequency ohmic heaters: Allowed for lighter magnetic devices and cheaper electrodes, reducing corrosion and pollution.

A high-frequency ohmic heater seems to offer advantages in terms of design and cost. The study suggests that high-frequency (HF) power supplies can minimize electrode corrosion in ohmic heating systems [36]-[45]. This is a valuable finding, as corrosion can impact system efficiency and longevity. By adopting high-frequency power supplies, ohmic heating systems could benefit from: Reduced electrode corrosion, increased system lifespan, improved overall efficiency. This research aims to investigate the relationship between frequency and corrosion in ohmic heating systems by designing high-frequency square wave inverter with variable frequency provision, so that it can determine the optimal frequency to minimize or eliminate corrosion, enhance the efficiency and lifespan of ohmic heating systems. Testing this inverter with simulated liquid beverages will provide valuable insights into the corrosion behavior. The development of high-performance driver circuits for inverter is crucial. Research and testing are necessary to ensure reliable and efficient operation. Some key considerations for driver circuit development include: Compatibility with power electronics switches, high-frequency operations, efficient switching and protection features.

Developing a high-frequency inverter power supply is crucial for ohmic heating systems to effectively kill bacteria. The challenge lies in creating an inverter with cutting-edge technical characteristics, specifically: High-frequency AC output (up to several kHz) & reliable power electronics switches and driver circuits. Laboratory testing and research are necessary to overcome these challenges and make this technology commercially viable. This work also discusses the design considerations, potential applications, or challenges in developing this technology further.

In the field of power electronics, the term inverter refers to a category of power conversion (or power conditioning) circuits that operate from a direct current (DC) voltage or current source and convert it into an alternating current (AC) voltage or current. An inverter performs the inverse function of an AC-to-DC converter. Although the input to an inverter is typically a DC source, it is often derived from an AC supply, such as a utility grid. For instance, the primary power input may be an AC utility supply, which is first converted to DC using an AC-to-DC converter, and subsequently inverted back to AC using an inverter. In such cases, the final AC output may differ in frequency and magnitude from the original AC input supplied by the utility.

Inverter can be broadly classified into two types:

a) Voltage Source Inverter (VSI) or Voltage Fed Inverter (VFI)
b) Current Source Inverter (CSI) or Current Fed Inverter (CFI)

The key points of these inverter topologies are, Voltage Source Inverter (VSI): Controls output AC voltage, suitable for applications requiring voltage regulation. Whereas Current Source Inverter (CSI): Controls output AC current, often used in applications requiring current regulation. In VSI design, achieving output voltage waveforms, independent of load is crucial for stability and performance.

Inverter can also be classified into single phase inverter and three phase inverter. The three main realizations of inverter are in the following forms:

I) Half –bridge inverter, II) Full-bridge inverter and III) Push-pull inverter.

This chapter focuses on the specifics of the half-bridge inverter design, including: Design procedures, driver circuit details, experimental results. These details will provide valuable insights into the performance and potential limitations of the half-bridge inverter.

2.2 Single-phase half-bridge inverter (VSI)

The single-phase half-bridge MOSFET-inverter shown in Fig. 2.1 operates by turning on *SW1* (upper MOSFET) for T/2, applying $V_{DC}/2$ across the load and turning on *SW2* (lower MOSFET) for the next T/2, reversing current direction where T is the total time period of an alternating wave. This switching pattern generates an AC output. Key considerations are preventing simultaneous switching of *SW1* and *SW2* and generating V_{DC} from a 50 Hz AC source using a bridge rectifier and filter circuit.

This work explores the control circuit design, bridge rectifier and filter circuit details further.

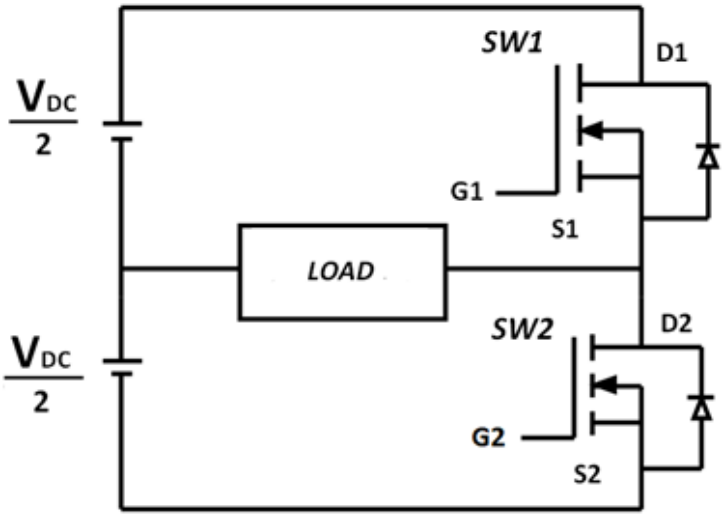

Figure 2.1: Half bridge MOSFET-inverter circuit.

2.3 Design of driver circuit for half bridge inverter

High-frequency inverter is crucial, and driver circuit design plays a pivotal role in achieving reliable and efficient operation for ohmic heating process to determine the frequency that eliminates corrosion. Therefore the key factors to be considered here are driver circuit design for high-frequency operation and inverter performance and reliability. This work discusses the driver circuit design considerations or potential experimental approaches further. The driver circuit needs to be designed or modified to; allow frequency adjustments under load and enable duty cycle changes under load. This will provide the flexibility to optimize the inverter's performance for corrosion reduction in ohmic heating application. Hence the key design considerations include:

a) Dynamic frequency control
b) Duty cycle adjustment
c) Reliability under varying load conditions

The primary function of a driver circuit is to generate a control voltage signal with varying frequency and pulse width, switch the power electronics switch on and off efficiently. Therefore the key design goals are low cost, fast turn-on and turn-off time and minimize

power dissipation during switching. The driver circuit's role in the on-state; providing adequate drive power (e.g. gate-source voltage for MOSFETs) to minimize conduction losses, ensuring the power switch remains in the on-state. In the off-state; providing reverse bias to minimize turn-off time, preventing unintended triggering due to stray transient signals. This ensures efficient and reliable operation of the power switches. This work explores specific design considerations or techniques for achieving these goals further [46]. To explore the driver circuit solutions for MOSFETs or IGBTs in inverter applications the key aspects are performance analysis under various conditions, parasitic component effects and transient and extreme operating conditions. The design procedures cover ground-referenced gate drive circuits, high-side gate drive circuits and coupled and transformer-isolated solutions. This research will help optimize driver circuit design for reliable and efficient inverter operation. This work discusses specific design challenges, component selections and experimental results further.

2.3.1 Choice of switching device

The selection of power switches depends on various factors:

i) Cost
ii) Availability of suitable ratings
iii) Ease of switching (on/off control)
iv) Forward voltage drop (impacting efficiency)

Ongoing advancements in power electronics introduces new devices and improve the existing ones, offering better performance and capabilities. In this work specific power switch options, application requirements, or design considerations has been discussed further.

Various solid-state power switches are compared in the table below-

Device	**Turn -on**	**Turn-off**	**Rating (upper)**	**Forward voltage drop**	**Switching time(μs)**
Thyristor	Short duration gate pulse	Zero current or voltage reversal	1200V/1500A	1.5V	20
Triac	As Thyristor	As Thyristor	1200V/300A	1.7V	20
GTO	As Thyristor	Reverse voltage gate pulse	1200V/600A	2.2V	25
BJT	Application of base current	Removal of base current	400V/250A	1.1V	10
Power transistor as Darlington	As BJT but lower base current	As BJT	900V/200A	1.5V	40
MOSFET	Application of gate voltage	Removal of base voltage	600V/40A	1.2V	>0.5
IGBT	Application of gate voltage	Removal of base voltage	1200V/50A	3.0V	>1

Table 2.1: Comparison of different type semiconductor switches.

MOSFETs and IGBTs are suitable for high-frequency inverter applications due to voltage-controlled operation that can be switched on and off by controlling the voltage across their gate-source (or gate-emitter) junction, nearly zero gates current during on state and high-frequency capability (1 kHz to 20 kHz or more). Their limitations include lack of reverse blocking capability. Despite this, they're ideal for this work due to their high-frequency performance. The specific design considerations, such as heat management or gate drive design for MOSFETs or IGBTs in this inverter application has been discussed further. They have high input impedance; can switch at high speeds, and support high current capacities. However, MOSFETs have a relatively high forward voltage drop and lower breakdown voltage compared to IGBTs. The limitations of IGBTs are discussed below.

1. IGBTs have lower switching speeds compare to MOSFETs, partly due to the tail current effect they exhibit during turn-off, as shown in Fig 2.2. Higher switching losses compare to MOSFETs, causes by the tail current effect.

2. Possibility of uncontrollable latch-up (stay on) under overstress condition (High dv/dt or di/dt).

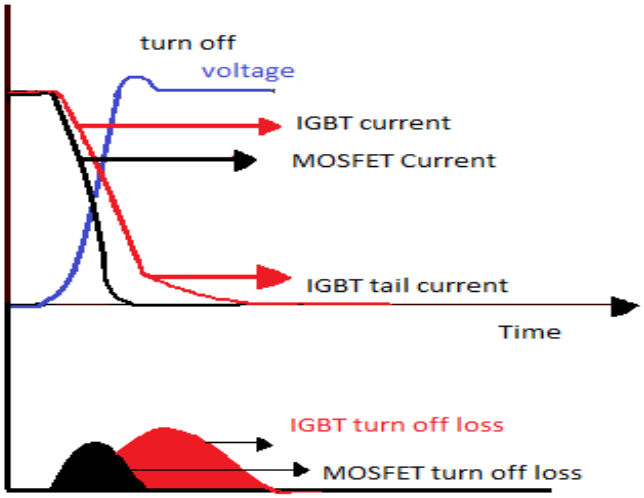

Figure 2.2: MOSFET and IGBT turn off behavior.

Clear selection criterions for MOSFETs vs. IGBTs are MOSFETs Suitable for Low-voltage (<300V), Low-to-medium power (<10kW) and high-frequency applications whereas IGBT is advantageous for higher voltage requirements. Therefore for a high-frequency inverter project MOSFETs are chosen for their suitability.

2.3.2 MOSFET

Ideal switch characteristics are zero on-resistance, infinite blocking voltage, no parasitic inductance, instantaneous switching and minimal energy for state change. Solid-state transistors, like MOSFETs, closely approximate these ideals, enabling efficient power switching circuits for various applications. Key requirements for switching devices are fast switching times relative to operating frequency (≤5% of period), suitability for high-frequency operation (MHz range). MOSFETs, particularly n-channel enhancement types, are well-suited due to fast switching times and majority carrier operation, eliminating minority carrier recombination delays. Their characteristics make them ideal for high-frequency switch-mode circuits. A cross-sectional view of an N-channel enhancement-type MOSFET is shown in Fig 2.3.

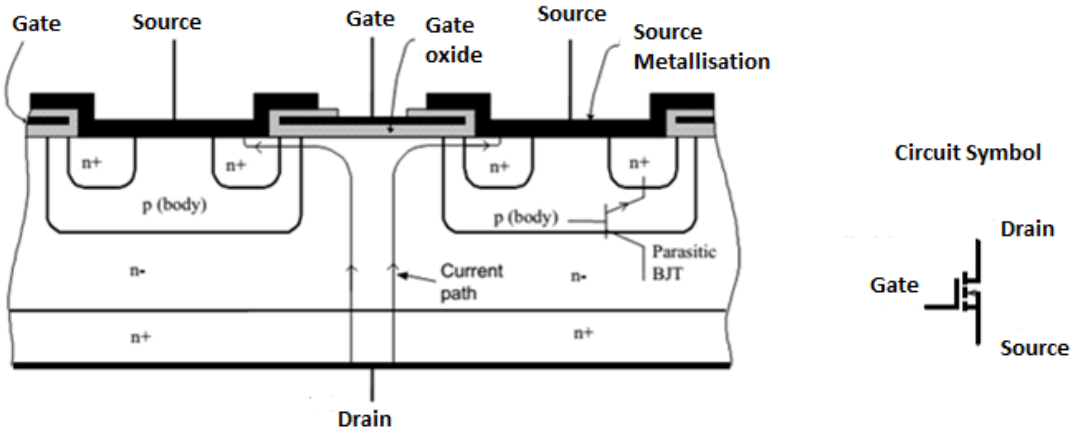

Figure 2.3: Structure of a vertical n-channel enhancement-type MOSFET and circuit symbol.

Theoretically MOSFET bandwidth limitations are channel length and charge carrier drift velocity determines switching time. Example; 1-micron channel length yields 12ps theoretical switching time. Practical limitations parasitic capacitances (die structure), stray impedances (packaging) and gate voltage change rate determines actual switching time. These external factors, rather than inherent physics, limit MOSFET switching speed. This research discusses gate drive design or parasitic mitigation strategies. Fig 2.4 shows the approximate equivalent circuit model of a power MOSFET. In the equivalent circuit, the various parasitic elements of the MOSFET are modeled as lumped components and these are added externally to an ideal MOSFET.

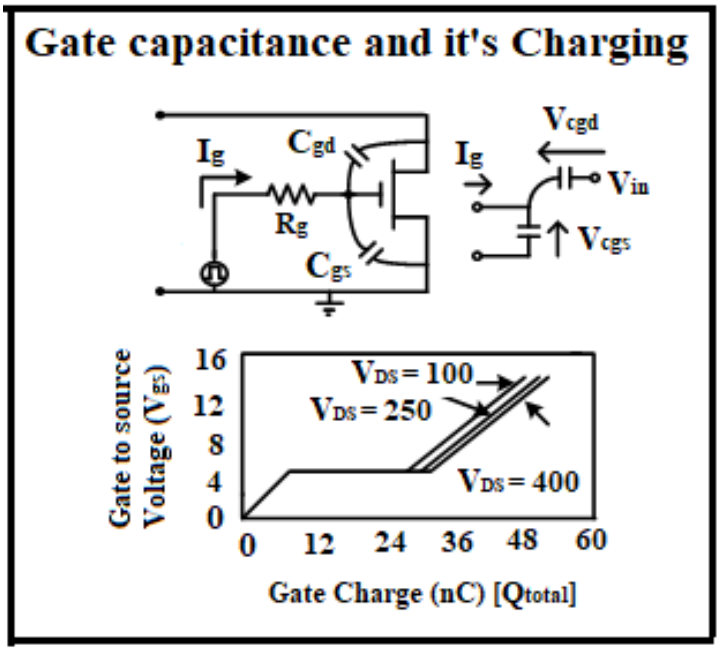

Figure 2.4: Approximate equivalent input circuit of a MOSFET gate.

Key factors for high-frequency MOSFET operation are gate resistance (R_g); distributed internal resistance affecting switching speed, gate capacitances C_{gd} (gate-drain) and C_{gs} (gate-source) form an RC (Resistance-Capacitance) network with R_g. Hence optimizing high-frequency performance requires minimizing the gate resistance (R_g) and gate capacitances (C_{gd} and C_{gs}). This enables faster switching times and efficient operations.

The short circuit between the source and the substrate gives MOSFETs an inherent reverse diode. The inverter is presumed to never function in the capacitive mode (i.e., a leading load current) in the MHz range. The reverse recovery ratings of the diode are therefore unimportant because it can be assumed that the MOSFET's integral diode never conducts at the end of the conduction period. A negative voltage across the MOSFET results when the midpoint voltage swings below or above the corresponding rail voltage due to excessive charge extraction from the midpoint during the dead time. At the start of the conduction period, this can cause the internal diodes to conduct briefly before the current reverses direction. The quantity of charge that passes through the diode at MHz frequencies is much lower than the reverse recovery charge. The MOSFET then conducts forward current normally when the current flowing through it reverses its direction. The charge taken out of the diode is therefore returned by the forward current. The key points regarding MOSFET turn-off and diode conduction; MOSFET turn-off dv/dt may be affected by charge removal from the integral diode during conduction and Non-linear output capacitance increases rapidly near zero drain-source voltage, preventing reverse diode conduction under normal load conditions. These factors impact MOSFET behavior and diode conduction in high-frequency applications. These works explores further the impact of output capacitance and investigate specific load conditions [46]-[47]. The main objectives are investigating feasibility of producing high-frequency power in the HF-band; maximize high-frequency power output using two MOSFETs. Whereas the key considerations are maximize DC power handling capability ($V_{DS} \times I_D$, V_{DS} Drain to source voltage, I_D Drain current), optimize MOSFET selection depends on high power ratings (500-600V region) and minimal capacitances for high-frequency operations. This approach aims to achieve the highest practical frequency and power output. Discuss specific MOSFET selection criteria and design optimization strategies in more detail. Trade-offs in MOSFET selection depends on higher current rating (larger die size) increases parasitic capacitances and Larger output capacitance which is decreases upper operating frequency, reduces power output and increases capacitive switching losses (non-zero voltage switching). Therefore balancing current rating and capacitance is crucial for optimal high-frequency performance.

It is always possible to add external discrete capacitance if it turns out to be required. When a MOSFET is switched at higher frequencies the primary limiting issue is driving the gate capacitance. The power dissipation in the internal gate resistance and gate-driver becomes problematic as the switching frequency is raised and the gate drive currents become excessive. Therefore, for high-frequency operation the internal distribution gate resistance, reverse transfer capacitance and gate-source capacitance should all be as low as possible. The MOSFET should have the highest power dissipation capacity because this will lower its operating temperature and improve its dependability when the load is mismatched. Another specification of importance is the ability of withstanding large voltage slew rates (dv/dt) at turn-off, higher operating frequency and higher current and higher supply voltage [48]. There is a distinction between normal turn-off dv/dt and reverse diode recovery dv/dt, whereas off-state dv/dt is not typically specified by manufacturers. Therefore, 100 V/ns for a 500 V MOSFET should be adequate for high-frequency operation. These researches discuss design implications or specific applications requiring high dv/dt capability. The switching performance will also be significantly impacted by any external stray impedance that is introduced to the MOSFET as a result of packaging and layout. The packaging should minimize the inductance of the gate, drain and source leads.

2.3.3 Switching losses

Switching losses in MOSFETs depends on Instantaneous power loss p (t) = $V_{DS} \times I_D$ during transitions, primary occurrence during crossover time (switching intervals) and increased with frequency, impacting operating temperature. So, minimizing switching losses is crucial for high-frequency inverter efficiency and maintaining MOSFET operating temperature within limits. Explore strategies to reduce switching losses or discuss thermal management for a high-frequency application is necessary [49].

- The sample calculation for switching loss is as follows:

Gate capacitance energy loss:

Energy store in equivalent capacitance C_{eq} is represented by $1/2(V_{gs})^2 \times C_{eq}$. Energy dissipated in R_g during charging is same as stored energy. Hence total loss is $(V_{gs})^2 \times C_{eq}$ (sum of turn-on and turn-off losses). This highlights the significance of gate capacitance and resistance in MOSFET switching losses. Now, if the driver's frequency is set to f, the total power needed (loss) equals $(V_{gs})^2 \times C_{eq} \times f$. Consequently, the gate drive needs to be capable of providing this power, which is contingent upon the frequency f. Therefore, the

need for gate drive power increases along with frequency. No ready-made inverter on the market can be pushed higher than the frequency at which it was intended.

In another manner, the needed energy (E) is $E=V_{gs}\times Q_{total}$, which must be delivered to the switch's gate terminal by the driver source if Q_{total} charge is used as the input to turn on the MOSFET. $P= V_{gs} \times Q_{total}\times f$ is the power equation for the frequency f. An example of this is provided below, assuming some random data.

- e.g.: $V_{gs} = 15V$,

  $Q_{total} = 10nC$,

  $f = 200$ kHz.

Hence required power for the gate of the MOSFET using above data is:

$P = 15 \times 10\times 10^{-9}\times 200\times 10^{3}= 30mW$.

So, it has been seen that if the frequency is increased the power required for the gate from the driver circuit will also be increased.

2.3.4 Driving the inverter

There are different ways to design a driver circuit for an inverter to control MOSFETs. The choice depends on factors like power needs, how fast it switches efficiency and complexity.

2.3.5 Principle of PWM

Electronic switches are found in an inverter. Thus, by executing multiple switching within the inverter with a constant DC input voltage it may optimize the harmonics and manage the output voltage. PWM works on the o/p voltage control principle.

2.3.6 Pulse Width Modulation (PWM) generator

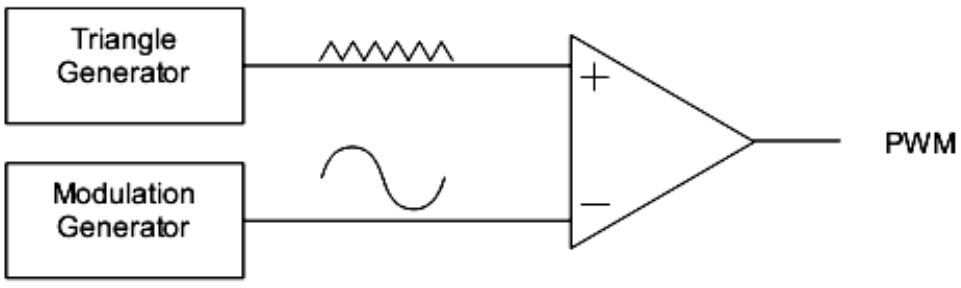

Figure 2.5: Pulse Width Modulation (PWM) generator.

The modulation generator generates a sine wave signal that controls the width of the pulses in Fig. 2.5 and, consequently, the RMS voltage output of the inverter, while the triangle signal serves as the inverter's carrier or switching frequency. Figure 2.6 displays the PWM generator's output.

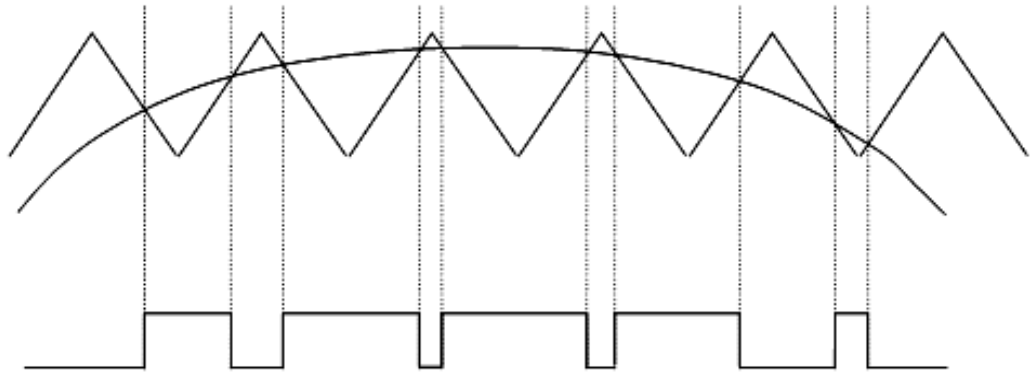

Figure 2.6: Output of PWM generator.

If a sinusoidal inverter output is required, PWM technology is applied. For each sinusoidal positive and negative half-cycle, switches turn on and off several times with varying pulse widths, resulting in high-frequency switching of solid-state devices (transistors, MOSFETs, and IGBTs). For example, for a 50Hz sine wave AC inverter output, the switching frequency becomes several times higher than 50Hz.

For a very high-frequency sinusoidal inverter (e.g., 20 kHz), the PWM switching frequency may need to be in the megahertz (MHz) range, making design and development challenging. To avoid this high switching frequency a high-frequency square wave inverter approach is adopted here. Since the inverter output is used for ohmic heating of liquid food, harmonics are less critical compared to applications involving other electrical loads, such as motors. Some potential approaches for designing the inverter driver circuit include.

2.3.7 Half bridge driver

The high and low-side switches must alternately be turned on and off at the appropriate frequency and duty-cycle in order for the half bridge inverter shown in Fig. 2.1 to work. The driving signal of the switch controls its state, which can be either on or off. The load network and the switches' output capacitance determine the necessary frequency and duty

cycle, where the duty cycle stays between 0% and 50%. The bandwidth of a half-bridge inverter can possibly go from DC to its highest practically possible working frequency because it is essentially an extremely broadband structure. The inverter driving circuitry must be able to drive the half-bridge inverter with a variable duty cycle and across the broadest range of frequencies in order to capitalize on this characteristic.

Key aspects of half-bridge inverter control:

i. Switch control via high and low-side drive signals
ii. PWM driver IC generates drive signals with variable frequency and duty cycle
iii. MOSFET gate capacitance charging/discharging crucial for switching
iv. Direct gate drive minimizes loop inductance, enabling fast switching
v. Independent power supply for gate drivers allows full bandwidth (MHz) operation

Fast switching times and variable duty cycle are essential for inverter performance.

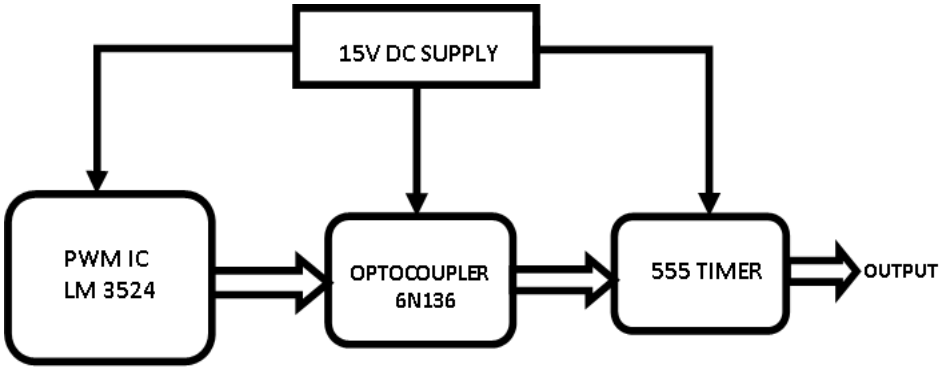

Figure 2.7: Block diagram of the driver circuit for MOSFET-inverter

The equivalent gate-source (C_{gs}) and gate-drain (C_{gd}) capacitance should be charged during turn on, along with the required charge (Q_{total}) with very short time shown in Fig 2.4. Data sheets for MOSFETs contain information on how much gate charge (Q_{total}) should be applied to the equivalent capacitance (C_{eq}). Hence, it can be said that gate current, $I_g=C_{eq}*V_{gsmax}/t_{on}$ for MOSFET. Where, V_{gsmax}=Maximum voltage across the capacitor C_{gs} and, t_{on}= Turn-on time of MOSFET. Depending on the inverter's power rating, this necessitates the right design of the driver power supply for this high gate current for a relatively brief period of time. Block diagram of the driver circuit for the MOSFET-inverter shown in Fig 2.7. PWM IC LM3524 has been used to construct a driver that controls the

inverter MOSFETs with the protective system. Isolation is very much needed for safety purpose of the outputs of PWM IC; optocoupler 6N136 is used to isolate the outputs of PWM IC from the power circuit. 555 timer is used here to enhance the charging current (I_g) of MOSFET at the time of turning on.

The fastest rise and fall times are possible by integrating the gate driver directly onto the same chip as the power MOSFET, which results in the lowest loop inductances [50]-[51]. This solution was left for future development because it was outside the project's scope and budget. Installing the gate driver straight from the gate to the source and designing the charging and discharging loop with the least amount of leakage inductance is the next best option. This was the method used for this inverter. The most practical method for creating the gate driver for this application, both financially and in terms of development time, is to use a PCB with a PWM IC: LM3524. Circuit diagram of said MOSFET driver is shown in Fig 2.8.

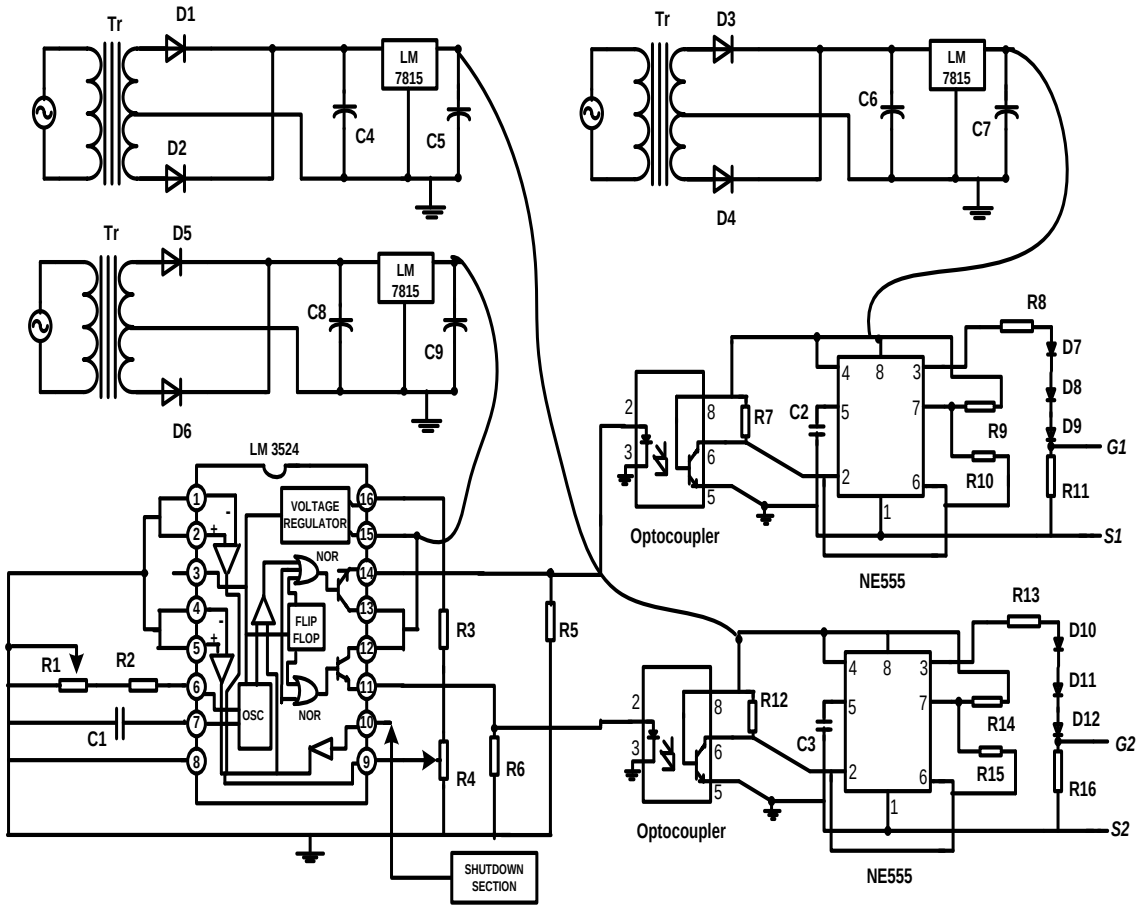

Figure 2.8: Driver circuit for half bridge inverter.

The various components and their functions in the developed driver circuit above are now being discussed.

2.4 Details of driver circuits parameters

Components are used to develop the driver circuit is given below-

2.4.1 Pulse Width Modulator IC LM3524

PWM IC LM3524 is used for the following reason:

- In switching regulator power supply, the IC LM3524 regulating Pulse Width Modulator (PWM) is frequently utilized as the control element.
- The IC LM3524 generates pulses, and its frequency can be adjusted.
- The width of the output pulses is also adjustable.

The internal block and pin diagram of the IC LM3524 are shown below in Fig 2.9, Fig 2.10, and Fig 2.11. Capacitor C_T and resistor R_T shown in Fig 2.9 are externally connected to pin numbers 6 and 7, respectively, for frequency control. The other pins perform their usual operations as per the IC LM3524 datasheet [52]. 15V DC input at pin no. 15 is necessary for activation of this IC. Pin No. 8 is connected to ground terminal. Pin No. 1 is the inverting input terminal and Pin No. 2 is the non-inverting input terminal of the internal error amplifier of IC LM3524. Pin No. 4 and 5 denote +CLSENSE and –CLSENSE terminal respectively. There is a reference voltage regulator within the IC which gives constant 5V DC output to its internal circuitry. To generate triangular wave for the internal oscillator of IC LM3524, a capacitor C_T is used. PWM pulses are generated at the output of this oscillator whose frequency can be varied by varying the value of the resistance R_T. Pulse width control is also possible by controlling the voltage drop across pin 9. Therefore a variable resistance is connected across pin 9 and pin 16 and variable point of this resistance is connected to ground pin 8, as pin 16 of IC LM3524 gives stable 5V. Finally two PWM pulses complementary to each other are obtained at the emitter terminal (pin 11 & 14) of the two internal transistors with respect to ground (blue and pink color).

Block Diagram of IC LM3524:

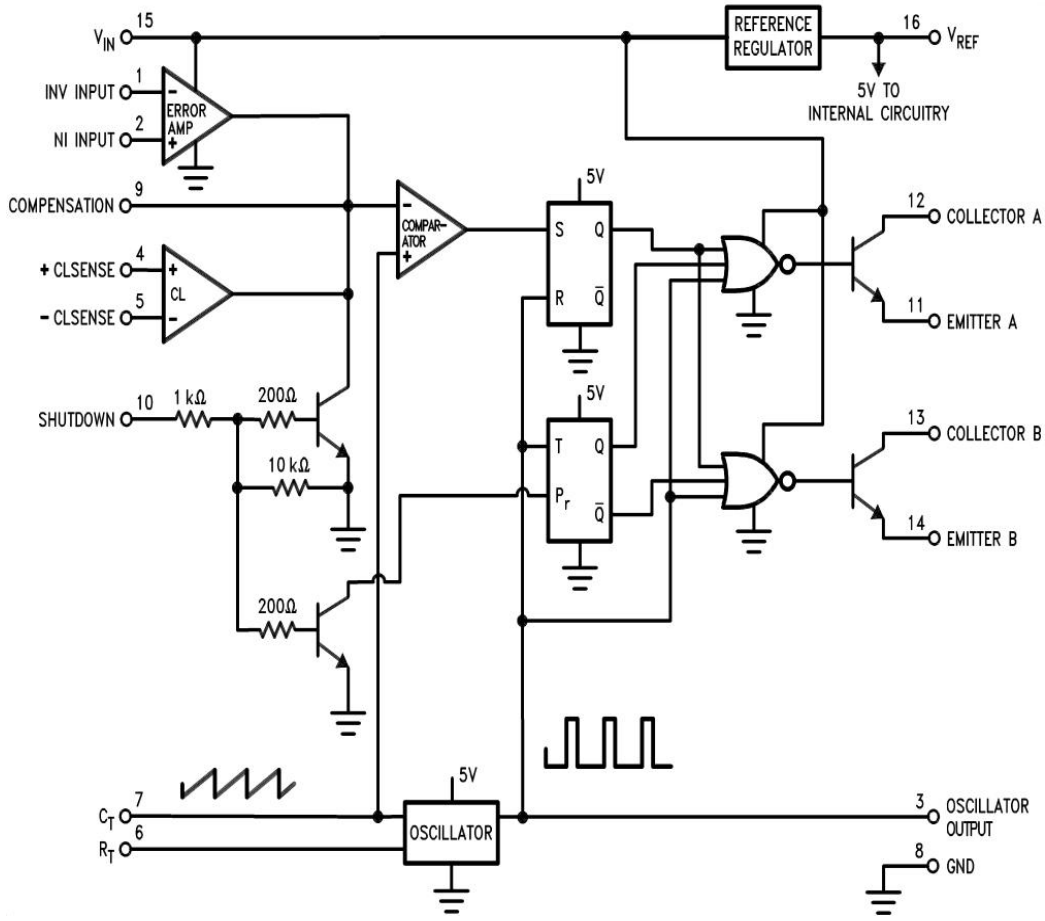

Figure 2.9: Block diagram of IC LM3524

PIN Diagram of IC LM3524:

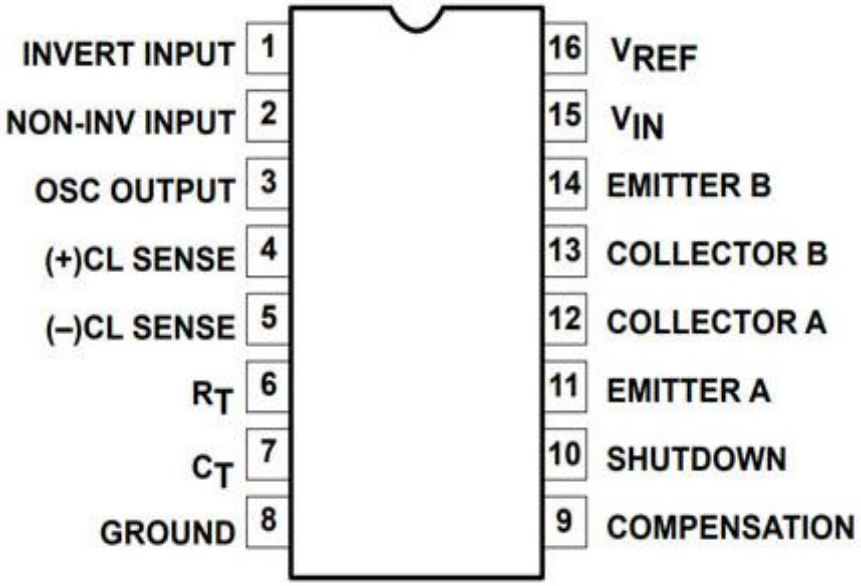

Figure 2.10: Pin diagram of IC LM3524

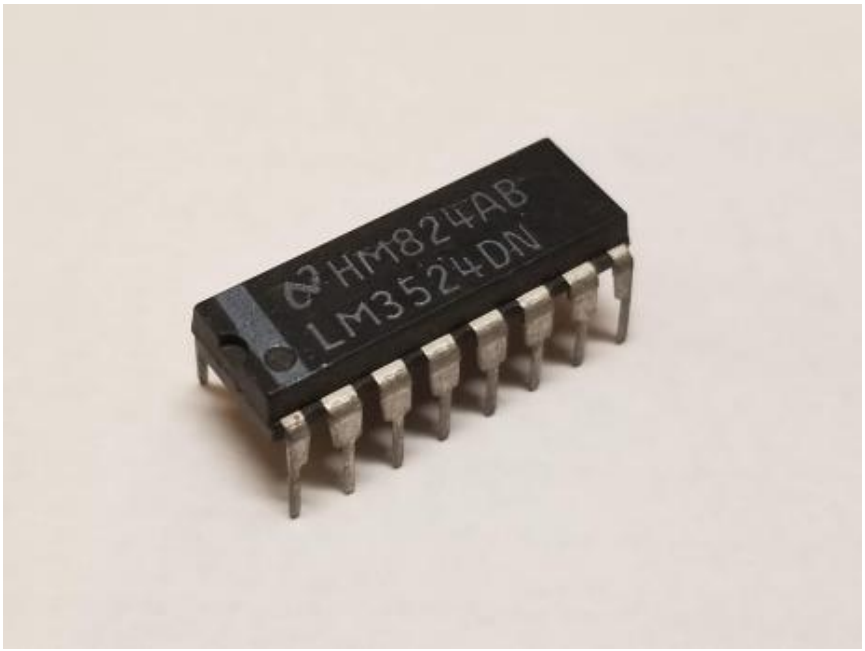

Figure 2.11: IC LM3524

Features of LM3524:

- 60V output capability
- Output current to 200mA DC
- Improved max. duty cycle at high frequencies
- Wide common mode input range for error-amp
- ±1% precision 5V reference with thermal shut-down
- Double pulse suppression
- One pulse per period (noise suppression)
- Synchronize through pin 3

Absolute Maximum Ratings:

- Collector supply voltage 55V
- Output current DC (each) 200 mA
- Supply voltage 40V
- Oscillator charging current (Pin 7) 5 mA
- Operating junction temperature-40°C to +125°C Range
- Internal power dissipation 1W

- Maximum junction temperature 150°
- Lead temperature (Soldering 4 sec.) 260°C
- Storage temperature range −65°C to +150°C

2.4.2 Optocoupler IC 6N136

Isolation is crucial in many applications, and various methods can be employed. When considering transformer-based isolation, several challenges arise:

- Challenges with transformer-based isolation:
    a) Unsatisfactory output at high frequencies
    b) High oscillations
    c) Design and fabrication complexities
- Optocoupler solution:
    A. Adopted 6N136 optocoupler for isolation
    B. Avoided transformer-related issues
    C. Met project requirements

Hence using of IC 6N136 optocoupler simplifies design and ensures reliable isolation.

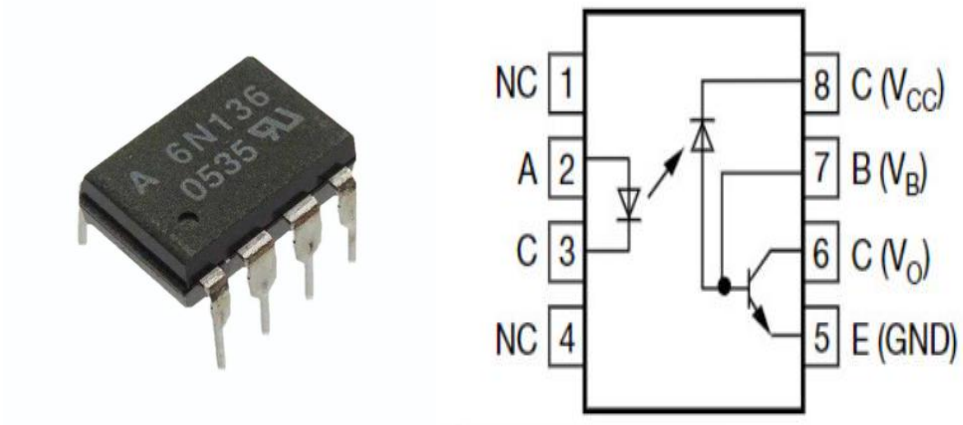

(a) (b)

Figure 2.12: (a) IC 6N136 (b) Pin diagram of Optocoupler IC 6N136.

Basics Optocoupler of 6N136:

IC 6N136 shown in Fig 2.12(a, b) is used for the optical isolation in between PWM output and MOSFET. Optical isolation basics are light Emitting Diode (LED) and photo-sensitive detector with insulating gap between elements ensures electrical isolation and prevents ground looping and equalizes potential differences. This eliminates current flow between isolated circuits, enables data transmission across different power circuits and reduces noise and interference. IC 6N136 optocoupler specifically a diode-transistor configuration, integrated photo detector and separate connections for photodiode bias and output-transistor collector enhance speed [53].

Features:

- TTL compatible
- Isolation test voltages: 5300 V_{RMS}
- Bandwidth 2.0 MHz
- High bit rates: 1.0 Mbit/s
- Open-collector output
- High common-mode interference immunity
- Lead (Pb)-free component
- External base wiring possible

2.4.3 NE555 Timer

Several timer and multivibrator applications are implemented using the 555 timer, an integrated circuit (chip). A monolithic timing circuit in this timer may generate precise and incredibly stable time delays or oscillations. One external resistor and capacitor accurately control the time in the time delay mode of operation. Two external resistors and one capacitor are used to precisely manage the duty cycle and the free running frequency for a steady oscillator operation. The output structure can source or sink up to 200mA, and the circuit may be activated and reset in response to falling waveforms.

Features:

- Max. operating frequency greater than 500kHz
- Turn-off time less than 2μs

- Operates in both astable and monostable mode
- Timing from microseconds to hours
- Adjustable duty cycle
- High output current
- Temperature stability of 0.005% per °C
- TTL compatible

Pin configuration:

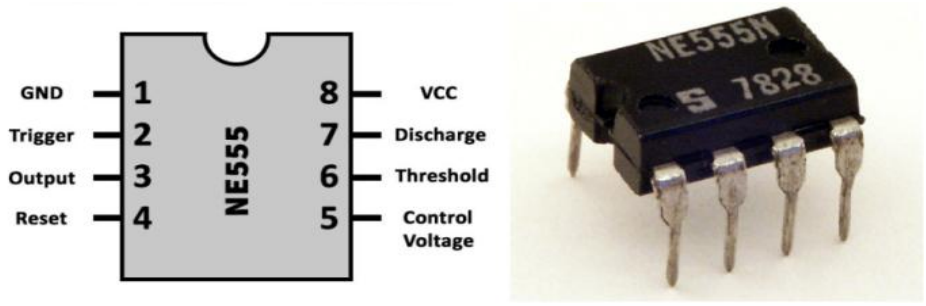

Figure 2.13: Pin diagram of 555 timers IC

A highly sophisticated device for producing precise time delays and oscillations is the 555 timer. While a counter timer can have a maximum time range for delay, a single 555 timer can produce time delays ranging from microseconds to hours. Fig. 2.13 displays 555 timers with an 8-pin design. A 555 timer can drive a 200mA load and be utilized with supply voltages between +5V and +18V. Both voltages are compatible with it. 555 timers are simple to operate and adaptable to a wide range of applications. Oscillators, pulse generators, ramps, and square wave generators are among the many uses. According to the IC 555 timer's datasheet, the other pins carry out their typical functions [54].

Key aspects of the H-bridge inverter driver design:

- **Isolation:** Optocoupler (6N136) ensure safety by isolating PWM IC outputs from the power circuit.
- **Duty cycle adjustment:** Additional inversion using 555 timers achieves the desired maximum 40% duty cycle.
- **Miller capacitance mitigation:** 555 timers help reduce the effect of Miller capacitance.
- **PCB design:** Hardware setup designed on a PCB for reliability and compactness.

- **Quick switching:** Small negative voltage during fall time enhances switching speed.

These design considerations of the driver circuit shown in Fig. 2.14 ensure efficient and reliable operation of the H-bridge inverter.

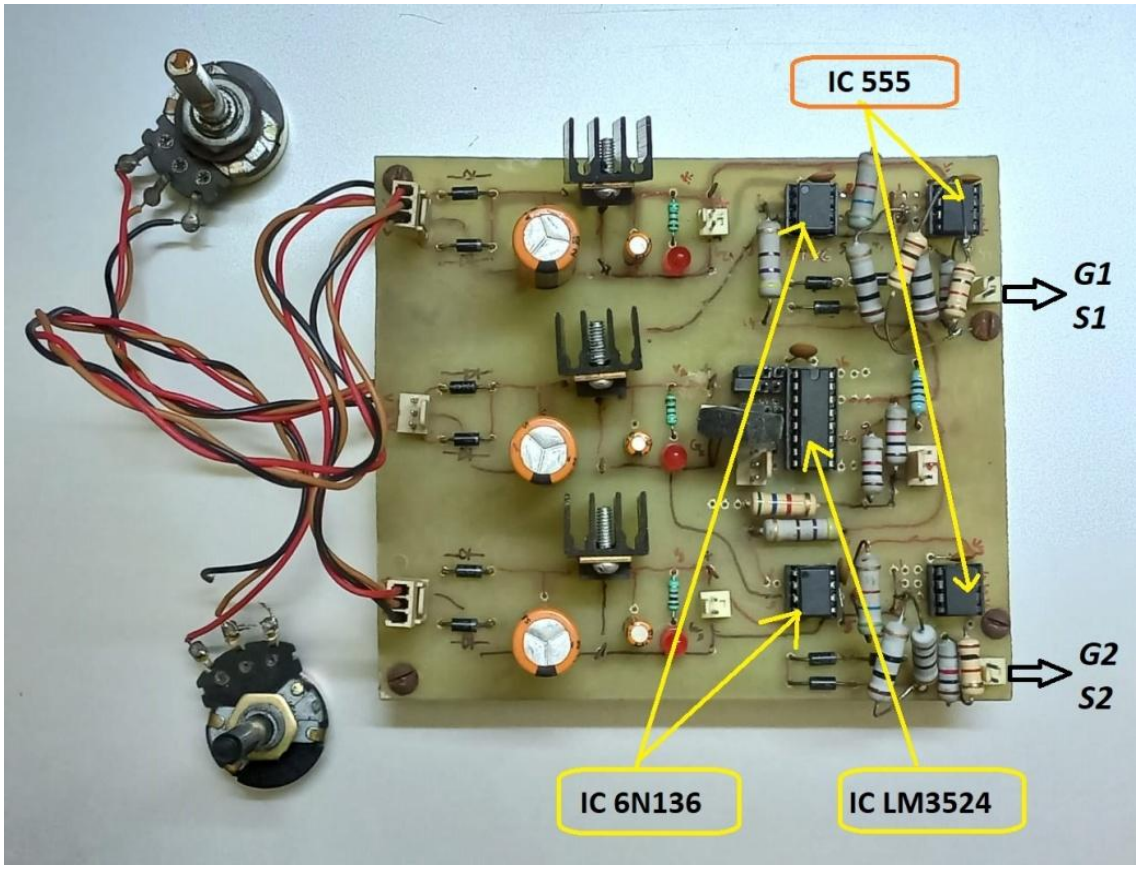

Figure 2.14: hardware setup of the H-bridge inverter driver.

2.5 Experimental output of the H-bridge driver circuit

i) Frequency (f_{osc}) Control:

The frequency of the driver voltage waveform is determined by the values of R_T (resistor) and C_T (capacitor) connected to the IC LM3524. Specifically R_T is represented by (R1 + R2) C_T is represented by C1 shown in Fig. 2.8. The frequency calculation formula is typically provided in the IC LM3524 datasheet.

$$f_{osc} = 1 / R_T C_T \qquad (2.1)$$

- Suppose the desired frequency of the driver output voltage is 10 kHz. For a fixed capacitor value of 10nF, the resistance value can be calculated as follows:

$$R_T = 1/ (f_{osc} \times C_T) = 1/ (10 \times 10^3 \times 10 \times 10^{-9})\ \Omega = 10k\Omega \quad (2.2)$$

Now, if the desired frequency of the driver output voltage is 15 kHz, the resistance value needs to be adjusted to:

$$R_T = 1/ (f_{osc} \times C_T) = 1/ (15 \times 10^3 \times 10 \times 10^{-9})\ \Omega = 6.66k\Omega \quad (2.3)$$

Hence, it is evident from the discussion that a variable resistor (potentiometer) is necessary for frequency control. This is achieved by connecting (R1) and (R2), a variable resistor, in series between pin 6 and pin 8 (ground) of the PWM IC LM3524.

ii) PWM Control (or Duty cycle control):

The LM3524 PWM IC generates a square wave modulated pulse (PWM) at pins 11 and 14. This modulation decides the duty cycle of the pulses. The IC has an internal saw tooth wave generator, whose frequency is controlled by an external resistance (R_T) and capacitance (C_T). By raising the analog input from 0 to 3.5V, the duty cycle of the MOSFET's 12V gate signal can be increased shown in Fig 2.15. A DC voltage power supply is applied to pin 9, and a triangular pulse is generated when capacitance C_T is connected to pin 7. These pins are connected to an internal comparator, which produces a variable pulse width output when the DC voltage at pin 9 is varied. This process generates a square wave PWM pulse at a particular frequency, making the IC LM3524 suitable for various applications.

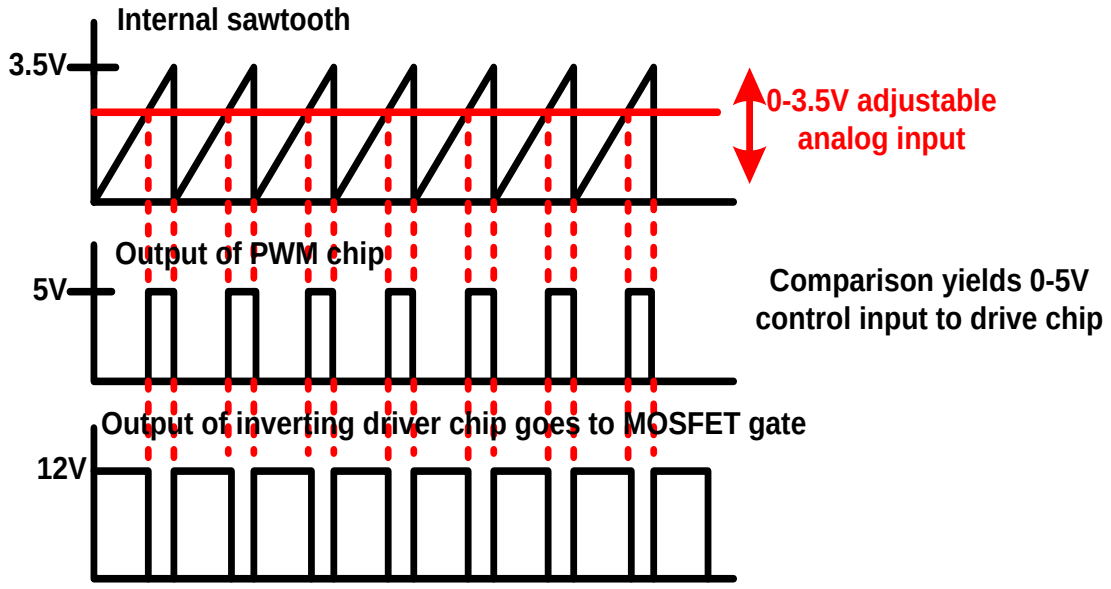

Figure 2.15: Output of inverting driving chip goes to MOSFET gate with controlled duty.

For the H-bridge inverter shown in Fig 2.1, the two MOSFETs should not conduct simultaneously. A dead band is required to prevent short circuits, depending on the MOSFET rating and load type. During operation, the maximum duty cycle is limited to 40% for each Power MOSFET, with a 20% dead band to avoid common conduction. Fig 2.16(a, b) illustrates the parameters for dead band generation, where a fixed resistor (R3) and variable resistor (R4) are connected in series across pins 16 and 8 for PWM control. This setup requires 3.2V at pin 9 for a maximum 40% duty cycle, obtained from the IC's 5V DC output at pin 16.

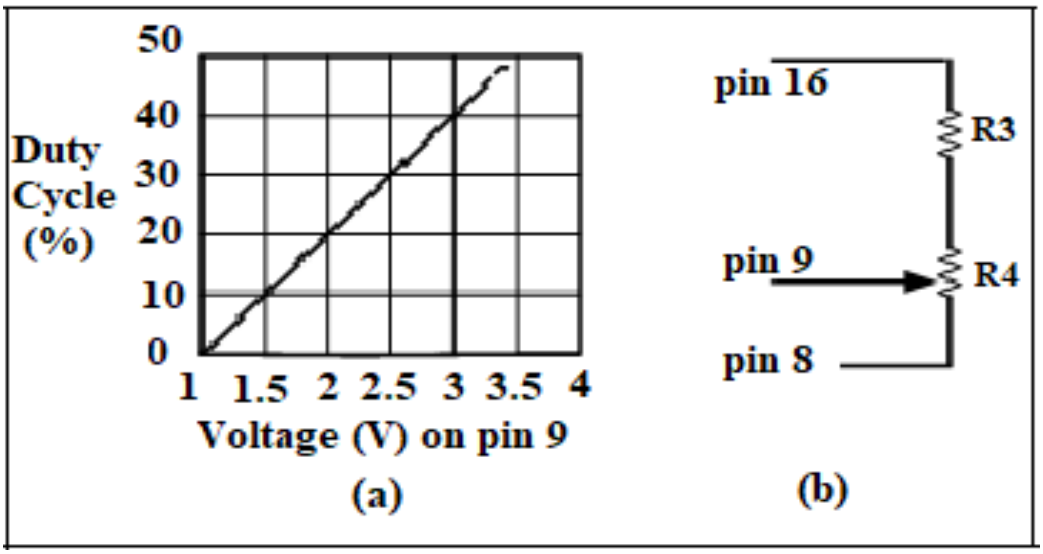

Figure 2.16 (a, b): Arrangement of duty cycle control of IC LM3524

2.5.1 Driver output voltage at various frequencies and duty cycle

The H-bridge driver outputs were tested and captured using a Digital Storage Oscilloscope (DSO) at various frequencies and duty cycles. These results are presented in Fig. 2.17 to 2.21.

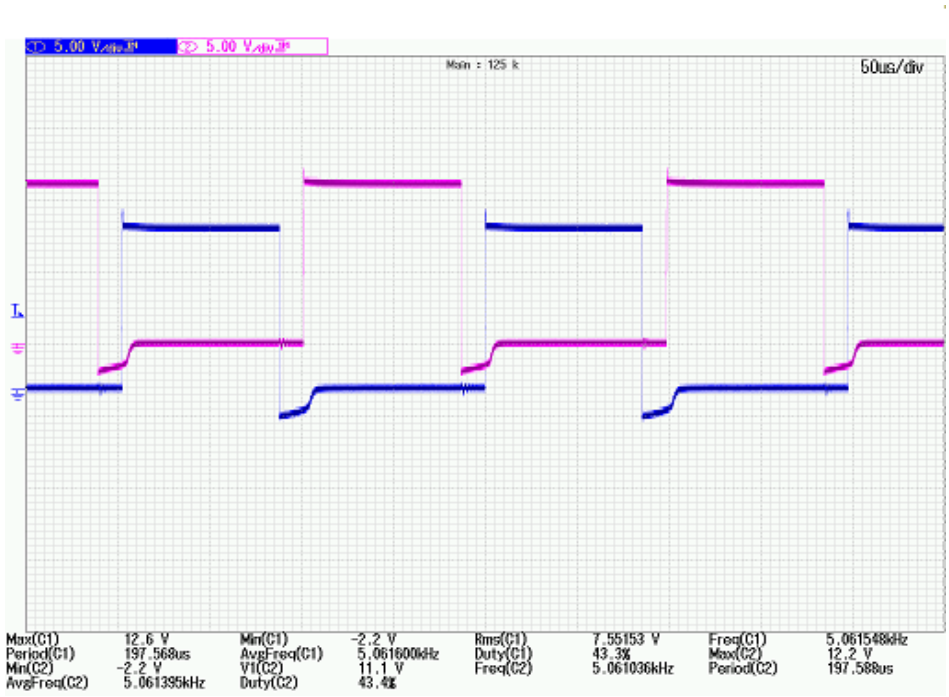

Figure 2.17**:** H-bridge driver output voltage at 5 kHz with 43% duty cycle.

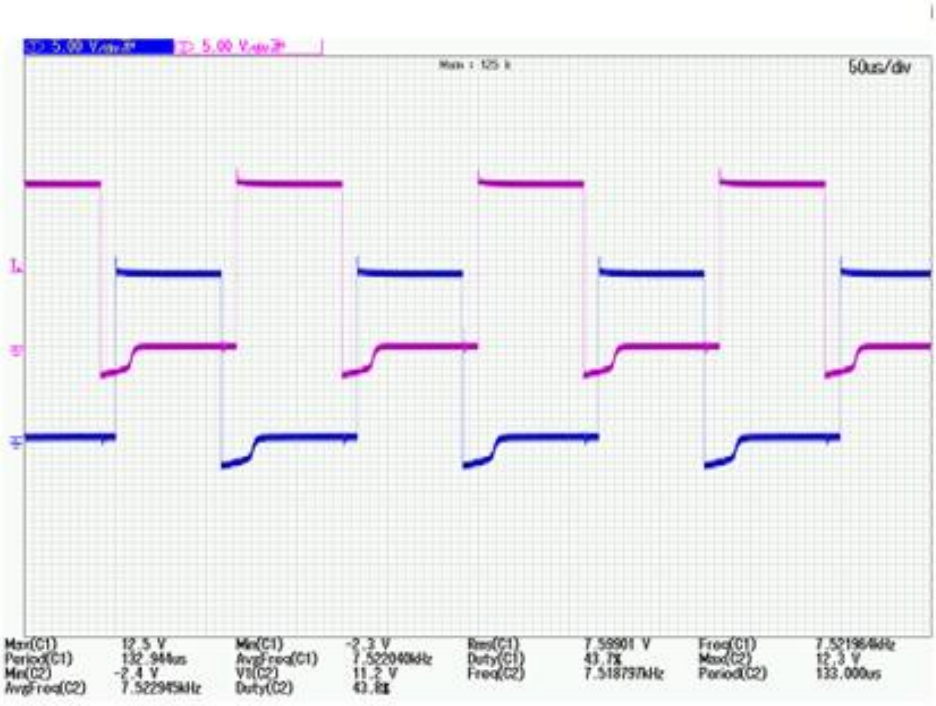

Figure 2.18: H-bridge driver output voltage at 7.5 kHz with 43% duty cycle.

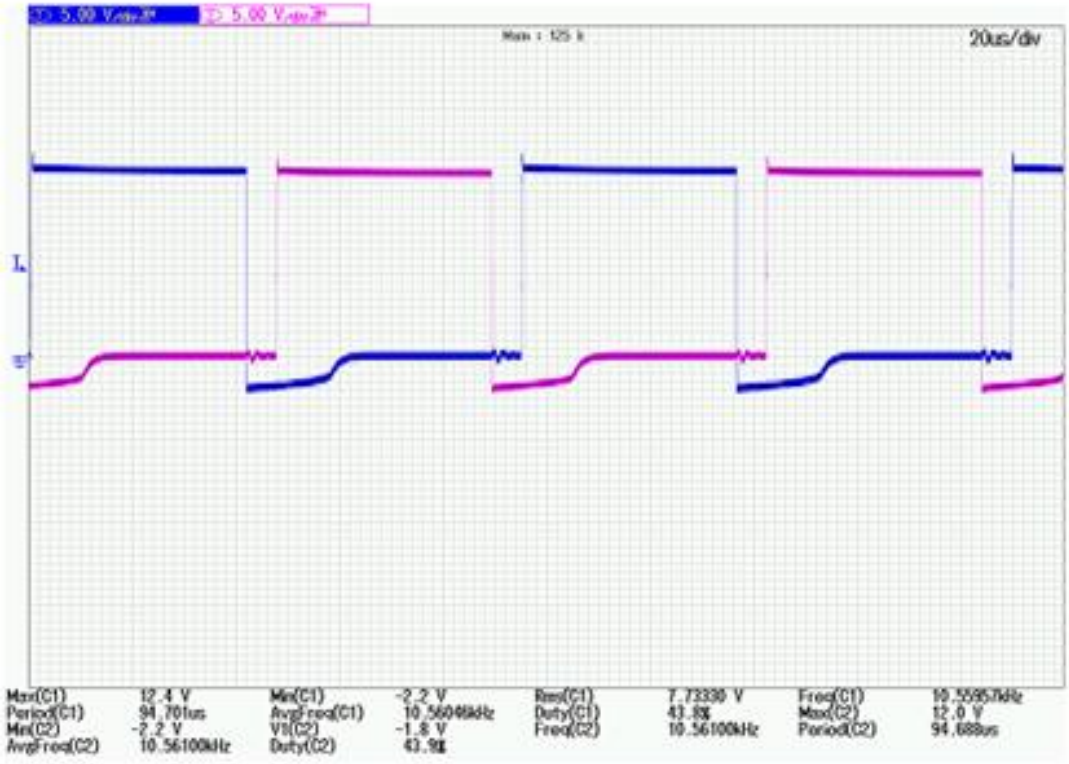

Figure 2.19: H-bridge driver output voltage at 10 kHz with 43% duty cycle.

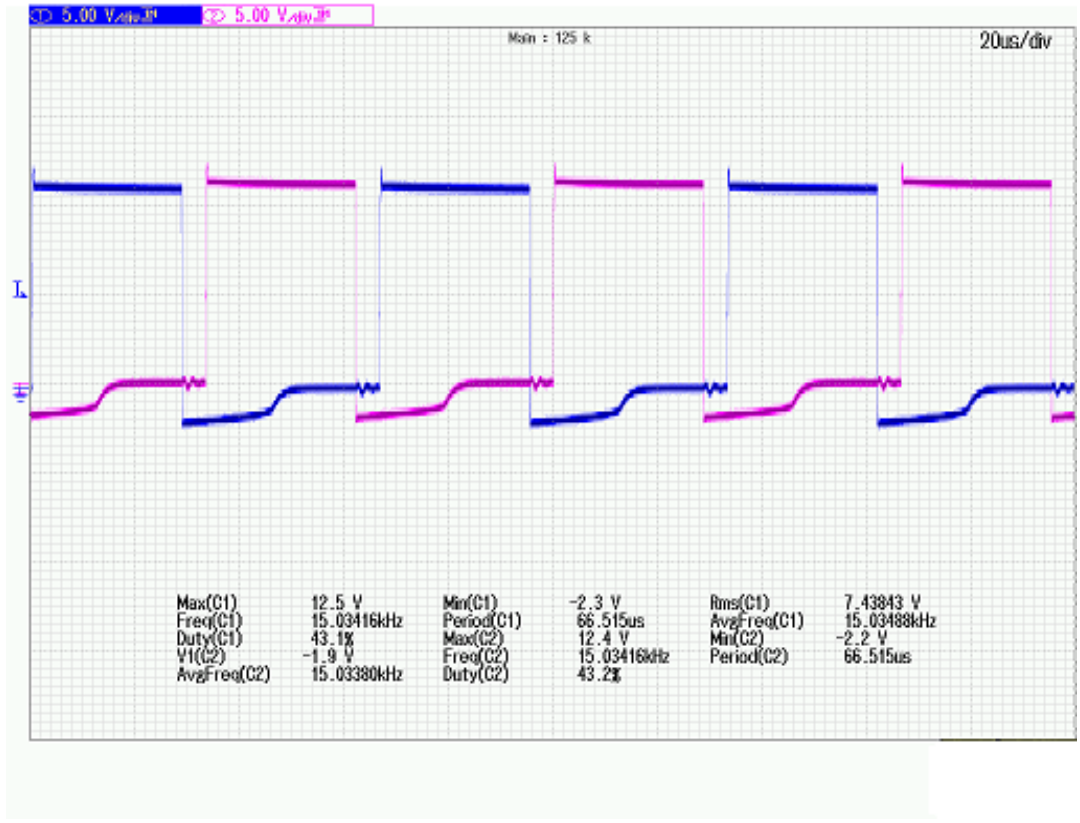

Figure 2.20: H-bridge driver output voltage at 15 kHz with 43% duty cycle.

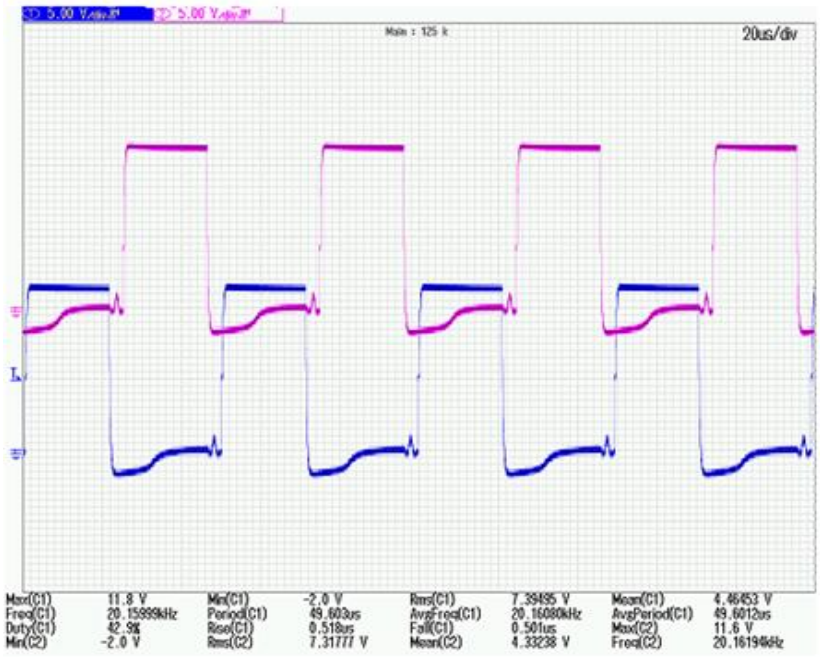

Figure 2.21: H-bridge driver output voltage at 20 kHz with 43% duty cycle.

2.6 Block diagram of high frequency square wave H-bridge inverter

The discussion now shifts to the power circuit for a half-bridge inverter, which includes various components. This follows the earlier exploration of the driver circuit for high-frequency operation. The power circuit's design and component selection are crucial for efficient energy conversion, reliable operation, safe functioning of the inverter. The half-bridge inverter's configuration and component choices will likely impact its performance, efficiency, and applications. Block diagram of complete high frequency half-bridge square wave inverter is shown below in Fig. 2.22.

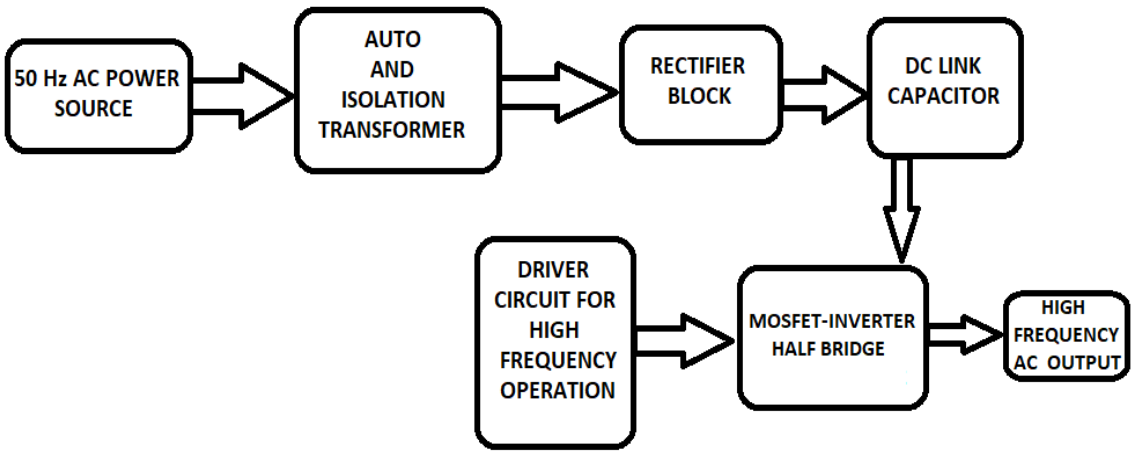

Figure 2.22: Block diagram for high frequency square wave inverter.

2.7 High frequency inverter along with components

The development of inverters involves several key blocks. These likely include driver circuit, power circuit, control circuit, protection circuitry. Each block plays a crucial role in the inverter's overall performance, efficiency and reliability.

a. AC Power Source; 220V, 50Hz.
b. An autotransformer for variable voltage.
c. A power isolated transformer.
d. A full bridge rectifier block
e. Stored energy element, a capacitor bank
f. Power MOSFETs in push pull configuration
g. A driver cum control circuit for the power MOSFETs

The high-frequency inverter was designed and developed in the laboratory, then tested thoroughly under various conditions. The key components used are described below. This practical implementation and testing likely ensured verifying the inverter's performance, evaluating the inverter's behavior under different conditions. The description of key components provides insight into the inverter's design and capabilities. These researches explore the components and their test results.

2.7.1 Auto transformer

Auto Transformer is otherwise called variable voltage transformer and its schematic diagram is shown in Fig 2.23(a, b).

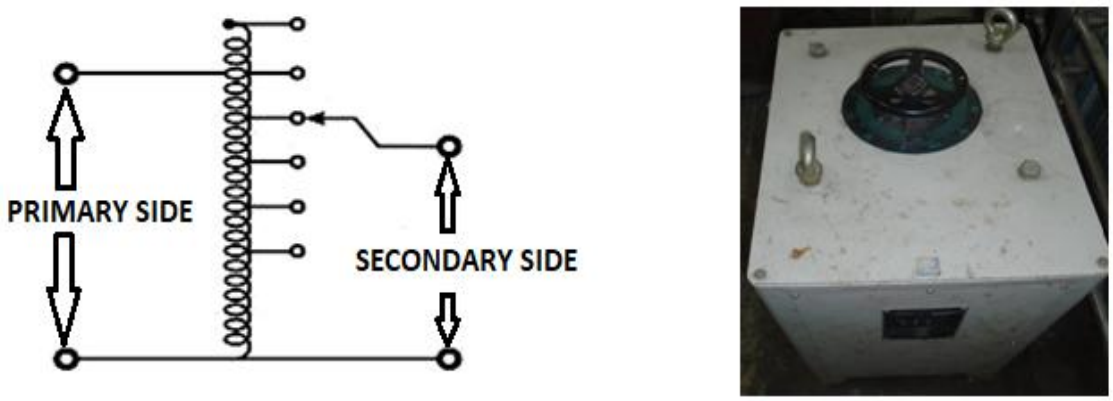

(a) (b)

Figure 2.23: (a) Winding diagram of auto transformer (b) Practical Auto transformer.

The autotransformer serves as a variac, allowing for adjustable voltage output. This is useful for providing different supply voltages to enable various test conditions. The variac's role is crucial in facilitating experimentation and testing.

2.7.2 Isolation transformer

The isolation transformer plays a crucial role in:

a. Electrical isolation: Separating primary and secondary circuits.
b. Noise reduction: Eliminating interference caused by ground loops.
c. Safety precaution: Protecting the inverter circuit from the main utility supply.

An isolation transformer completely encloses the shock hazard within the device and removes the bonding; practical isolation transformer is shown in Fig.2.24.

Figure 2.24: Isolation transformer.

2.7.3 Diode rectifier

The process of changing an alternating voltage or current into a direct voltage or current is called rectifying. The rectifier is the name of the apparatus used for rectification. There are primarily two types of rectifiers: half wave rectifiers and full wave rectifiers.

The diode bridge, also known as a bridge rectifier, converts AC input voltage to DC output voltage, regardless of input polarity. Diode bridges are commonly used in power supplies and rectification applications. The bridge rectifier circuit and pulsating DC output from the rectifier are shown in Fig. 2.25(a, b).

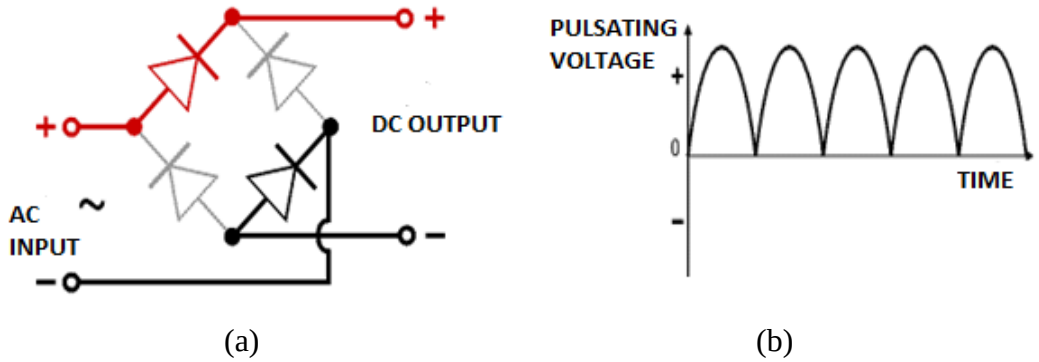

(a) (b)

Figure 2.25: (a) Bridge rectifier circuit (b) Pulsating DC output of rectifier.

The bridge rectifier offers advantages like full-wave rectification, Cost-effective, Fewer wires and no center tap needed hence size and weight reduces. Bridge rectifiers are widely used in power supplies and applications where efficient AC-DC conversion is crucial. The practical diode bridge rectifier used in this work is shown in Fig. 2.26.

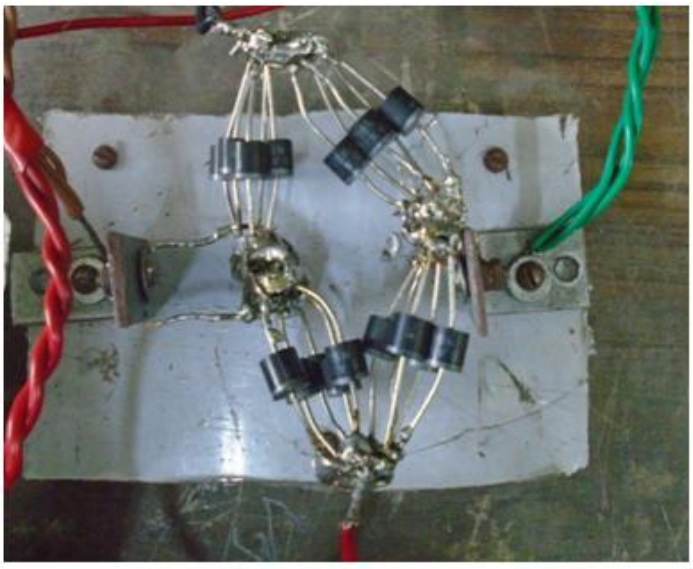

Figure 2.26: Practical diode bridge rectifier.

2.7.4 DC link capacitor

A filter or DC link capacitor is positioned across the output terminals of the bridge rectifier, as shown in Fig. 2.27, because the rectifier's output is a pulsing DC voltage, as seen in Fig.

2.25(b), rather than a pure DC voltage. DC link capacitors are typically made using electrolytic capacitor technology, which offers a low cost per farad, making it an attractive choice.

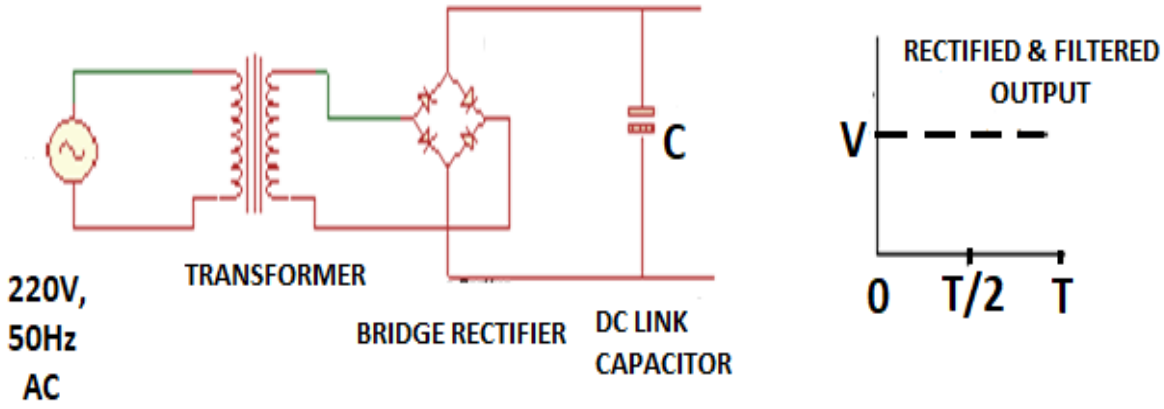

Figure 2.27: Diode bridge rectifier circuit with bus rectified and filtered output.

2.7.5 Selection of DC link capacitor

The choice between aluminum and tantalum electrolytic capacitors depends on factors like cost and application requirements. In this project, an aluminum electrolytic capacitor was chosen for the DC link due to its cost-effectiveness; Less expensive than tantalum capacitors and meeting required specifications. Aluminum electrolytic capacitors are widely used in power supply applications.

This aluminum electrolytic capacitor can generally be classified into following three main types.

a. Snap-in capacitor,
b. plug-in capacitor,
c. Screw-terminal capacitor.

Screw terminal capacitors are chosen for their superior features likely due to high current handling, reliability, and suitable for demanding applications. The selection of screw terminal aluminum electrolytic capacitor for the DC link ensures robust performance. The practical screw terminal aluminum electrolytic DC link capacitor is shown in Fig. 2.28.

Figure 2.28: Screw terminal aluminum electrolytic DC link capacitor.

2.7.6 Calculation of the capacitance value

kVA (kilo volt-ampere) rating of the isolation transformer:

= 400×50 VA

= 20kVA

Whereas kVA rating of auto transformer (Source):

= 230×28 VA

= 6.44kVA

So, output kVA of the isolation transformer

= 6.44kVA

Now, consider Power factor ＝ 0.8

Therefore output kW of isolation transformer = 6.44×0.8 kW

= 5.152kW

Supply frequency = 50 Hz = 50 cycles/second

So, energy stored in capacitor in 50 cycles/second = 5152 Joules

Energy stored in capacitor in 1 cycle/second = 5152/50

= 103.04 Joules

Therefore, $1/2 \times CV^2 = 103.04$ Joules

Let, V ＝ 200V

For high-frequency drive applications, although the MOSFET is capable of withstanding

higher voltages, the practical operating voltage of the MOSFET has been intentionally limited to 200V in this work. This ensures reliable performance, thermal stability, and optimal switching behavior under high-frequency conditions.

Hence, $C = (103.04 \times 2)/ 200^2$ F

$= 5.15 \times 10^{-3}$ F

=5000 μF (approx.)

Peak voltage V_P across capacitor $C = 200 \times \sqrt{2}$

So, $V_P = 282.84$V

Therefore, the voltage rating of the capacitor must be greater than or equal to this voltage. In this research, capacitors with a voltage rating of 450V DC are used, and multiple screw terminal aluminum electrolytic DC link capacitors are used to meet the required rating.

2.8 Power switches

Ongoing research and development lead to new devices and improved power handling capabilities. MOSFET is identified as suitable for high-frequency applications due to its characteristics. The discussion focuses on MOSFETs used in the project, including datasheet analysis.

2.8.1 Different types of MOSFET used in this work

2SK727

Features:

a. Low on-resistance.
b. High speed switching.
c. Low driving power.
d. No secondary breakdown.
e. Avalanche- proof
f. High voltage.

The schematic diagram and packaging of 2SK727 MOSFET are shown in Fig. 2.29(a, b). Table 2.2 shows the absolute maximum ratings of MOSFET 2SK727 [55].

(a) (b)

Figure 2.29: (a) Equivalent circuit schematic (b) Packaging of 2SK727 MOSFET.

Absolute Maximum Ratings (T_c=25˚C):

Items	**Symbols**	**Ratings**	**Units**
Gate –source peak voltage	V_{GSS}	±20	V
Continuous Drain Current	I_D	5	A
Drain Source Voltage	V_{DSS}	900	V
Continuous reverse drain current	I_{DR}	5	A
Pulsed drain current	$I_{D(puls)}$	20	A
Max. power dissipation	P_D	125	W
Operating and storage temperature range	T_{ch}	150	˚C
	T_{stg}	-55 ~ + 150	˚C

Table 2.2: Absolute maximum rating of 2SK727 MOSFET.

IRF840

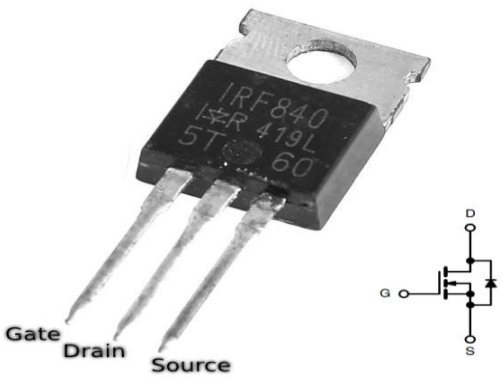

Figure 2.30: Symbol and packaging of MOSFET IRF840.

The schematic diagram and packaging of IRF840 MOSFET are shown in Fig. 2.30. Features and absolute maximum ratings of MOSFET IRF840 are given below [56].

Features:

1. Maximum continuous drain current is 8A; drain to source voltage is 500V.
2. On state drain to source resistance $R_{DS\ (ON)} = 0.850\Omega$.
3. Single Pulse Avalanche Energy Rated.
4. SOA is Power Dissipation Limited.
5. Nanosecond Switching Speeds.
6. Linear Transfer Characteristics.
7. High Input Impedance.
8. Fast Switching.

Absolute Maximum Ratings at 25°C (T_C):

1. Drain to Source Voltage. V_{DS}=500 V
2. Drain to Gate Voltage (R_{GS}= 20kΩ) , V_{DGR} =500 V
3. Continuous Drain Current. I_D =8.0 A
4. Pulsed Drain Current. I_{DM} =32 A
5. Gate to Source Voltage. V_{GS} =20 V
6. Maximum Power Dissipation. P_D =125 W
7. Single Pulse Avalanche Energy Rating.E_{AS}=510mJ
8. Operating and Storage Temperature. T_J = -55°C to 150°C
9. Maximum Temperature for Soldering. T_L= 300°C

IRF P460

The Packaging and terminals of MOSFET IRFP460 is shown in Fig. 2.31. Features and absolute maximum ratings of MOSFET IRFP460 are given below [57].

Features:

1. 20A, 500V
2. $R_{DS\ (ON)} = 0.270\Omega$

3. Single pulse avalanche energy rated
4. SOA is power dissipation limited
5. Nanosecond switching speeds
6. Linear transfer characteristics
7. High input impedance

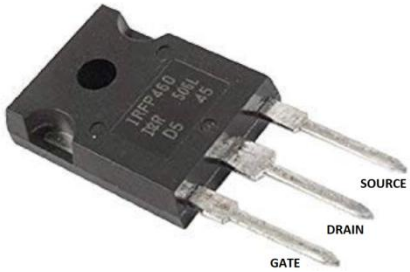

Figure 2.31: Packaging and terminals of MOSFET IRFP460.

Initially, this project utilized IRF840 and 2SK727 MOSFETs. Later, the IRFP460 was introduced due to its higher current rating, as specified in the datasheet, to enhance the overall current-handling capability and reduce thermal stress. Note that stresses beyond the 'Absolute Maximum Ratings' may cause permanent damage, and operating beyond these conditions is not recommended.

2.9 Snubber circuit

At the beginning of the switching cycle, the switch is open and no current (I_D) flows through it. As the switch turns on, the current gradually increases while the voltage across the switch begins to fall. At turn-off, the situation is reversed. During switching on, the current (I_D), and during switching off, the voltage do not immediately reach their final values. As a result, switching losses occur. This is illustrated in Fig. 2.32.

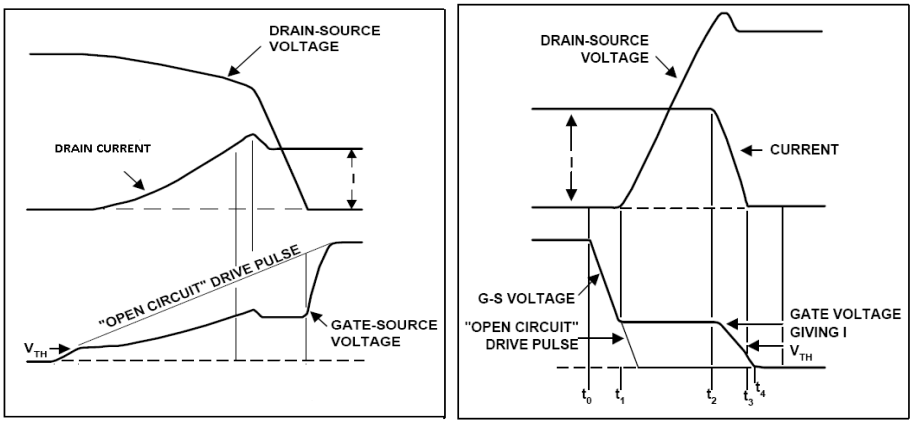

Figure 2.32: Voltage and current waveforms of the switch during turn-on and turn-off.

To increase performance and provide protection, circuits known as snubbers are placed across semiconductor switching devices. Snubber has numerous uses, such as:

a) Reduce total losses due to switching
b) Limit di/dt or dv/dt
c) Transfer power dissipation from the switch to a resistor or a useful load
d) Shape the load line to keep it within the safe operating area (SOA)
e) Reduce or eliminate voltage or current spikes
f) Reduce EMI by damping voltage and current ringing

The purpose and types of snubbers are to limit peak voltage and reduce switching losses during turn-off. There are two types of snubbers mainly RC damping network and RCD turn-off snubber mostly used. RCD snubber is selected for its advantages over RC snubber in the inverter circuit. RCD snubbers are often preferred for their effectiveness in reducing voltage spikes and losses.

2.9.1 RCD snubber design

An RCD snubber is a circuit typically used in power electronics to protect switching devices (like transistors) from voltage spikes caused by inductive loads. It consists of a resistor (R), capacitor (C), and diode (D) shown in Fig 2.33. The RCD snubber offers several advantages over a basic RC snubber, particularly in applications where energy dissipation and voltage clamping are important.

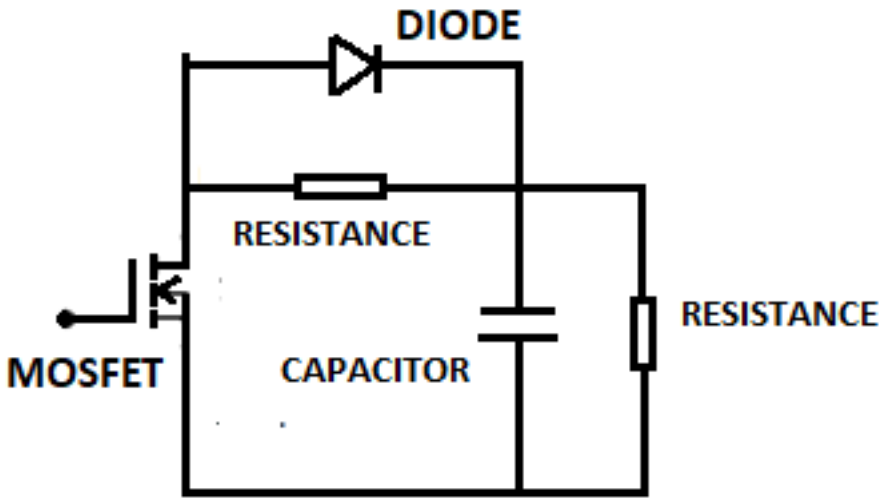

Figure 2.33: RCD snubber.

The RCD snubber likely offers advantages such as:

a. Much better load lines can be achieved, allowing the load line to pass well within the SOA.
b. In addition to peak voltage limiting, this is reduction of the total circuit loss, including both switching and snubber losses.
c. The shunt capacitance across the switch is a useful part of the snubber
d. Less loss.

These benefits contribute to enhanced circuit performance and reliability.

2.10 Development and observations on high frequency inverter

The half-bridge inverter, which generates the high-frequency power supply, operates on a 230V, 50Hz source that is controlled by an autotransformer. Electrical isolation from the main supply is guaranteed by an isolation transformer. An electrolytic capacitor is used to lessen ripple in the DC output after converting AC to DC using a diode rectifier bridge. By restricting di/dt or dv/dt, RCD snubbers placed across the drain and source of MOSFETs reduce switching losses. In order to investigate the thermal properties of MOSFETs under different loads; a tungsten filament lamp was tested using the designed inverters and experimental setup. Stabilization of the temperature was noted at various frequencies.

2.10.1 Experiment on half bridge inverter

To investigate the thermal characteristics of MOSFETs for different load currents and temperature stabilization, the Ohmic heating unit configuration complete with an half bridge inverter has been designed and tested as shown in Fig 2.34. A tungsten filament lamp load setup is employed as shown in Fig 2.35.

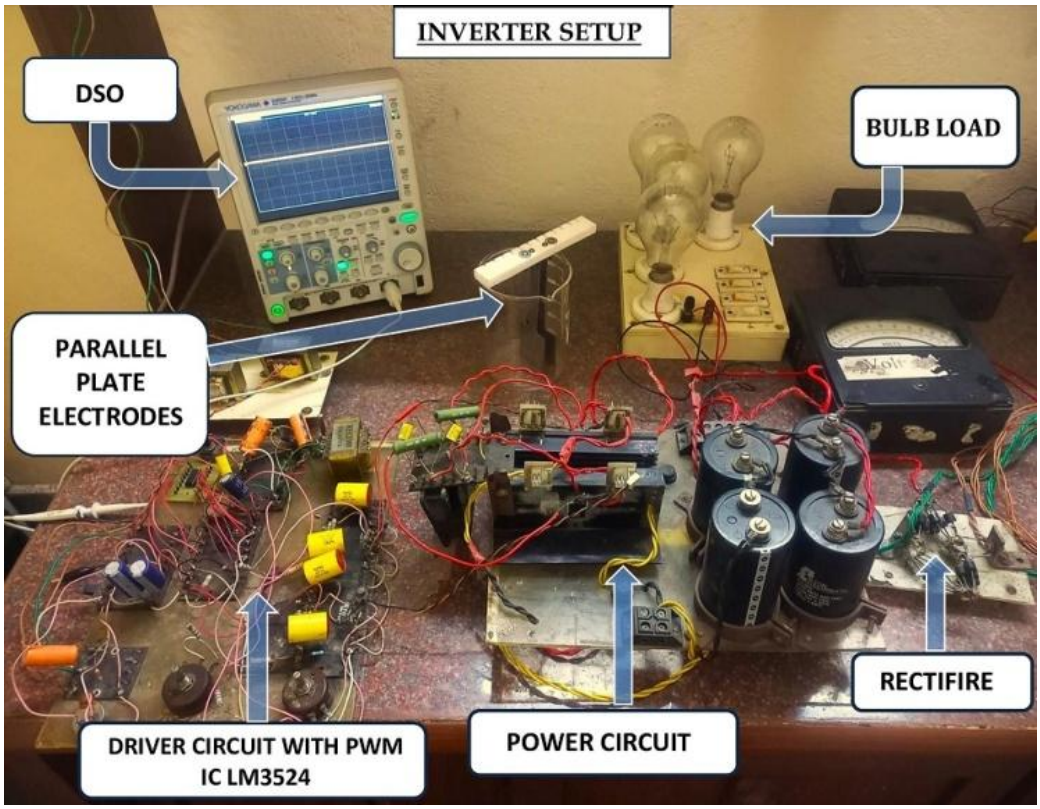

Figure 2.34: Half bridge inverter setup.

Figure 2.35: Tungsten filament bulb load.

2.10.2 Thermal performance of Half-bridge inverter using IRF840 MOSFET

The experimental results of the thermal characteristics of the half-bridge inverter using IRF840 MOSFET as a switch are presented in Tables 2.3 to 2.6 for different frequencies. The switching frequency is given by the equation: $f = 1/C_T . R_T$. The capacitor (C_T) and resistor (R_T) are connected to pins 7 and 6 respectively, of the PWM IC LM3524.

f C_T R_T	Supply Voltage DC	Input Current DC	Time	Temp. of Lower MOSFET (*SW2*)	Temp. of Upper MOSFET (*SW1*)	Load
f =5.0kHz	150V	0.1A	5 min.	31˚C	32˚C	
C_T=4.7nF	150V	0.1A	30 min.	34˚C	34˚C	600W (Bulb)
R_T =37k	150V	0.1A	60 min.	34˚C	34˚C	

Table 2.3: Thermal analysis of an inverter MOSFET operating at 5kHz using IRF840 as the switching device.

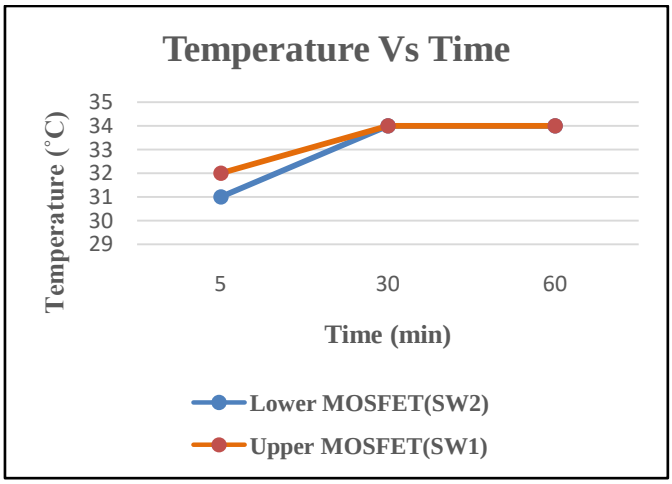

Figure 2.36: Temperature rise versus time of two MOSFETs (*SW1* and *SW2*) of H-bridge inverter at 5kHz operation.

2.10.2.1 Inverter output voltage wave across the tungsten filament bulb load at 5 kHz

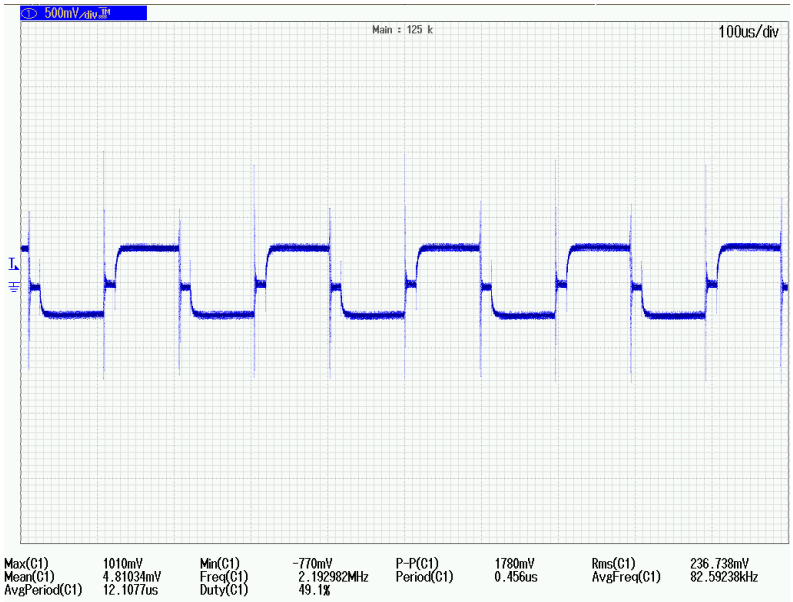

Figure 2.37: Inverter output voltage wave across the tungsten filament bulb load for Table 2.3.

f C_T R_T	Supply Voltage DC	Input Current DC	Voltage Across the load	Time	Temp. of Lower MOSFET (*SW2*)	Temp. of Upper MOSFET (*SW1*)	Load
f =8kH$_Z$	200V	1.4A	78.4V	10 min.	28˚C	42˚C	
C_T=4.7nF	200V	1.4A	78.4V	25 min.	35˚C	45˚C	900W (Bulb)
R_T =27k	200V	1.4A	78.4V	35 min.	35˚C	47˚C	
f=5.9kH$_Z$	200V	1.8A	75V	10 min.	28˚C	37˚C	1100W (Bulb)
C_T=4.7nF	200V	1.5A	75V	20 min.	34˚C	46˚C	
R_T=37k	200V	1.5A	75V	40 min.	35˚C	46˚C	900W (Bulb)

Table 2.4: Thermal analysis of an inverter MOSFET operating at 8 and 5.9kHz using IRF840 as the switching device.

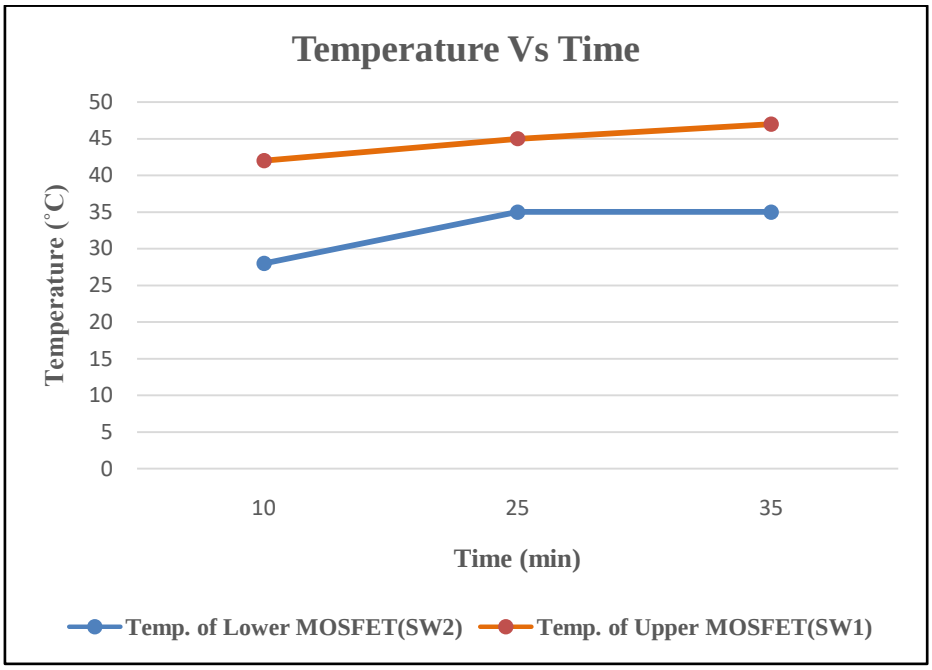

Figure 2.38: Temperature rise versus time of two MOSFETs (*SW1* and *SW2*) of H-bridge inverter at 8kHz operation.

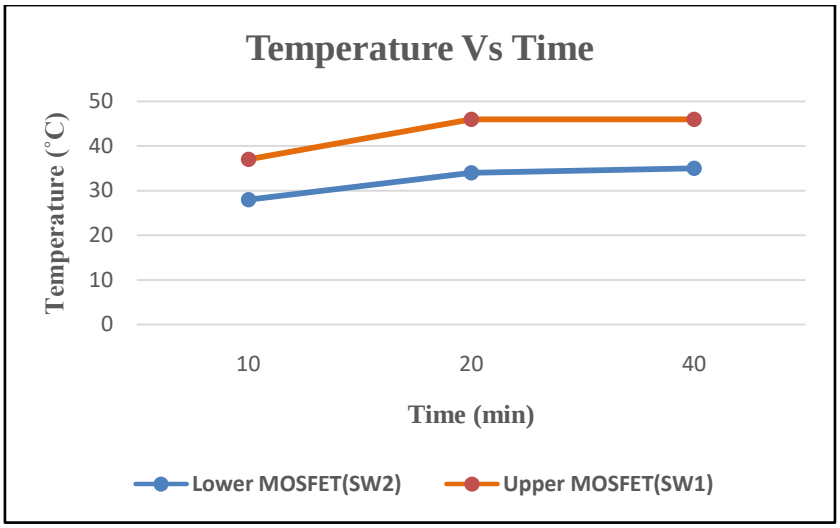

Figure 2.39: Temperature rise versus time of two MOSFETs (*SW1* and *SW2*) of H-bridge inverter at 5.9kHz operation.

f C_T R_T	Supply Voltage DC	Input Current DC	Voltage Across the load	Time	Temp. of Lower MOSFET (*SW2*)	Temp. of Upper MOSFET (*SW1*)	Load
f=10kH$_Z$	180V	1.7A	74.5V	10 min.	26˚C	41˚C	
C_T=10nF	180V	1.7A	74.5V	20 min.	26˚C	45˚C	
R_T=10k	200V	1.8A	94V	25 min.	25˚C	48˚C	1100W (Bulb)
	200V	1.8A	94V	35 min.	27˚C	54˚C	
	200V	1.8A	94V	50 min.	27˚C	55˚C	

Table 2.5: Thermal analysis of an inverter MOSFET operating at 10kHz using IRF840 as the switching device.

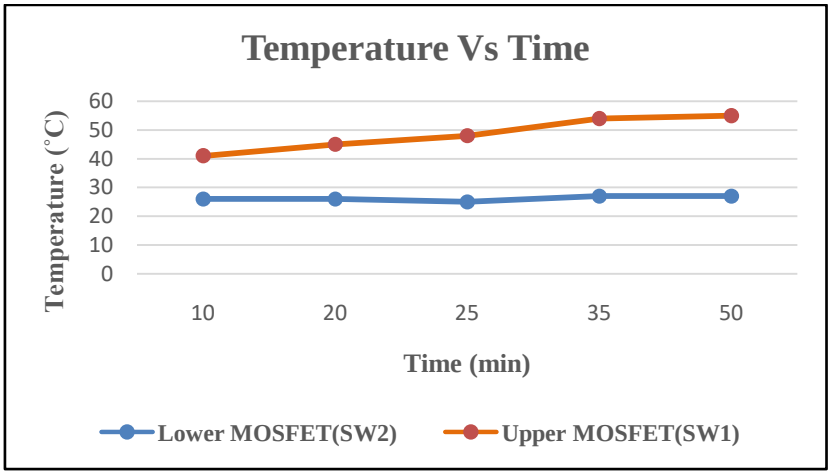

Figure 2.40: Temperature rise versus time of two MOSFETs (*SW1* and *SW2*) of H-bridge inverter at 10kHz operation.

2.10.2.2 Inverter output voltage wave across the tungsten filament bulb load at 10 kHz

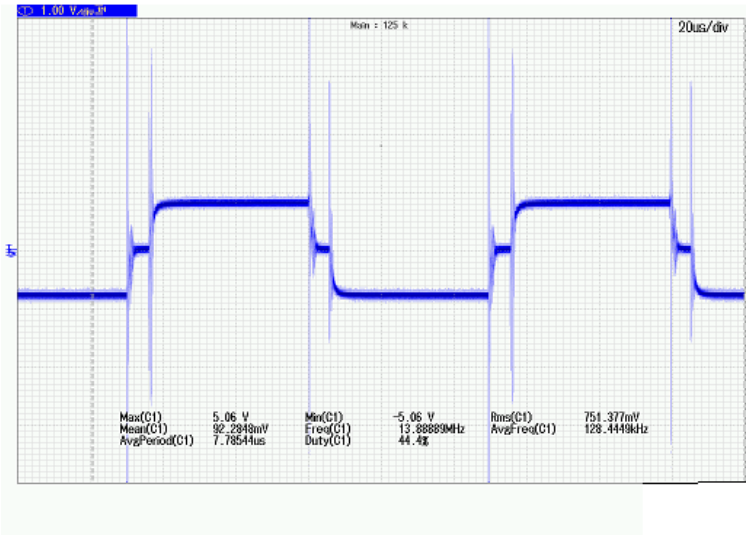

Figure 2.41: Inverter output voltage wave across the tungsten filament bulb load for Table 2.5.

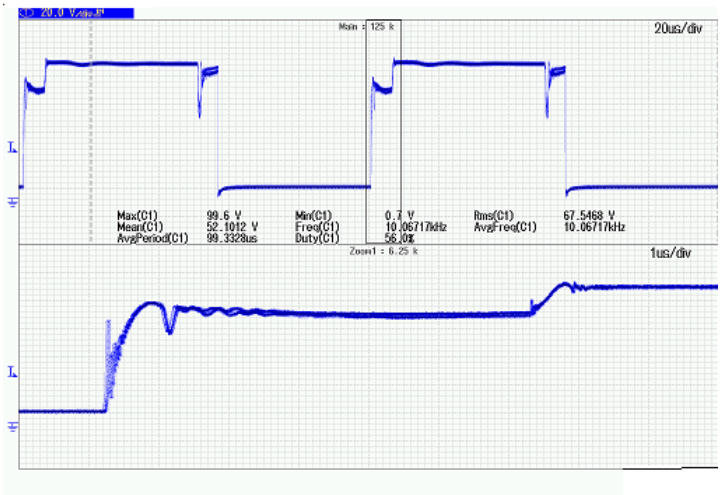

Figure 2.42: Rising part of the driver circuit output voltage during loading condition for Table 2.5.

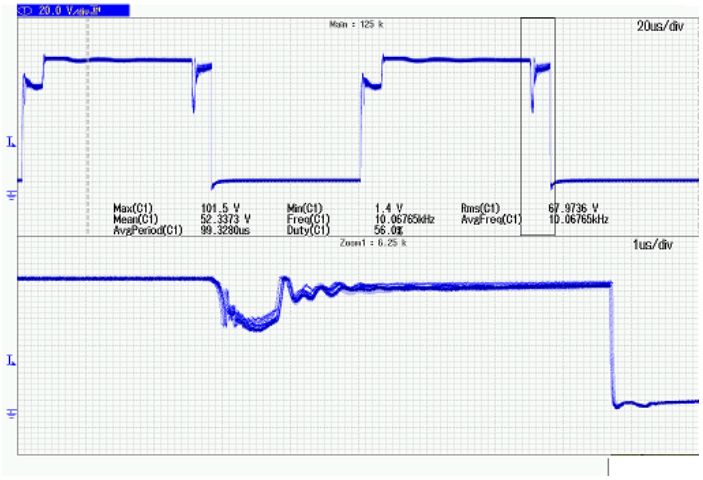

Figure 2.43: Falling part of the driver circuit output voltage during loading condition for Table 2.5.

f C_T R_T	Supply Voltage DC	Input Current DC	Voltage Across the load	Time	Temp. of Lower MOSFET (*SW2*)	Temp. of Upper MOSFET (*SW1*)	Load
f=10kH$_Z$	180V	1.7A	78V	10 min.	29˚C	39˚C	1100W (Bulb)
C_T=10nF	180V	1.7A	78V	30 min.	32˚C	52˚C	
R_T=10k	180V	1.7A	78V	50 min.	32˚C	56˚C	
	180V	1.7A	78V	70 min.	32˚C	56˚C	

Table 2.6: Thermal analysis of an inverter MOSFET operating at 10kHz using IRF840 as the switching device.

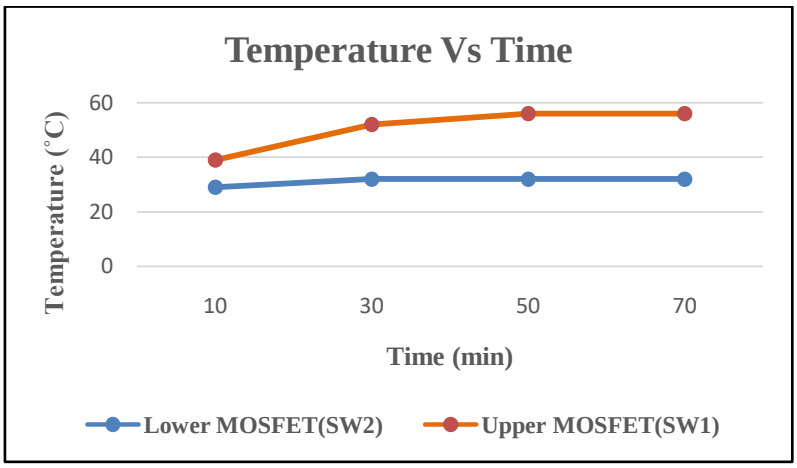

Figure 2.44: Temperature rise versus time of two MOSFETs (*SW1* and *SW2*) of H-bridge inverter at 10kHz operation.

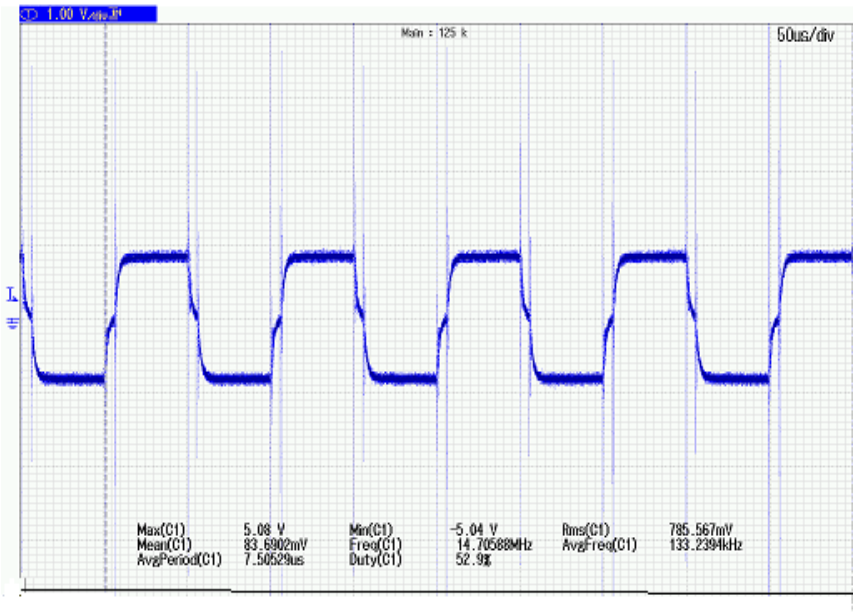

Figure 2.45: Inverter output voltage wave across the tungsten filament bulb load for Table 2.6.

The developed inverters and experimental setup were tested using a tungsten filament lamp load setup to study the thermal characteristics of the MOSFETs under varying load currents. Table 2.3 to 2.6 and Fig 2.36 to 2.45 illustrate the loading characteristics. When the inverter's input voltage was set to 200 V DC, the current through the load was 1.4 A, and the load voltage was 78 V with a 900 W lamp load switched on at 8 kHz. After a few minutes, the lamp load was increased to 1100W, resulting in a current draw of 1.8A. It was observed that the temperature rapidly increased from 47°C to 70°C, potentially risking damage to the MOSFETs due to thermal instability. To prevent damage, the lamp load was reduced back to 900W, bringing the temperature to a safer range. This indicates that the current-carrying capability of the MOSFET is frequency-dependent in this case, 1.8A at 8 kHz, despite the device being rated for 8A. Similarly, the frequency was set to 10 kHz by adjusting the C_T and R_T values. Initially, the inverter input voltage was 180V (DC), and the output was connected to an 1100W load, resulting in a load current of 1.7A as shown in Table 2.6. When the load was increased to 1200W and the input voltage increased to 200V (DC), the current draw rose to 2.2A. However, at this point, the MOSFET failed due to excessive heating, reaching approximately 85°C. This highlights the importance of thermal management and MOSFET selection for reliable operation under varying conditions. From these experimental results, it is evident that the IRF840 MOSFET cannot reliably handle currents greater than or equal to 2.5A in the given inverter circuit in this system. Therefore, the rating of the MOSFETs must be carefully considered to ensure safe and reliable operation. This is essential for the final design of a half-bridge inverter intended for ohmic heating applications at high frequencies up to 20 kHz.

Fig 2.45 shows the inverter output voltage wave across the tungsten filament bulb load for Table 2.6. From this figure it is observed that the area of the upper half is higher than the area of lower half which is giving a slight difference of current conduction between the upper and lower. So higher current conduction gives higher temperature rise in the upper MOSFET. This may be due to manufacturing dissimilarities of source capacitor practically used both are not identical. These are the practical difficulties of half bridge inverter (Fig 2.1).

2.10.3 Thermal performance of Half-bridge inverter using 2SK727 MOSFET

Similar experiments were conducted using the MOSFET 2SK727 in the half-bridge inverter, with performance results shown in Table 2.7 and Figures 2.46-2.47.

f C_T R_T	Supply Voltage DC	Input Current DC	Voltage Across the load	Time	Temp. of MOSFET Lower (*SW2*)	Temp. of Upper MOSFET (*SW1*)	Load
f =10kH$_Z$	200V	2.2A	90V	5 min.	35˚C	49˚C	1100W (Bulb)
C_T=10nF	200V	2.2A	90V	20 min.	40˚C	50˚C	
R_T=10k	200V	2.2A	90V	30 min.	42˚C	51˚C	
	200V	2.2A	90V	40 min.	42˚C	51˚C	

Table 2.7: Thermal study of inverter MOSFET (2SK727) at 10 kHz.

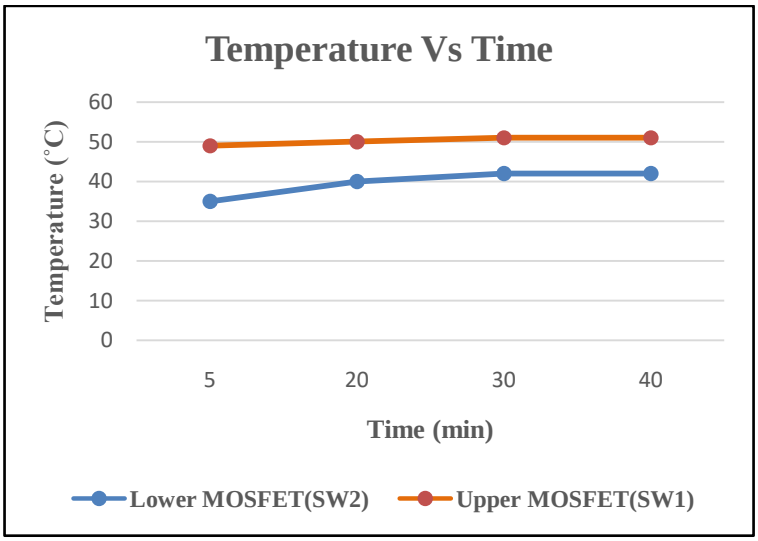

Figure 2.46: Temperature rise versus time of two MOSFETs (*SW1* and *SW2*) of H-bridge inverter at 10kHz operation.

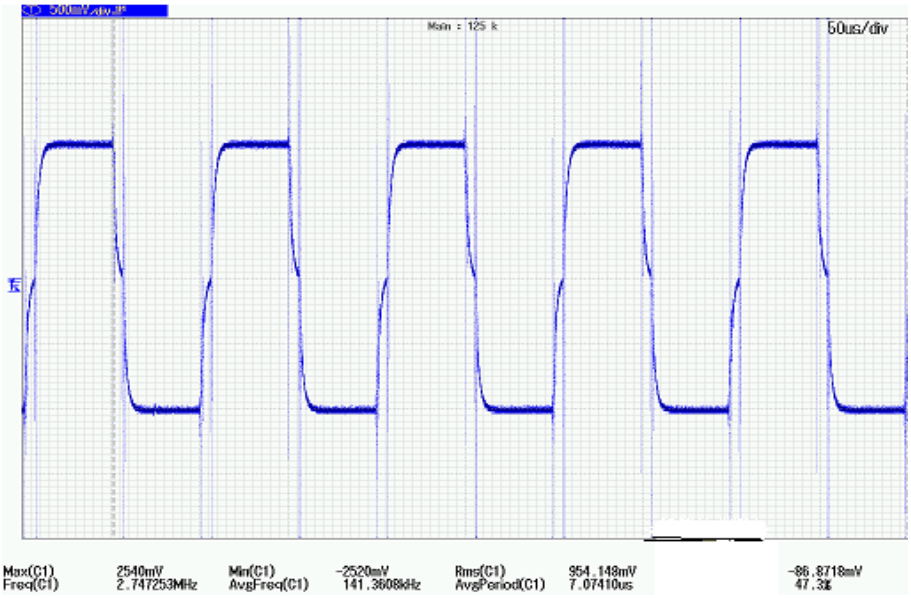

Figure 2.47: Inverter output voltage wave across the tungsten filament bulb load for Table 2.7.

At a frequency of 10 kHz, the experimental data in Table 2.7 shows that with a 200V DC input, the 900W load results in comparatively lower load current and MOSFET temperature. Increasing the lamp load from 900W to 1100W raises the current from 1.6A to 2.2A.

One of the key limitations of the half-bridge inverter is the requirement for a high-voltage DC bus and a voltage divider across the DC link capacitors, which can lead to voltage imbalance and capacitor stress over time. Additionally, half-bridge inverters are more sensitive to shoot-through faults and require more complex gate drive isolation. Thermal stress on the MOSFETs also tends to be higher due to uneven current sharing during high-frequency switching, especially under varying load conditions. These issues are less prominent in push-pull inverters, which allow for transformer-based isolation, simpler drive circuitry, and better thermal distribution between devices. As a result, to overcome these challenges and ensure stable operation under higher loads and frequencies, the push-pull inverter topology is considered a more robust alternative. Replacing optocoupler with totem pole circuit improved performance. The totem pole circuit likely offered improved signal integrity and reduced delays, thereby enhancing overall system reliability, as discussed in Chapter 3.

2.11 Summary

The use of optocouplers for interfacing power and driver circuits initially seemed like a viable solution, but it presented significant challenges. At higher frequencies, the optocouplers introduced uneven delays and signal distortion, leading to MOSFET failures. Moreover, maintaining the precise dead time required for safe switching of the MOSFETs became increasingly difficult. This resulted in cross-conduction, where both MOSFETs in the half-bridge configuration were inadvertently turned on simultaneously causing a short circuit and subsequent failure. These issues highlight the limitations of optocouplers in high-frequency applications.

Chapter-3

DESIGN AND DEVELOPMENT OF HIGH FREQUENCY PUSH-PULL INVERTER USING FERRITE CORE TRANSFORMER FOR OHMIC HEATING AND EXPERIMENTS ON LIQUID CONDUCTORS-FOODS

3.1 Introduction

In the half-bridge inverter configuration discussed in chapter 2, the temperature rise of the upper and lower MOSFETs is unequal, with the upper MOSFET typically exhibiting higher temperatures. This can lead to failure of the upper MOSFET at high currents below its rating, highlighting a significant drawback of the half-bridge design. This issue may be exacerbated when driving liquid conductor loads. To address this limitation, a modification to the half-bridge inverter has been undertaken, incorporating a push-pull operation with a ferrite core transformer.

This chapter explores the design and implementation of a push-pull inverter utilizing a ferrite core transformer. The push-pull topology offers advantages in terms of efficiency, power density, and simplicity, making it suitable for various applications. The ferrite core transformer plays a crucial role in stepping up or down the voltage, while also providing electrical isolation. By utilizing a ferrite core transformer, the system achieves improved magnetic coupling, reduced core losses, and higher switching frequencies compared to conventional iron core designs. The focus of this chapter is to present the working principles, advantages, and implementation considerations of the push-pull inverter, with special attention to the role of the ferrite core in optimizing performance. This chapter will discuss the theoretical aspects, design considerations, and practical implementation of the push-pull inverter with a ferrite core transformer, highlighting its potential benefits and limitations.

3.2 Push-pull inverter

The push-pull inverter's key characteristics include:

i. **Circuit configuration:** Two semiconductors and a center-tapped transformer.
ii. **Operation:** One semiconductor conducts per half-cycle, reducing voltage drop.
iii. **Simplified drive circuit:** Common ground for both power semiconductors eliminates need for insulated voltage sources.

This design offers advantages in terms of simplicity and efficiency. The center-tapped transformer enables efficient voltage transformation, while the push-pull topology allows for balanced operation, where circuit of push-pull inverter showed in Fig 3.1. This work explores more about push-pull inverter applications, design considerations and transformer selection.

When Gate-Source voltage is greater than the threshold voltage the upper MOSFET (SW1) conducts for the time duration as decided by the on-time of the driver pulse voltage waveform. At the same time the lower MOSFET (SW2) should be turned off, else there will be a direct short circuit of the supply terminal via the upper and lower MOSFET. In the push-pull inverter when the upper MOSFET (SW1) conducts, the lower MOSFET (SW2) experiences a peak inverse voltage (PIV) of twice the supply voltage. A suitable dead time is introduced when SW1 turns off, ensuring both MOSFETs don't conduct simultaneously, preventing shoot-through and potential damage. The dead time depends on MOSFET ratings and power circuit parameters. A gate-source voltage greater than the threshold voltage is applied to the lower MOSFET (SW2), causing it to conduct for a duration determined by the on-time of its driver voltage waveform. In this case, the lower MOSFET conducts and the PIV (Peak Inverse Voltage) of upper MOSFET gets equal to twice of the supply voltage. Thus, a square wave voltage pulse is obtained at the secondary terminal of the center tapped ferrite core transformer and the inverter output is a square wave power output. Operational frequency of the inverter is high, matching the frequency of the driver signal, and is practically compatible with the associated MOSFET and power circuit.

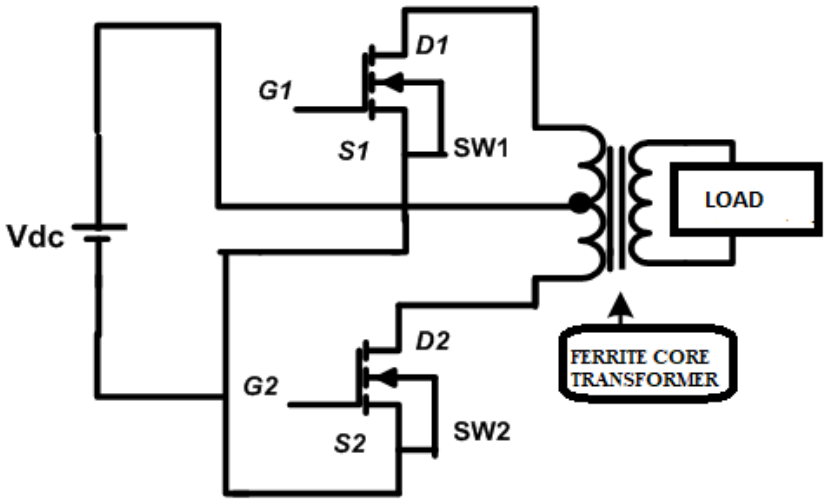

Figure 3.1: Push-pull inverter circuit.

3.3 Requirements of high frequency ferrite core transformer

Iron and its magnetic alloys were used to meet the demand for magnetic materials in the early days of the electrical industry [58]. But when higher frequencies were introduced, the conventional methods of lowering eddy current losses such as lamination or iron powder cores were no longer practical or economical. According to S. Hilpert's 1909 publication in Germany, this insight sparked a resurgence of interest in "magnetic insulators." The combination of necessary magnetic properties and the high electrical resistance of oxides was easily understood to produce a magnetic material that was especially well suited for high frequency operation.

An example of a magnetic core is a ferrite core, which is used to form the windings of electric transformers and other wound components like inductors. High frequency applications are better suited for ferrite cores [59], whereas low frequency applications are best suited for steel laminations. Both materials come in different grades, each of which is best suited for a particular use. Ordinary laminated cores made of steel lamination can only be used under specific operating conditions and within the working frequency range of 50 to 60 Hz. For high frequencies in the range of kHz, however, the laminated core cannot be used because core loss, which is comprised of eddy current loss and hysteresis loss, varies with frequency and frequency squared, respectively. The supply frequency to the transformer in this research work varies between 1 to 20 kHz, so ferrite cores must be used for such a frequency range.

3.3.1 Ferrite core transformer in push-pull inverter

In high-frequency push-pull inverters, a ferrite core transformer is commonly used because ferrite materials have low eddy current and hysteresis losses at high frequencies (typically tens to hundreds of kHz). This makes them well-suited for compact, efficient power conversion. The push-pull topology drives the transformer alternately with two switches, allowing efficient AC signal generation from a DC source shown in Fig 3.1.

3.3.2 Design of ferrite-core transformer

The operating frequency and power decide the operation of transformer according to their wide band pulse etc. The design of transformer for a specific cooling system depends on maximum magnetic flux density, maximum current density and maximum voltage per turn. If the function of the transformer exceeds these limits, then it may destroy the transformer. But pulse transformer is designed for high frequency and low power signal. So, the input to

an inverter transformer for higher frequency and higher power, one should design with the combined objectives of both power and pulse transformer which is called wide band transformer. As frequency raises the required laminations thickness becomes extremely thin which is impracticable to reduce the eddy current. So, transformer core material should be made up of selected ferrites having low eddy current loss. Ferrite cores can be designed in various shapes and geometries to suit specific applications. The choice of core geometry depends on factors like frequency, power handling, and space constraints. The Dimension of ferrite core transformer consider in this work is shown in Fig 3.2.

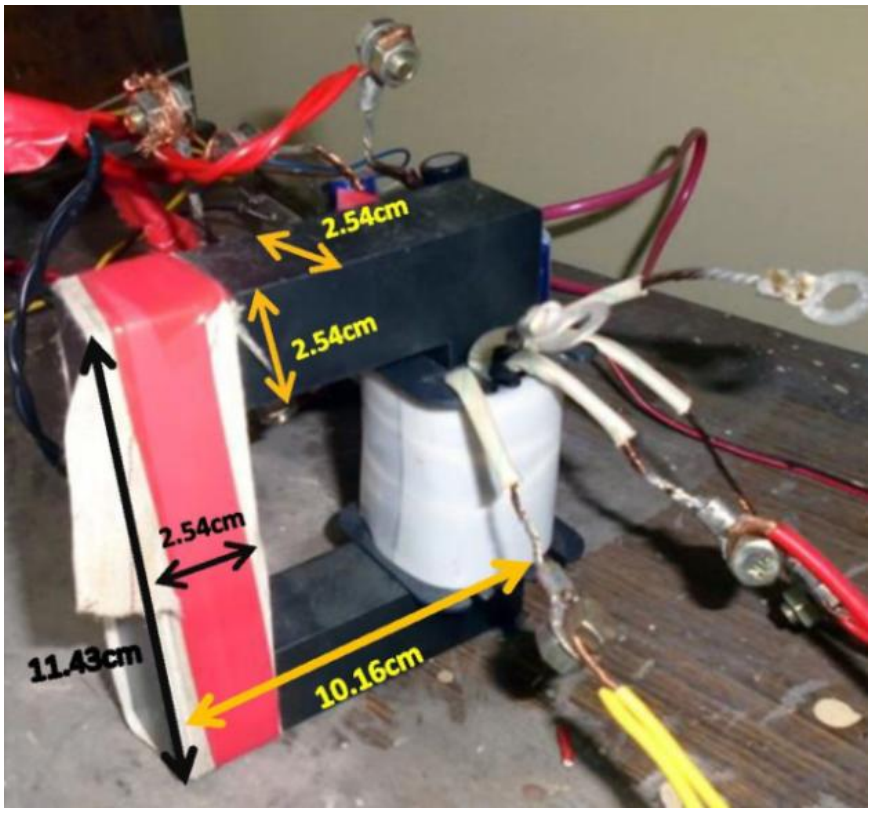

Figure 3.2: Dimension of ferrite core transformer.

The following factors listed in the equations here that determine the ferrite core transformer's performance [60]–[62], which are important to design the high frequency transformer:

Voltage induced in a coil is-

$$V = n\frac{d\emptyset}{dt} = nA_e\frac{dB}{dt} \quad (3.1)$$

Where,

n= No of turns in a coil

Ø= magnetic flux

A_e= Cross section area of the core

B= Magnetic flux density

From (3.1), the change in flux density i.e. ΔB can be derived as-

$$\int Vdt = nA_e \int dB \tag{3.2}$$

Or

$$V.\Delta t = nA_e \Delta B \tag{3.3}$$

Or

$$\Delta B = \frac{1}{nA_e} V.\Delta t \tag{3.4}$$

Here, V.Δt is known as volt-second. This volt-second is the key to determine ΔB, both for symmetrical and asymmetrical operation. In this work symmetrical operation of maximum magnetic flux density (B) has been considered. Size of the core of high frequency transformer in the push-pull inverter has been designed by using the area product (A_P) mentioned below-

$$A_P = A_e A_w = \frac{V_1.D_{on}.2I_{1rms}}{f_s.\Delta B.J.k} \tag{3.5}$$

Where,

V_1= Input voltage

I_{1rms}= Input rms current

A_w= Window area of the core

D_{on}= Duty cycle

f_s= Switching frequency

J= Current density of the conductor

k= Filling factor

The product of switching frequency f_s and allowable ΔB for a particular ferrite core is known as figure of merit which decides the size of core A_P. In high frequency operation the magnetic losses (P) in a core material decided by-

$$P = K.f^{n}.(\Delta B)^{m} \quad (3.6)$$

Where, K is proportionality constant, 'n' and 'm' are the given numbers for a particular material. In this work the aim of the variation of supply frequency to the transformer is up to several 100 kHz. Hence the optimum choice of the ferrite core material is Manganese-Zinc ferrites. Any core has a limited frequency range because higher frequency causes a rise in copper losses and core losses, which reduces efficiency of the transformer because larger core can handle the losses when there is high frequency range. Higher flux densities are constrained by core loss, which increases the core material temperature and the core may also go into saturation. In order to achieve an acceptable temperature rise over ambient, the peak flux density must be such as overall total (core and copper) losses becomes small value. The transformer was designed with a core made of Manganese Zinc ferrites for an operating frequency up to 100 kHz. The dimensions of the core are shown in Fig 3.2. Furthermore, it is assumed that iron loss in the core contributes to half of the temperature rise, while copper loss in the winding contributes for the other half [60]-[63].

A sample calculation of power handling capacity (P_o) [64]-[66] of the above mentioned transformer for 20 kHz frequency is shown below-

$$P_o = \frac{A_P.K_{topology}.B_{max}.f_s}{D_{cma}} \quad (3.7)$$

Where,

$K_{topology}$= 0.001 for push-pull inverter

B_{max}= maximum flux density in Gauss

D_{cma}= Cir.mils/amp

Hence,

$A_P=A_e.A_w=21.93cm^4$

Bobbin area of the winding should be included with the area product. Therefore, the approximate area product can be consider as,

$A_P=21.93\times1.5=32.89cm^4$

So power handling capacity using (3.7) P_o will be-

P_o=2.02kW

For B_{max} = 2000 Gauss, taken from the frequency vs. maximum flux density plot for L-type ferrite material at 20 kHz, and D_{cma} = 650 cir.mils/amp, respectively. The L material is formulated for high-temperature and high-frequency applications, designed for power supplies operating from 0.5 to 3 MHz. The Curie temperature is high for this ferrite material, at 300°C.

3.4 Driver circuit using totem pole

The driver power supply must be properly designed to handle the high gate current for a shorter period of time, based on the inverter's power rating, especially in high switching frequency applications. Some limitations regarding high-speed operations have been observed in the half-bridge driver discussed in the previous chapter during inverter operation. These issues are overcome by designing the driver circuit with a higher charging current and a totem-pole setup. For faster switching operation, the gate capacitance of the MOSFET needs to charge and discharge quickly. Hence, a higher charging current is needed at the input side of the MOSFET during turn-on, while a faster discharge is required during turn-off. A brief discussion of turn-on and turn-off process of MOSFET considering its gate capacitances shown in Fig 2.4, hence a design calculation are being presented below, which helps to develop the driver circuit for high frequency requirement. During turn-on, the equivalent circuit of the gate-source (C_{gs}) and gate-drain (C_{gd}) capacitances must be charged, and the total amount of charge (Q_{total}) required for this must be supplied from control circuit. When the driver supplies the maximum gate pulse voltage (V_{gsmax} = 15V), it rises to the threshold value of around 4V by charging the gate-to-source capacitance, enabling the MOSFET to start conducting. This initiates a rise in drain-to-source current from zero. The high voltage of drain swings to ground and during this time heavy charging occurs to gate-drain capacitance [67]-[68], which is nonlinear in nature. This gate-source voltage (V_{gs}) known as Miller-voltage remains almost constant shown in Fig 2.4. As the drain voltage drops to near ground, the gate-source voltage (V_{gs}) rises to its maximum value (V_{gsmax} = 15V) due to the charging process. The total gate charge (Q_{total}) required charging the equivalent capacitance (C_{eq}) of the MOSFET can be found in the device's datasheet.

3.4.1 Design and calculation of gate current (I_g) for turning on the MOSFETs

The design of the gate current (I_g) required turning on the MOSFETs is proposed in this work. The following symbols are considered from the Fig 2.4 and named as:

V_{cgs}= Voltage across the capacitor C_{gs}

V_{cgd}=Voltage across the capacitor C_{gd}

V_{gsmax}=Maximum voltage across the capacitor C_{gs}

V_{in}=Voltage applied across drain to source

ΔV_{cgs}=Voltage change across the capacitor C_{gs}

ΔV_{cgd} = Voltage change across the capacitor C_{gd}

Now,

at t=0 ,V_{cgs}=0 and $\Delta V_{cgs} = V_{gsmax}$ for t = ∞;

at t=0, $V_{cgd} = - V_{in}$ and $\Delta V_{cgd} = V_{gsmax}$ for t = ∞;

Total charge stored by the input capacitance of the MOSFET:-

$$Q_{total} = V_{gs} * C_{gs} + (V_{gs} + V_{in})C_{gd} \quad (2.4)$$

and,

$$C_{eq} = Q_{total}/V_{gsmax} = C_{gs} + M_{effect} \quad (2.5)$$

Where,

$M_{effect} = C_{gd}(1 + V_{in}/V_{gsmax})$=Miller effect

Similarly,

$$Q_{total} = I_g * t_{on} = C_{eq} * V_{gsmax} \quad (2.6)$$

Hence,

$$I_g = (C_{eq} * V_{gsmax}/t_{on}) \quad (2.7)$$

- A sample design calculation performed for the driver developed in laboratory referring the datasheet of 2SK727 MOSFET as below:

V_{in} = 100V;

Q_{total} = 28nC;

Q_{gs} = 17nC;

Q_{gd} = 11nC;

Let, V_{gsmax} =15V and V_{in}=100V,

Junction capacitance of the MOSFET will be-

$$C_{gs} = (17*10^{-9})/15 = 1133pF. \quad (2.8)$$

and

$$C_{gd}(1 + V_{in}/V_{gsmax})*V_{gsmax} = Q_{gd} = 11*10^{-9} \quad (2.9)$$

Hence,

C_{gd} = 95pF.

So equivalent capacitance will be:-

$$C_{eq} = C_{gs} + C_{gd}\{1 + (V_{in}/V_{gsmax})\} = 1228pF \quad (2.10)$$

Therefore the required gate current for turning on the MOSFETs taking the turn-on time 100nS will be-

$$I_g = (C_{eq} * V_{gsmax})/t_{on} = (1228*15*10^{-12})/100*10^{-9} = 0.184A \quad (2.11)$$

Therefore it is found in gate drive calculation that gate current (I_g) equal to 0.184A, has to be supplied for very small time in 100nS. This requires proper design of driver power source for this high gate current within a very small time, depending on power rating of inverter. Hence, a similar PWM IC LM3524 with some modification of H-bridge driver circuit is used for development of driver for controlling the MOSFETs. A totem pole circuit and a separate transistor as current booster are used to speed up the turning on and off process of inverter-MOSFETs which finally reduces switching losses at higher frequency. The block diagram of the driver circuit using totem-pole is shown in Fig 3.3.

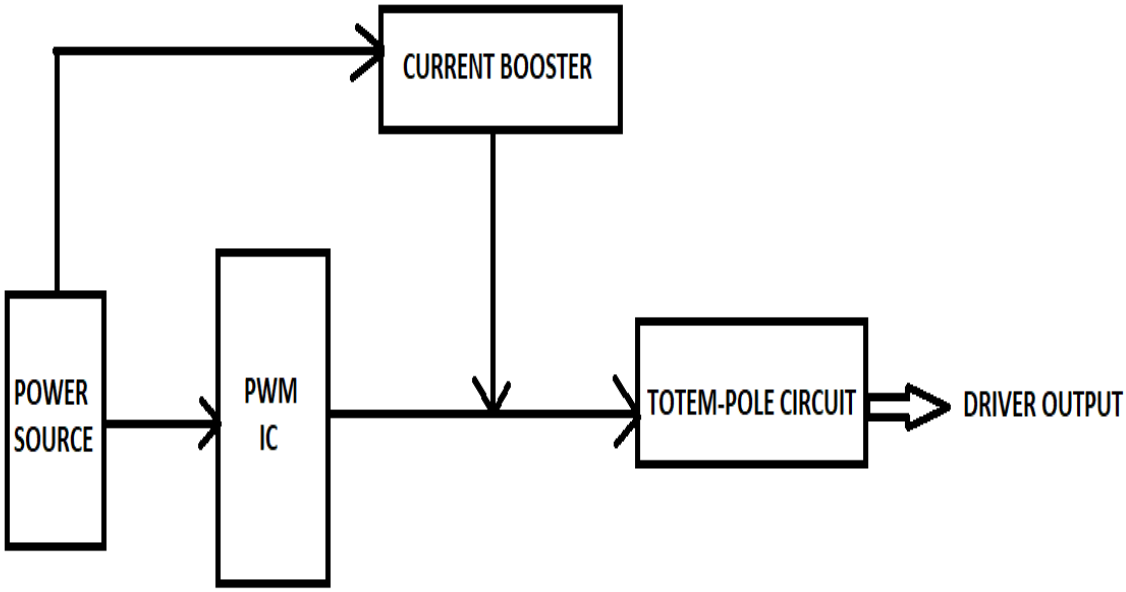

Figure 3.3: Block diagram of the driver circuit using totem pole.

A novel high-frequency driver using a totem-pole configuration has been designed and developed in the laboratory, featuring popular driver circuit solutions that have been tested and analyzed for their performance. The design of the driver circuit is crucial for high-frequency inverters, and the salient components of this developed driver circuit are shown in Fig 3.4, with symbols representing their usual meaning. The power source block provides the required

voltage to the PWM IC and current booster transistor, ensuring proper functionality.

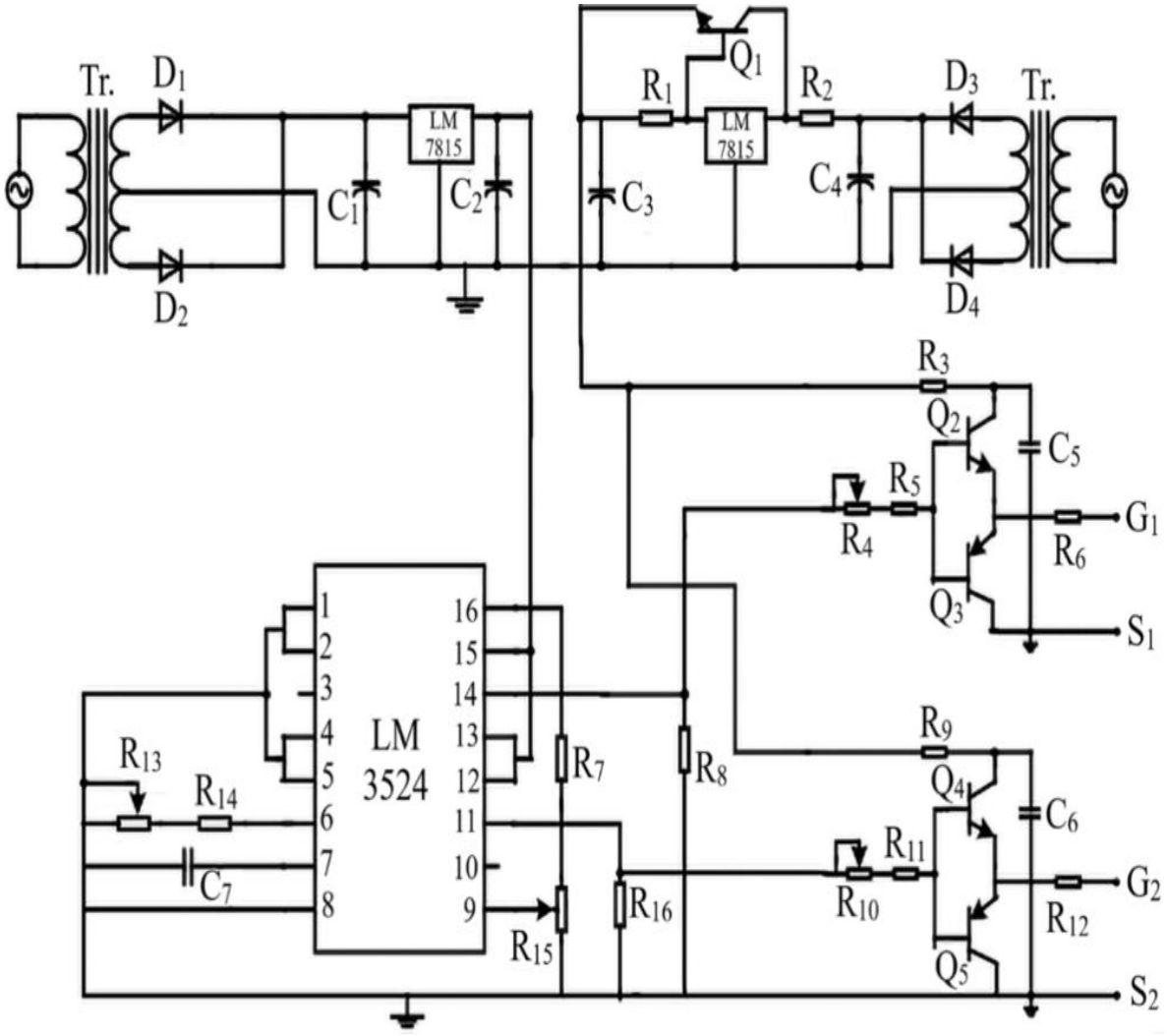

Figure 3.4: Driver circuit using totem pole for inverter-MOSFETs.

3.4.2 Module and components used for the gate driver

The main components of the developed driver circuit, as illustrated in Fig 3.4, are discussed in detail below.

1. A DC regulated power source of 15V DC across capacitor (C_3) using LM7815 having sufficient capacity of current by a paralleled transistor (Q_1) is incorporated to cater the demand of high charging current initially to the gate-source capacitor of the MOSFETs for turning on the switch.

2. A totem pole circuit is used for having speedy switch-off of the MOSFETs from conducting state providing active grounding of gate to ensure the transition time as low as possible to avoid the cross conduction of the inverter switches [49].

3.4.3 Frequency & duty cycle control of the driver

Frequency (f_{osc}) of the driver circuit output is obtained by $f_{osc} \approx 1 / RC_7$, where $R = (R_{14} + R_{13})$. Thus frequency is controlled by the resistance R_{14} and R_{13} connected to pin 6 whereas a fixed capacitance C_7 is connected to pin 7 of IC LM3524 and duty cycle of the driver output pulses is changeable; this control is done by varying voltage on pin. 9 by a variable resistance R_{15} connected to the IC LM3524 shown in Fig 3.4. The hardware setup of the driver circuit using totem pole, including all the components, is shown in Fig 3.5.

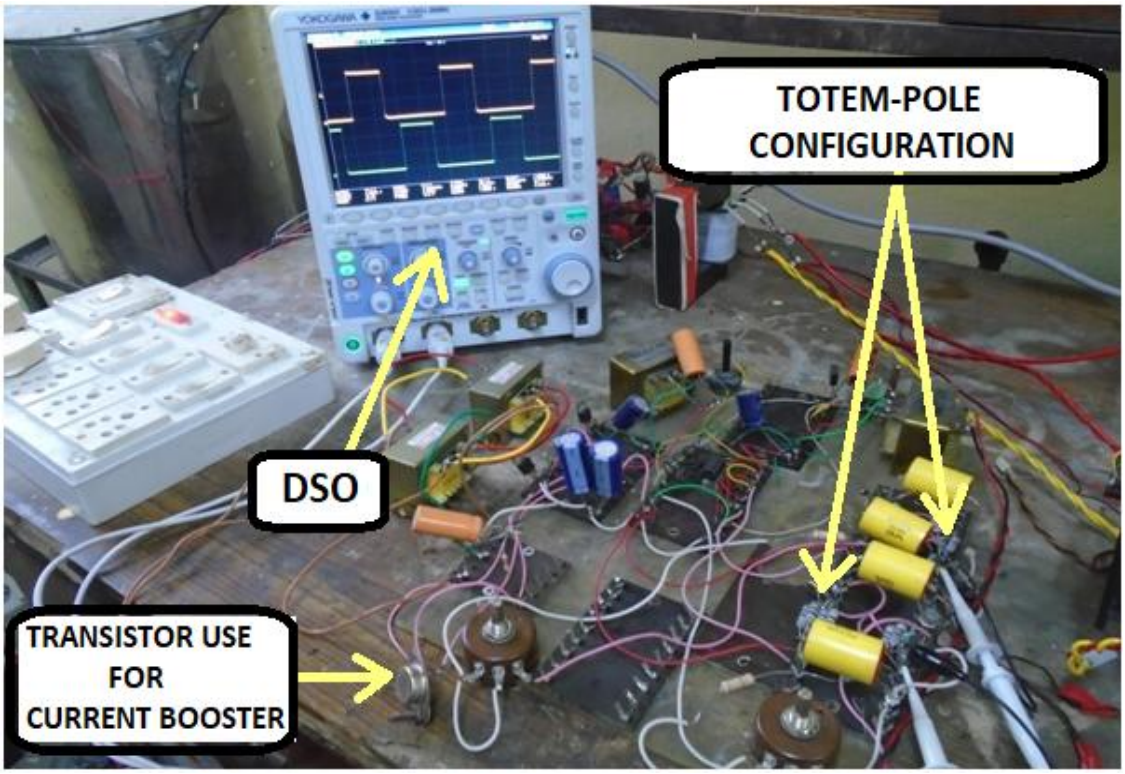

Figure 3.5: Hardware setup of the driver circuit using totem pole.

3.5 Driver output voltage using totem pole at various frequency and duty cycle

The driver circuit designed and fabricated in the laboratory has undergone thorough testing, and its performance has been documented using a Digital Storage Oscilloscope (DSO). The DSO captures crucial characteristics, including voltage pulses, rise time, fall time,

frequency, and duty cycle. The results show sharp rise and fall times for the gate signal voltage, even at high frequencies, which is vital for efficient switching of high-speed power semiconductor devices like MOSFETs. Fig 3.6 to 3.9 illustrates the driver output voltage for various frequencies and duty cycles when the MOSFET's gate-source terminals are not connected to the driver output. Output-voltage pulses across G_1-S_1 and G_2-S_2 of the totem-pole driver are displayed in blue and pink color.

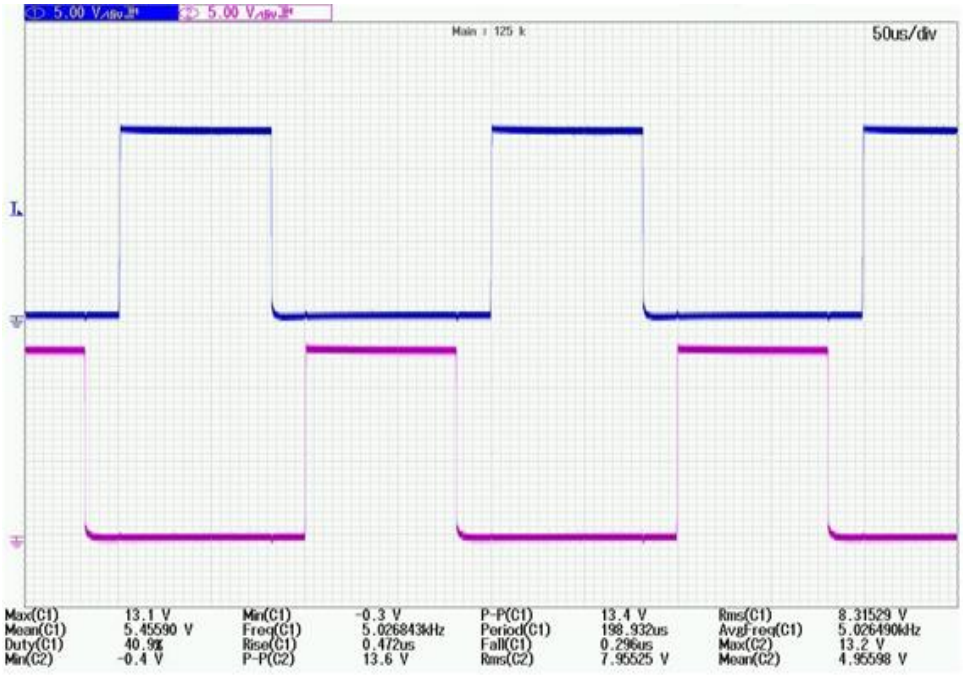

Figure 3.6: Driver output voltage using totem pole at frequency 5 kHz with 40% duty cycle.

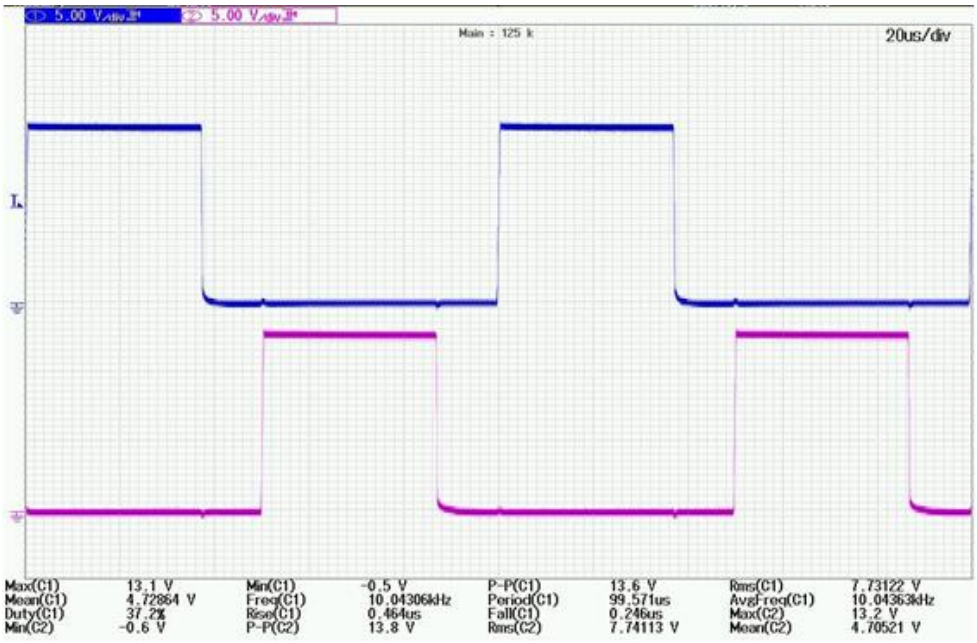

Figure 3.7: Driver output voltage using totem pole at frequency 10 kHz with 37.2% duty cycle.

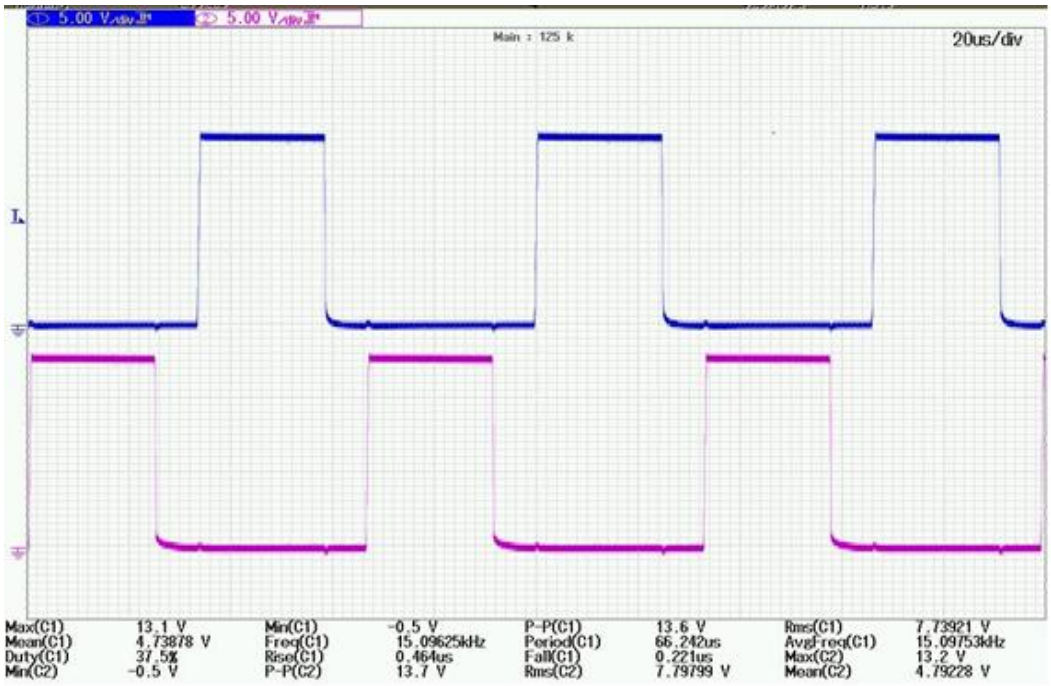

Figure 3.8: Driver output voltage using totem pole at frequency 15 kHz with 37.5% duty cycle.

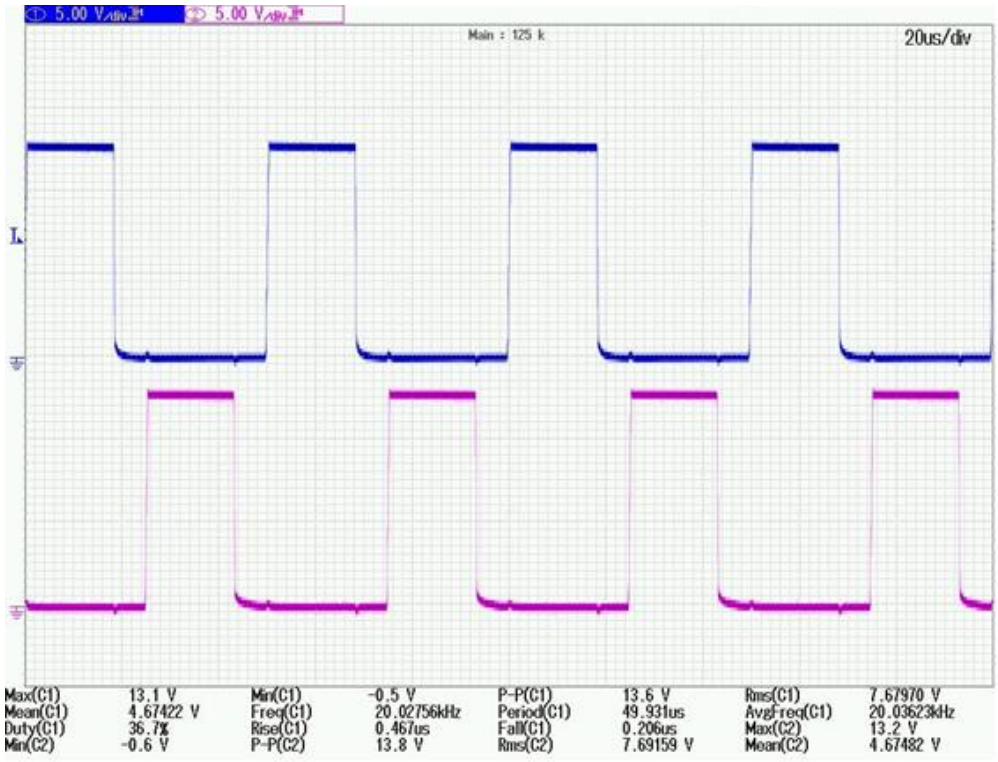

Figure 3.9: Driver output voltage using totem pole at frequency 20 kHz with 36.7% duty cycle.

3.6 Driver output voltage with MOSFET Connection

Fig 3.10 to 3.15 illustrates the driver output voltage for various frequencies and duty cycles when the MOSFET's gate-source terminals are connected to the driver output, showcasing both 'off' and 'on' conditions.

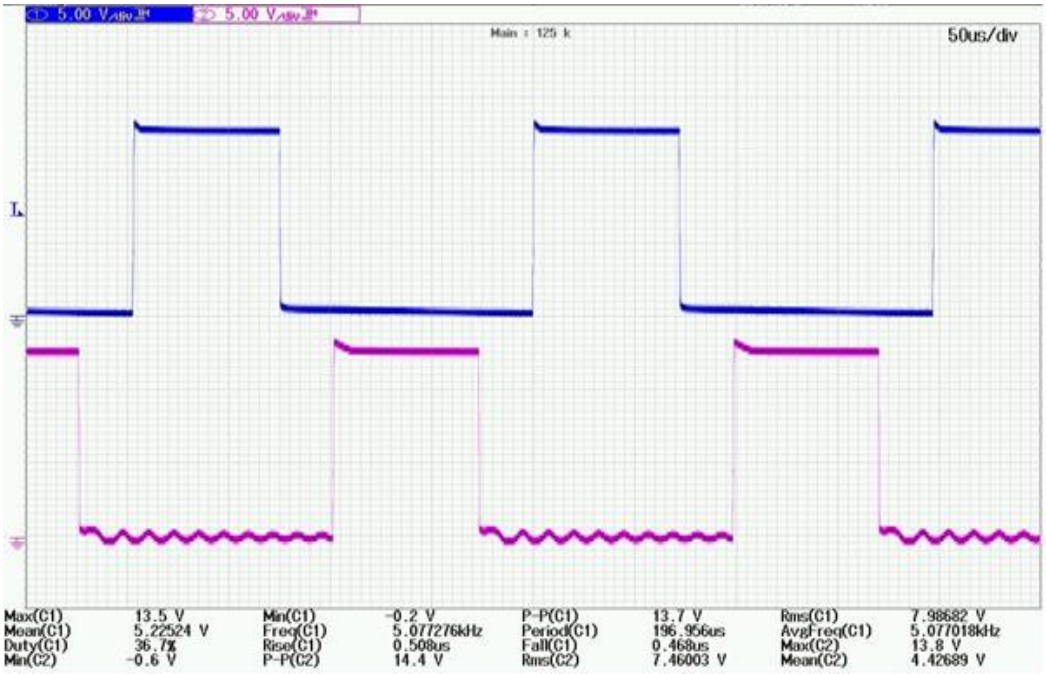

Figure 3.10: Driver output voltage at frequency 5 kHz when gate-source terminal is connected.

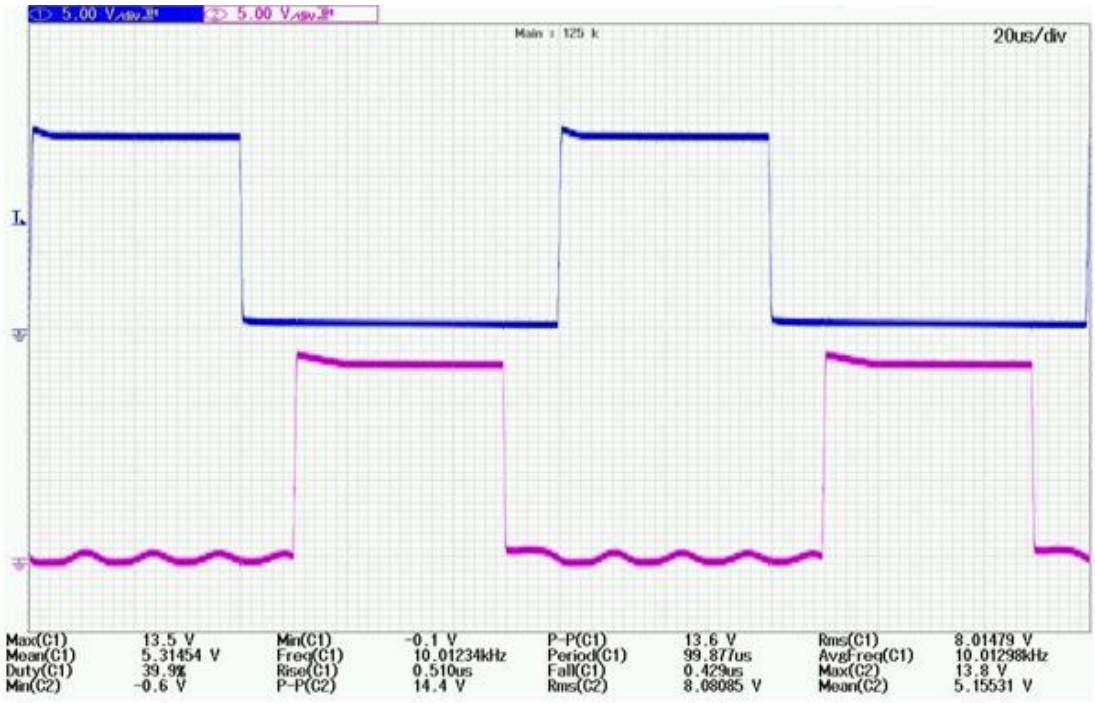

Figure 3.11: Driver output voltage at frequency 10 kHz when gate-source terminal is connected.

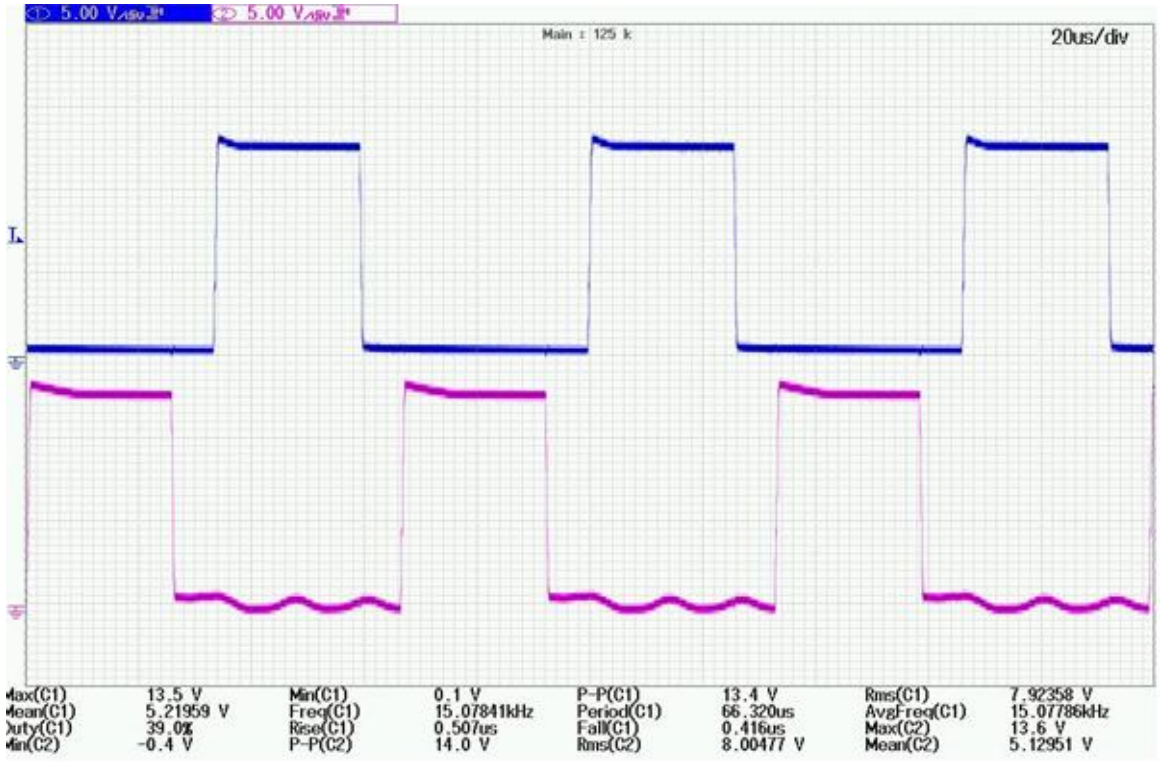

Figure 3.12: Driver output voltage at frequency 15 kHz when gate-source terminal is connected.

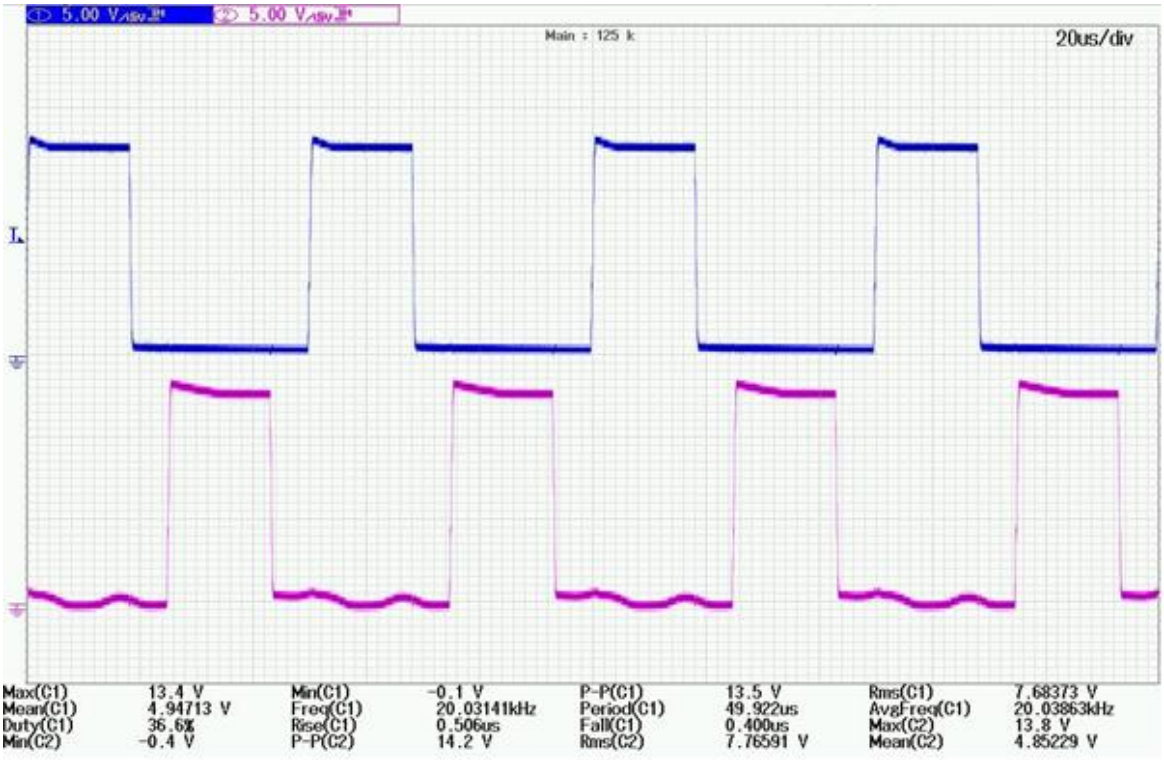

Figure 3.13: Driver output voltage at frequency 20 kHz when gate-source terminal is connected.

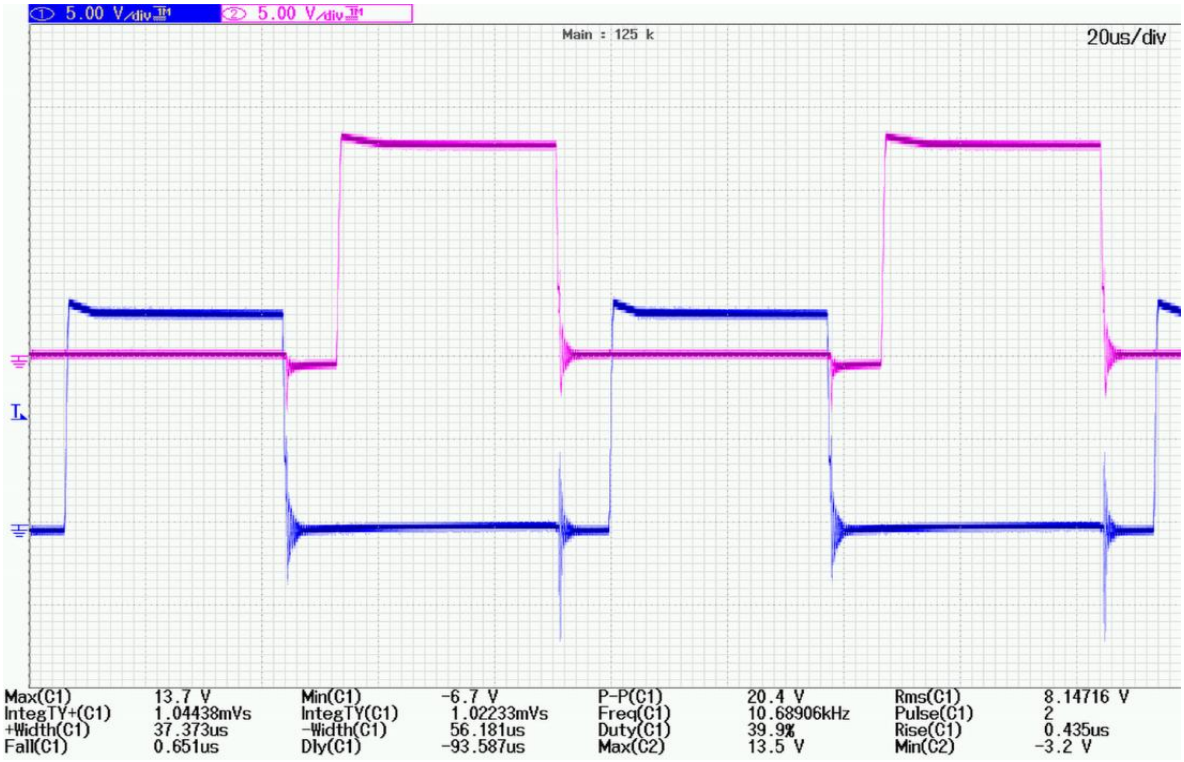

Figure 3.14: Driver output voltage pulses across gate-source while MOSFETs are conducting (on) at 10 kHz.

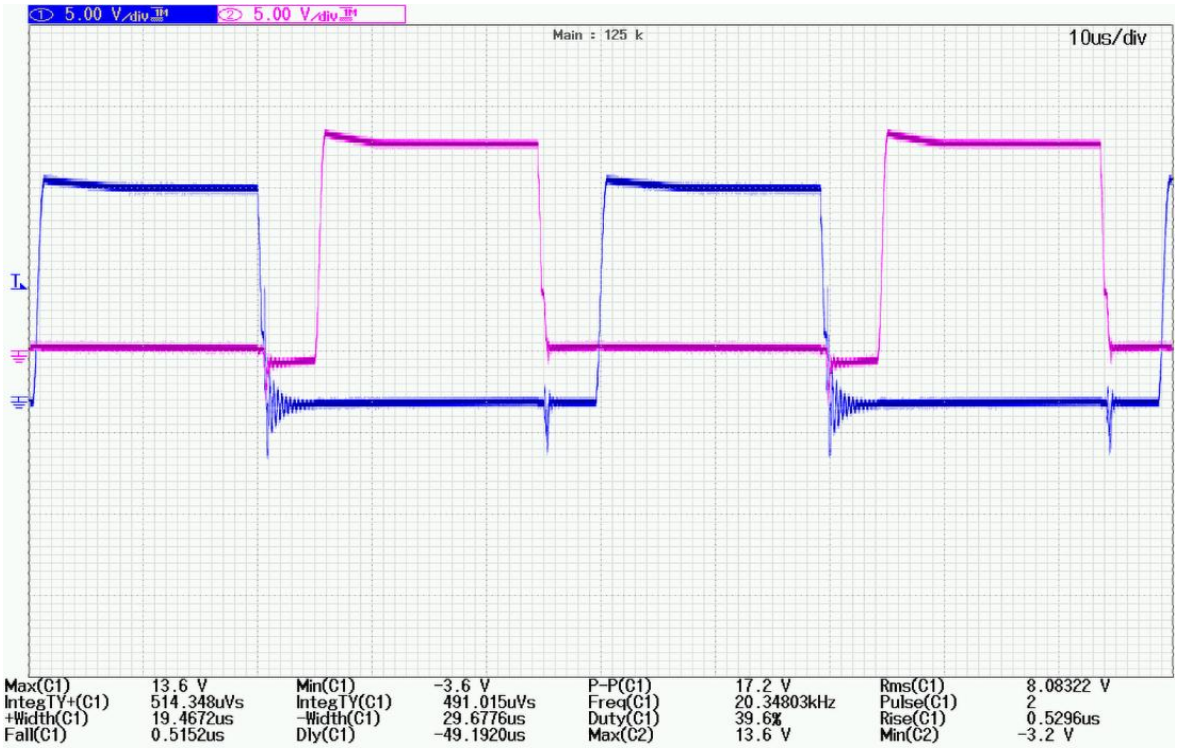

Figure 3.15: Driver output voltage pulses across gate-source while MOSFETs are conducting (on) at 20 kHz.

The impact of parasitic components, transient, and extreme operating conditions in the test of above driver is displayed in Fig 3.15. A high frequency oscillation in the turn on and turn off duration is being observed which is detrimental for the reliable operation of the driver MOSFETs. So a compact PCB design can minimize this.

3.7 Experiment on push-pull inverter

The complete setup of push-pull type inverter with ferrite core transformer and pressurized vessel for liquid conductor load is shown in Fig 3.16. Ferrite core transformer is designed by 3:1 ratio having higher current in the secondary side for the push-pull setup.

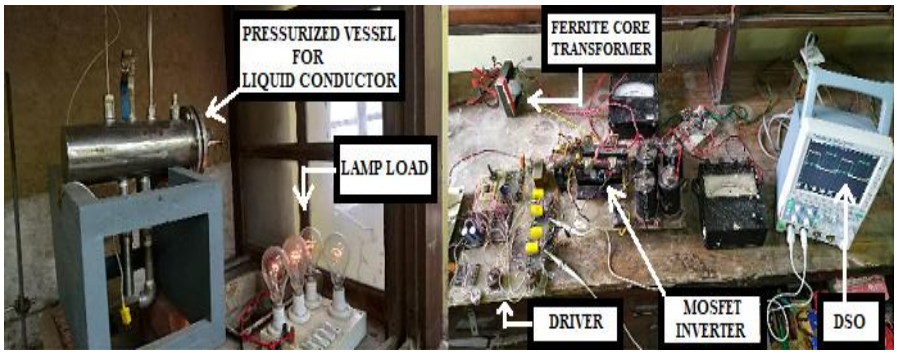

Figure 3.16: Push-pull inverter setup with ferrite core transformer.

3.7.1 Thermal performance of push-pull inverter using IRF840 MOSFET

The experimental results of thermal characteristics of the push-pull inverter using IRF840 MOSFET as a switch are presented in Tables 3.1 to 3.4 and Fig 3.17 to 3.24 for different frequencies. The switching frequency is given by the equation: $f = 1/C_t . R_t$. The capacitor (C_t) and resistor (R_t) are connected to pins 7 and 6 respectively, of the PWM IC LM3524. Where C_t is considering as C_7 and R_t is the addition of (R_{14} + R_{13}) shown in Fig 3.4.

3.7.1.1 Thermal analysis of the IRF840 MOSFET in inverter operation at 10.5 kHz

f C_t R_t	Supply Voltage DC	Input Current DC	Voltage Across the load	Time	Temp. of lower MOSFET (SW2)	Temp. of Upper MOSFET (SW1)	Load
	100V	1.5A	75V	10 min.	44˚C	46˚C	1000W (Bulb)
f=10.5kHz	120V	1.7A	90V	10 min.	52˚C	64˚C	
C_t=10nF	140V	1.7A	112V	10 min.	60˚C	65˚C	900W (Bulb)
R_t =10k	140V	1.7A	112V	20 min.	68˚C	73˚C	
	140V	1.8A	109V	15 min.	56˚C	60˚C	1000W (Bulb)
	140V	1.8A	109V	30 min.	76˚C	80˚C	

Table 3.1: Thermal study of inverter MOSFET(IRF840) at 10.5 kHz.

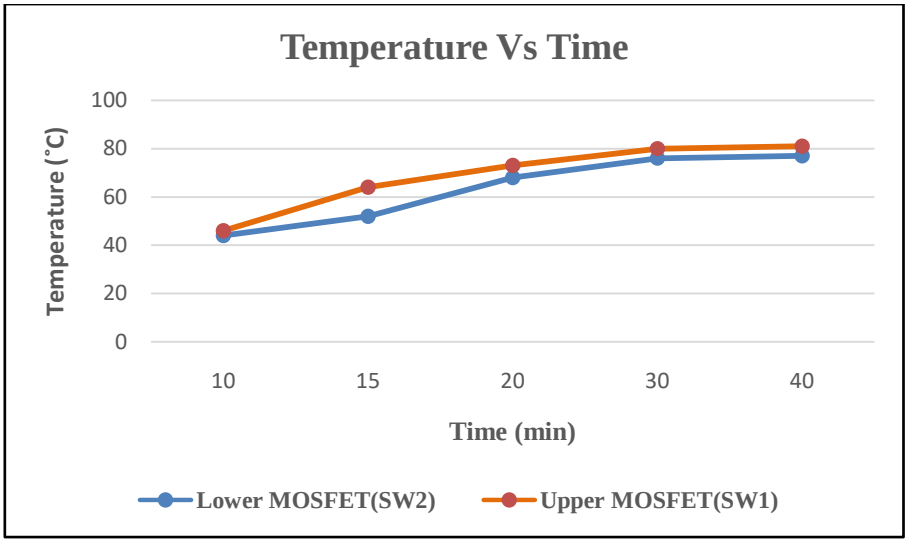

Figure 3.17: Temperature rise versus time of two MOSFETs (SW1 and SW2) at 10.5 kHz operation.

3.7.1.2 Inverter output voltage wave across the tungsten filament bulb load at 10.5 kHz

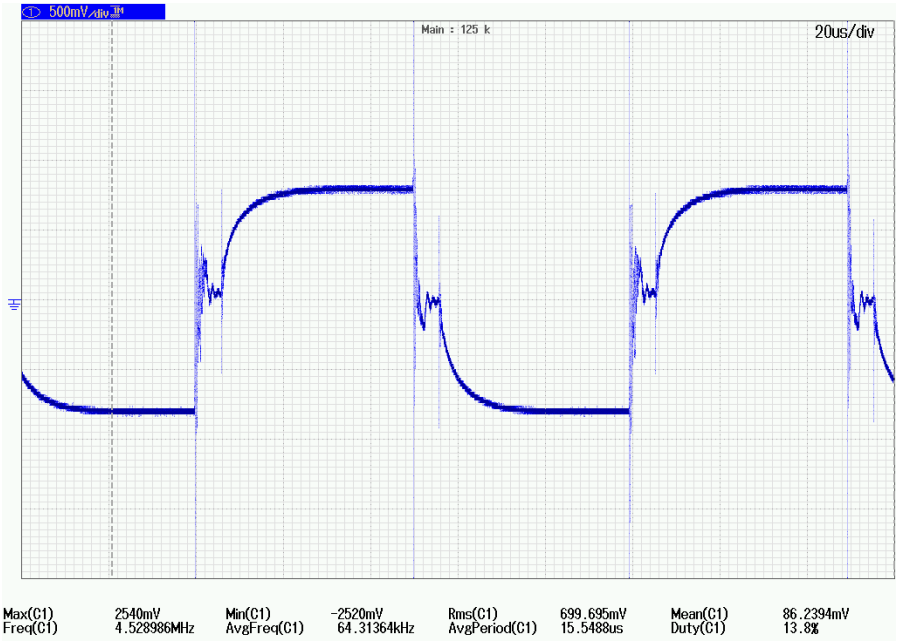

Figure 3.18: Inverter output voltage wave across the tungsten filament bulb load for Table 3.1 (1000W).

High frequency oscillation found during the turn on and turn off of the push-pull inverter MOSFETs displayed on Fig 3.18. This may be due to the oscillation in the driver circuit as well as use of ferrite core. However push-pull technology avoids any possibilities of cross conduction. This is a more prominent if the operating frequency increases to very high value. So the development of high frequency inverter requires more care than the low frequency inverter.

f C_t R_t	Supply Voltage DC	Input current DC	Voltage Across the load	Time	Temp. of lower MOSFET (SW2)	Temp. of Upper MOSFET (SW1)	Load
$f=10.5kH_Z$	110V	1.5A	98V	10 min.	38˚C	40˚C	
$C_t=10nF$	110V	1.5A	98V	20 min.	43˚C	46˚C	400W
$R_t=10k$	110V	1.5A	98V	30 min.	43˚C	47˚C	(110V-Bulb)
	110V	1.5A	98V	50 min.	44˚C	49˚C	
	110V	1.5A	98V	60 min.	44˚C	49˚C	

Table 3.2: Thermal study of inverter MOSFET(IRF840) at 10.5 kHz.

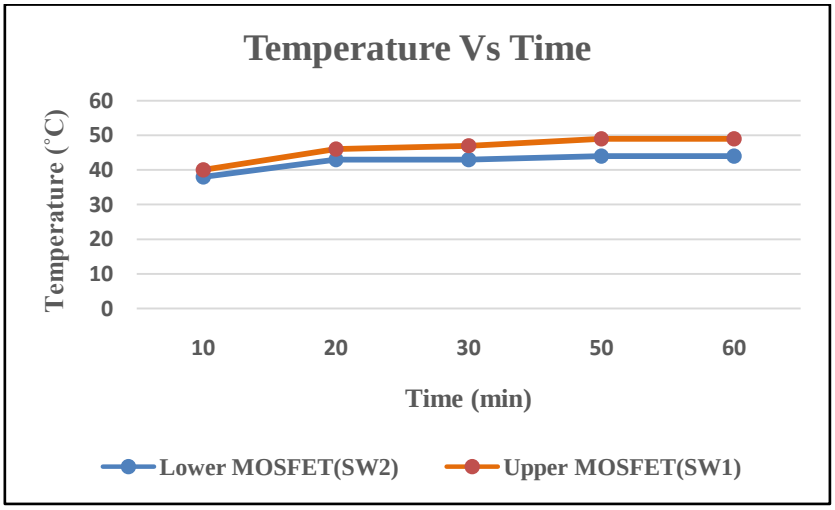

Figure 3.19: Temperature rise versus time of two MOSFETs (SW1 and SW2) at 10.5 kHz operation.

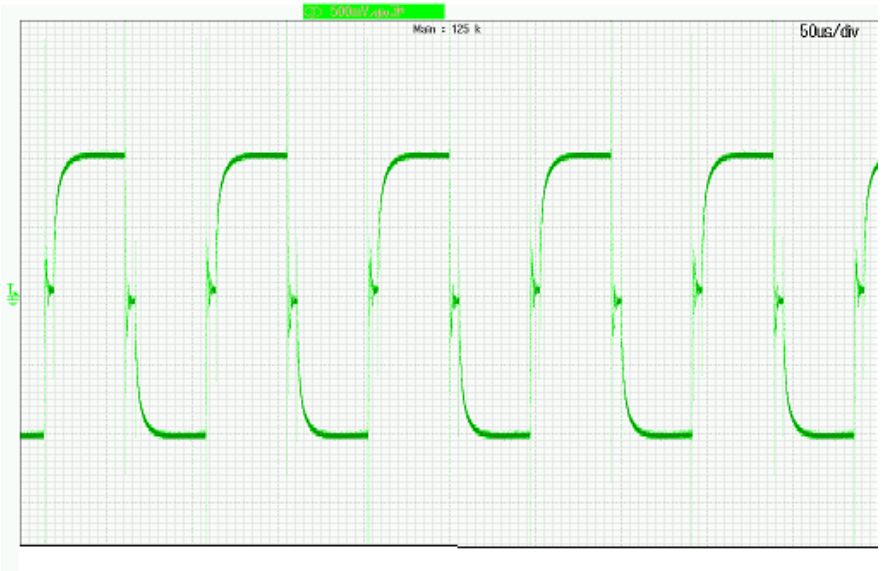

Figure 3.20: Inverter output voltage wave across the tungsten filament bulb load for Table 3.2.

3.7.1.3 Thermal analysis of the IRF840 MOSFET in inverter operation at 7.5 kHz

f C_t R_t	Supply Voltage DC	Input current DC	Voltage Across the load	Time	Temp. of lower MOSFET (SW2)	Temp. of upper MOSFET (SW1)	Load
$f = 7.5kH_Z$	110V	1.5A	97V	10 min.	44˚C	44˚C	
$C_t = 10nF$	110V	1.5A	97V	20 min.	45˚C	46˚C	400W (110V-Bulb)
$R_t = 14k$	110V	1.5A	97V	40 min.	51˚C	49˚C	
	110V	1.5A	97V	60 min.	51˚C	49˚C	

Table 3.3: Thermal study of inverter MOSFET(IRF840) at 7.5 kHz.

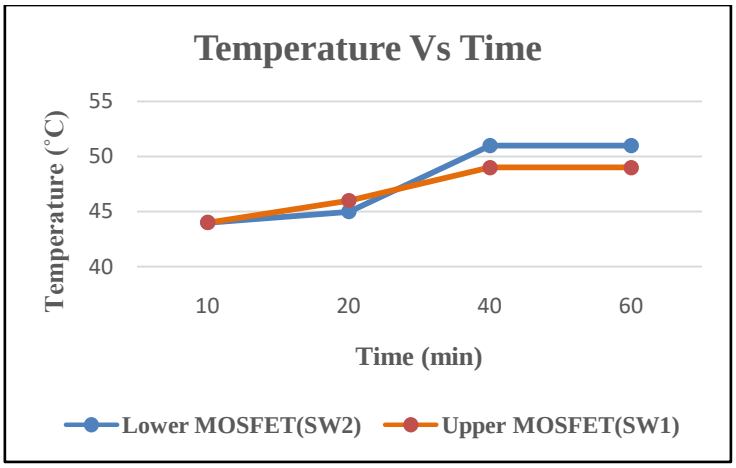

Figure 3.21: Temperature rise versus time of two MOSFETs (SW1 and SW2) at 7.5 kHz operation.

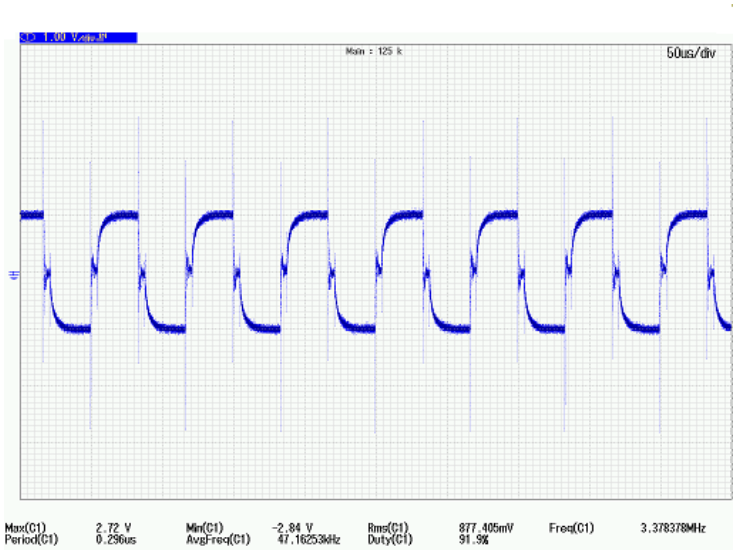

Figure 3.22: Inverter output voltage wave across the tungsten filament bulb load for Table 3.3.

3.7.1.4 Thermal analysis of the IRF840 MOSFET in inverter operation at 15 & 5 kHz

f C_t R_t	Supply Voltage DC	Input current DC	Voltage Across the load	Time	Temp. of lower MOSFET (SW2)	Temp. of upper MOSFET (SW1)	Load
$f = 15kH_Z$ $C_t = 10nF$ $R_t = 6.6k$	110V	1.5A	94V	10 min.	40˚C	43˚C	400W (110V-bulb)
	110V	1.5A	94V	30 min.	42˚C	50˚C	
	110V	1.5A	94V	50 min.	42˚C	50˚C	
$f = 5kH_Z$ $C_t = 10nF$ $R_t = 20k$	110V	1.5A	94V	10 min.	40˚C	44˚C	
	110V	1.5A	94V	30 min.	44˚C	49˚C	
	110V	1.5A	94V	60 min.	45˚C	53˚C	
	110V	1.5A	94V	70 min.	45˚C	53˚C	

Table 3.4: Thermal study of inverter MOSFET(IRF840) at 15 and 5 kHz.

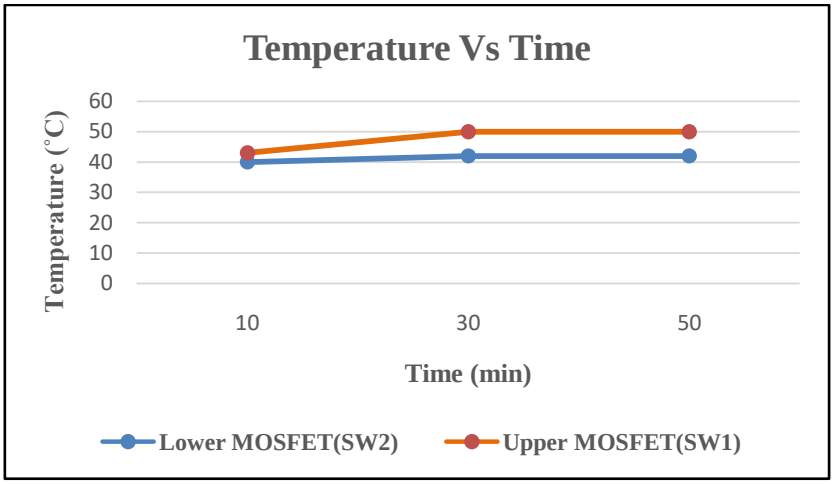

Figure 3.23: Temperature rise versus time of two MOSFETs (SW1 and SW2) at 15 kHz operation.

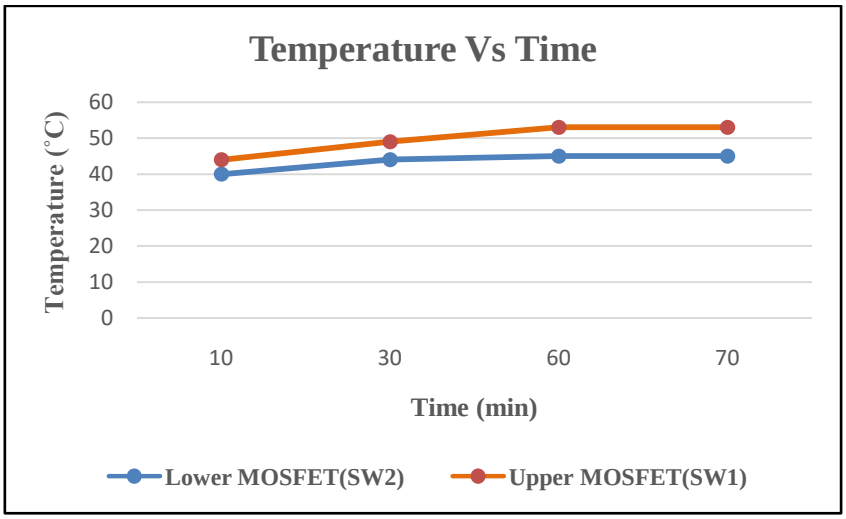

Figure 3.24: Temperature rise versus time of two MOSFETs (SW1 and SW2) at 5 kHz operation.

The push-pull inverter experiment (Table 3.1) shows both MOSFETs reaching a stable temperature. Thermal stability is observed, unlike in previous experiments (Half bridge). Similar temperature stability is seen in Tables 3.2-3.4 for supply voltage: 110V, load: 400W, 110V tungsten bulb. Voltage across the load varies with frequency (Tables 3.1-3.3), despite constant load and supply voltage. Oscillations at the beginning of inverter output observe due to the presence of loop inductance and ferrite core transformer.

3.7.2 Thermal performance of push-pull inverter using 2SK727 MOSFET

The experimental results of thermal characteristics of the push-pull inverter using 2SK727 MOSFET as a switch are presented in Tables 3.5 to 3.7 and Fig 3.25 to 3.32 for different frequencies.

3.7.2.1 Thermal analysis of the 2SK727 MOSFET in inverter operation at 15 & 7.5 kHz

f C_t R_t	Supply Voltage DC	Input current DC	Voltage Across the load	Time	Temp. of lower MOSFET (SW2)	Temp. of upper MOSFET (SW1)	Load
$f=15kH_Z$ $C_t=10nF$ $R_t=6.6k$	170V	2.19A	157V	10 min.	41˚C	43˚C	800W (220V-Bulb)
	170V	2.19A	157V	30 min.	45˚C	50˚C	
	170V	2.19A	157V	40 min.	45˚C	50˚C	
$f=7.5kH_Z$ $C_t=10nF$ $R_t=14k$	170V	2.19A	157V	10 min.	43˚C	47˚C	
	170V	2.19A	157V	20 min.	45˚C	50˚C	
	170V	2.19A	157V	30 min.	45˚C	50˚C	

Table 3.5: Thermal study of inverter MOSFET(2SK727) at 15 and 7.5 kHz.

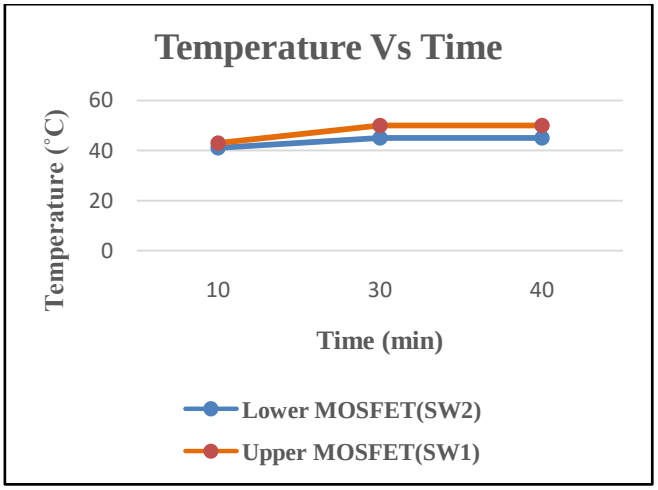

Figure 3.25: Temperature rise versus time of two MOSFETs (SW1 and SW2) at 15 kHz operation.

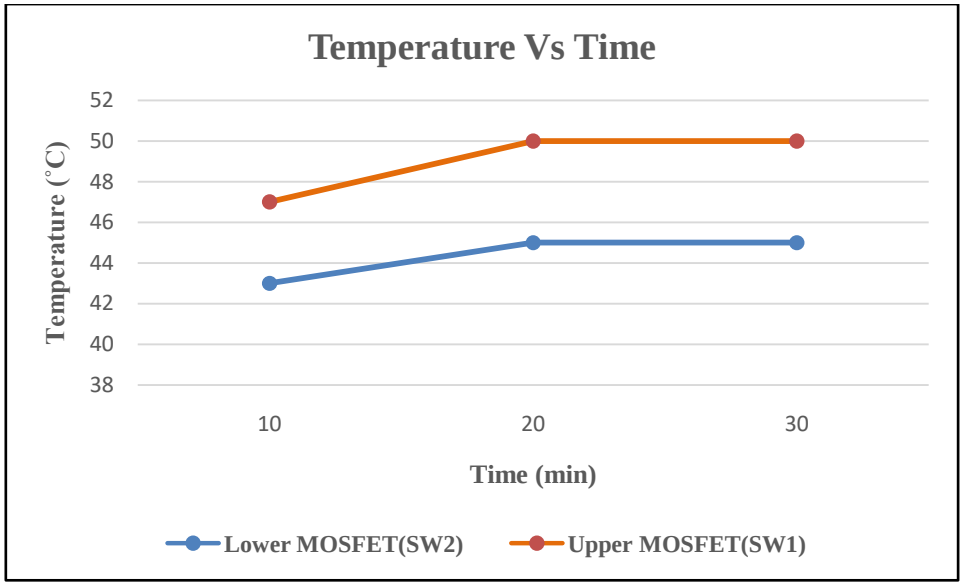

Figure 3.26: Temperature rise versus time of two MOSFETs (SW1 and SW2) at 7.5 kHz operation.

3.7.2.2 Inverter output voltage wave across the tungsten filament bulb load at 15 kHz

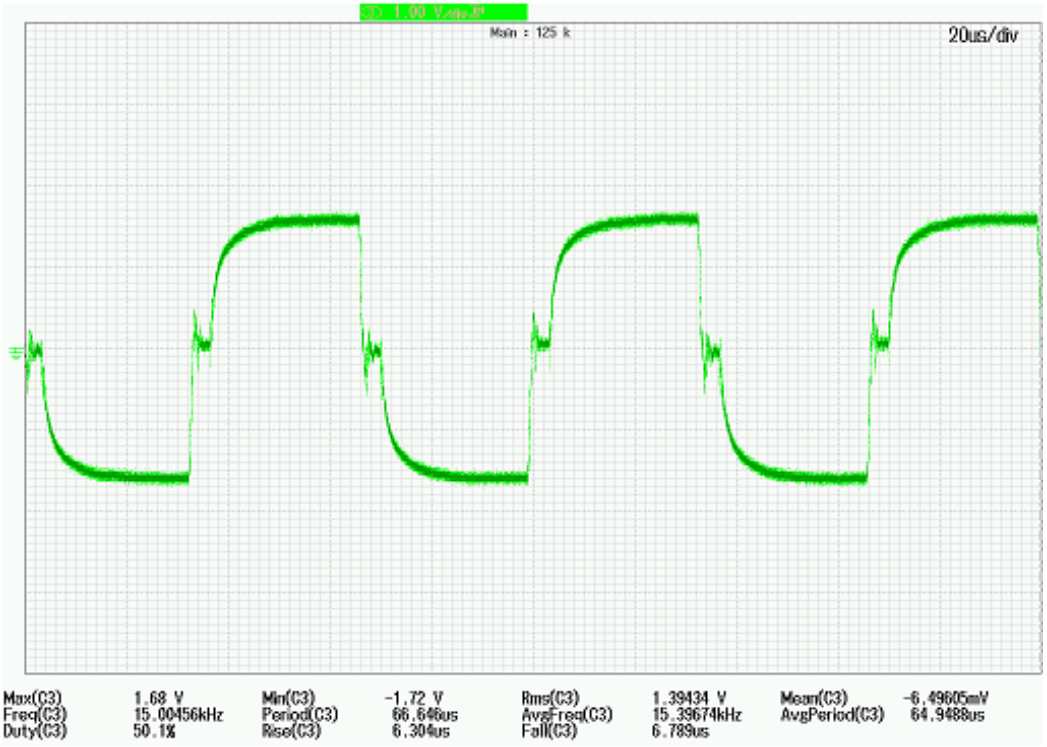

Figure 3.27: Inverter output voltage wave across the tungsten filament bulb load for Table 3.5(15 kHz frequency).

3.7.2.3 Thermal analysis of the 2SK727 MOSFET in inverter operation at 15 & 10 kHz

f C_t R_t	Supply Voltage DC	Input current DC	Voltage Across the load	Time	Temp. of lower MOSFET (SW2)	Temp. of upper MOSFET (SW1)	Load
$f = 15kH_Z$ $C_t = 10nF$ $R_t = 6.6k$	120V	2.5A	96V	10 min.	43˚C	46˚C	1200W (220V-Bulb)
	120V	2.5A	96V	35 min.	57˚C	63˚C	
	120V	2.5A	96V	50 min.	57˚C	63˚C	
$f = 10kH_Z$ $C_t = 10nF$ $R_t = 10k$	120V	2.5A	100V	10 min.	44˚C	47˚C	
	120V	2.5A	100V	30 min.	52˚C	58˚C	
	120V	2.5A	100V	60 min.	55˚C	60˚C	
	120V	2.5A	100V	70 min.	55˚C	60˚C	

Table 3.6: Thermal study of inverter MOSFET(2SK727) at 15 and 10 kHz.

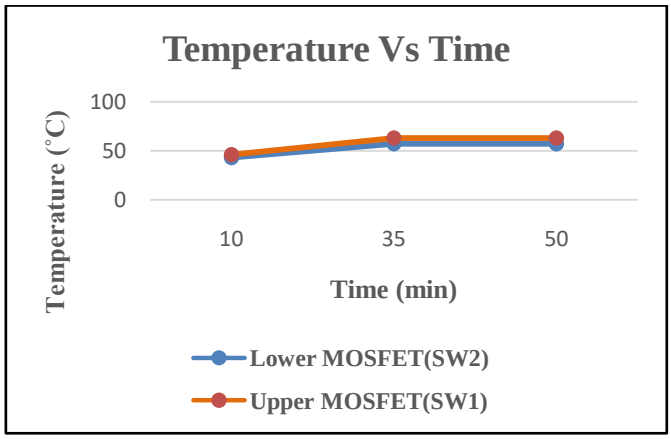

Figure 3.28: Temperature rise versus time of two MOSFETs (SW1 and SW2) at 15 kHz operation.

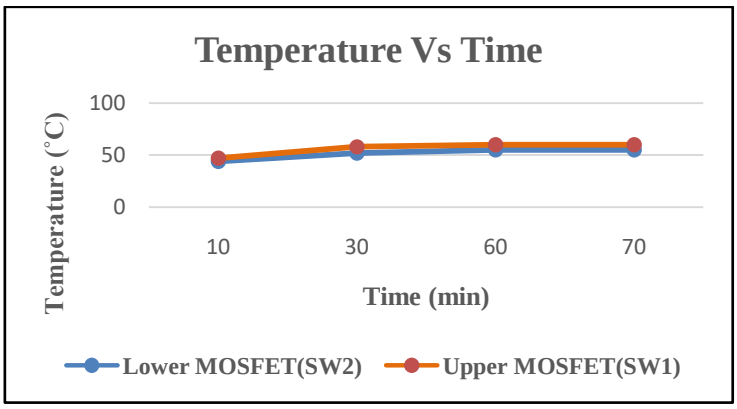

Figure 3.29: Temperature rise versus time of two MOSFETs (SW1 and SW2) at 10 kHz operation.

3.7.2.4 Thermal analysis of the 2SK727 MOSFET in inverter operation at 7.5 & 20 kHz

f C_t R_t	Supply Voltage DC	Input current DC	Voltage Across the load	Time	Temp. of lower MOSFET (SW2)	Temp. of upper MOSFET (SW1)	Load
$f = 7.5kH_Z$ $C_t = 10nF$ $R_t = 14k$	110V	2.5A	95V	10 min.	44˚C	46˚C	1200w (220V-Bulb)
	110V	2.5A	95V	30 min.	47˚C	53˚C	
	110V	2.5A	95V	40 min.	50˚C	57˚C	
	110V	2.5A	95V	50 min.	50˚C	57˚C	
$f = 20kH_Z$ $C_t = 10nF$ $R_t = 5k$	200V	3.7A	130V	10 min.	56˚C	63˚C	1400W (220V-Bulb)
	200V	3.7A	130V	20 min.	58˚C	65˚C	
	200V	3.7A	130V	30 min.	58˚C	65˚C	

Table 3.7: Thermal study of inverter MOSFET(2SK727) at 7.5 and 20 kHz.

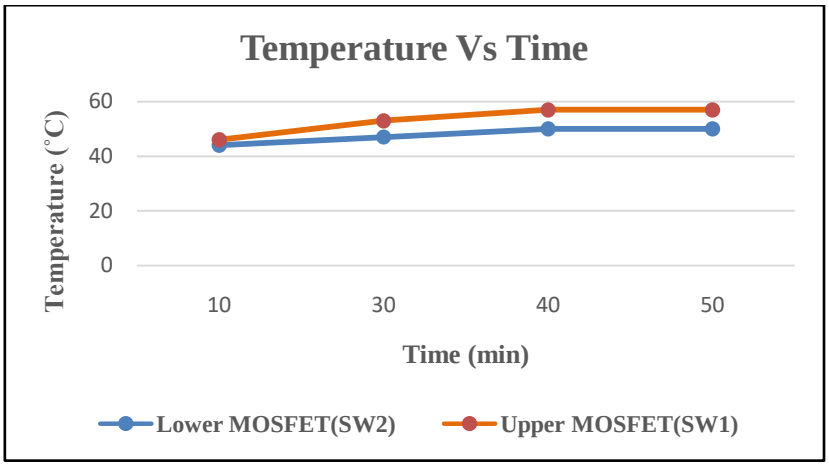

Figure 3.30: Temperature rise versus time of two MOSFETs (SW1 and SW2) at 7.5 kHz operation.

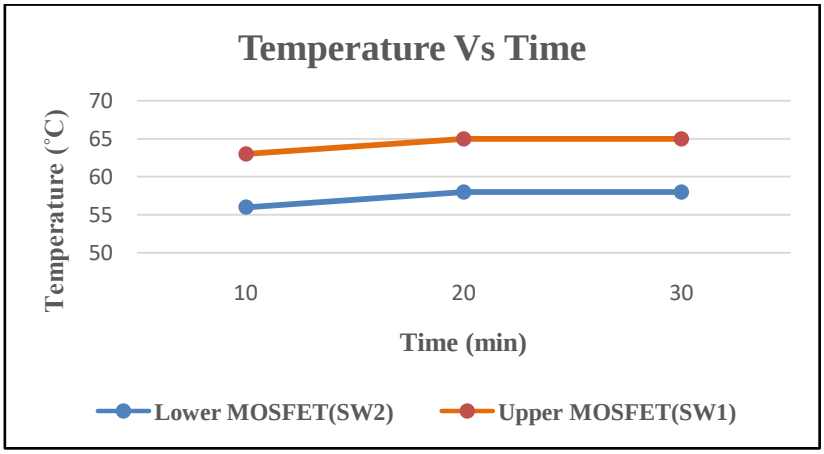

Figure 3.31: Temperature rise versus time of two MOSFETs (SW1 and SW2) at 20 kHz operation.

3.7.2.5 Inverter output voltage wave across the tungsten filament bulb load at 20 kHz

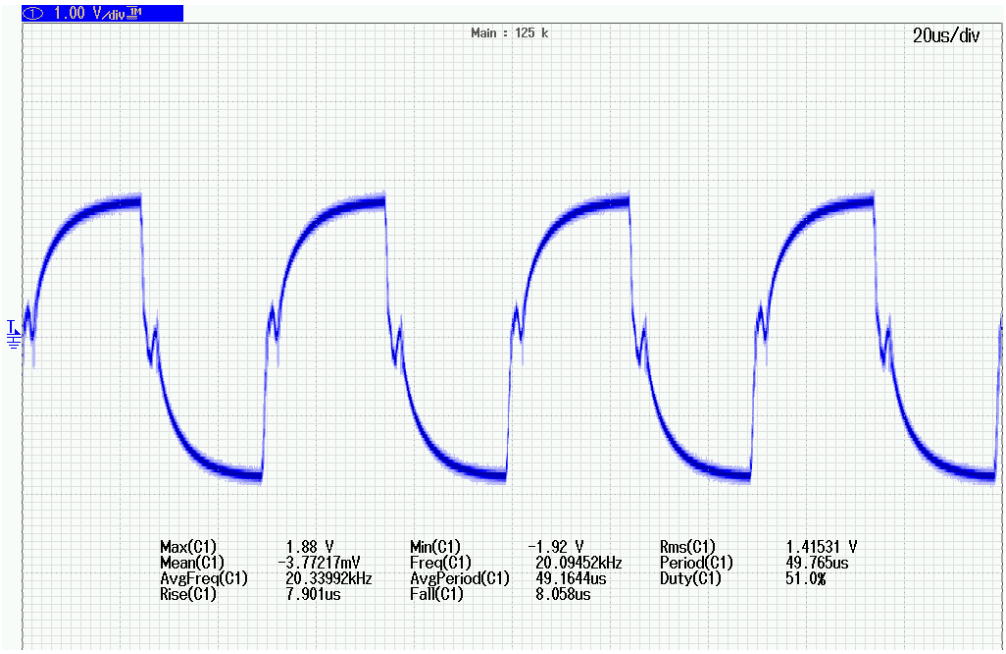

Figure 3.32: Inverter output voltage wave across the tungsten filament bulb load for Table 3.12(20 kHz frequency).

The MOSFET IRF840 was replaced with the 2SK727 to enhance current handling capability. With a supply voltage of 170V and a current of 2.2A through the switches, the setup was tested with an 800W lamp load. After one hour, both MOSFETs stabilized at a temperature of 50˚C, demonstrating reliability superior to the previous half-bridge inverter design. To further test the setup, the current was increased by adjusting the load and supply voltage, with the frequency set to 20 kHz. At this frequency, the supply voltage was increased to 200V (as shown in Table 3.7), resulting in a current of 3.7A through the switches and a lamp load of 1400W. Under these conditions, the temperature stabilized at 65˚C after half an hour of operation.

3.8 Study on ohmic heating's impact on liquid food materials

The physical and chemical characteristics of the metal electrodes have a significant influence on electrochemical reactions at the electrode/solution interface in this method. Various electrode materials have been used for ohmic heating studies up to this point. In the current study, a variety of simulated liquid samples were processed by ohmic heating in order to investigate the impact of heating on the quality of the final product. To begin, experiments were conducted using available power supplies and four different types of metal electrodes,

stainless steel 304 (SS304), stainless steel 316 (SS316), titanium and gold plated silver electrodes. Secondly, a high frequency power supply unit was developed to reduce the DC effect and prevent electrode corrosion during heating.

Ohmic heating treatment was first initiated using a stainless steel 304 electrode and an electrical source that was available (50Hz). After heating, the solution's color changed when treated with an SS304 electrode at a low concentration of NaCl, or less than 1% NaCl. The identical electrode was also tested with KCl and Na_2SO_4 solutions at varying concentrations, and the results revealed a striking color shift with suspended particles in the test sample. The samples were then processed using SS316 electrodes, and a noticeable color shift was seen.

3.8.1 Electrode details

There are over a hundred different kinds of stainless steel. Stainless steel (304) and 316 are iron-chromium alloys with at least 11% chromium that are resistant to corrosion and high temperatures. As a member of the austenitic family of stainless steels, grade 316 is primarily alloyed with silicon (1.5–3%), molybdenum (2–3%), nickel (10–14%), and chromium (16–18%). Two additional metal electrodes have been tried in this work in addition to SS 304 and 316 electrodes: titanium, which has high corrosion resistance and biocompatibility qualities, and gold-plated silver electrodes. The electrodes have a parallel plate arrangement and are rectangular in shape. Every electrode had the same geometric measurements and was rectangular (5.08 cm × 5.08 cm). The electrodes' thickness was 0.1 cm and the distance between them was 1.27 cm for all treatments, electrodes are shown in Fig 3.33 & Fig 3.34.

Figure 3.33: Stainless steel electrodes (SS 304, 316).

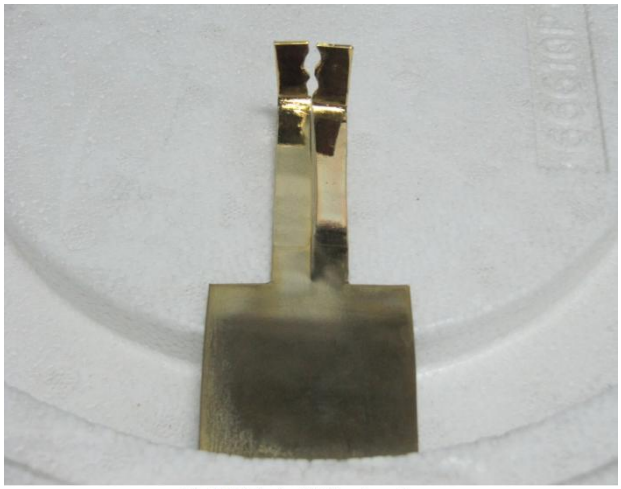

Gold Plated Electrode

Figure 3.34: Gold plated electrode.

3.8.2 Analysis of electrode corrosion induced by ohmic heating at 50 Hz AC supply

Scanning electron microscopy (SEM) and energy dispersive X-ray spectroscopy (EDX) analysis were used to look at deposits that developed on the electrode surface and metal ion migration into the heating solution. Initially, EDX analysis was used to assess the compositions of the electrodes' building materials before the heating. After the sample's ohmic heating was finished in each experiment, a 10.00 (± 0.03) ml sample of the processed material and a 10.00 (± 0.03) ml sample of the corresponding untreated solution were taken as references. For additional research, all of the samples were aseptically collected in narrow mouth conical flasks and wrapped with brown paper and cotton.

The electrodes were left to dry for about an hour at room temperature following each experiment cycle. A piece of stainless steel spatula was then used to carefully scrape off the deposits of the elements on the surface of both electrodes. An INCA-X SIGHT MODEL 7582 and a JEOL-JSM 6360 Scanning Electron Microscope from Oxford Instruments' Metallurgical and Material Science Department at Jadavpur University were used to study the surface of the collected deposit. The green coconut water sample was also subjected to the "Element Line Scan" (ELS) experiment. A JEOL JSM-6360 scanning electron microscope fitted with an INCA-X Sight Model 7582 Oxford energy dispersive x-ray analyzer (SEM-EDX) was used to determine the chemical compositions of electrode deposits. After mounting each of the deposited samples on the carbon tape, the analysis was carried out at an

accelerating voltage of 20 kV. INCA Energy+ software was used to obtain the results. For every deposit sample, just a few replicate measurements were taken.

3.8.3 SEM-EDX analysis of ohmic heating effects

Certain unfavorable events happened during heating, as evidenced by a noticeable color shift that was most likely caused by electrode corrosion. Therefore, it was thought that the components of the electrode building material must be added to the processed material if some electrode material is corroding through it. All of the electrode material was evaluated using EDX before to heat treatment in order to determine the initial compositions of the metal electrodes. Following heating, SEM-EDX and ELS were used to further examine the treated materials. In scanning electron microscopy, molecules in the sample interact with a high-voltage electron beam in an evacuated chamber to produce a variety of signals that provide information about the sample surface. These signals are then detected to create an image. Images from this study's examination of metal ion migration into the heating media and deposits that developed on the electrode surfaces are displayed below.

3.8.3.1 EDX information on electrodes prior to ohmic heating treatment

EDX information on electrodes prior to heat treatment is presented graphically

Element	**Weight%**	**Atomic%**
Cr K	16.64	17.99
Mn K	1.94	1.98
Fe K	67.24	67.69
Ni K	10.56	10.11
Cu K	0.36	0.32
Mo L	3.26	1.91
Totals	100.00	

Table 3.8: 304-grade stainless steel electrode (control)

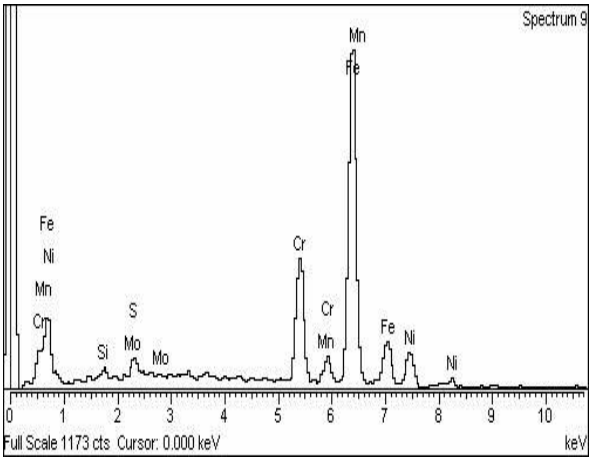

Figure 3.35: Stainless steel 304 electrode EDX graph (Control)

Element	Weight%	Atomic%
Si K	0.90	1.75
S K	1.08	1.84
Cr K	16.57	17.42
Mn K	2.27	2.26
Fe K	67.60	66.16
Ni K	11.02	10.26
Mo L	0.57	0.32
Totals	100.00	

Table 3.9: 316-grade stainless steel electrode (control)

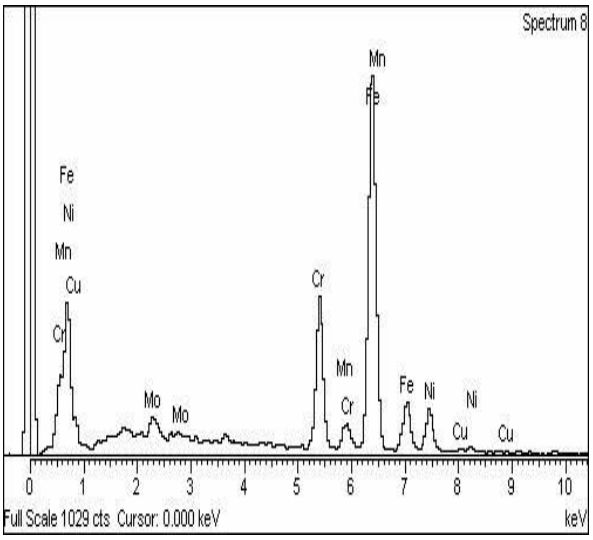

Figure 3.36: Stainless steel 316 electrode EDX graph (Control)

Element	Weight%	Atomic%
C K	8.90	15.48
N K	23.46	34.99
O K	21.88	28.58
Al K	3.21	2.48
Ti K	40.67	17.74
V K	0.54	0.22
Fe K	1.35	0.50
Totals	100.00	

Table 3.10: Titanium electrode (Control)

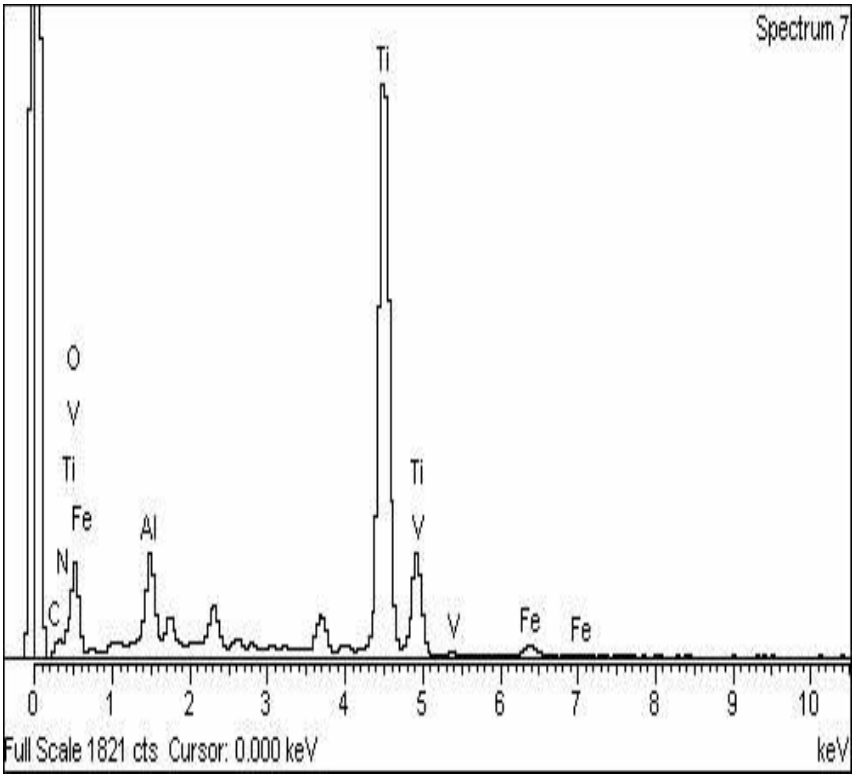

Figure 3.37: Titanium electrode EDX graph (Control)

Element	Weight%	Atomic%
Ni K	71.59	89.37
Ag L	0.17	0.12
Au M	28.24	10.51
Totals	100.00	

Table 3.11: Gold plated electrode (Control)

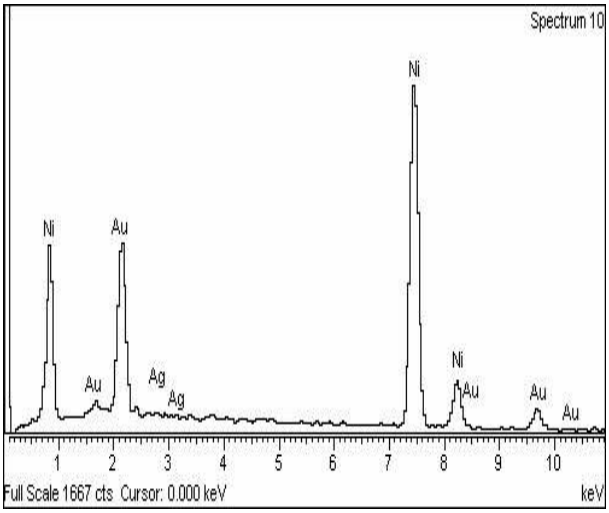

Figure 3.38: Gold plated electrode EDX graph (Control)

3.8.3.2 Graphical presentation of SEM-EDX results for electrodes after heat treatment

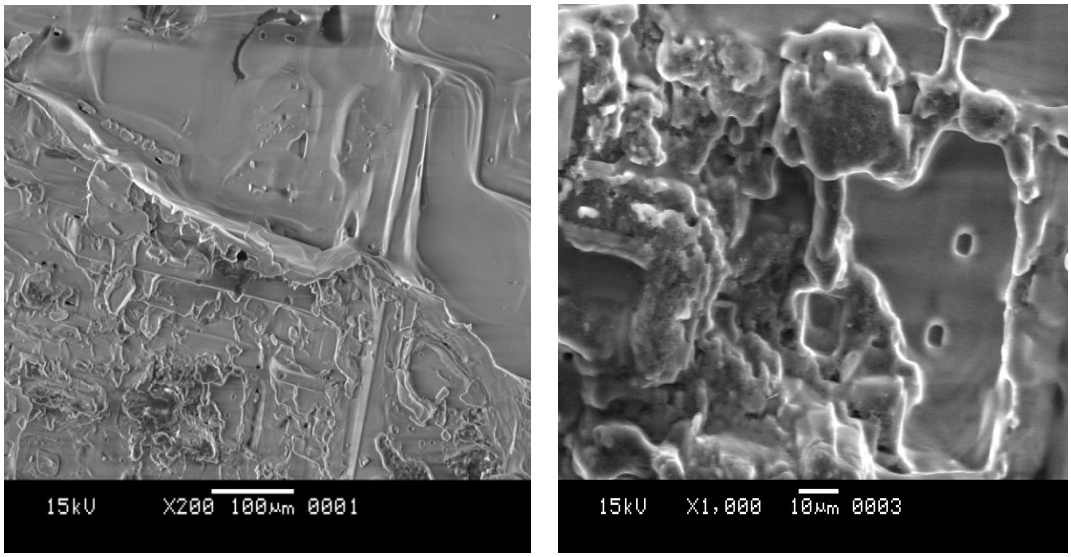

Figure 3.39: SEM image of a 0.5% NaCl solution.

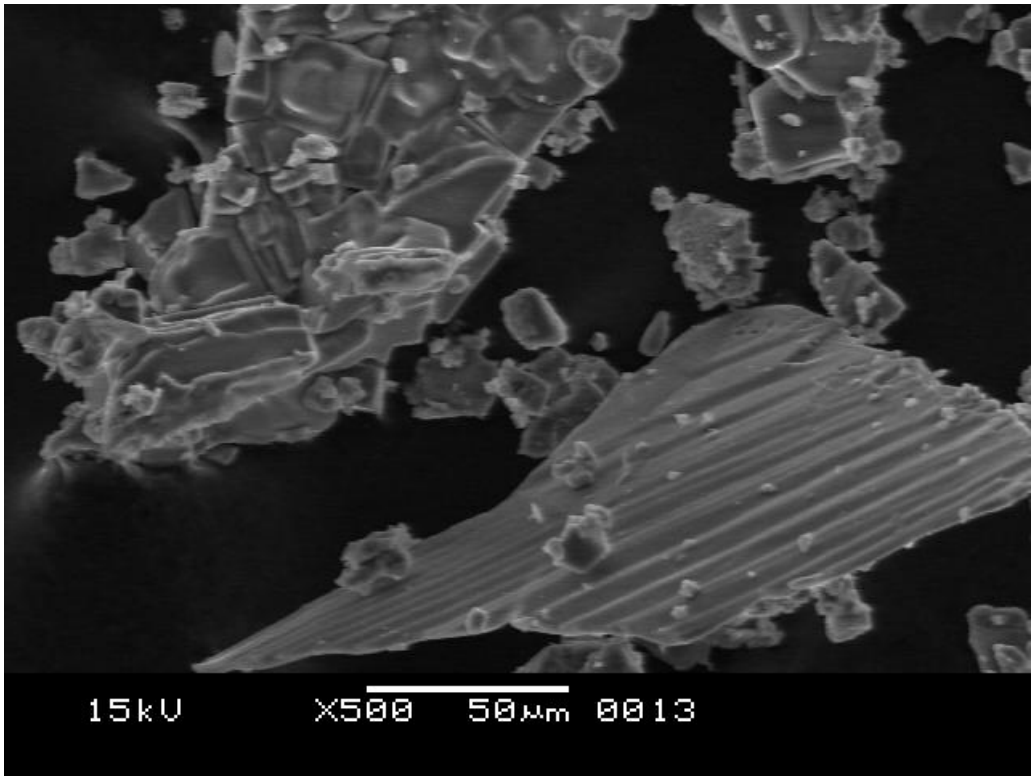

Figure 3.40: SEM image of a 0.5% NaCl solution.

3.8.3.3 Results of the 0.5% NaCl solution's EDX (SS 304) after heating

Element	Weight%	Atomic%
Na K	38.72	49.77
P K	0.00	0.00
S K	0.20	0.19
Cl K	59.43	49.53
Fe K	0.49	0.26
Ag L	1.13	0.17
Au M	0.03	0.08
Totals	100.00	

Table 3.12: Results of the 0.5% NaCl solution's EDX (SS 304).

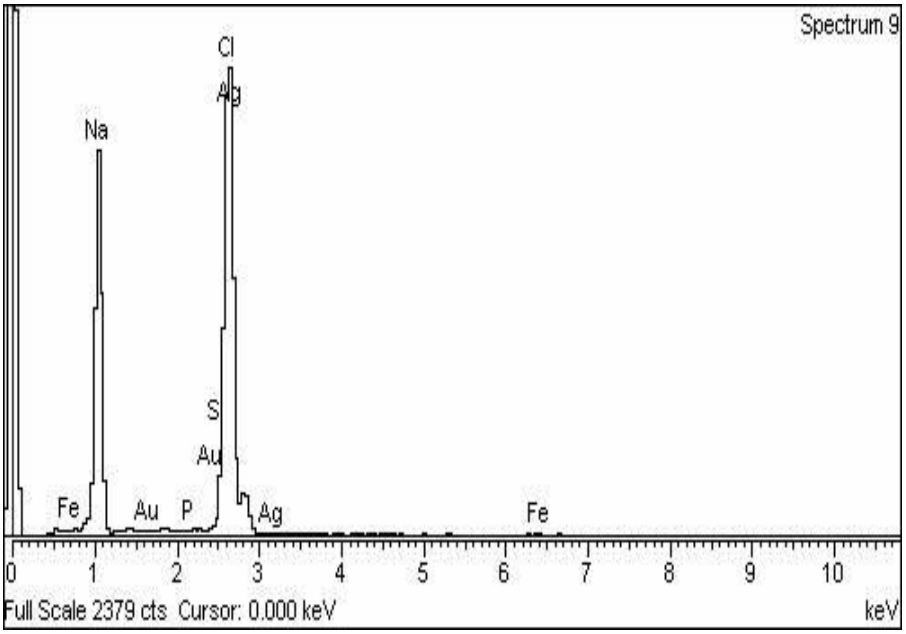

Figure 3.41: 0.5% NaCl solution's EDX (SS 304).

3.8.3.4 Results of the 0.5% NaCl solution's EDX (SS 316) after heating

Element	Weight%	Atomic%
O K	29.58	44.01
Na K	29.74	30.79
Mg K	0.09	0.09
Al K	0.19	0.16
Cl K	32.29	21.68
K K	0.29	0.17
Ca K	0.45	0.27
Cr K	0.76	0.35
Fe K	4.55	1.94
Ni K	1	0.3
Mo L	1.17	0.24
Totals	100.00	

Table 3.13: Results of the 0.5% NaCl solution's EDX (SS 316 electrode).

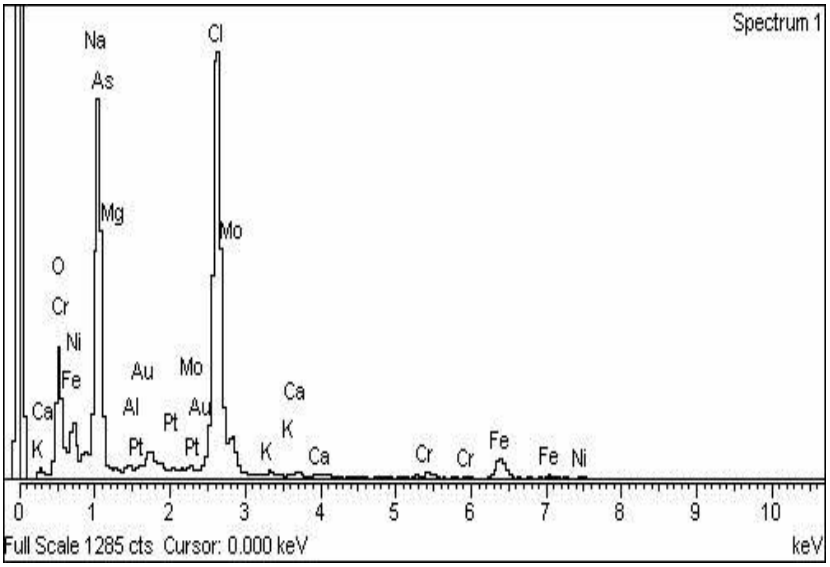

Figure 3.42: 0.5% NaCl solution's EDX (SS 316 electrode).

3.8.3.5 EDX result of the 0.5% NaCl solution's rough surface (unclean electrode).

Element	Weight%	Atomic%
Na K	43.99	55.58
Cl K	52.73	43.20
Ca K	0.08	0.06
Sc K	0.13	0.09
Cr K	0.28	0.16
Fe K	0.42	0.22
Cu K	0.74	0.34
Ag L	1.02	0.28
Pt M	0.60	0.09
Totals	100.00	

Table 3.14: EDX result of the 0.5% NaCl solution's rough surface (unclean electrode).

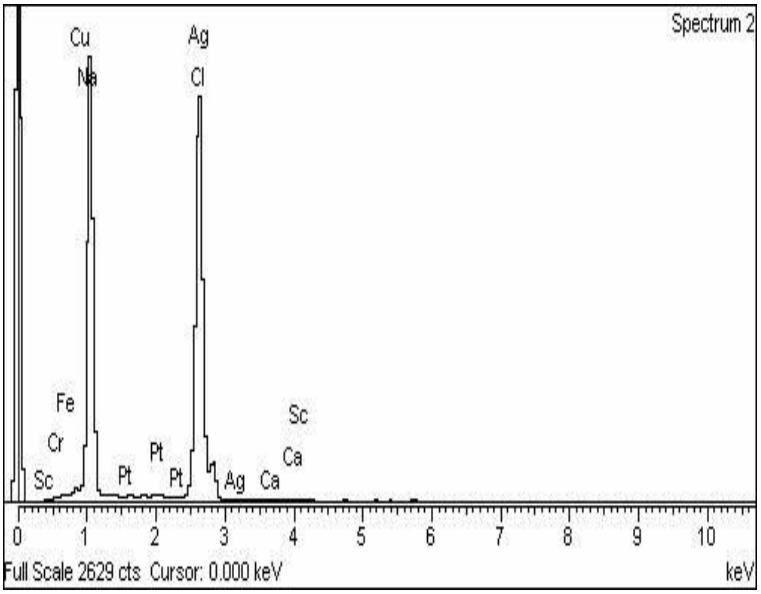

Figure 3.43: 0.5% NaCl solution's rough surface (unclean electrode).

3.8.3.6 EDX result of 0.5% NaCl solution's flat surface (SS 304).

Element	**Weight%**	**Atomic%**
Na K	39.84	51.05
Cl K	57.67	47.92
Sc K	0.11	0.07
Cr K	0.17	0.10
Fe K	0.39	0.21
Ni K	0.48	0.24
Cu K	0.26	0.12
Ag L	0.68	0.18
Cd L	0.39	0.10
Totals	100.00	

Table 3.15: EDX result of 0.5% NaCl solution's flat surface (SS 304).

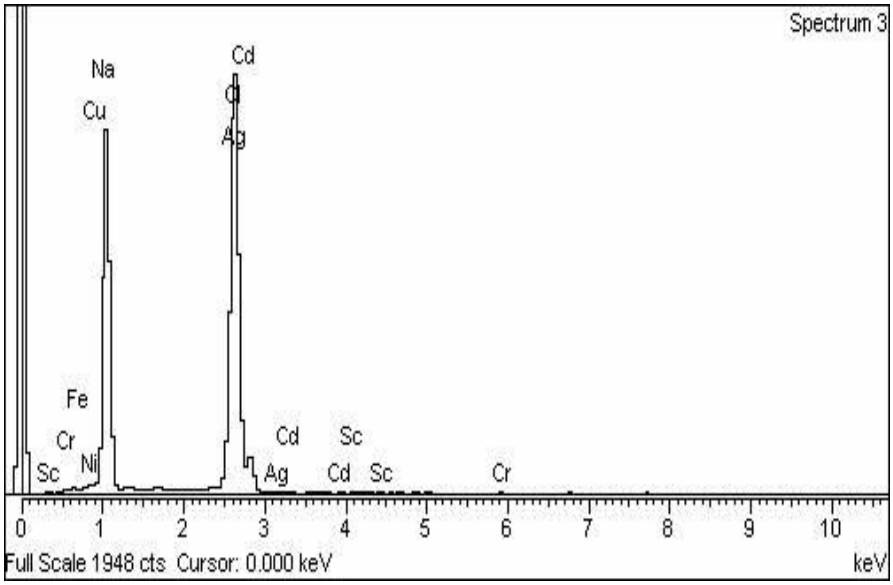

Figure 3.44: 0.5% NaCl solution's flat surface (SS 304).

3.8.3.7 EDX result of 0.1% NaCl solution for gold plated electrode after heating

Element	**Weight%**	**Atomic%**
Na K	41.97	53.01
Al K	0.18	0.19
Cl K	56.49	46.28
K K	0.20	0.15
Fe K	0.45	0.23
Ag L	0.27	0.07
Au M	0.45	0.07
Totals	100.00	

Table 3.16: EDX result of 0.1% NaCl solution for gold plated electrode.

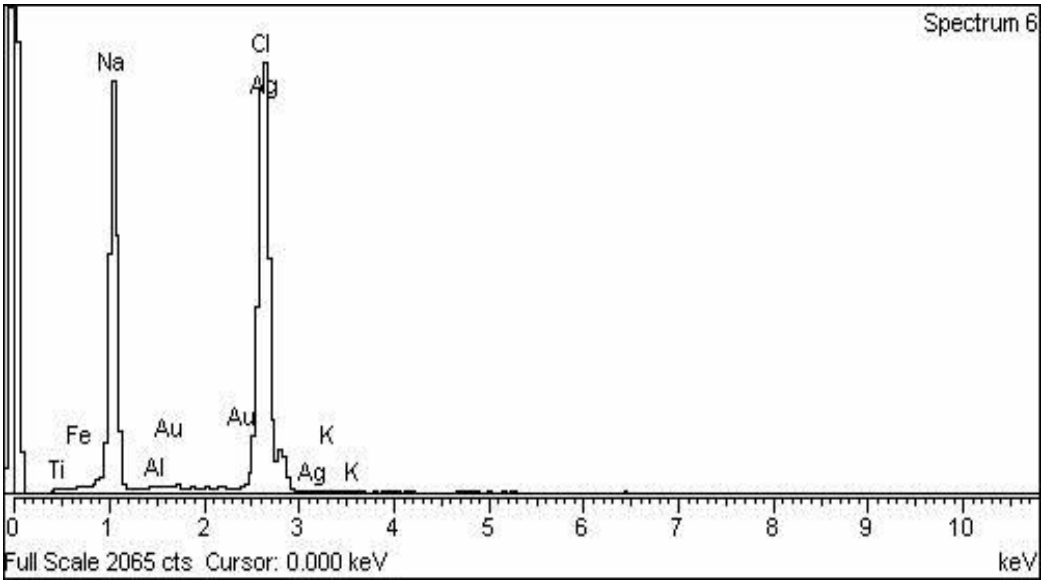

Figure 3.45: 0.1% NaCl solution for gold plated electrode.

3.8.3.8 EDX result of 0.1% NaCl solution for gold titanium electrode after heating

Element	**Weight%**	**Atomic%**
Na K	40.27	51.15
Cl K	58.33	48.04
Ca K	0.30	0.22
Sc K	0.32	0.21
Ti K	0.79	0.25
Totals	100.00	

Table 3.17: EDX result of 0.1% NaCl solution for gold titanium electrode.

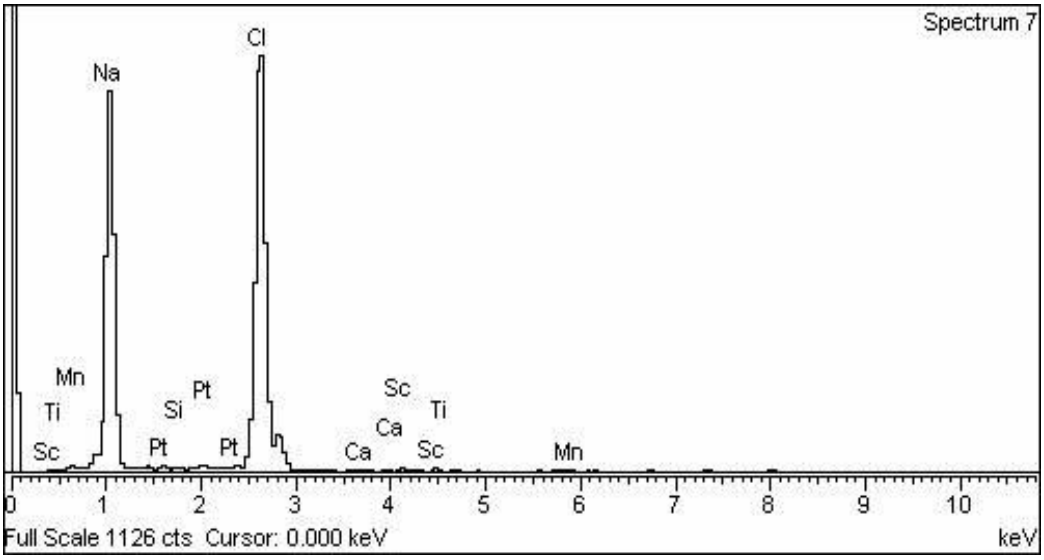

Figure 3.46: 0.1% NaCl solution for gold titanium electrode.

Sample: 1% NaCl solution, AC supply (50 Hz) and unclean electrode.

Final Colour: Deep Brown

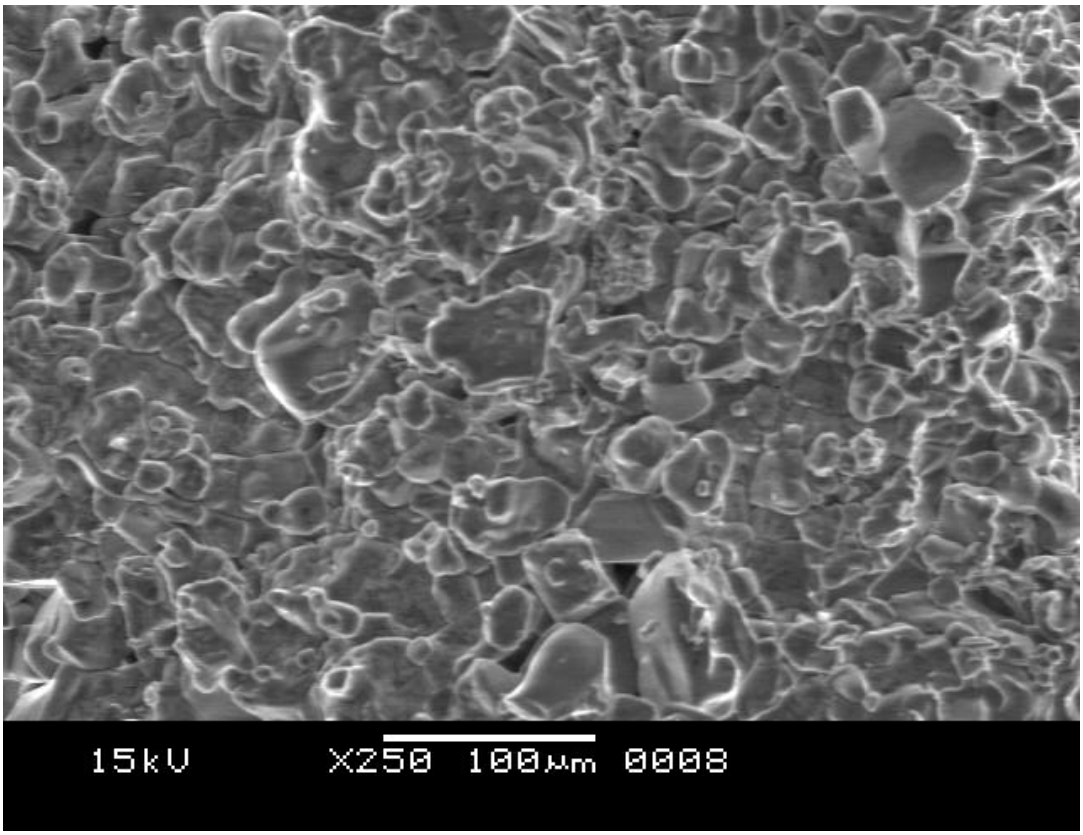

Figure 3.47: SEM image of a 1% NaCl solution

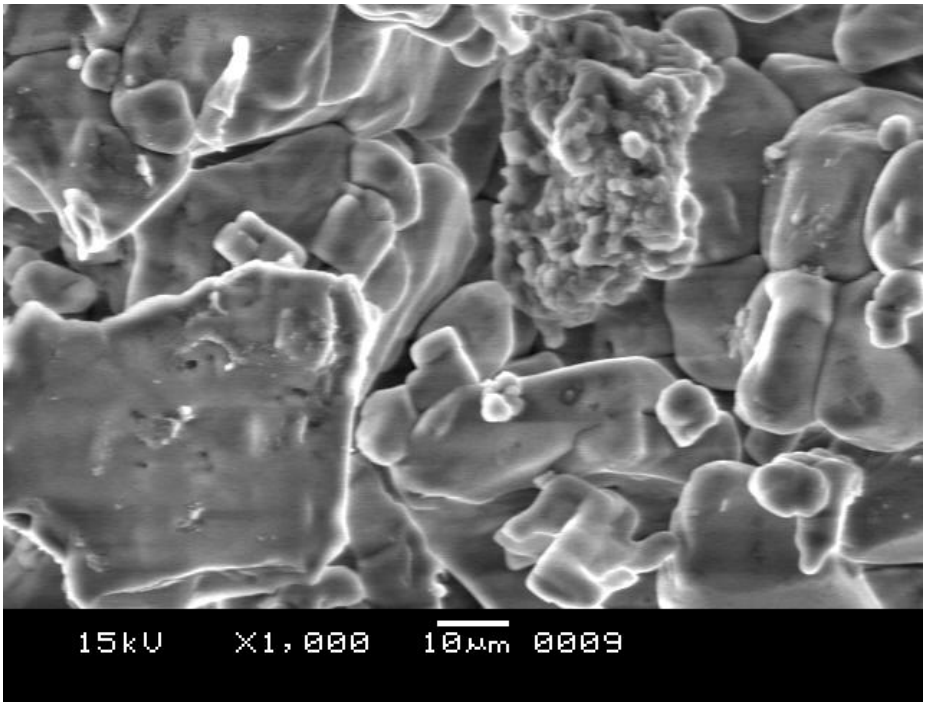

Figure 3.48: SEM image of a 1% NaCl solution.

The components of the electrode building material are present in the processed material, according to the SEM-EDX results for each electrode. The EDX table revealed the presence of Mn, Si, Cu, Mo, Ni, Co, and other elements during processing with SS 304 & 316 electrodes (Table 3.8-3.17). After heating with titanium electrodes, a considerable amount of titanium was found in the processed sample. Because the processed material is enriched with electrode construction material, the electrode material is corroding through the processed material, according to the overall electrode corrosion study.

3.9 Liquid sample heating using push-pull inverter

The experimental investigation successfully demonstrated the thermal characteristics of MOSFETs in a push-pull inverter setup, providing valuable insights into temperature stabilization and thermal behavior under various load conditions. Finally, different liquid samples are heated, and corrosion at different frequencies and duty cycles is examined. The experiment was conducted using Parallel plate electrode setup shown in Fig 3.49 with different frequency supply system (push-pull inverter), different time of operation, different concentration of salt and acid etc. The study of inverter outputs for heating at different type liquid loads (1%, 2% NaCL solution) show that the effect of the corrosion of electrode is minimized when frequency is increased from 50 Hz to 20 kHz.

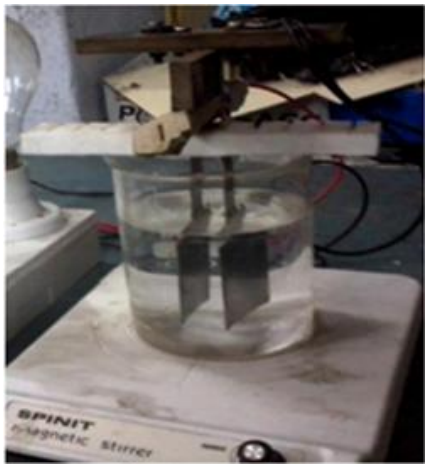

Figure 3.49: Parallel plate electrode setup

Salts and acids are present in the majority of semisolid foods and liquid drinks. The following is revealed by the experimental results for various liquid conductors with varying combinations of electrodes, time duration, acid and salt concentrations, and regulated and unregulated electrical supply. All the solution even containing a little % NaCl showed colour changes whether it is regulated AC or unregulated AC. Various electrodes like stainless steel 304, stainless steel 316, titanium and gold plated stainless steel 316 are used to perform the heating process in the laboratory. Parallel plate electrode of stain less steel (316) configuration shown in Fig 3.49, has been used to heat liquids. The electrodes are spaced 1/2" apart in all treatments, and their dimensions and thicknesses of 6" x 6" and 1mm are taken into account.

Liquid (1 or 2% NaCl solution) is heated by this ohmic heater and the temperature rises as current passes through it. It is observed that initial current changes at a low voltage, as time passes temperature of liquid rises and current also changes, does not remain constant. There is a gradual increase of the current with rising temperature in time. This shows that the conductivity depends on temperature and it increases non-linearly with temperature. So the control of the current is required to limit the current with the specification of power supply; otherwise, it will be damaged. Also the timing of the rising temperature can also be controlled by voltage and current control. Using this experimental setup electrode corrosion was studied at different frequencies, conductivity and temperature characteristics of the liquid with respect to time for different solution were observed, which is shown in Table 3.18. The push-pull inverter's output, with its variable frequency range, is designed to heat liquid conductors (such as salt water) for ultra-high temperature heating applications, including sterilization of liquid beverages. It has been shown that, in comparison to power frequency

sine wave alternating current, the corrosion phenomenon of the electrode would significantly decrease. Similarly, it is discovered that 10 kHz alternating current would result in a more noticeable improvement than 5 kHz alternating current when compared to other high frequency alternating current waveforms; the heated liquid conductor would no longer be discolored. The conditions of electrode at various frequencies are shown in Fig 3.51 and 3.55 and the voltage wave for NaCl solution at 10 and 20 kHz is shown in Fig 3.50 and 3.54. These findings suggest that increasing the frequency further could potentially eliminate corrosion entirely. The high-frequency power inverter developed in this study shows promise as an ohmic heater for sterilizing liquid food conductors at ultra-high temperatures. Notably, the results indicate that ohmic heating at frequencies above 5 kHz preserves the color of liquid solutions with lower NaCl concentrations, highlighting the potential benefits of this technology. Fig 3.52(a, b, c) and Fig 3.53(a, b, c) shows the various curve of Current vs. Time and Temperature vs. Time for different solution and frequency where it is clearly seen that the current is changing non linearly with time as the temperature increases. It was also found that conductivity of coconut water respectively higher than others, which is also heated into the pressurized vessel for liquid chamber connected at the output terminal of the push pull inverter shown in Fig 3.16. The high frequency inverter voltage wave across coconut water when being heated, raising the temperature of the liquid in a pressurized vessel shown in Fig 3.56. It can be said that the continuous load current at high frequency through the liquid load power heating be similar to the voltage wave as because of the load is resistive type.

3.9.1 Ohmic heating of 1% & 2% NaCl solution at 1kHz, 5kHz & 10 kHz frequency

Sample	Time (min)	Temp (^0C)	Freq. (kHz)	I/P Voltage	Current (Amp)	Color	Corrison
1% Nacl	31 min.	97^0C	1kHz	28V	11.2Amp.	Tinge Yellow	Occur on edge Of electrode
1% Nacl	32 min.	96^0C	5kHz	28V	11Amp	No Change	Not Visible
1% Nacl	35 min	98^0C	10kHz	28V	11.5Amp	No change	Not Visible
2% Nacl	14 min.	97^0C	1kHz	28V	18Amp	Tinge Yellow	Occur on the Edge of electrode
2% Nacl	15 min.	97^0C	5kHz	28V	18Amp	No Change	Not Visible
2% Nacl	15 min.	97^0C	10kHz	28V	18Amp	No Change	Not Visible

Table 3.18: Results for 1% & 2% Nacl solution at different frequencies.

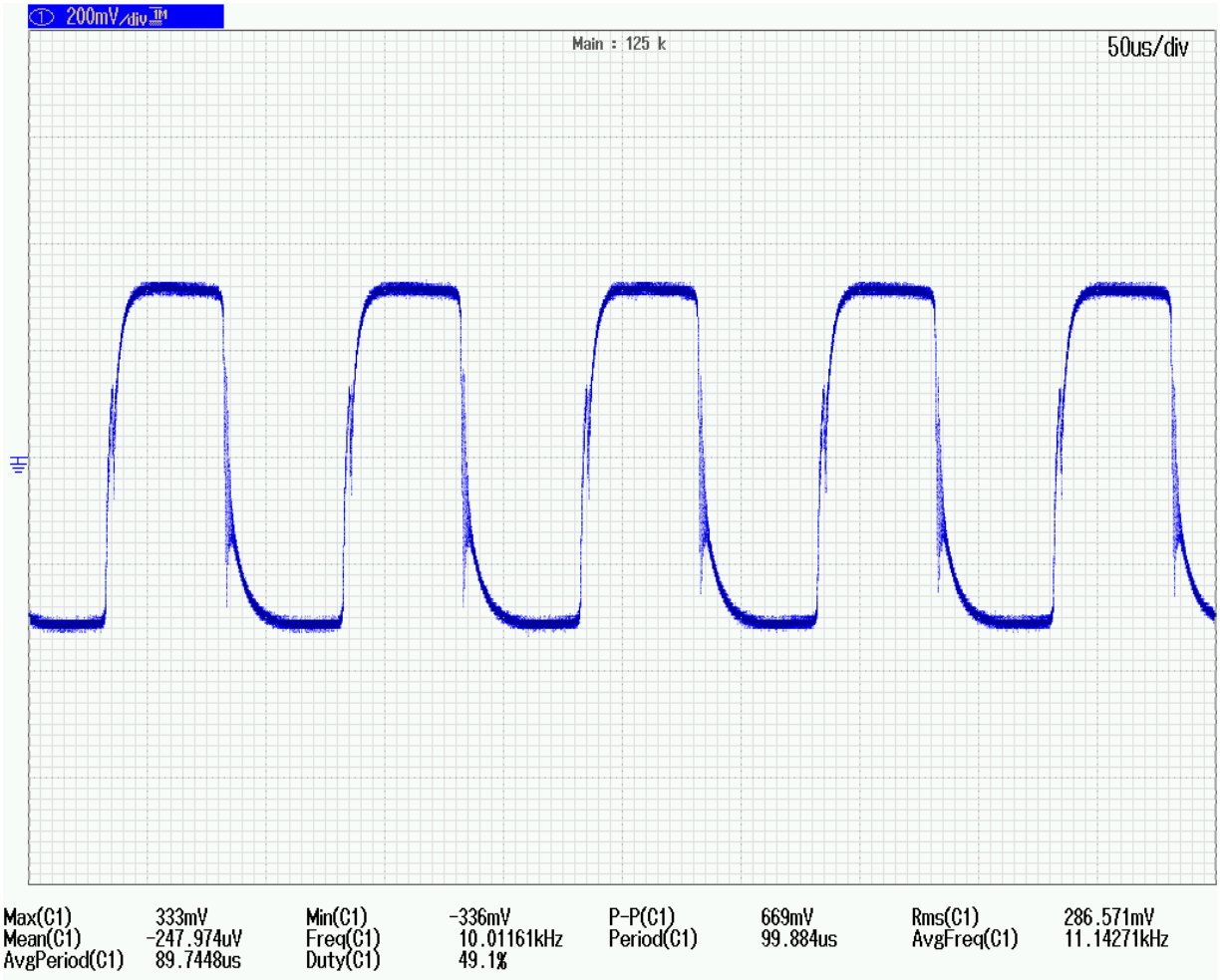

Figure 3.50: Output voltage wave across NaCl solution for 10 kHz.

3.9.2 Corrosion of electrodes made of stainless steel (SS 316) for different frequency (50 Hz- 5kHz- 10kHz) after ohmic heating treatment

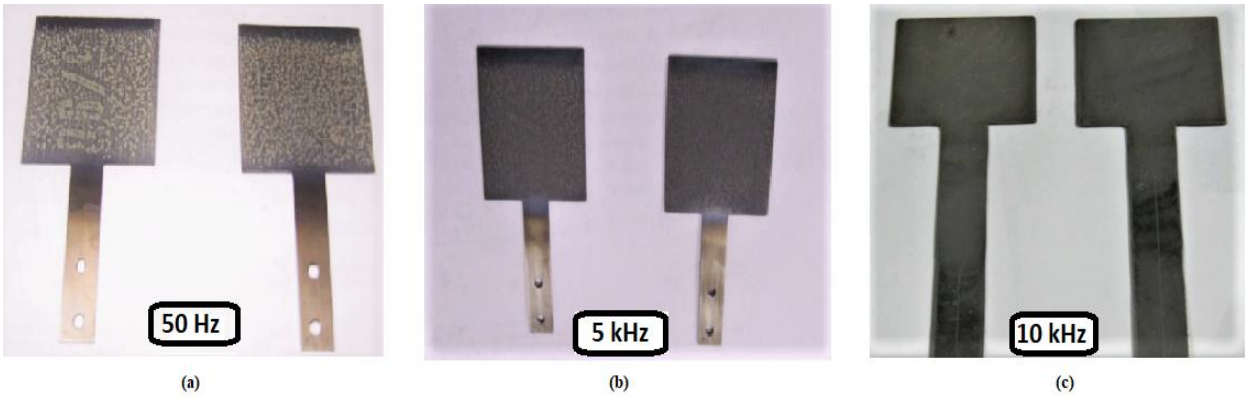

(a) (b) (c)

Figure 3.51: Corrosion of electrodes made of stainless steel for different frequency (50 Hz- 5kHz- 10kHz).

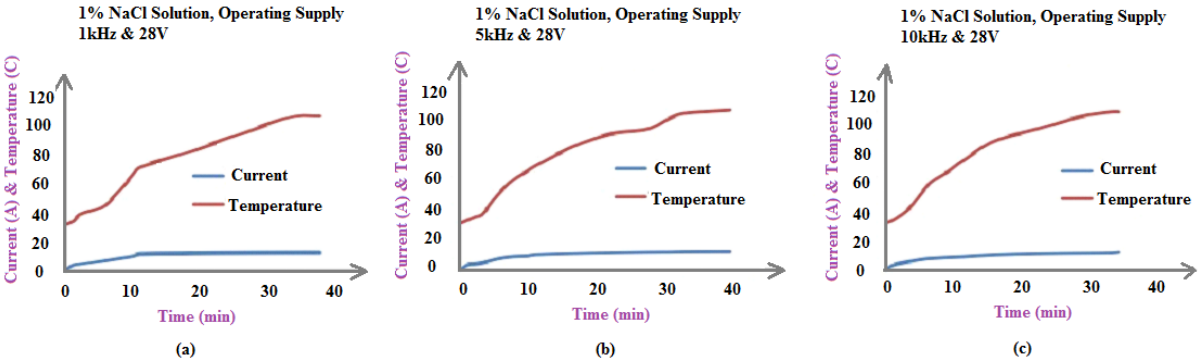

Figure 3.52: (a,b,c): System Current vs. Time & Temperature of liquid (1% NaCl solution) vs. Time for variable operating frequency

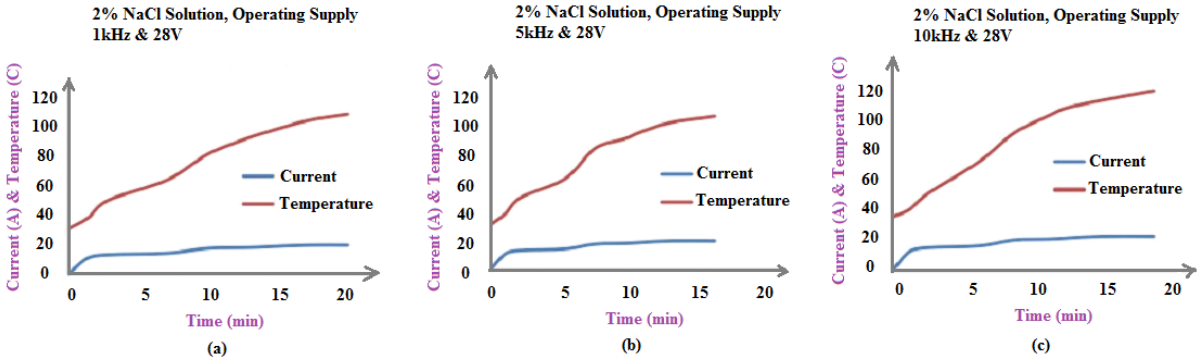

Figure 3.53: (a,b,c): System Current vs. Time & Temperature of liquid (2% NaCl solution) vs. Time for variable operating frequency

3.9.3 Voltage across NaCl solution during heating at 20 kHz.

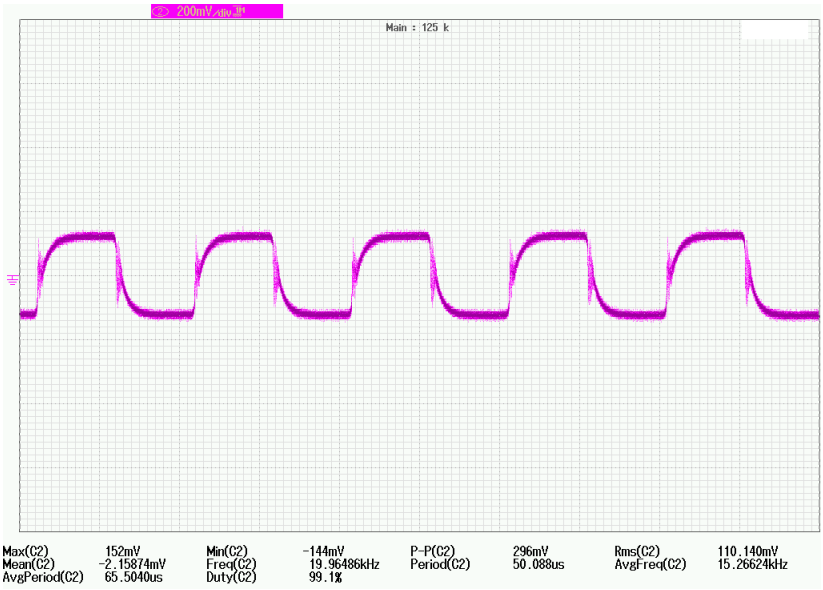

Figure 3.54: Output voltage wave across NaCl solution for 20 kHz.

3.9.4 Corrosion of electrodes made of stainless steel (SS 316) for different frequency (50Hz-20kHz) after ohmic heating treatment

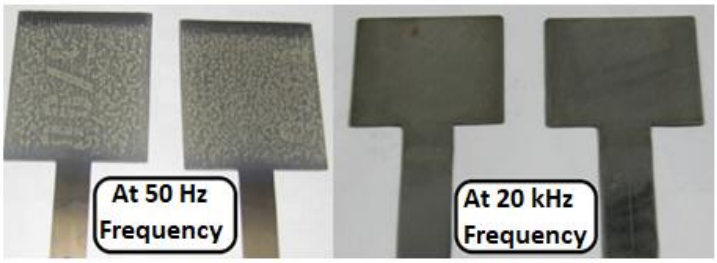

Figure 3.55: Corrosion of electrodes made of stainless steel for different frequency (50 Hz- 20kHz).

3.9.5 Voltage across coconut water during heating treatment at 10.36 kHz.

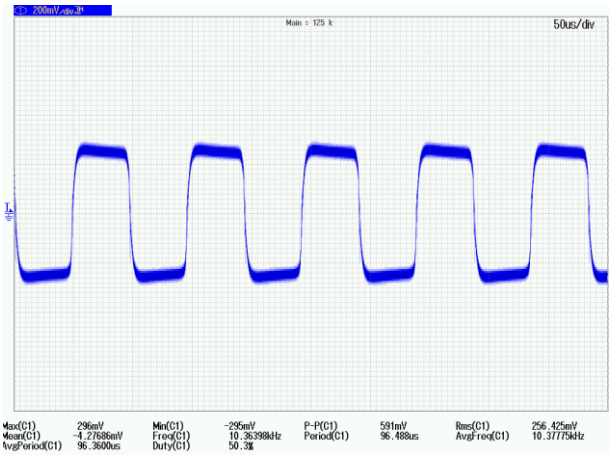

Figure 3.56: Output voltage wave across coconut water at 10.36 kHz frequency.

3.10 Summary

It is observed that there is no longer any discoloration in the heated liquid conductor while the inverter is operating beyond 5 kHz, though frequency is increased and operated the inverter about 20 kHz. It follows that this corrosion can be totally eliminated if the frequency is raised even further. Therefore, in the future, this high frequency power inverter will be a promising ohmic heater to sterilize the liquid food conductor at ultra-high temperature in food processing industry.

When the concentration of the solution increases as shown in Table 3.18, the heating rate becomes faster and the time required for reaching the same temperature is shorter compared to a lower concentration. This happens because higher concentration allows more current to flow. However, the corrosion effect remains the same with respect to frequency.

Chapter-4

DESIGN AND DEVELOPMENT AND SOME STUDIES ON HIGH FREQUENCY POWER INVERTER USING ARDUINO MICROCONTROLLER

4.1 Introduction

Unlike traditional inverters discussed in the earlier chapters, this inverter uses a microcontroller to generate precise Pulse Width Modulation (PWM) signals for controlling the power switches. The Arduino Uno, based on the ATmega328P microcontroller, is a widely used platform due to its ease of programming, affordability, and versatility in handling digital control operations. An inverter using Arduino Uno is a circuit designed to convert DC power into AC power using digital control techniques. Initially, the inverter is tested in simulation software like Proteus where the circuit design, pulse width modulation (PWM) signals, and optocoupler response are analyzed without hardware components. The Arduino Uno, which serves as the core microcontroller (ATmega3285P), generates PWM signals to drive MOSFETs in an H-bridge or push-pull topology. These switching signals are used to convert DC input into a modified or square wave AC output. Once the software simulation confirms proper functionality, the design is implemented in hardware using components like transformers, power transistors, and filters to achieve the desired AC output. Finally hardware prototype is tested under various load conditions to ensure efficiency and stability, making it a cost-effective and scalable solution for small-scale power conversion applications. The inverter's design and implementation process typically follows a two-phase approach: software simulation of driver circuit and hardware realization. This ensures that the circuit functions optimally before physically constructing the system. The primary objective of the simulation phase is to verify the feasibility of the inverter's operation under different conditions.

4.2 Simulation and testing of microcontroller based driver using software

The Arduino Uno is programmed to generate high-frequency PWM signals using its built-in Timer1 module. These PWM signals drive MOSFETs or IGBTs in an H-bridge or push-pull configuration to create an AC waveform from a DC source. The output waveform characteristics, such as frequency and duty cycle are analyzed using simulation tools. The simulation helps in identifying the potential issues such as switching losses, dead time

requirements, and overheating risks, allowing for necessary optimizations before hardware implementation. First of all, the technical specifications must be discussed in detail to ensure a clear understanding of the system's capabilities and limitations. This includes key parameters such as operating voltage, power consumption, speed, and performance characteristics. Analyzing these specifications is crucial for selecting the right components and ensuring compatibility with the intended application.

4.2.1 Technical specifications

Arduino Uno is one of the most popular microcontroller boards in the Arduino family. It is based on the ATmega328P microcontroller and is widely used for prototyping, embedded systems, IoT (Internet of Things) applications and power electronics projects. Its ease of use, open-source nature, and extensive community support make it a favorite among beginners and professionals alike. Details of technical specifications are mentioned below.

Feature	**Specification**
Operating Voltage	5V
Microcontroller	ATmega328P (8-bit AVR)
Input Voltage (Limits)	6-20V
Analog Input Pins	6
Digital I/O Pins	14 (6 PWM)
DC Current per I/O Pin	20mA
Input Voltage (Recommended)	7-12V
SRAM	2 KB
Clock Speed	16 MHz
Power Consumption	~50 mA
Flash Memory	32 KB (0.5 KB used by boot loader)
EEPROM	1 KB
USB Connectivity	Yes (USB Type B)
Communication	UART, I2C, SPI
Dimensions	68.6mm x 53.4mm
Weight	~25g

The ATmega328P is an 8-bit microcontroller from the Atmel AVR family (now owned by Microchip Technology). It is the core microcontroller used in Arduino Uno, Arduino Nano, and other development boards. It is known for its low power consumption, high performance, and ease of use in various projects. The ATmega328P comes in different packages (DIP, TQFP, QFN), but the most common is DIP-28 (used in Arduino Uno). Pin descriptions of ATmega328P IC shown in Fig 4.1.

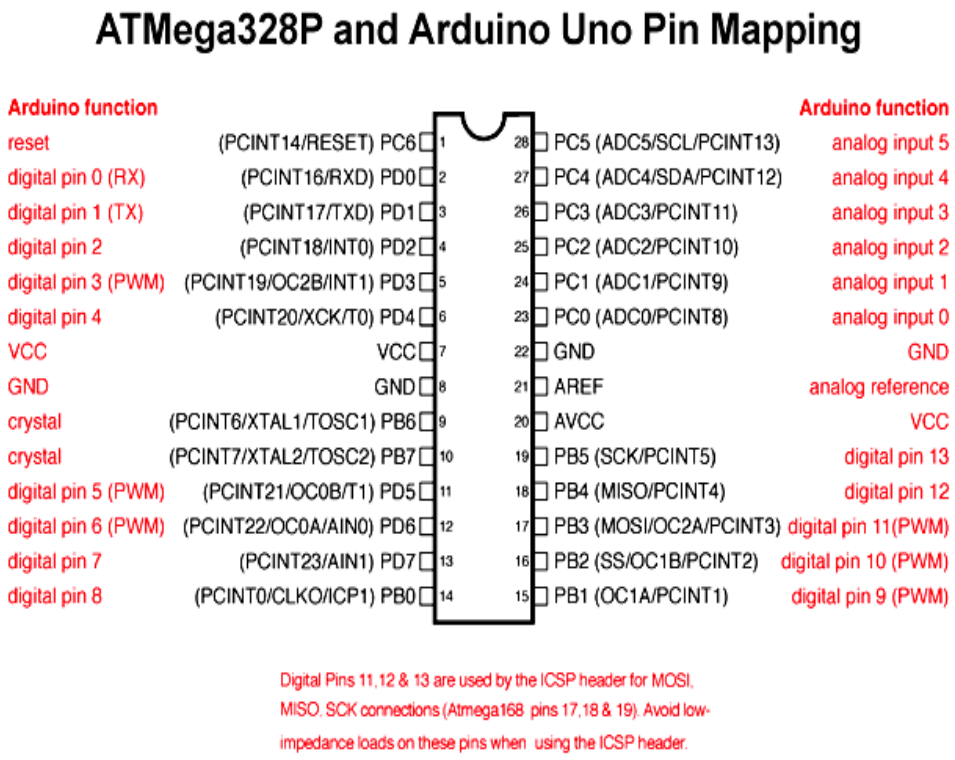

Figure 4.1: Pin descriptions of ATmega328P IC.

Pin	**Function**
VCC	Power supply (1.8V – 5.5V)
GND	Ground
AVCC	Analog power supply (for ADC)
AREF	Analog reference voltage
RESET	Active low reset
PB0 - PB7	Digital I/O, SPI (MISO, MOSI, SCK)
PC0 - PC5	Analog inputs (ADC0 - ADC5)
PD0 - PD7	Digital I/O, UART (RX, TX), I2C (SDA, SCL)

1. **Timers & PWM**
   - **Timer0 & Timer2** (8-bit) → Used for delays, PWM, and time-based operations.
   - **Timer1** (16-bit) → Used for precision timing, frequency measurement, and PWM.
2. **ADC (Analog-to-Digital Converter)**
   - 10-bit resolution.
   - 6 input channels (PC0 - PC5).
   - Supports differential measurement and adjustable voltage reference.
3. **Communication Interfaces**
   - **UART**: Serial communication (RX, TX).
   - **SPI**: High-speed data transfer (MISO, MOSI, SCK).
   - **I2C (TWI)**: Interfacing with sensors, displays, and peripherals (SDA, SCL).

Finally, the program was developed and uploaded to the Arduino Uno using the Arduino IDE. The corresponding software and driver circuit diagram are shown in Fig 4.2; outputs at different frequencies and duty cycle have been generated, captured using a virtual oscilloscope (DSO), and are presented here for analysis. These outputs demonstrate the system's ability to produce variable pulse signals, at the end which can be utilized in pulse-width modulation (PWM) techniques for operation of inverter-MOSFETs.

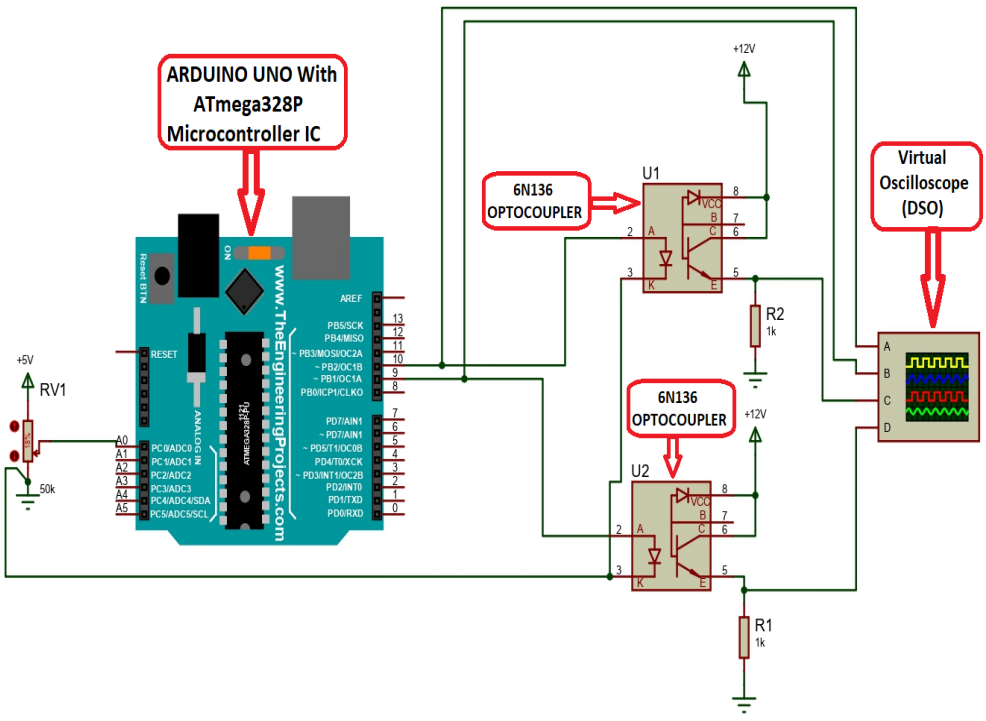

Figure 4.2: Driver circuit design in Proteus software.

4.2.2 Driver output voltage pulses in simulation at different frequency (1kHz, 3kHz, 5kHz, 10kHz, 12.5kHz and 16kHz)

Several outputs i.e. alternate pulses with varying frequencies and duty cycles that were recorded in a virtual oscilloscope (DSO) are produced and provided here from Fig 4.3 to Fig 4.8.

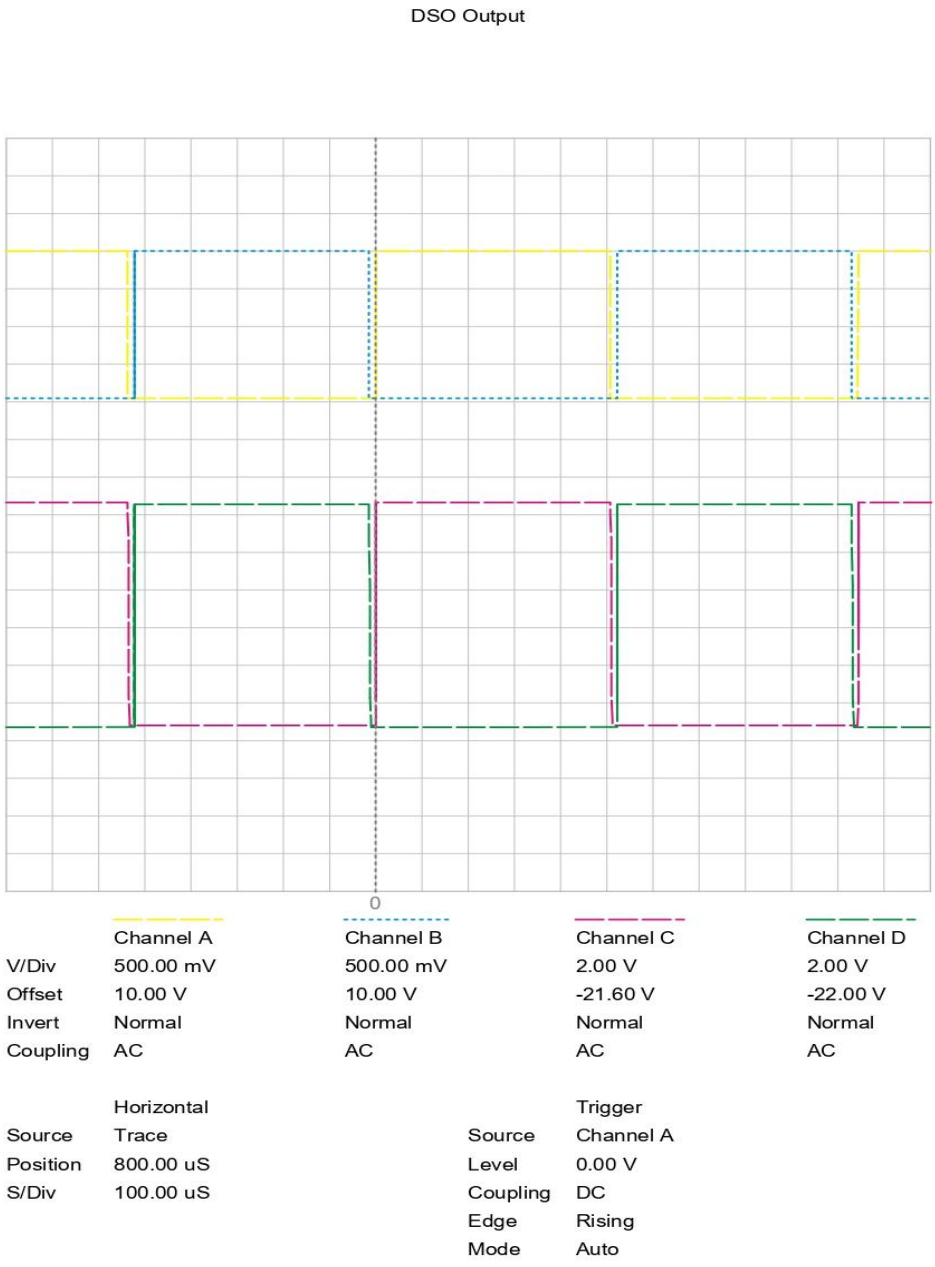

Figure 4.3: 1 kHz frequency alternate pulse voltages before the optocoupler (yellow and blue) and after the optocoupler (red and green).

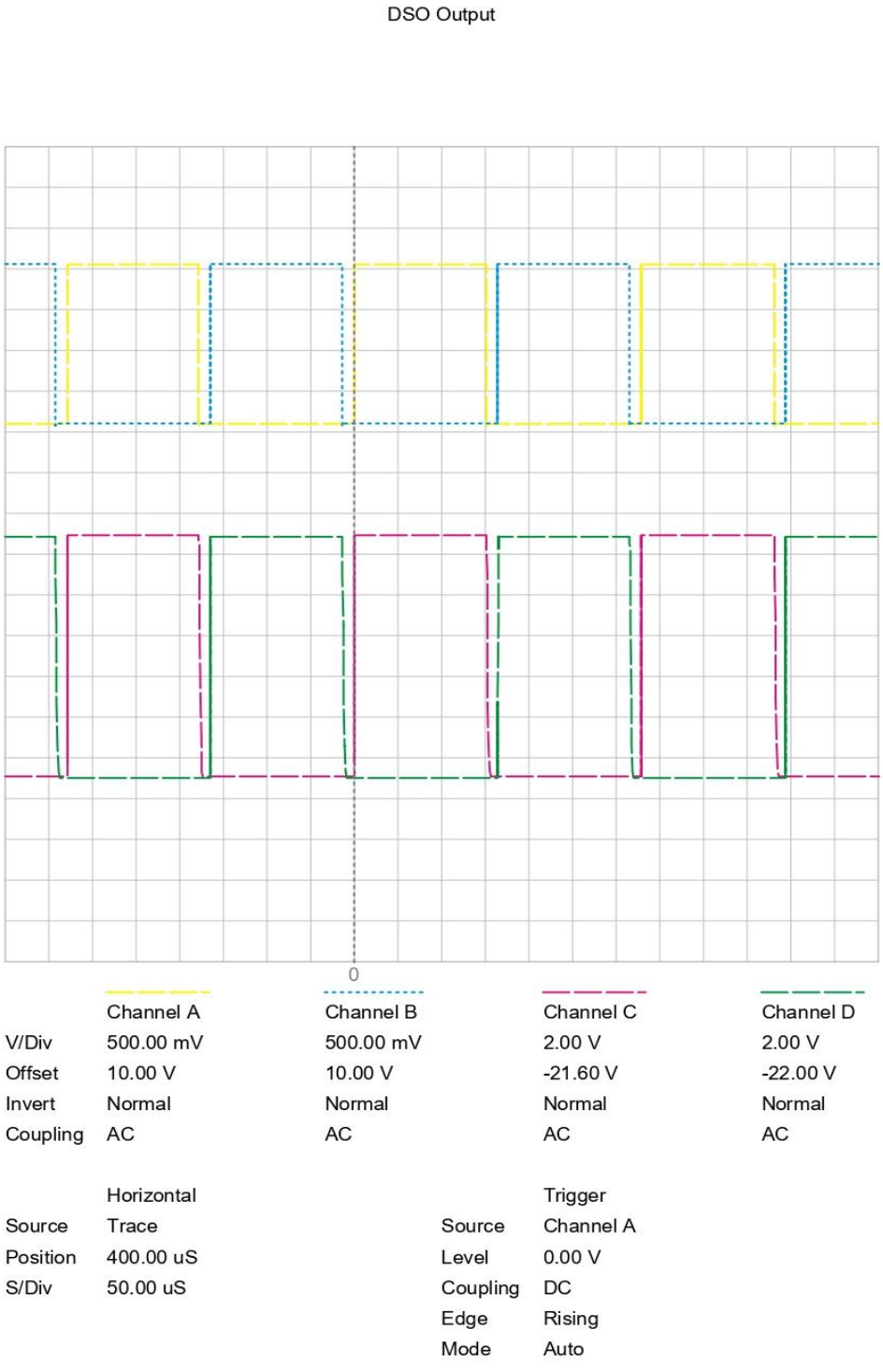

Figure 4.4: 3 kHz frequency alternate pulse voltages before the optocoupler (yellow and blue) and after the optocoupler (red and green).

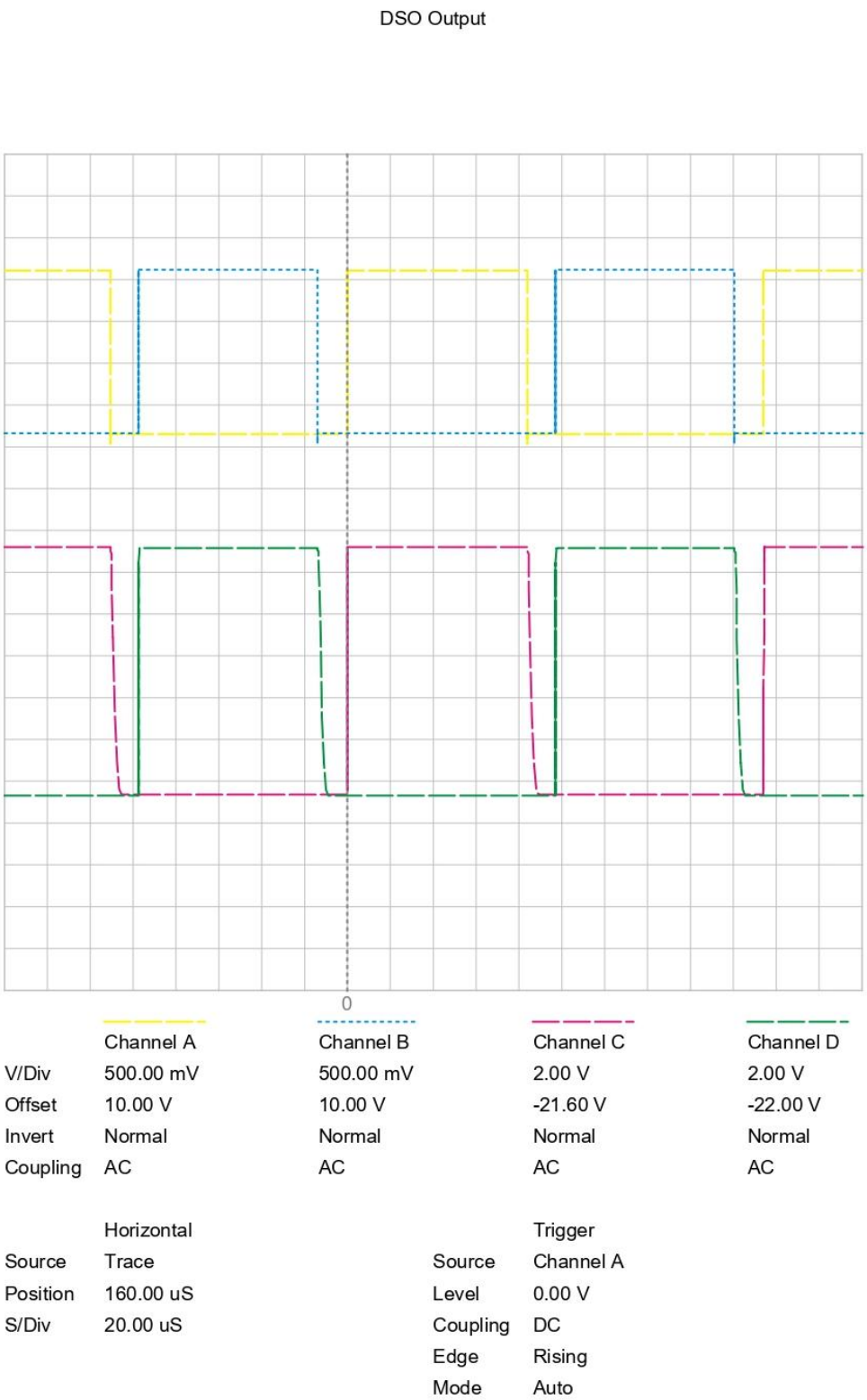

Figure 4.5: 5 kHz frequency alternate pulse voltages before the optocoupler (yellow and blue) and after the optocoupler (red and green).

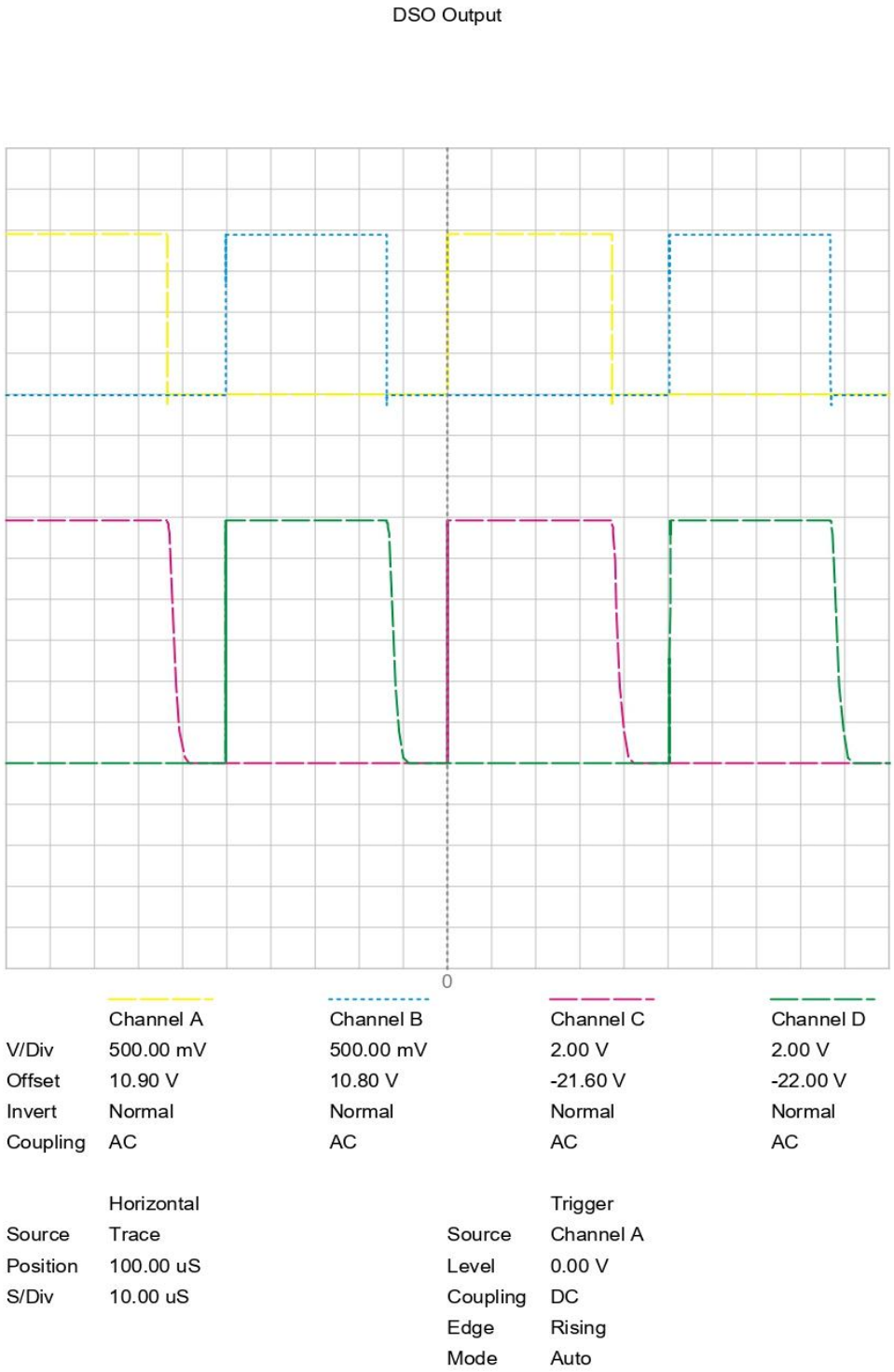

Figure 4.6:10 kHz frequency alternate pulse voltages before the optocoupler (yellow and blue) and after the optocoupler (red and green).

DSO Output

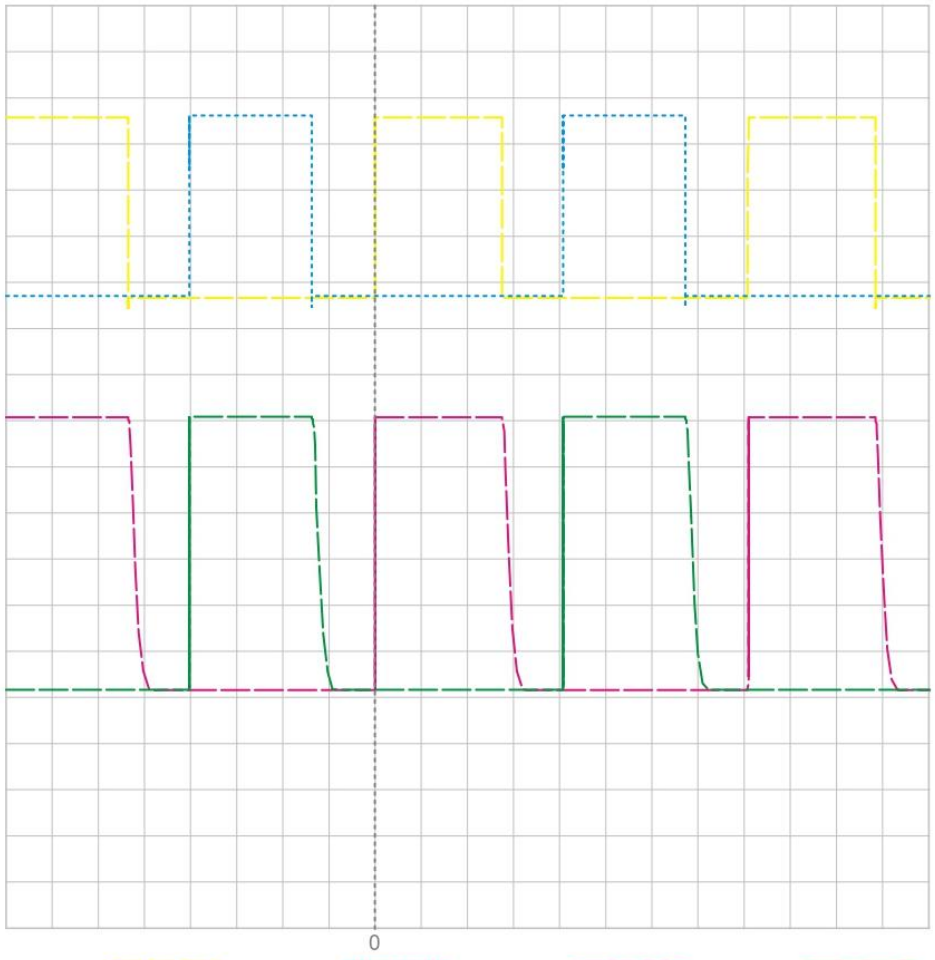

	Channel A	Channel B	Channel C	Channel D
V/Div	500.00 mV	500.00 mV	2.00 V	2.00 V
Offset	10.00 V	10.00 V	-21.60 V	-22.00 V
Invert	Normal	Normal	Normal	Normal
Coupling	AC	AC	AC	AC

Horizontal		Trigger	
Source	Trace	Source	Channel A
Position	80.00 uS	Level	0.00 V
S/Div	10.00 uS	Coupling	DC
		Edge	Rising
		Mode	Auto

Figure 4.7:12.5 kHz frequency alternate pulse voltages before the optocoupler (yellow and blue) and after the optocoupler (red and green).

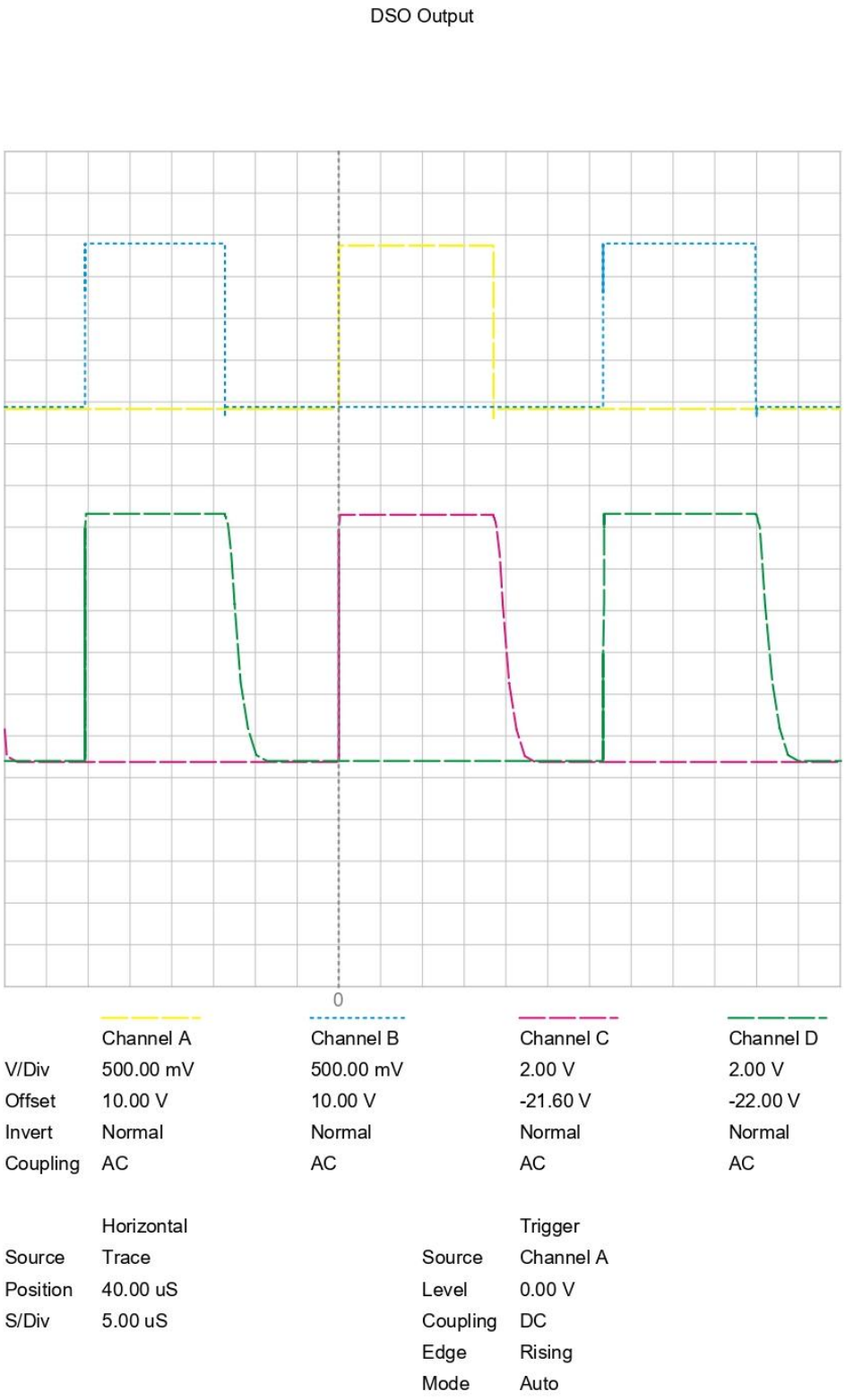

Figure 4.8:16 kHz frequency alternate pulse voltages before the optocoupler (yellow and blue) and after the optocoupler (red and green).

4.3 Hardware design and implementation of driver output voltage pulses

After achieving satisfactory simulation results, the inverter driver is implemented using physical components. The key hardware elements are included here in the Fig 4.9 shown below. A real Arduino Uno, along with other components like a variable resistor for frequency control, has been incorporated into a zero PCB board. The compiled program built on a PC using the Arduino IDE software is interfaced with the Arduino Uno board. Finally, a digital storage oscilloscope (DSO) was used to record the alternating output pulses at various frequencies shown in Fig 4.10 to 4.16, which are presented below.

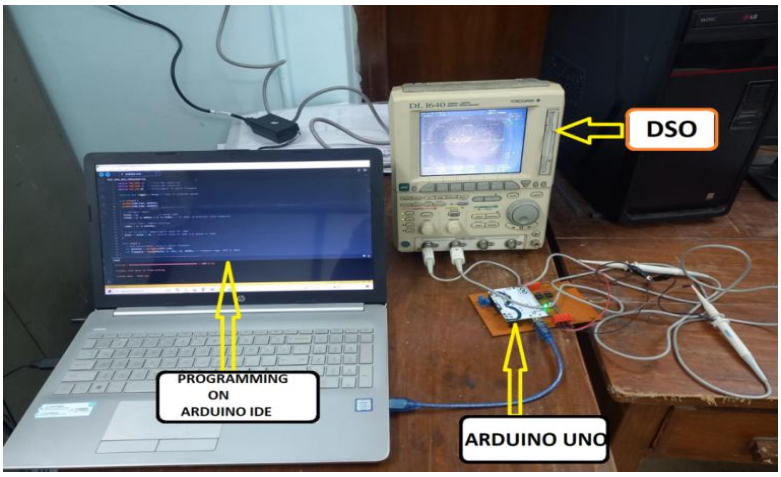

Figure 4.9: Testing of driver circuit using Arduino Uno.

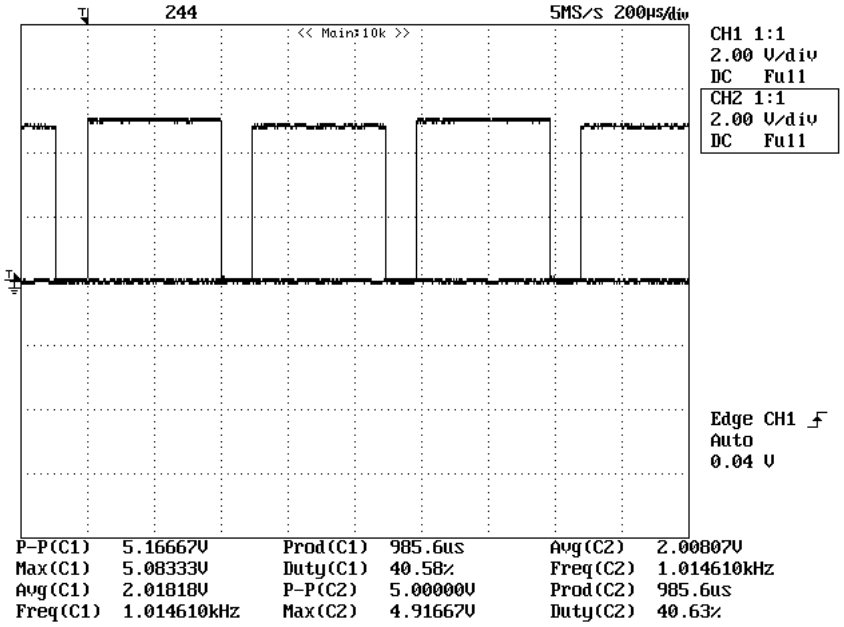

Figure 4.10: 1 kHz frequency alternate pulse voltages from ATmega328P microcontroller IC.

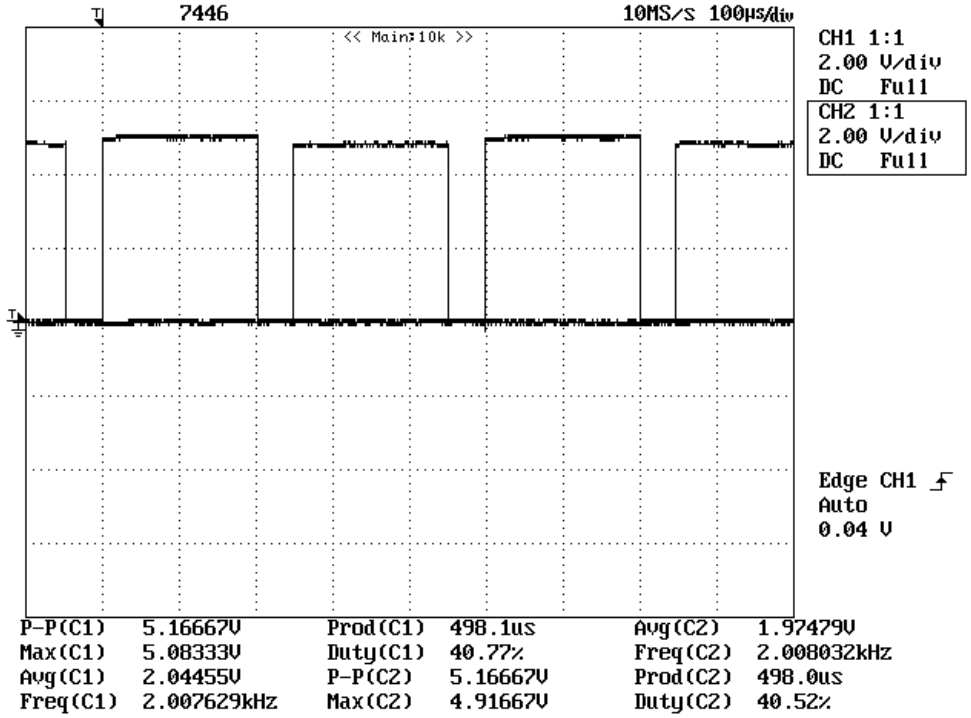

Figure 4.11: 2 kHz frequency alternate pulse voltages from ATmega328P microcontroller IC.

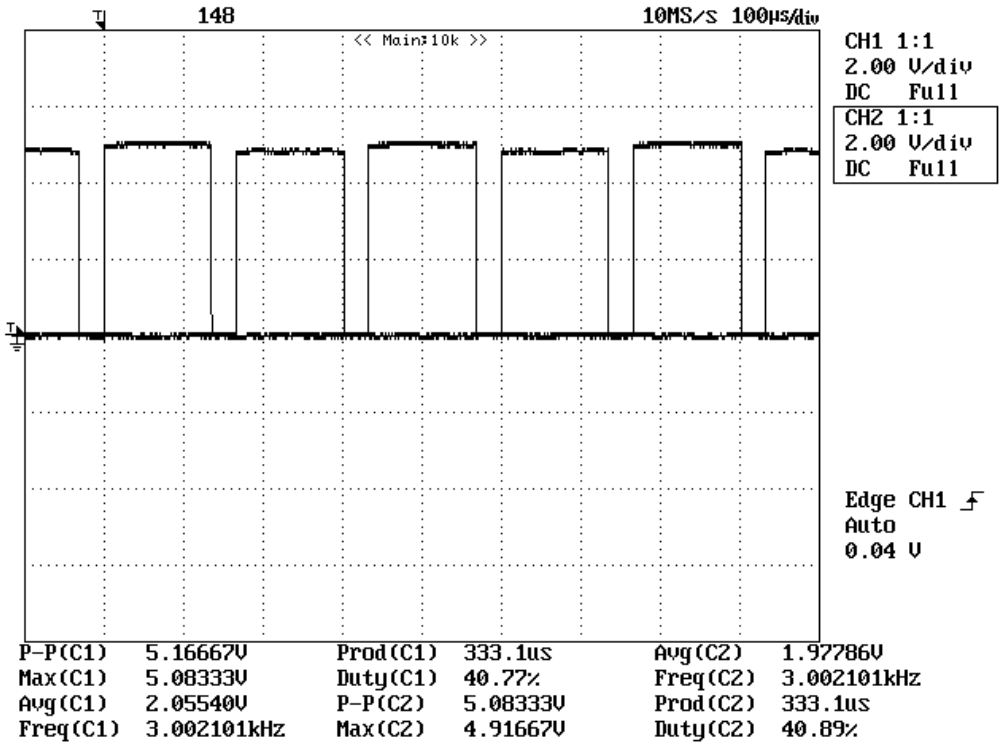

Figure 4.12: 3 kHz frequency alternate pulse voltages from ATmega328P microcontroller IC.

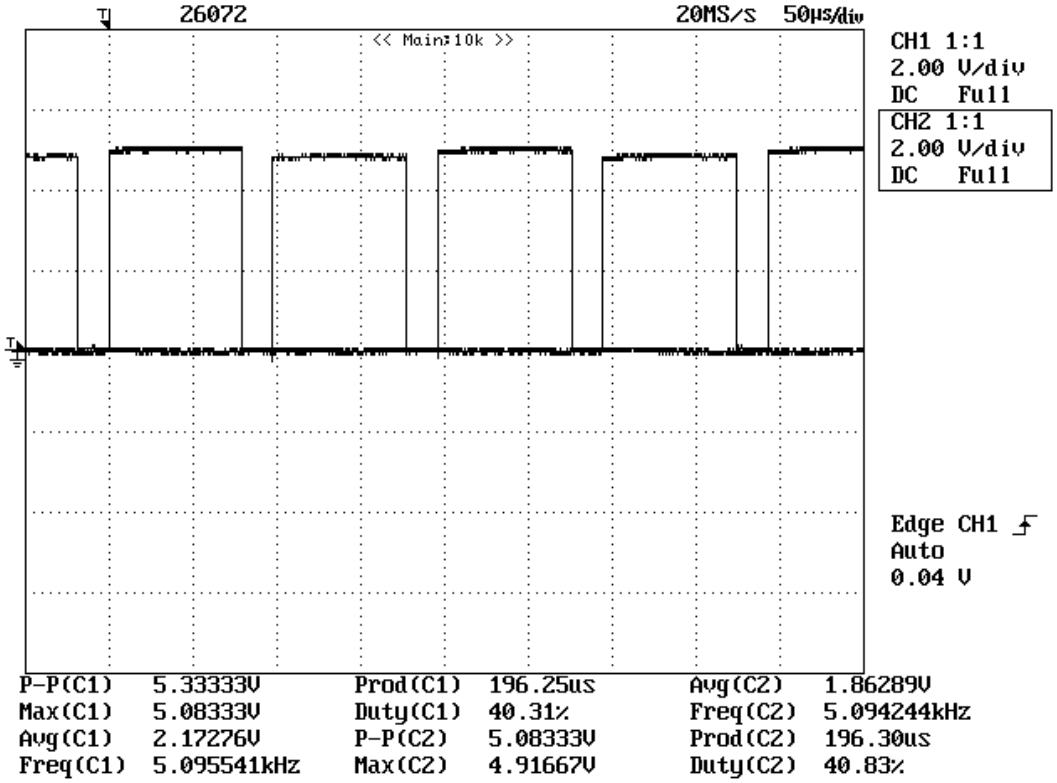

Figure 4.13: 5 kHz frequency alternate pulse voltages from ATmega328P microcontroller IC.

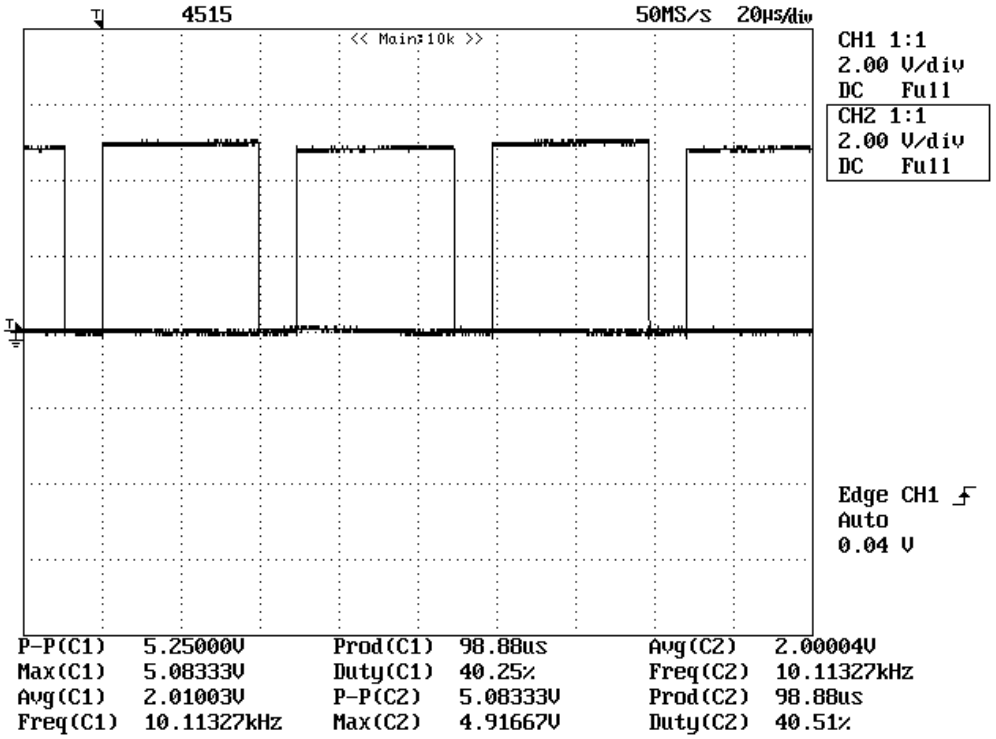

Figure 4.14:10 kHz frequency alternate pulse voltages from ATmega328P microcontroller IC.

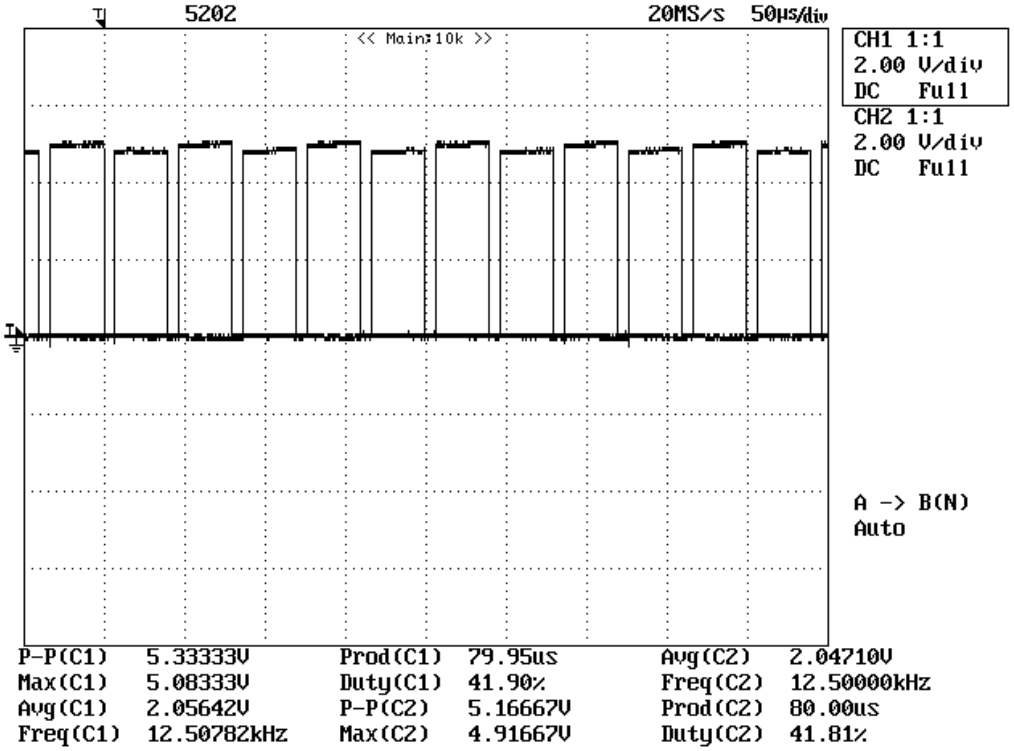

Figure 4.15:12 kHz frequency alternate pulse voltages from ATmega328P microcontroller IC.

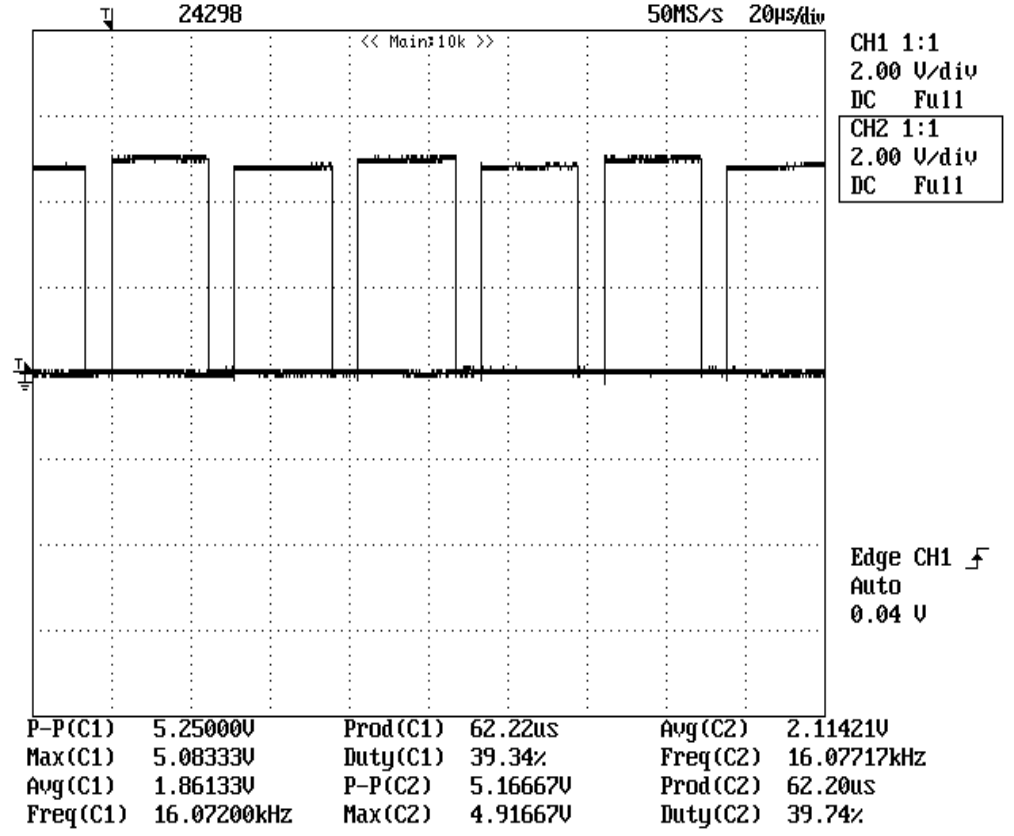

Figure 4.16: 16 kHz frequency alternate pulse voltages from ATmega328P microcontroller IC.

4.4 Testing and performance evaluation

After assembling the hardware setup, the inverter is tested under various loading conditions to evaluate its performance. 6N136 is used for isolation which is a high-speed optocoupler designed for applications that require galvanic isolation and fast signal transmission. It consists of an infrared LED and a photo detector with an integrated high-gain amplifier. It provides isolation between a low-voltage microcontroller (e.g., Arduino) and high-voltage circuits. Isolates control logic circuit from Inverter-MOSFETs. The optocoupler not only isolates the circuits but also enhances the voltage level from 5V to 12V in this driver circuit which is required to turn-on the power MOSFETs. Push-pull type inverter using ferrite core transformer including all the components as discussed earlier is being adopted here for higher frequency operation shown in Fig. 4.17. Various experimental analysis has been done with and without loaded condition of this microcontroller based inverter and captured different wave shapes using DSO, shown in Fig. 4.18 to 4.39 where tungsten filament bulb consider as electrical load. Initially, the inverter is tested at a higher frequency to ensure stability and proper operation. If the results are satisfactory, the system will then be tested using a liquid load to evaluate its performance under realistic operating conditions.

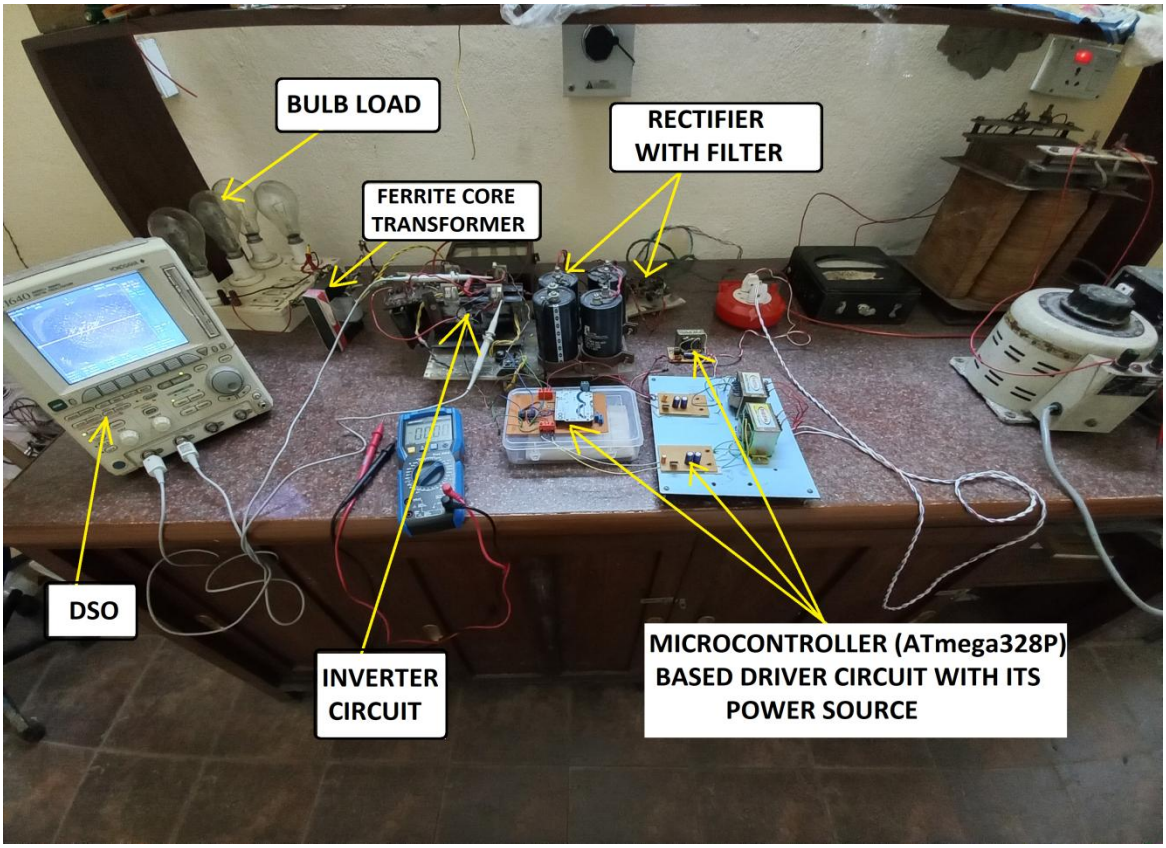

Figure 4.17: Push-pull inverter setup with microcontroller based driver.

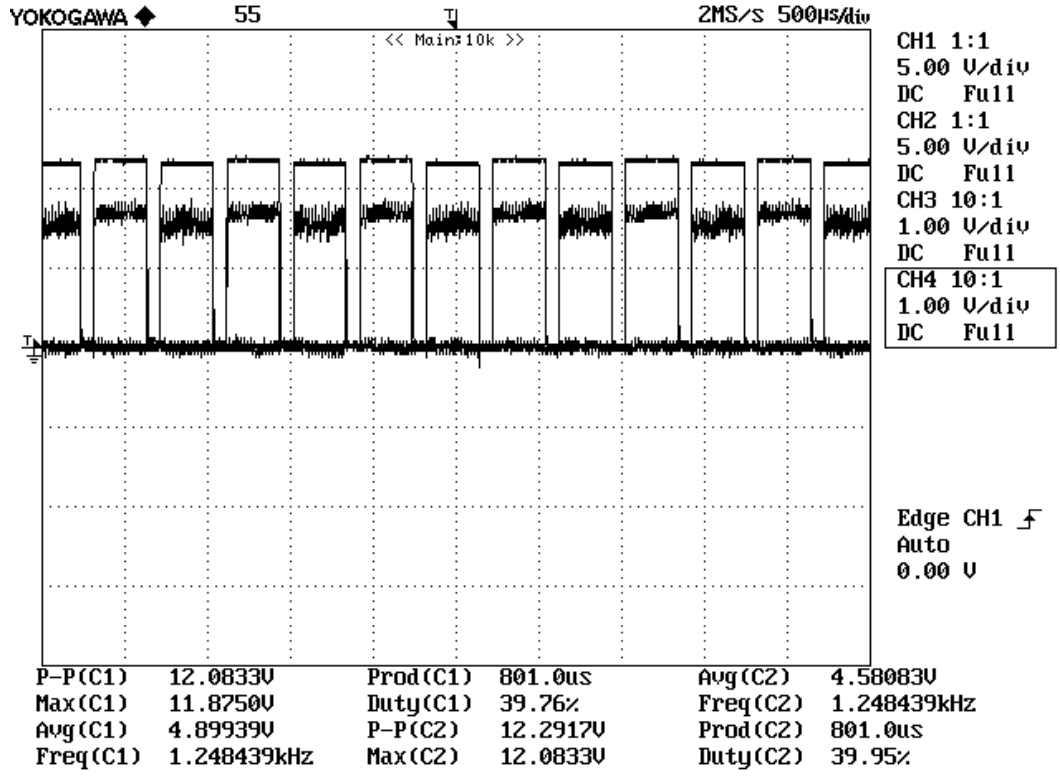
YOKOGAWA
55
2MS/s 500µs/div
<< Main:10k >>
CH1 1:1
5.00 V/div
DC Full
CH2 1:1
5.00 V/div
DC Full
CH3 10:1
1.00 V/div
DC Full
CH4 10:1
1.00 V/div
DC Full
Edge CH1
Auto
0.00 V
P-P(C1) 12.0833V
Max(C1) 11.8750V
Avg(C1) 4.89939V
Freq(C1) 1.248439kHz
Prod(C1) 801.0us
Duty(C1) 39.76%
P-P(C2) 12.2917V
Max(C2) 12.0833V
Avg(C2) 4.58083V
Freq(C2) 1.248439kHz
Prod(C2) 801.0us
Duty(C2) 39.95%

(a)

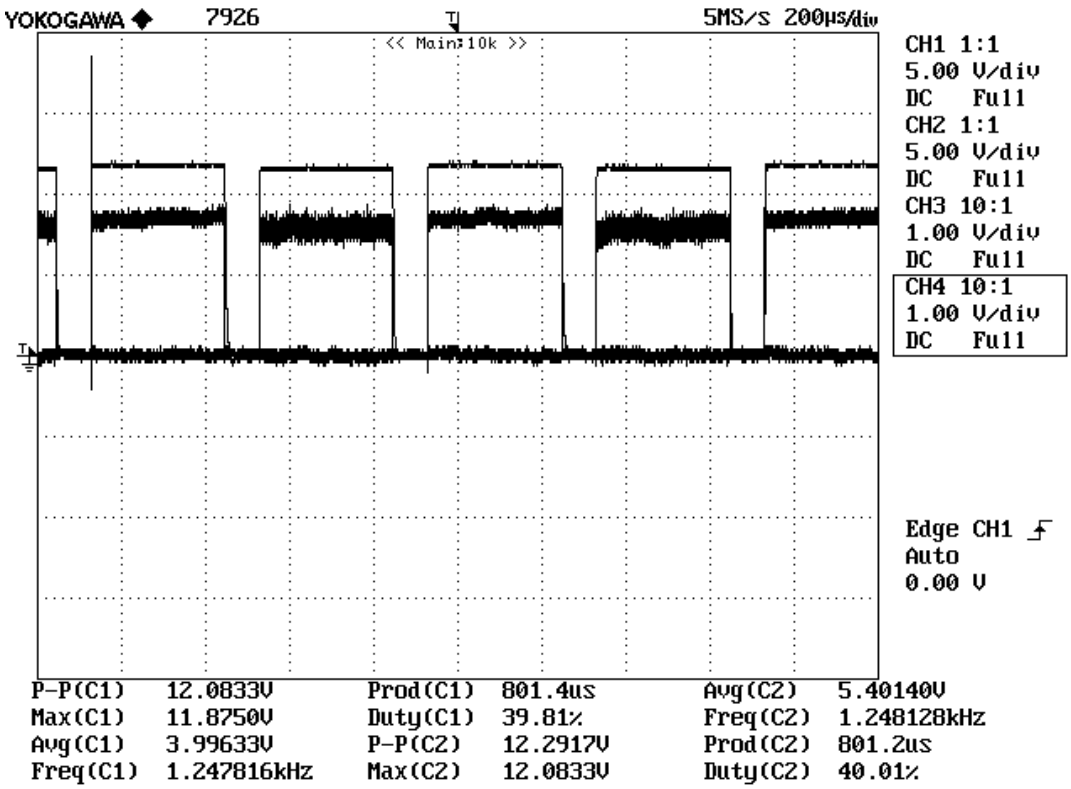
YOKOGAWA
7926
5MS/s 200µs/div
<< Main:10k >>
CH1 1:1
5.00 V/div
DC Full
CH2 1:1
5.00 V/div
DC Full
CH3 10:1
1.00 V/div
DC Full
CH4 10:1
1.00 V/div
DC Full
Edge CH1
Auto
0.00 V
P-P(C1) 12.0833V
Max(C1) 11.8750V
Avg(C1) 3.99633V
Freq(C1) 1.247816kHz
Prod(C1) 801.4us
Duty(C1) 39.81%
P-P(C2) 12.2917V
Max(C2) 12.0833V
Avg(C2) 5.40140V
Freq(C2) 1.248128kHz
Prod(C2) 801.2us
Duty(C2) 40.01%

(b)

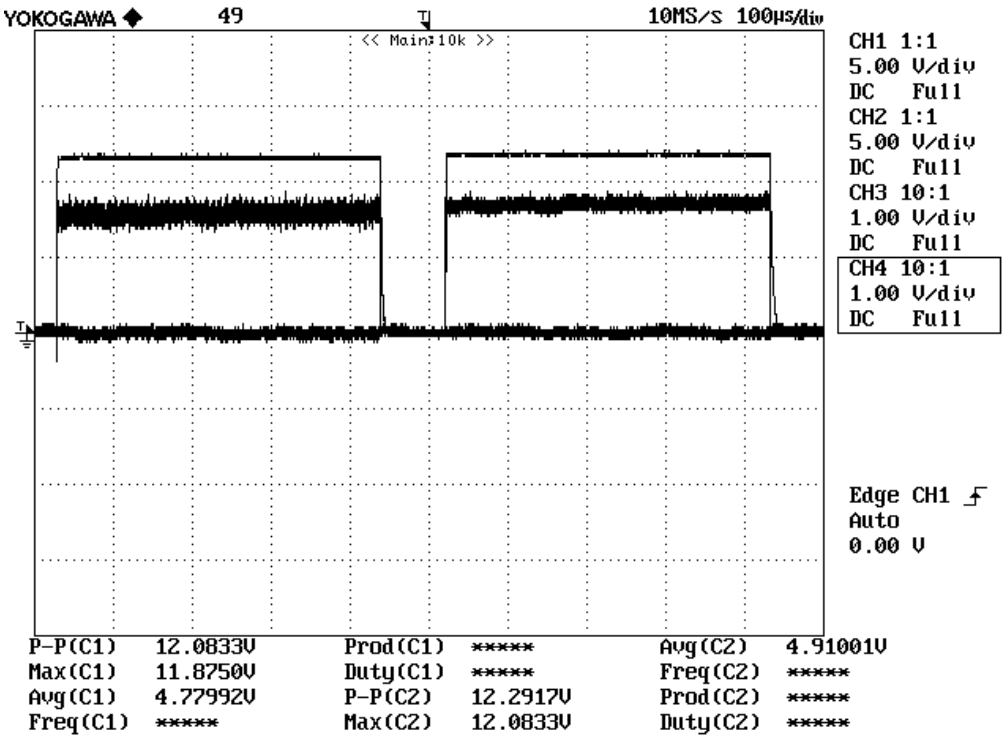

(c)

Figure 4.18 (a, b,c): 1.2 kHz output voltage pulses from secondary side of optocoupler 6N136.

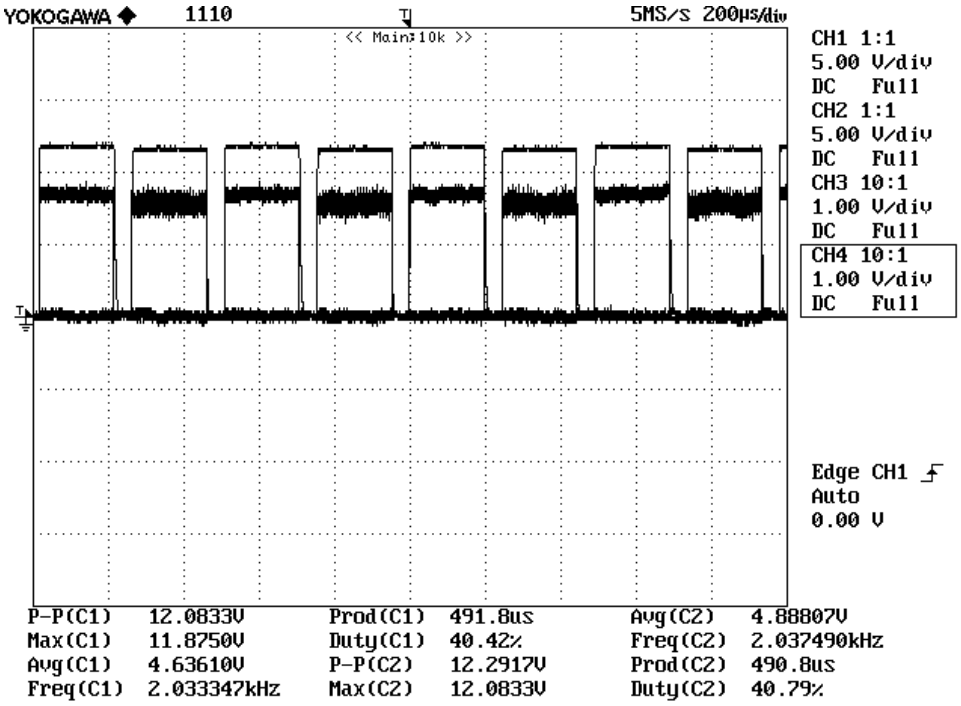

(a)

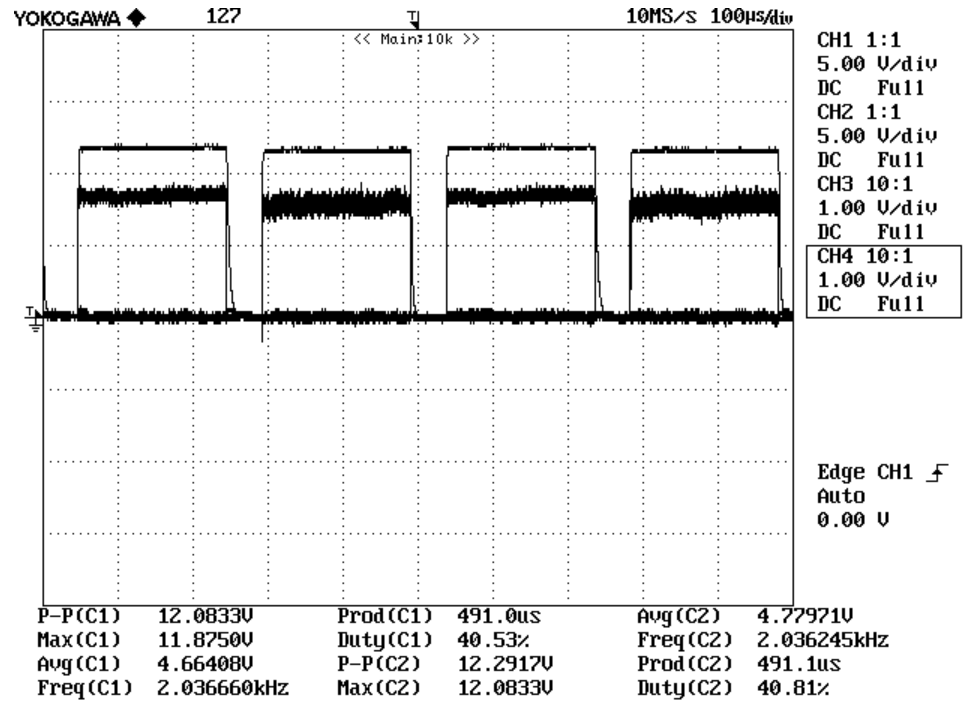

(b)

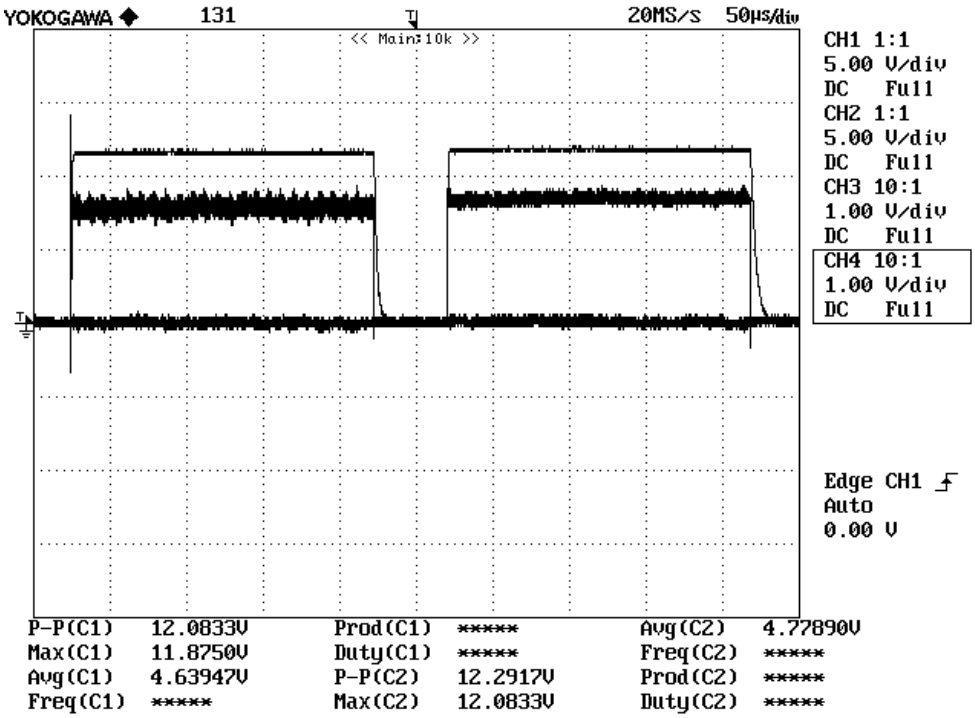

(c)

Figure 4.19 (a, b, c): 2 kHz output voltage pulses from secondary side of optocoupler 6N136.

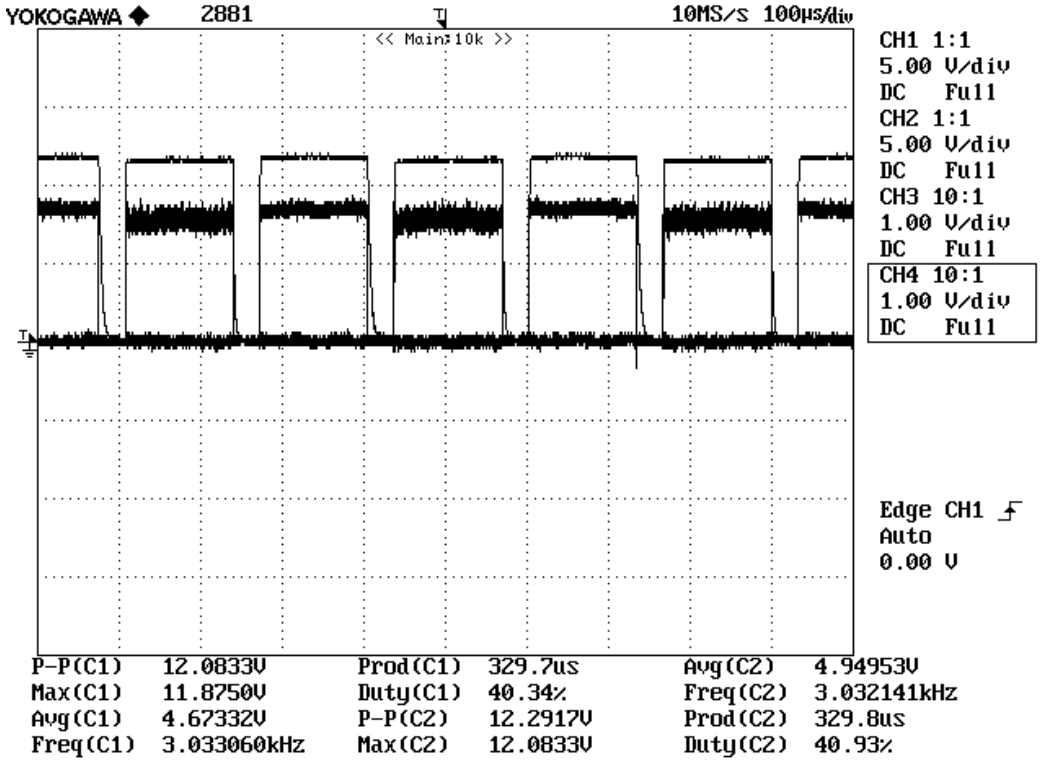
YOKOGAWA
2881
10MS/s 100µs/div
<< Main:10k >>
CH1 1:1
5.00 V/div
DC Full
CH2 1:1
5.00 V/div
DC Full
CH3 10:1
1.00 V/div
DC Full
CH4 10:1
1.00 V/div
DC Full
Edge CH1
Auto
0.00 V
P-P(C1) 12.0833V
Max(C1) 11.8750V
Avg(C1) 4.67332V
Freq(C1) 3.033060kHz
Prod(C1) 329.7us
Duty(C1) 40.34%
P-P(C2) 12.2917V
Max(C2) 12.0833V
Avg(C2) 4.94953V
Freq(C2) 3.032141kHz
Prod(C2) 329.8us
Duty(C2) 40.93%

(a)

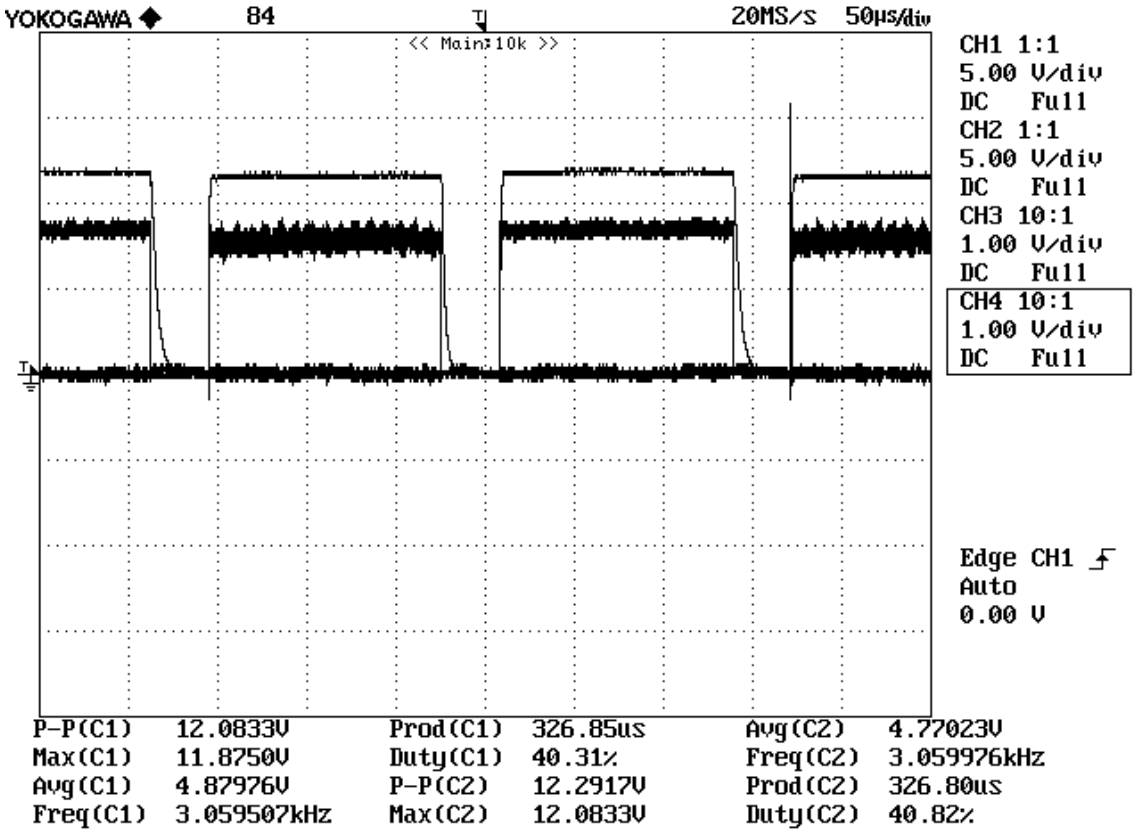
YOKOGAWA
84
20MS/s 50µs/div
<< Main:10k >>
CH1 1:1
5.00 V/div
DC Full
CH2 1:1
5.00 V/div
DC Full
CH3 10:1
1.00 V/div
DC Full
CH4 10:1
1.00 V/div
DC Full
Edge CH1
Auto
0.00 V
P-P(C1) 12.0833V
Max(C1) 11.8750V
Avg(C1) 4.87976V
Freq(C1) 3.059507kHz
Prod(C1) 326.85us
Duty(C1) 40.31%
P-P(C2) 12.2917V
Max(C2) 12.0833V
Avg(C2) 4.77023V
Freq(C2) 3.059976kHz
Prod(C2) 326.80us
Duty(C2) 40.82%

(b)

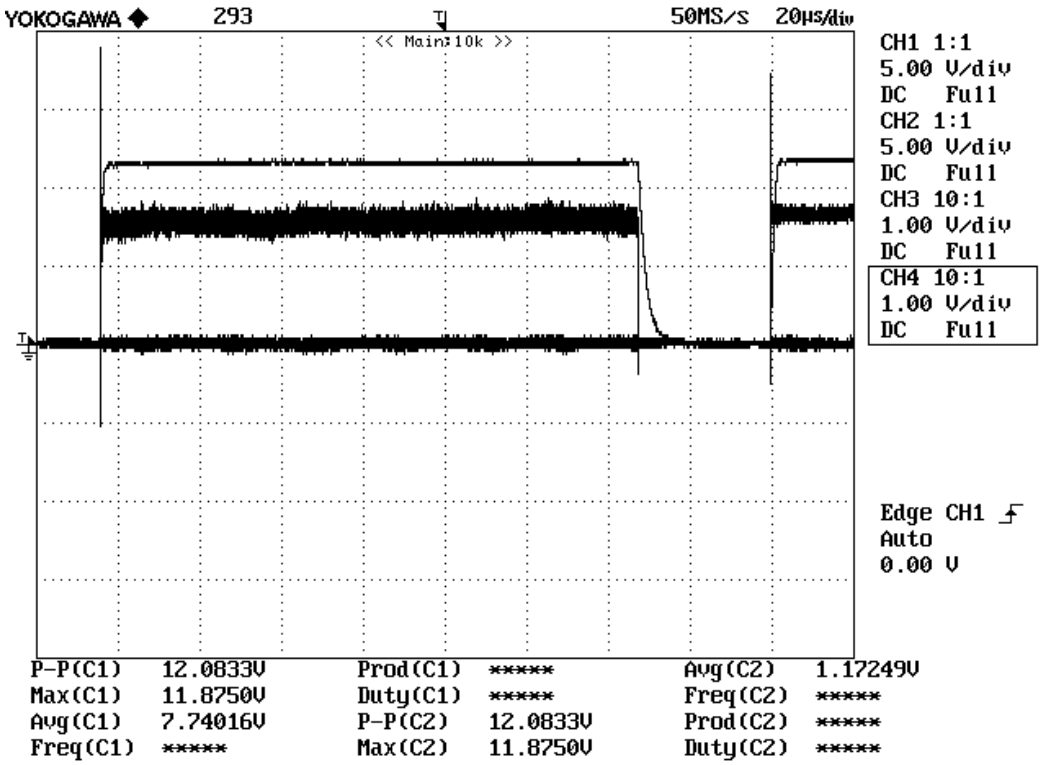

(c)

Figure 4.20 (a, b, c): 3 kHz output voltage pulses from secondary side of optocoupler 6N136.

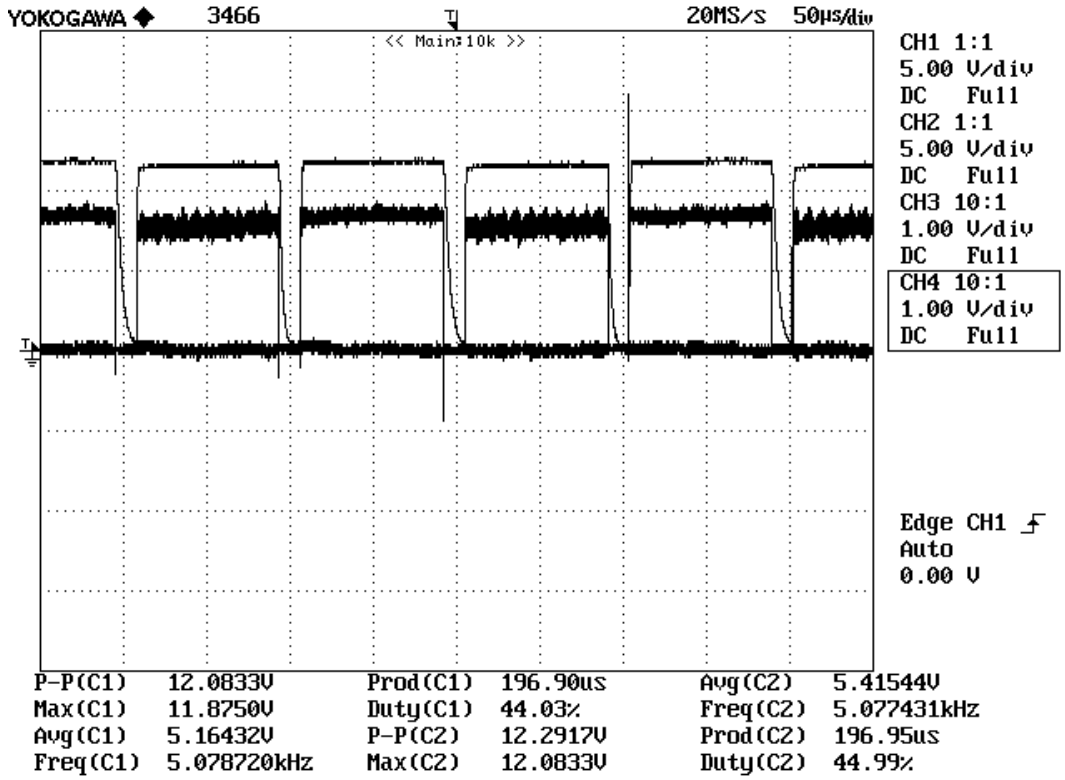

(a)

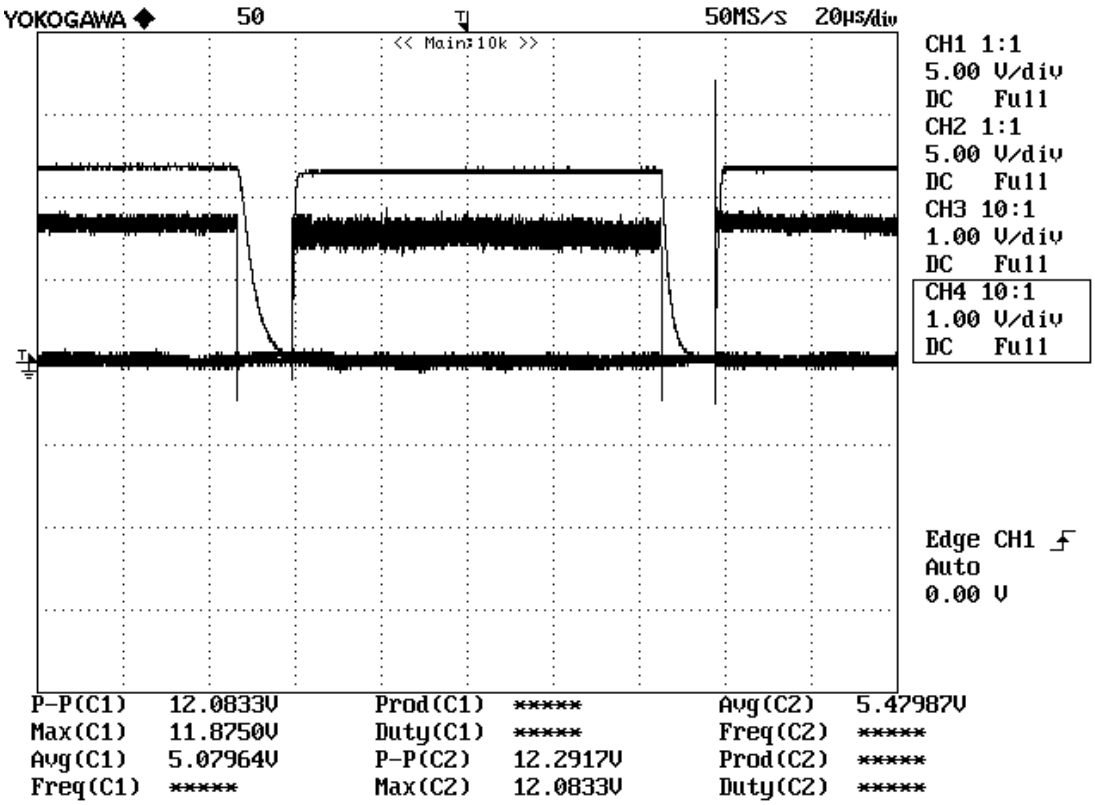

(b)

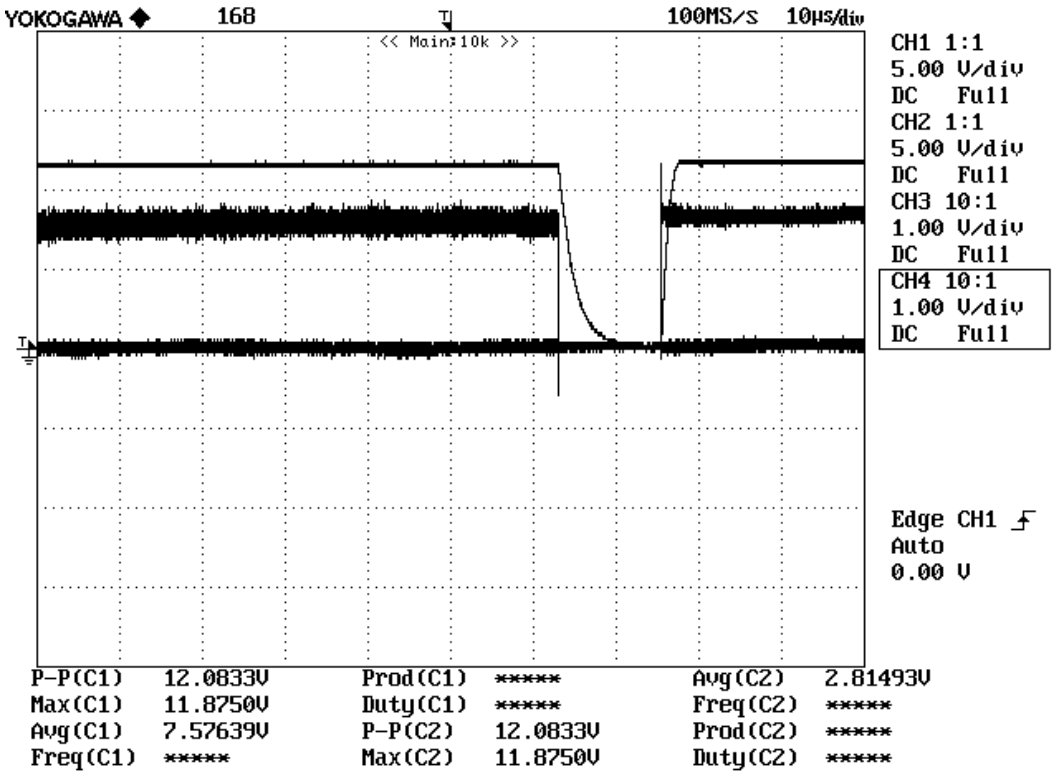

(c)

Figure 4.21 (a, b, c): 5 kHz output voltage pulses from secondary side of optocoupler 6N136.

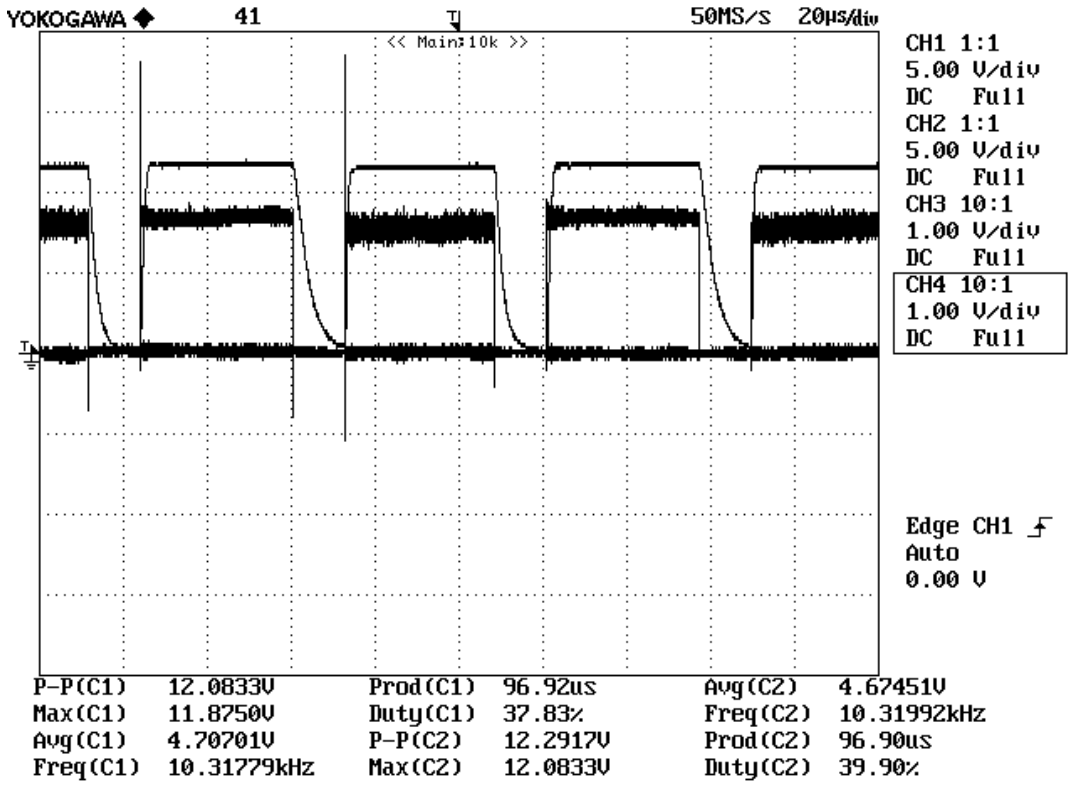
YOKOGAWA
41
50MS/s 20µs/div
<< Main:10k >>
CH1 1:1
5.00 V/div
DC Full
CH2 1:1
5.00 V/div
DC Full
CH3 10:1
1.00 V/div
DC Full
CH4 10:1
1.00 V/div
DC Full
Edge CH1
Auto
0.00 V
P-P(C1) 12.0833V
Max(C1) 11.8750V
Avg(C1) 4.70701V
Freq(C1) 10.31779kHz
Prod(C1) 96.92us
Duty(C1) 37.83%
P-P(C2) 12.2917V
Max(C2) 12.0833V
Avg(C2) 4.67451V
Freq(C2) 10.31992kHz
Prod(C2) 96.90us
Duty(C2) 39.90%

(a)

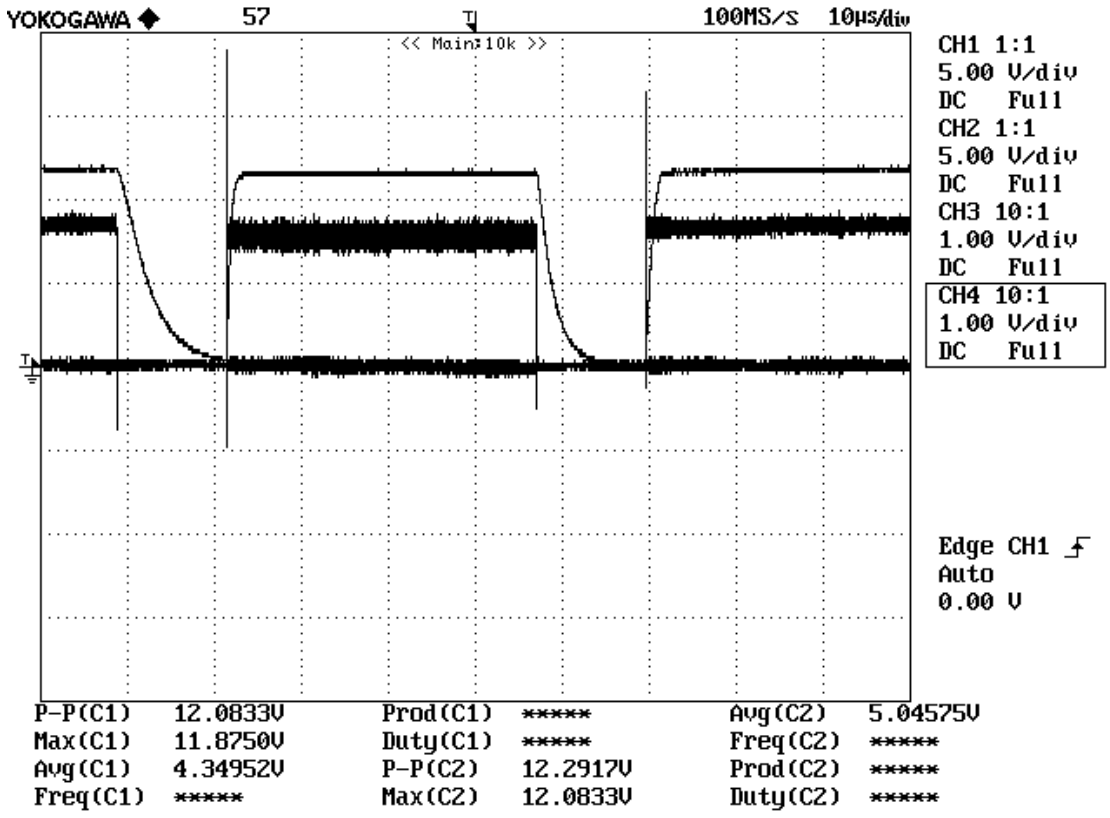
YOKOGAWA
57
100MS/s 10µs/div
<< Main:10k >>
CH1 1:1
5.00 V/div
DC Full
CH2 1:1
5.00 V/div
DC Full
CH3 10:1
1.00 V/div
DC Full
CH4 10:1
1.00 V/div
DC Full
Edge CH1
Auto
0.00 V
P-P(C1) 12.0833V
Max(C1) 11.8750V
Avg(C1) 4.34952V
Freq(C1) *****
Prod(C1) *****
Duty(C1) *****
P-P(C2) 12.2917V
Max(C2) 12.0833V
Avg(C2) 5.04575V
Freq(C2) *****
Prod(C2) *****
Duty(C2) *****

(b)

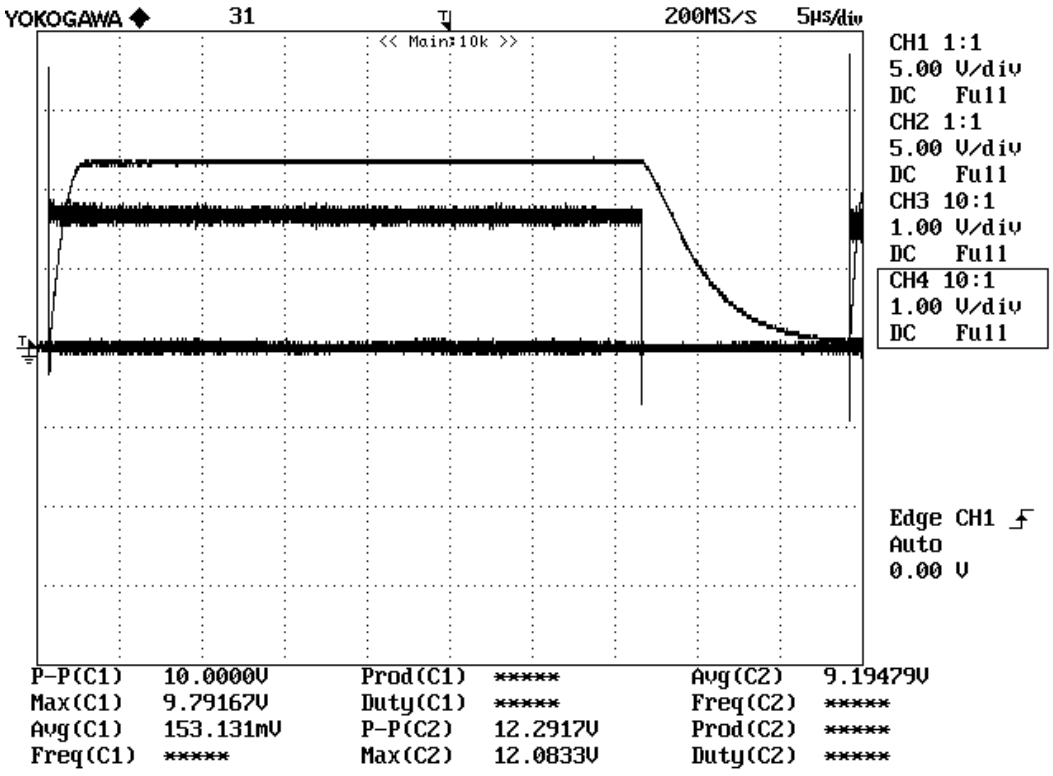

(c)

Figure 4.22 (a, b, c): 10.3 kHz output voltage pulses from secondary side of optocoupler 6N136.

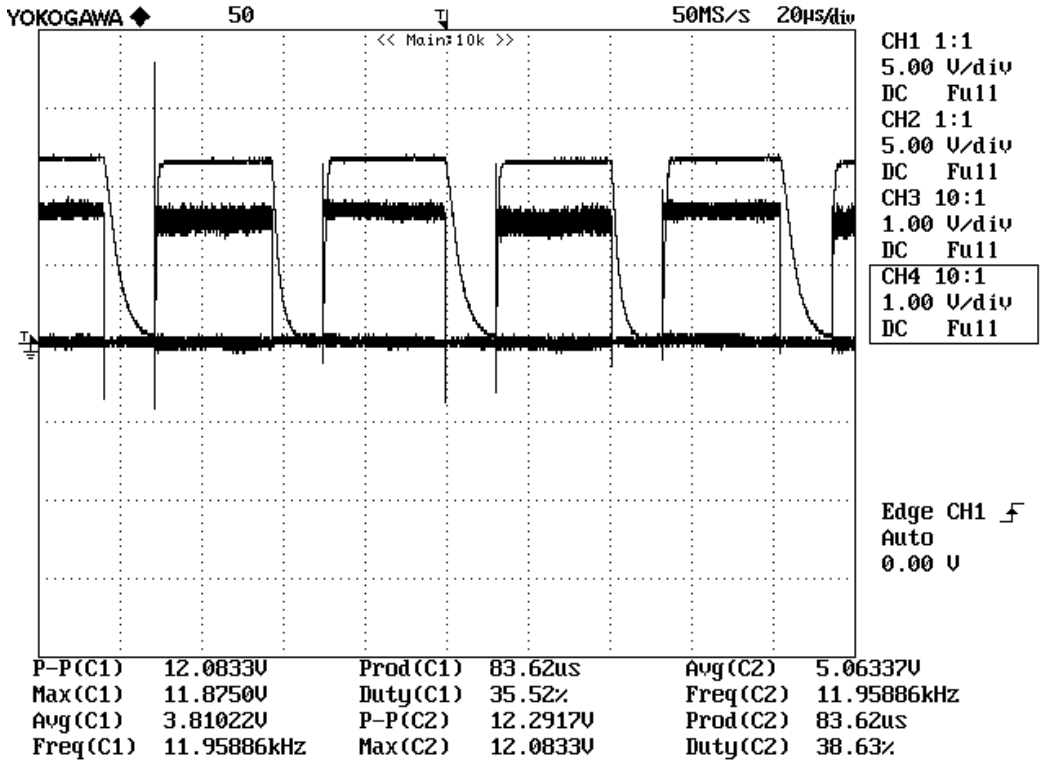

(a)

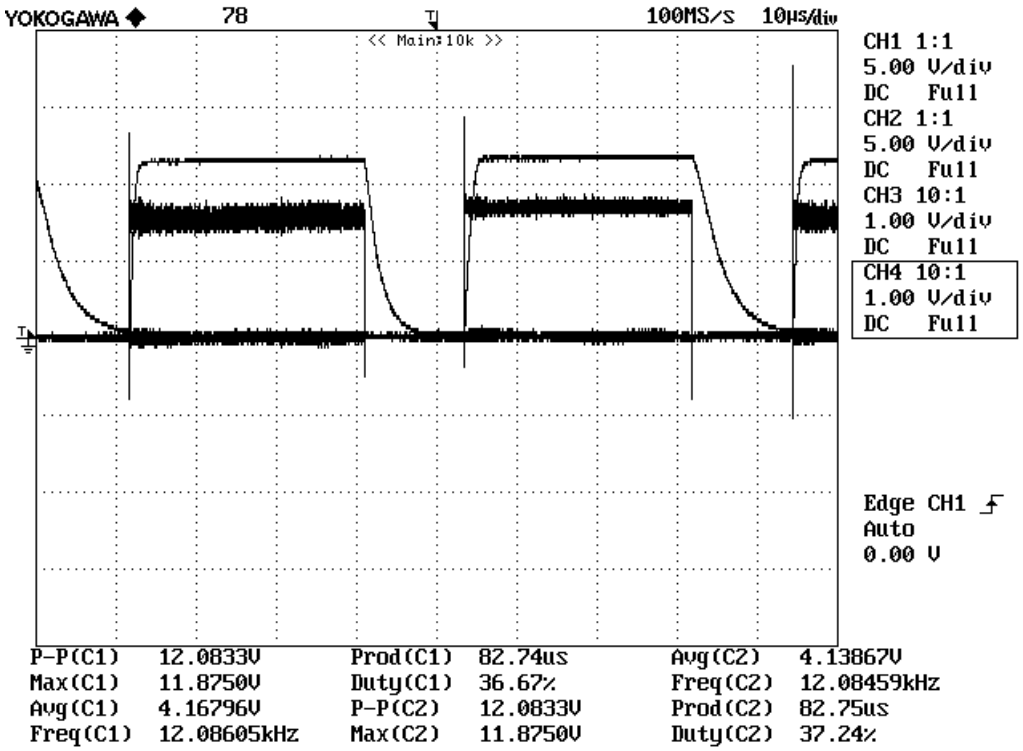

(b)

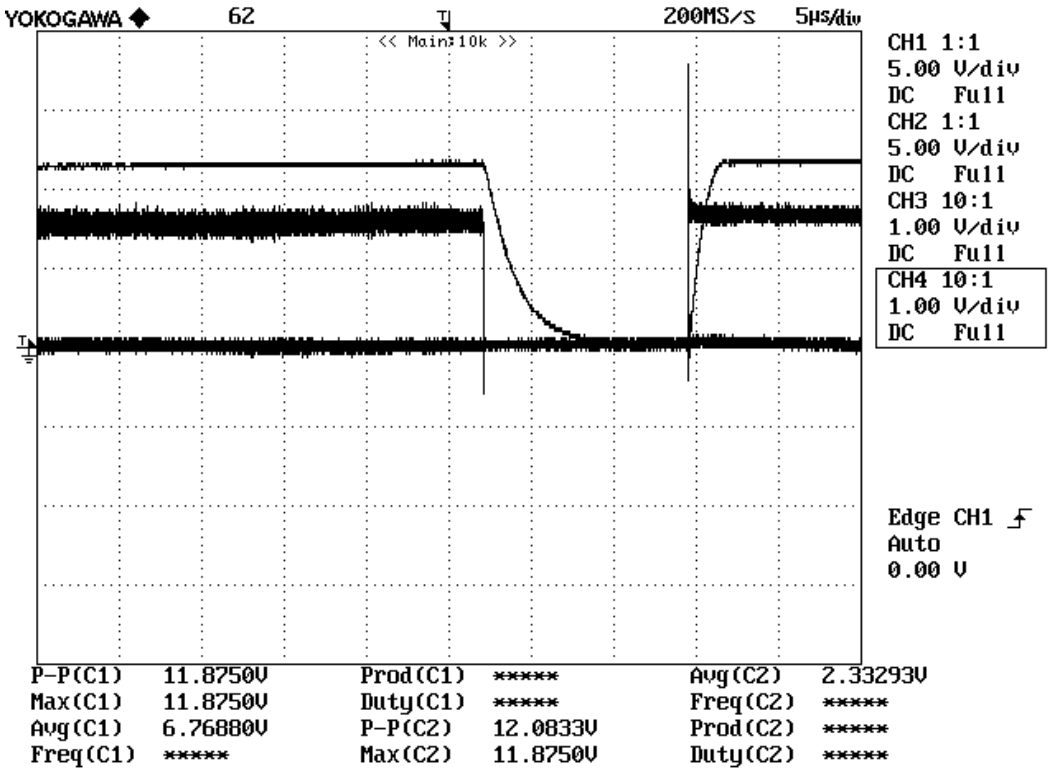

(c)

Figure 4.23 (a, b, c): 12 kHz output voltage pulses from secondary side of optocoupler 6N136.

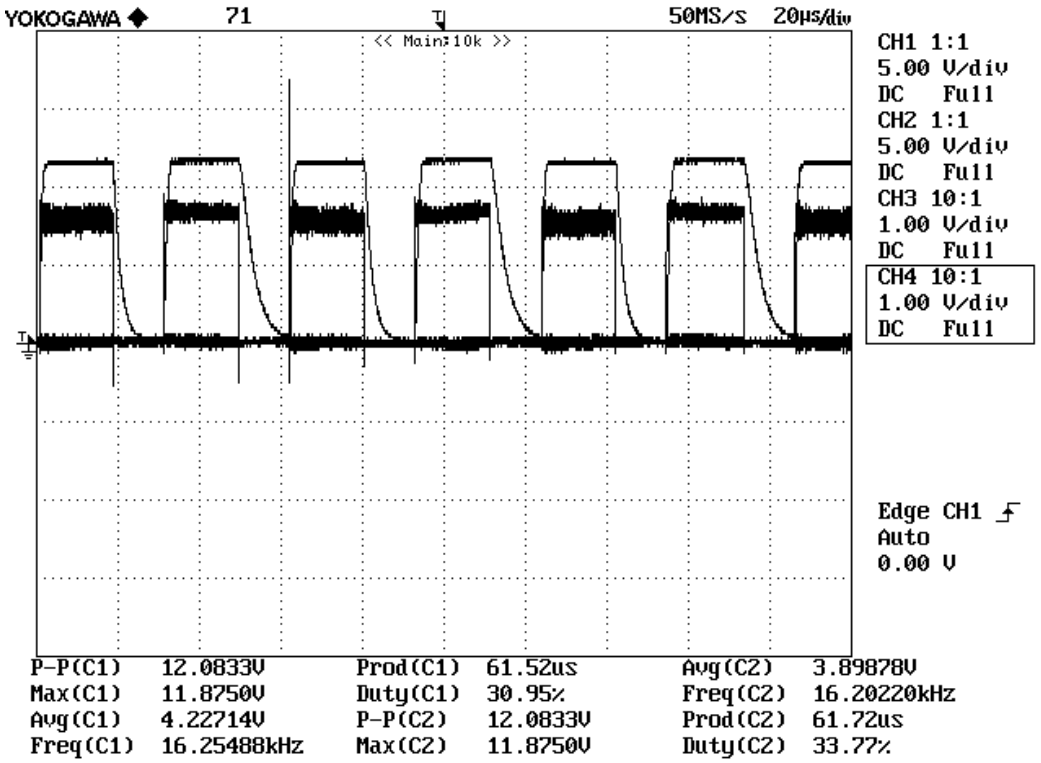
YOKOGAWA
71
50MS/s 20µs/div
<< Main:10k >>
CH1 1:1
5.00 V/div
DC Full
CH2 1:1
5.00 V/div
DC Full
CH3 10:1
1.00 V/div
DC Full
CH4 10:1
1.00 V/div
DC Full
Edge CH1
Auto
0.00 V
P-P(C1) 12.0833V
Max(C1) 11.8750V
Avg(C1) 4.22714V
Freq(C1) 16.25488kHz
Prod(C1) 61.52us
Duty(C1) 30.95%
P-P(C2) 12.0833V
Max(C2) 11.8750V
Avg(C2) 3.89878V
Freq(C2) 16.20220kHz
Prod(C2) 61.72us
Duty(C2) 33.77%

(a)

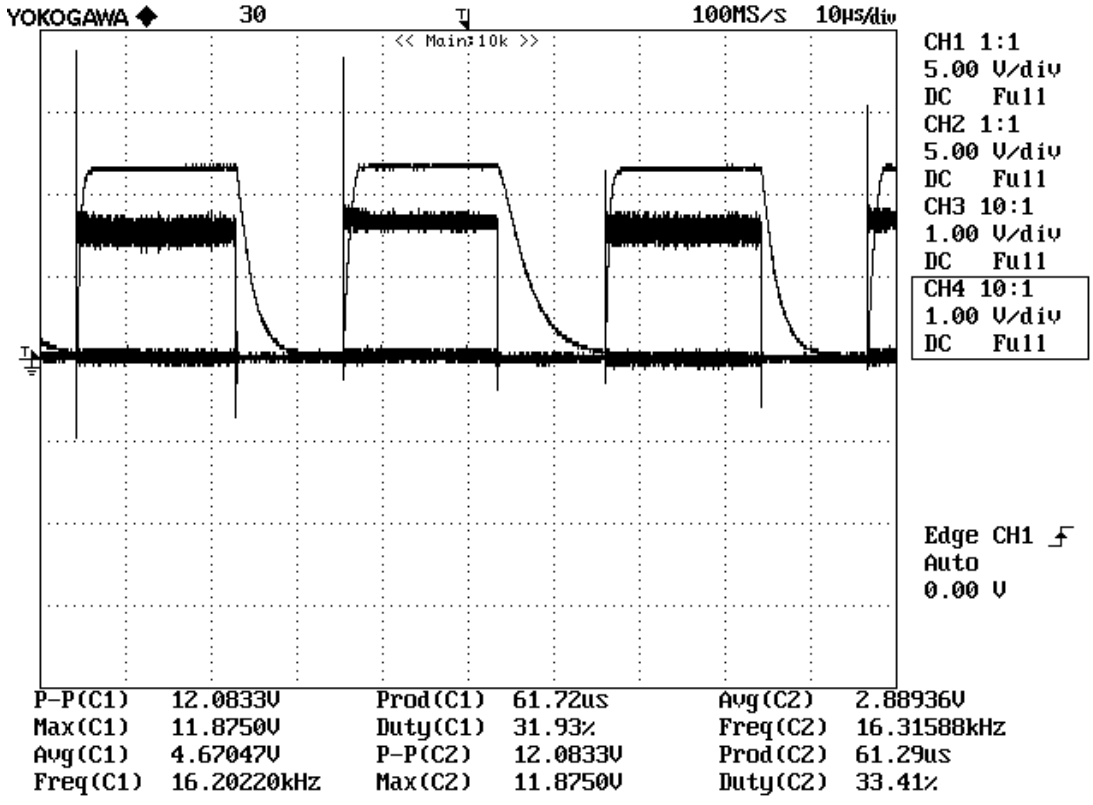
YOKOGAWA
30
100MS/s 10µs/div
<< Main:10k >>
CH1 1:1
5.00 V/div
DC Full
CH2 1:1
5.00 V/div
DC Full
CH3 10:1
1.00 V/div
DC Full
CH4 10:1
1.00 V/div
DC Full
Edge CH1
Auto
0.00 V
P-P(C1) 12.0833V
Max(C1) 11.8750V
Avg(C1) 4.67047V
Freq(C1) 16.20220kHz
Prod(C1) 61.72us
Duty(C1) 31.93%
P-P(C2) 12.0833V
Max(C2) 11.8750V
Avg(C2) 2.88936V
Freq(C2) 16.31588kHz
Prod(C2) 61.29us
Duty(C2) 33.41%

(b)

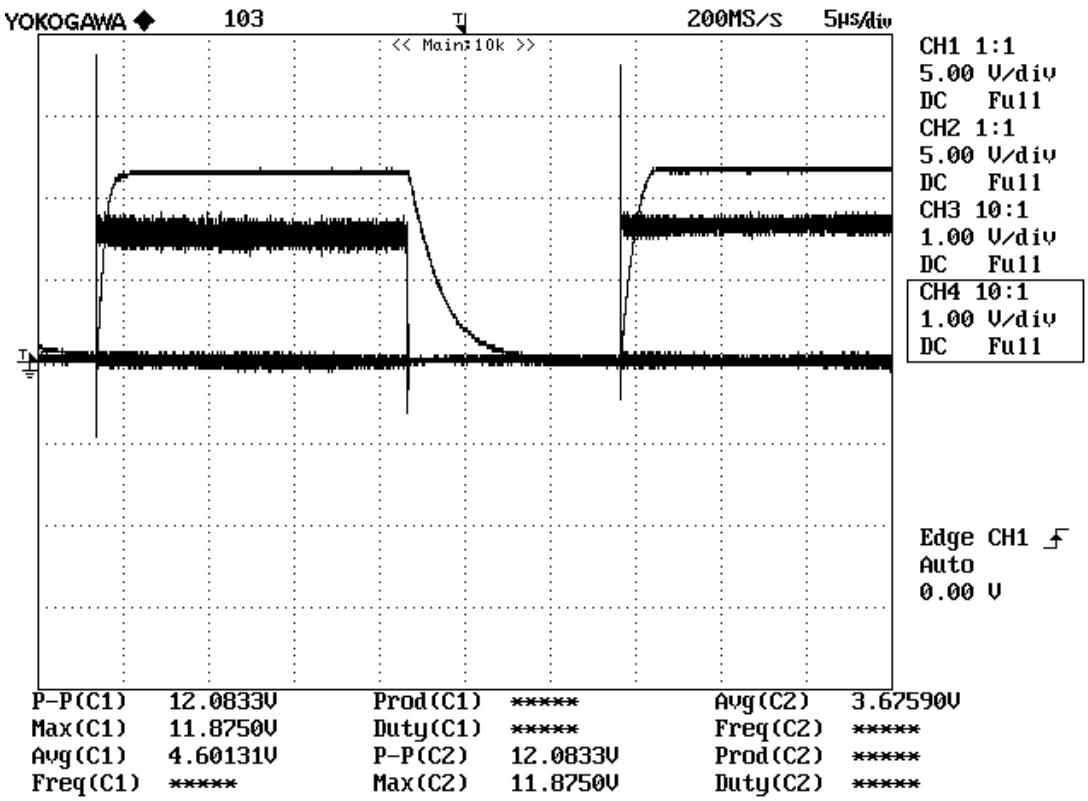

(c)

Figure 4.24 (a, b, c): 16.3 kHz output voltage pulses from secondary side of optocoupler 6N136.

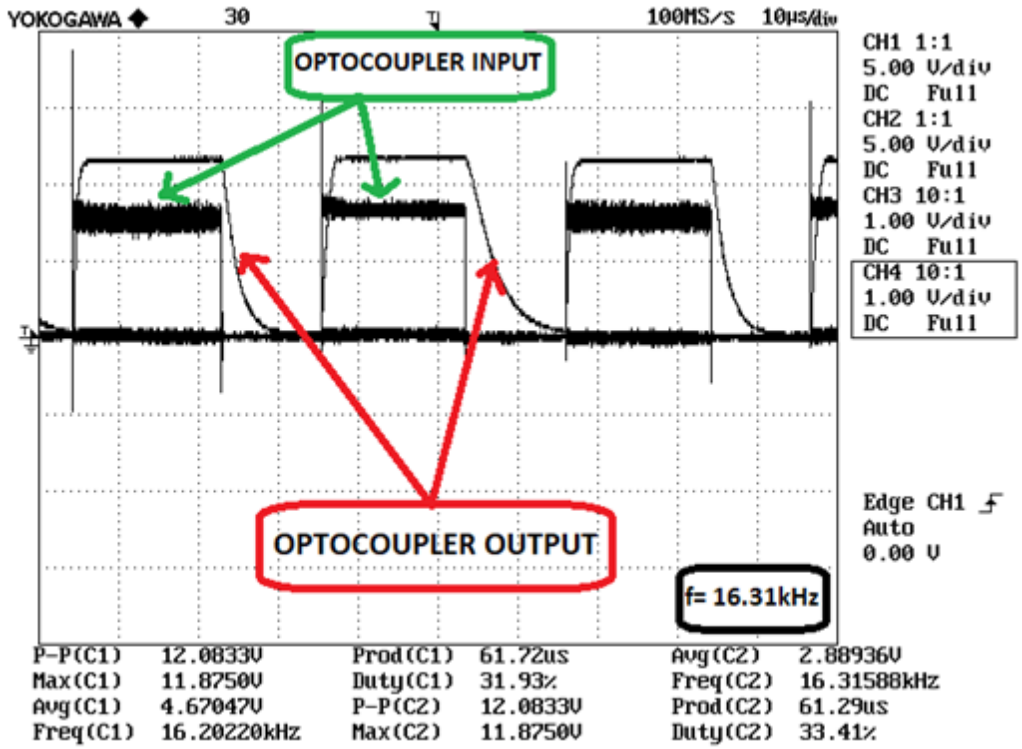

Figure 4.25: Delay pulse voltage from optocoupler output.

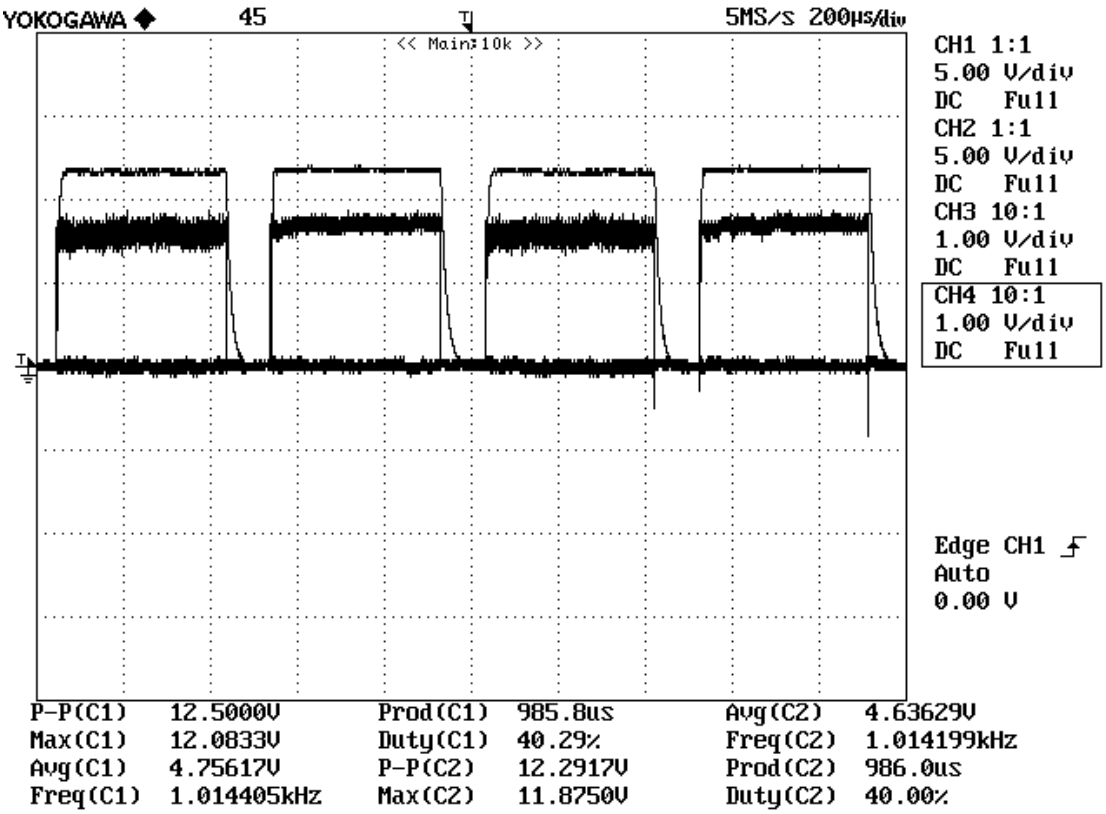

Figure 4.26: 1 kHz alternate pulse voltages across Gate-Source of MOSFET-inverter without applying drain voltage.

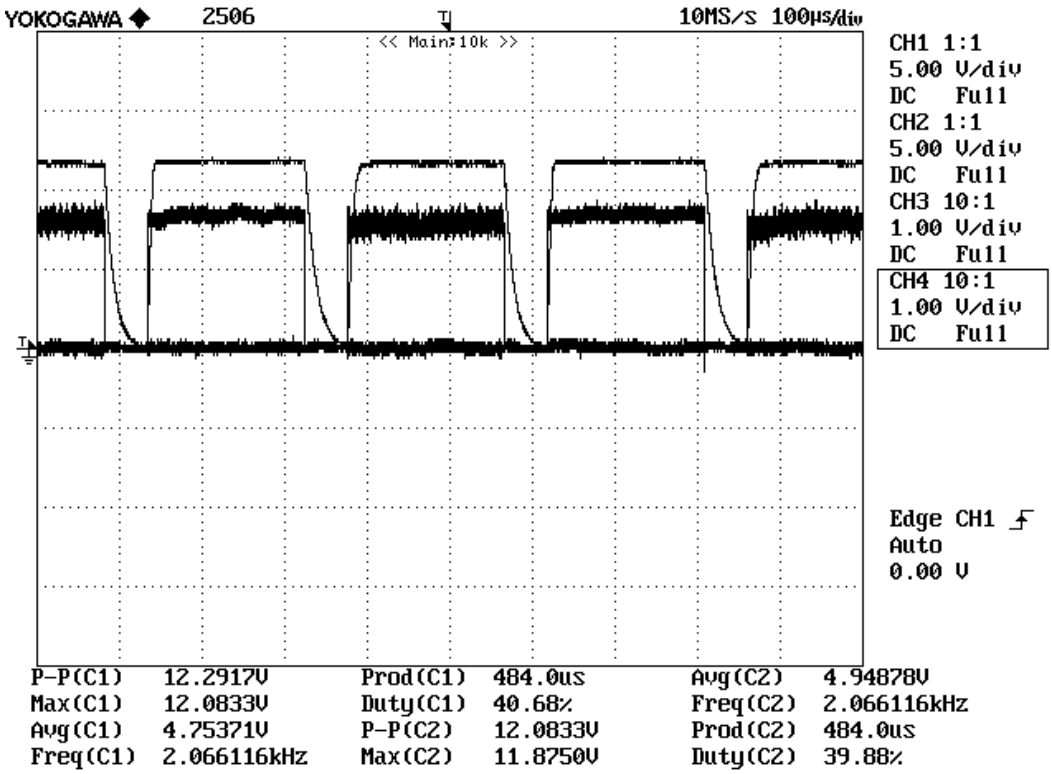

Figure 4.27:2 kHz alternate pulse voltages across Gate-Source of MOSFET-inverter without applying drain voltage.

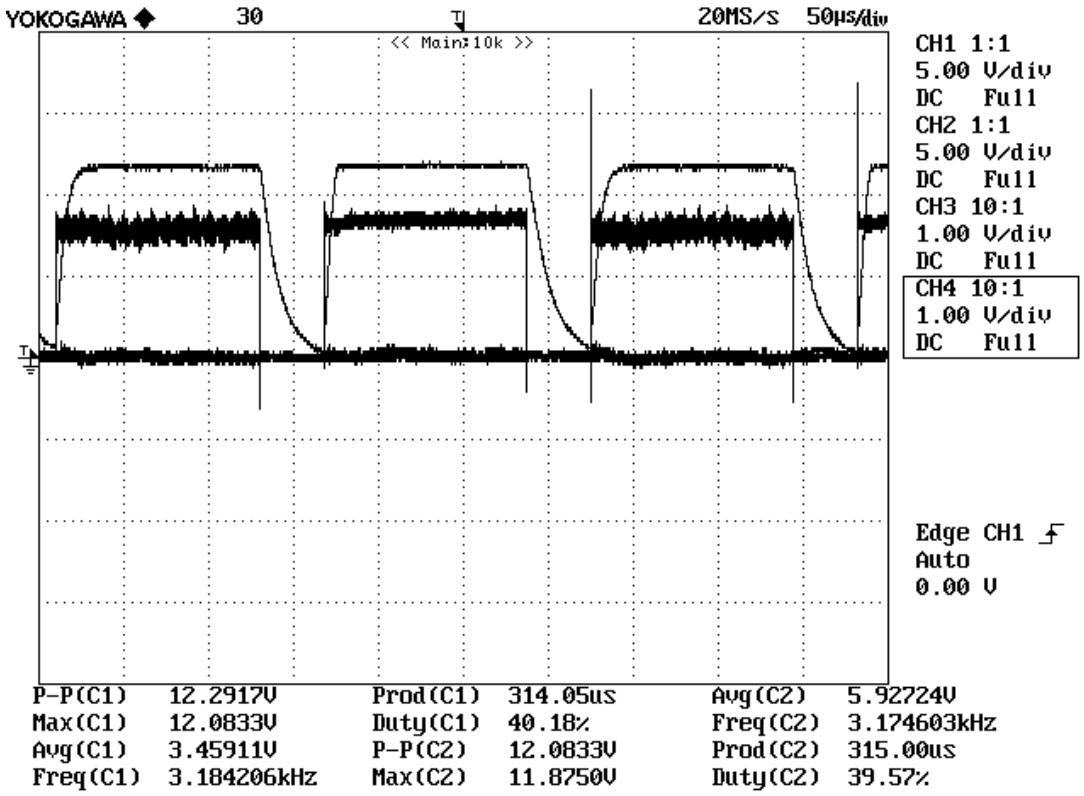

Figure 4.28: 3.17 kHz alternate pulse voltages across Gate-Source of MOSFET-inverter without applying drain voltage.

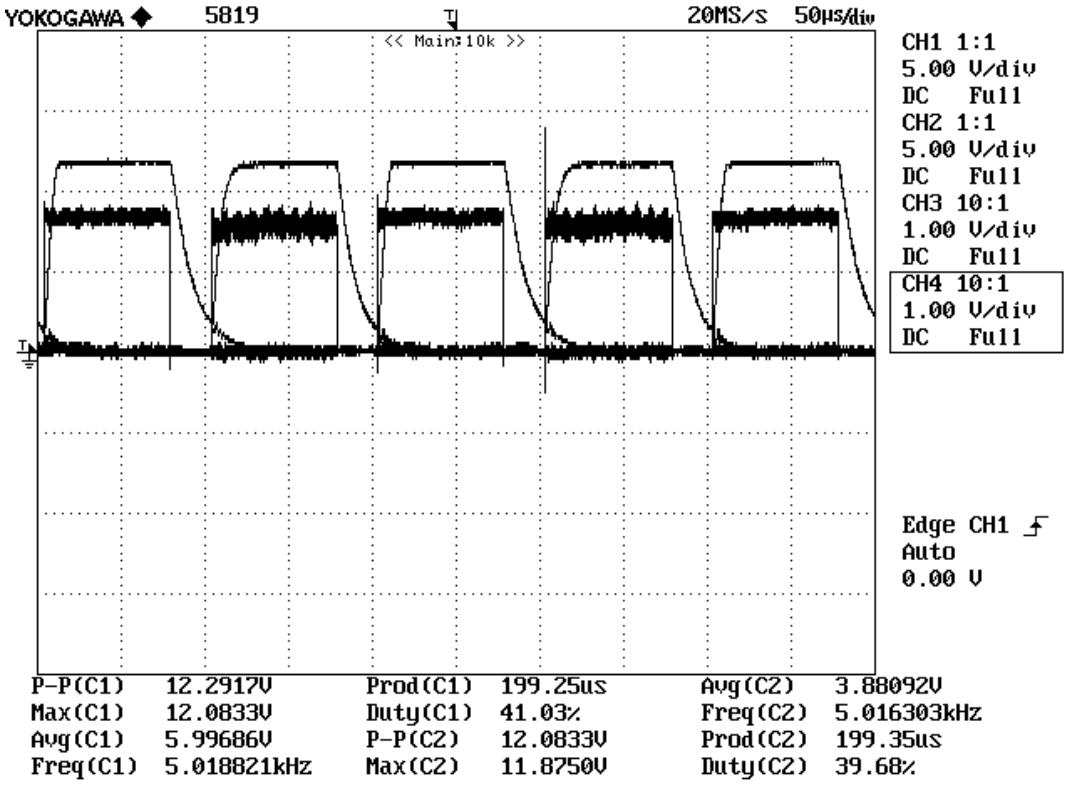

Figure 4.29:5 kHz alternate pulse voltages across Gate-Source of MOSFET-inverter without applying drain voltage.

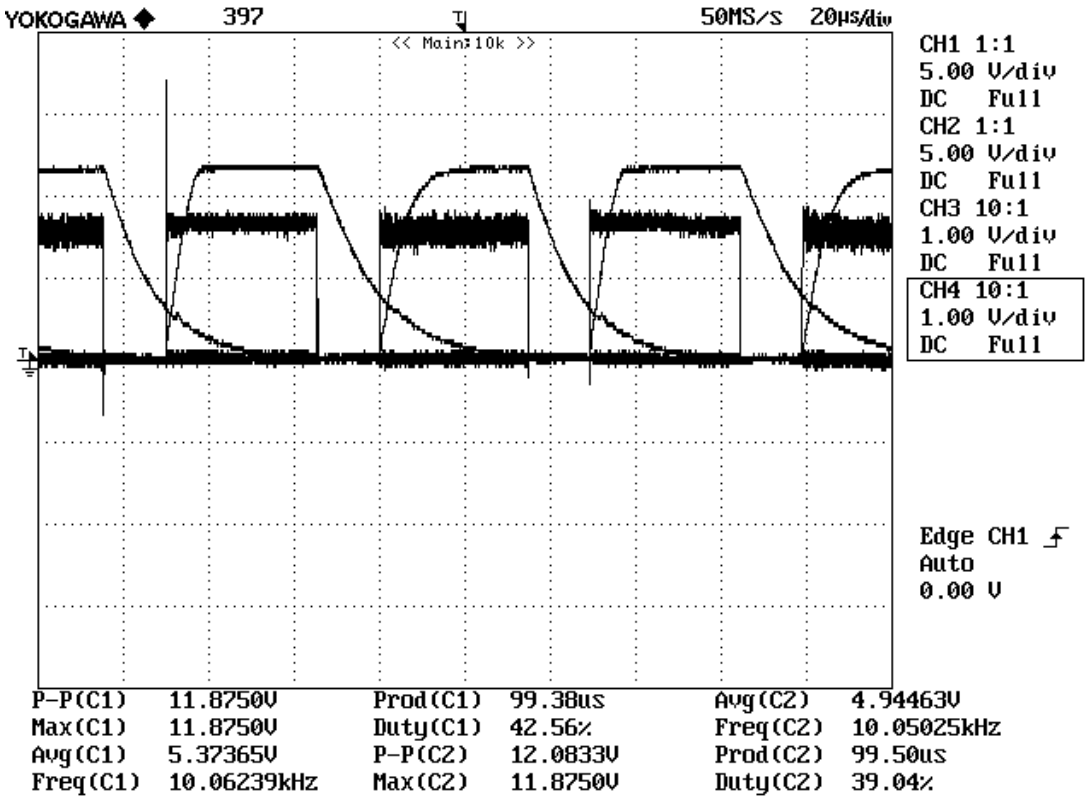

Figure 4.30: 10 kHz alternate pulse voltages across Gate-Source of MOSFET-inverter without applying drain voltage.

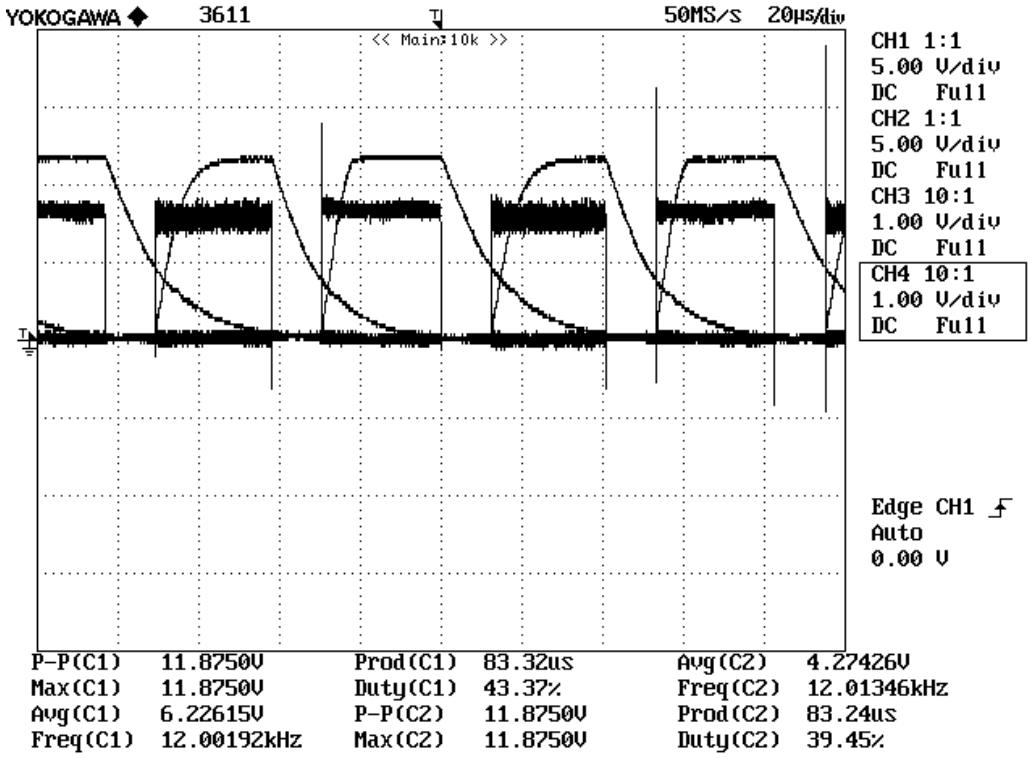

Figure 4.31: 12 kHz alternate pulse voltages across Gate-source of MOSFET-inverter without applying drain voltage.

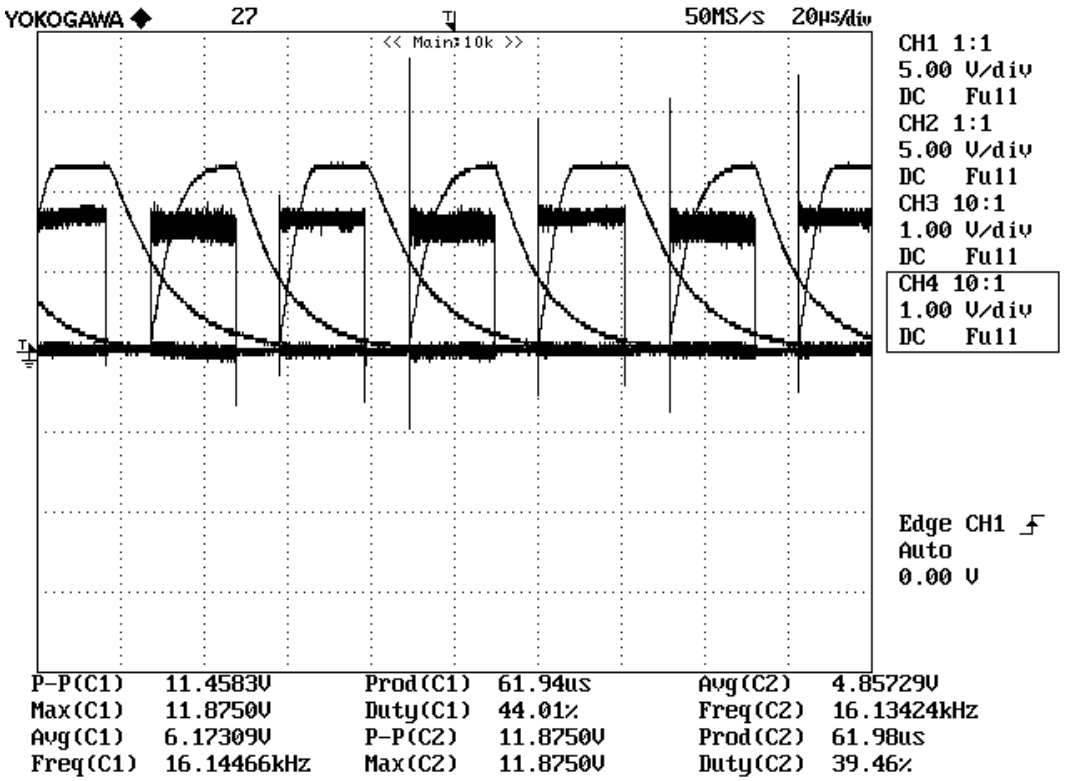

Figure 4.32: 16.1 kHz alternate pulse voltages across Gate-Source of MOSFET-inverter without applying drain voltage.

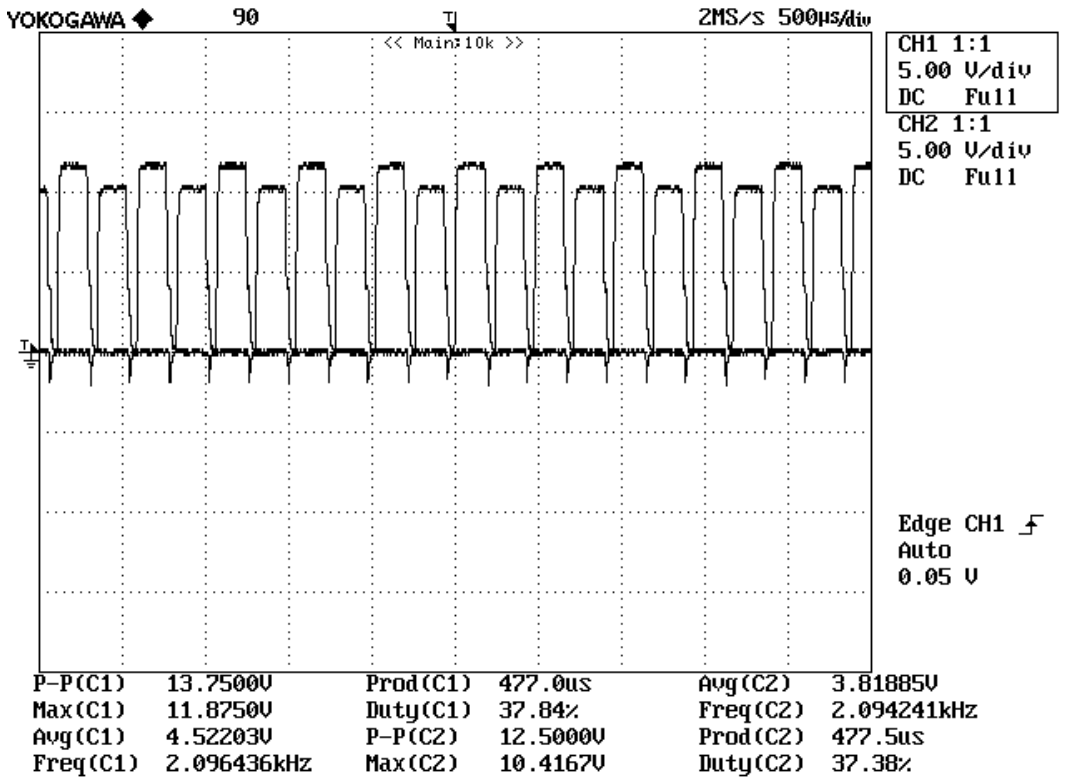

(a)

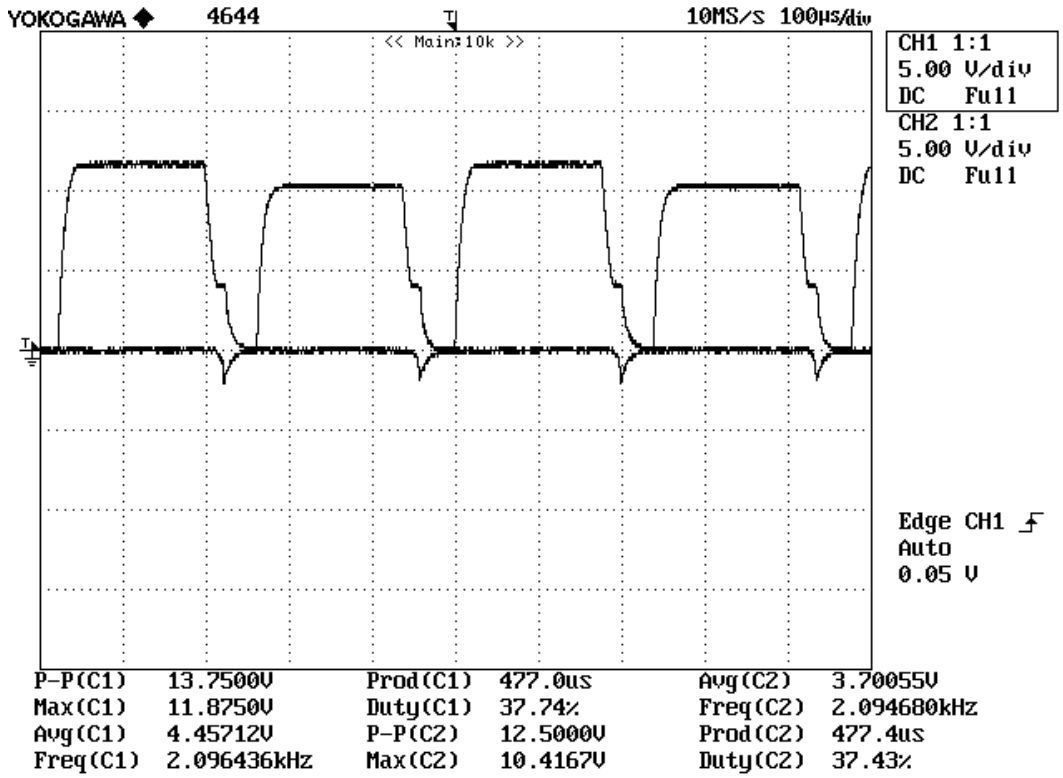

(b)

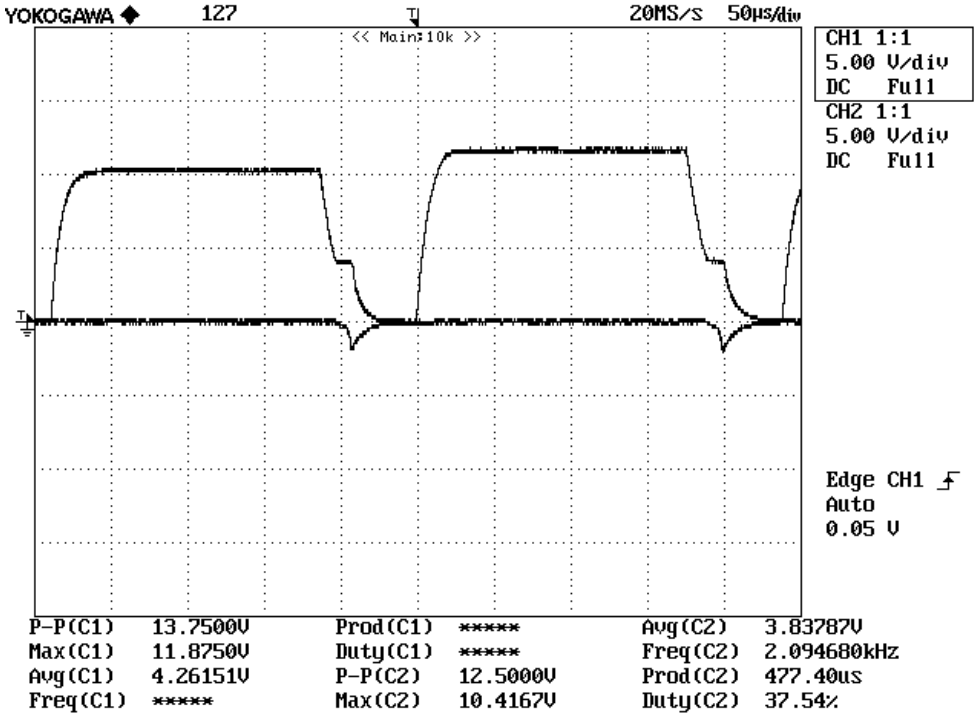

(c)

Figure 4.33 (a, b, c): Driver output pulse voltages across Gate-Source while MOSFETs are conducting (On) in inverter operation at 2 kHz.

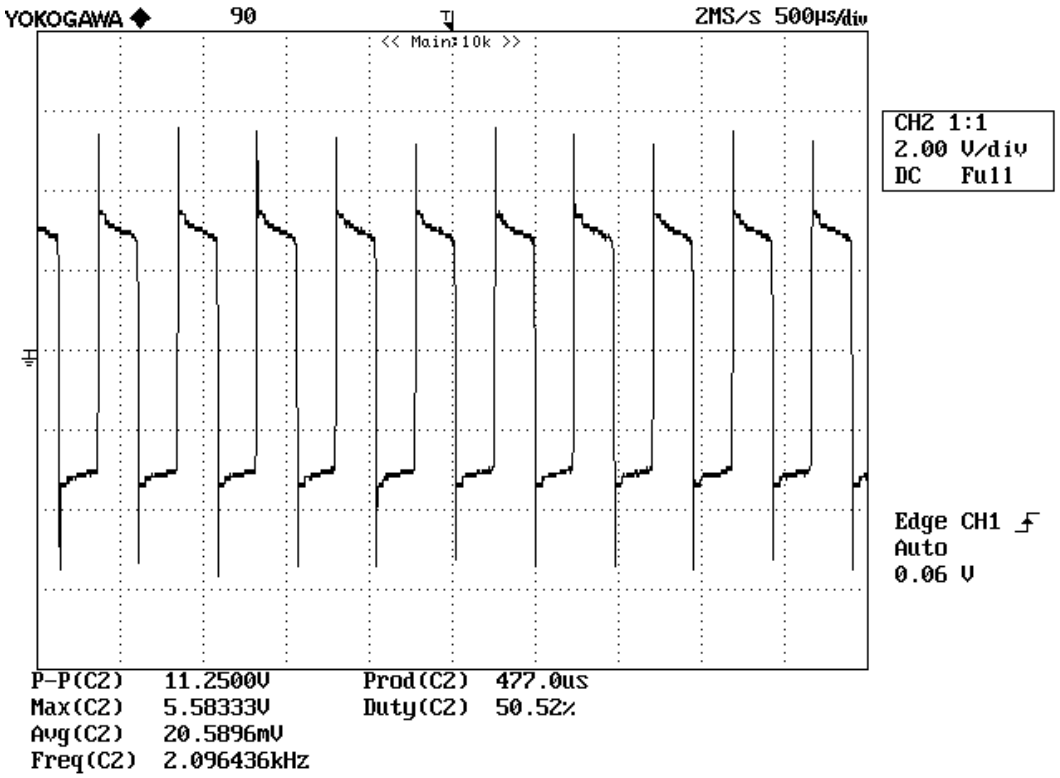
YOKOGAWA
90
2MS/s 500µs/div
<< Main:10k >>
CH2 1:1
2.00 V/div
DC Full
Edge CH1
Auto
0.06 V
P-P(C2) 11.2500V
Max(C2) 5.58333V
Avg(C2) 20.5896mV
Freq(C2) 2.096436kHz
Prod(C2) 477.0us
Duty(C2) 50.52%

(a)

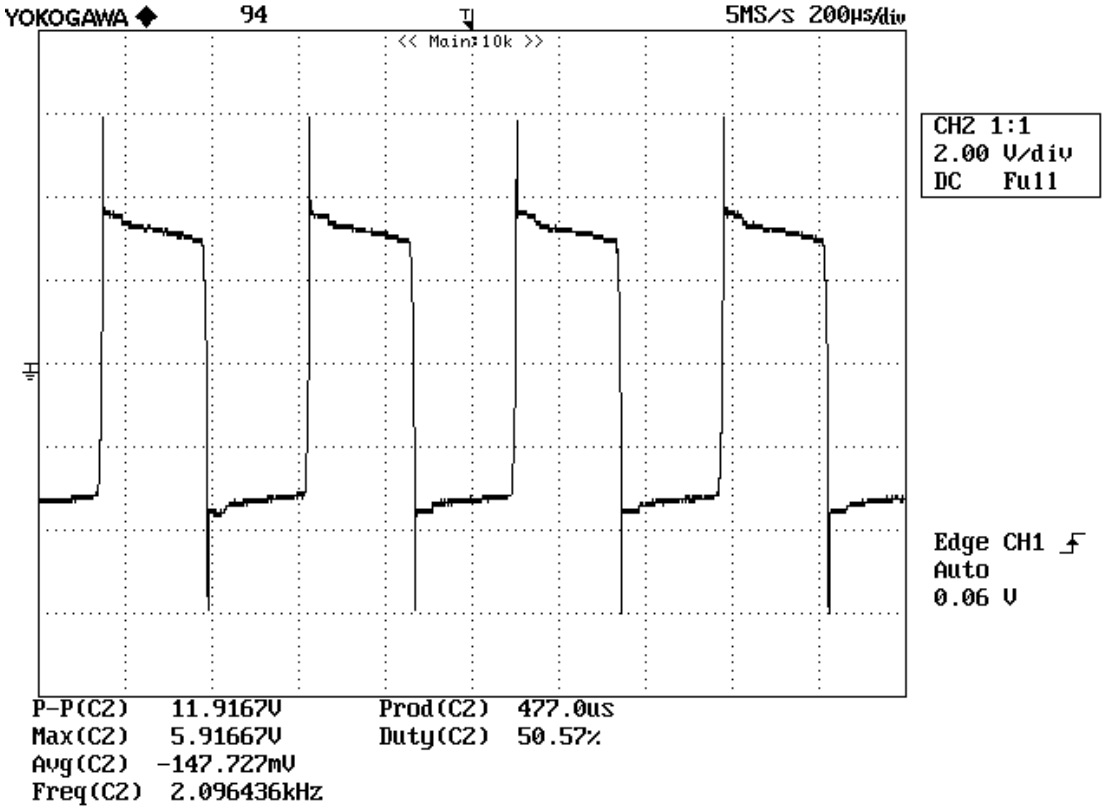
YOKOGAWA
94
5MS/s 200µs/div
<< Main:10k >>
CH2 1:1
2.00 V/div
DC Full
Edge CH1
Auto
0.06 V
P-P(C2) 11.9167V
Max(C2) 5.91667V
Avg(C2) -147.727mV
Freq(C2) 2.096436kHz
Prod(C2) 477.0us
Duty(C2) 50.57%

(b)

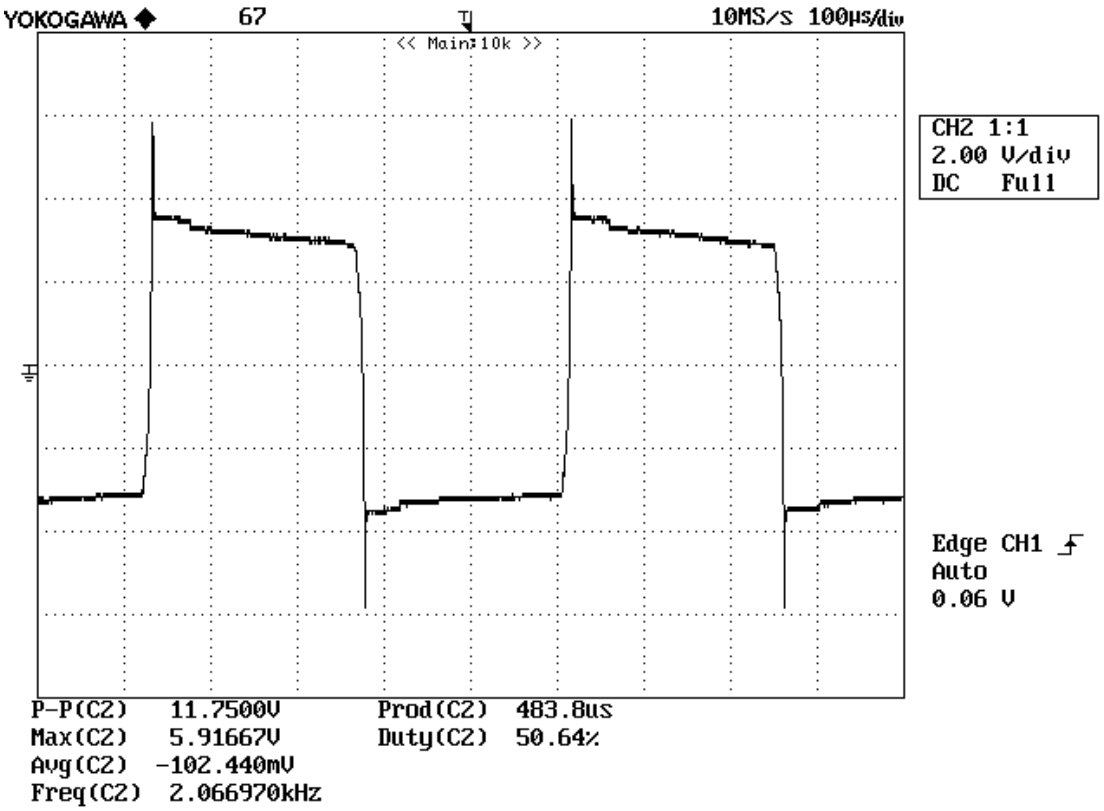

(c)

Figure 4.34 (a, b, c): Inverter output voltage for 2 kHz frequency at no load condition.

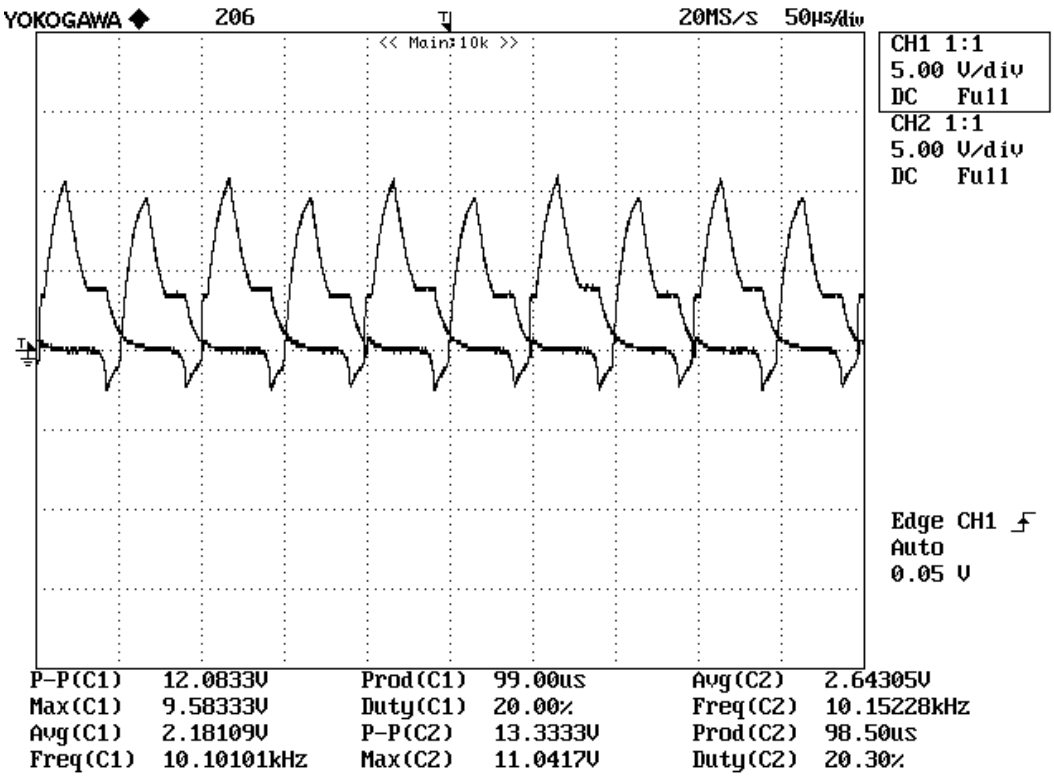

(a)

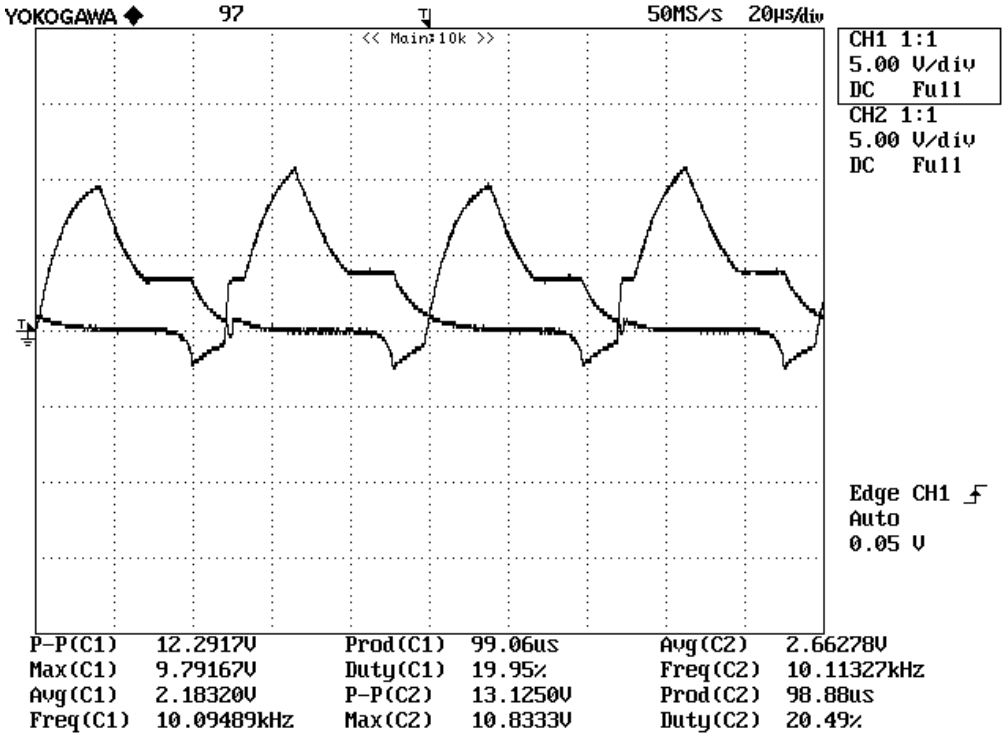

(b)

Figure 4.35 (a, b): Driver output pulse voltages across Gate-Source while MOSFETs are conducting (On) in inverter operation at 10.11 kHz.

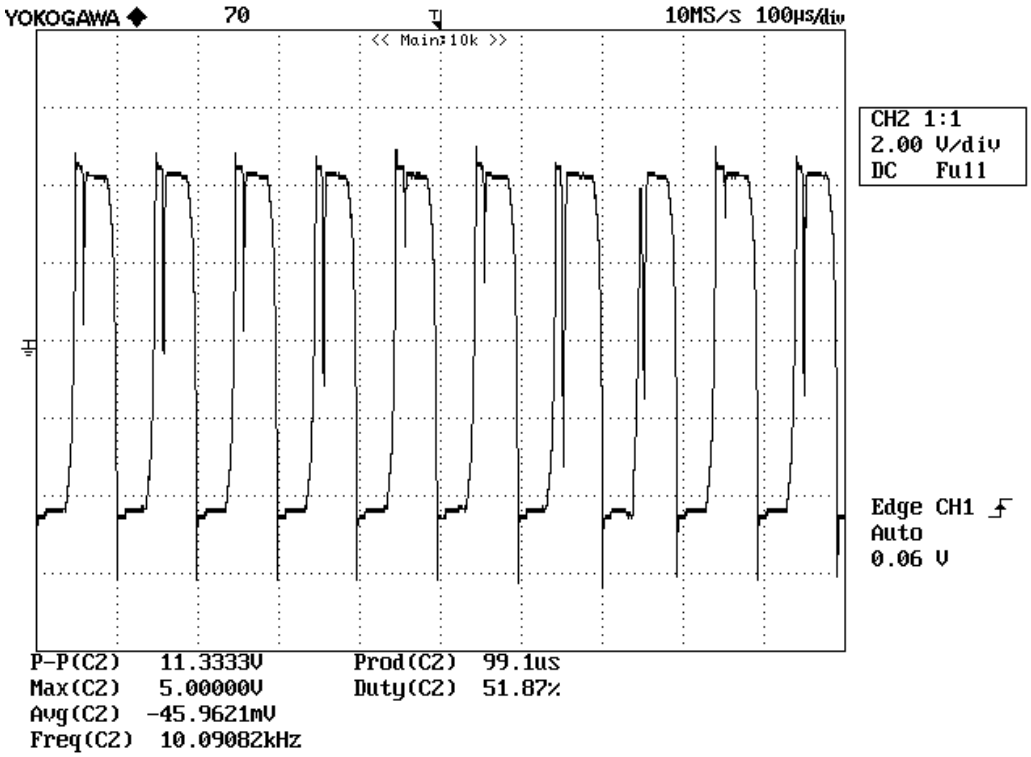

(a)

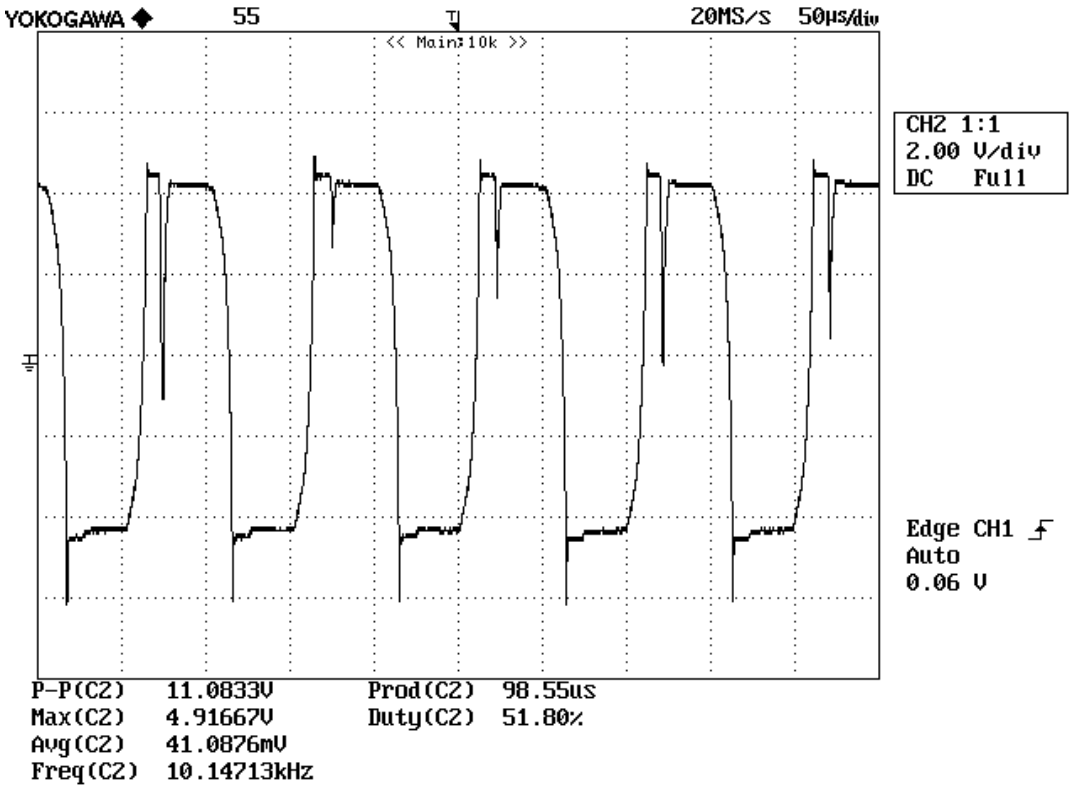

(b)

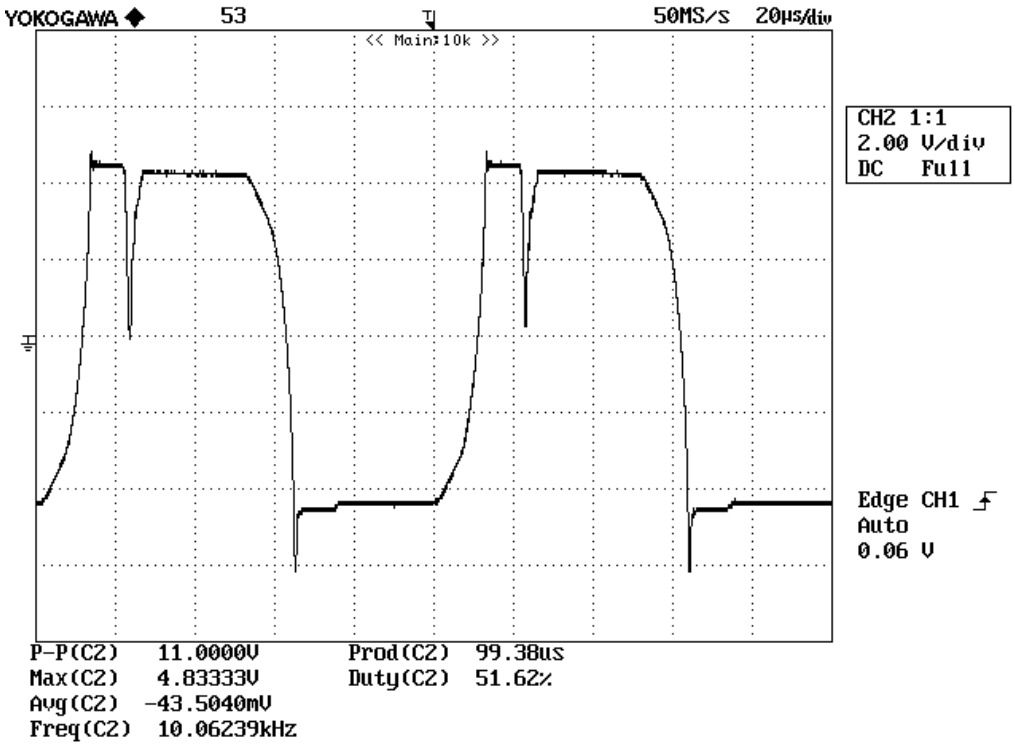

(c)

Figure 4.36 (a, b, c): Inverter output voltage for 10 kHz frequency at no load condition.

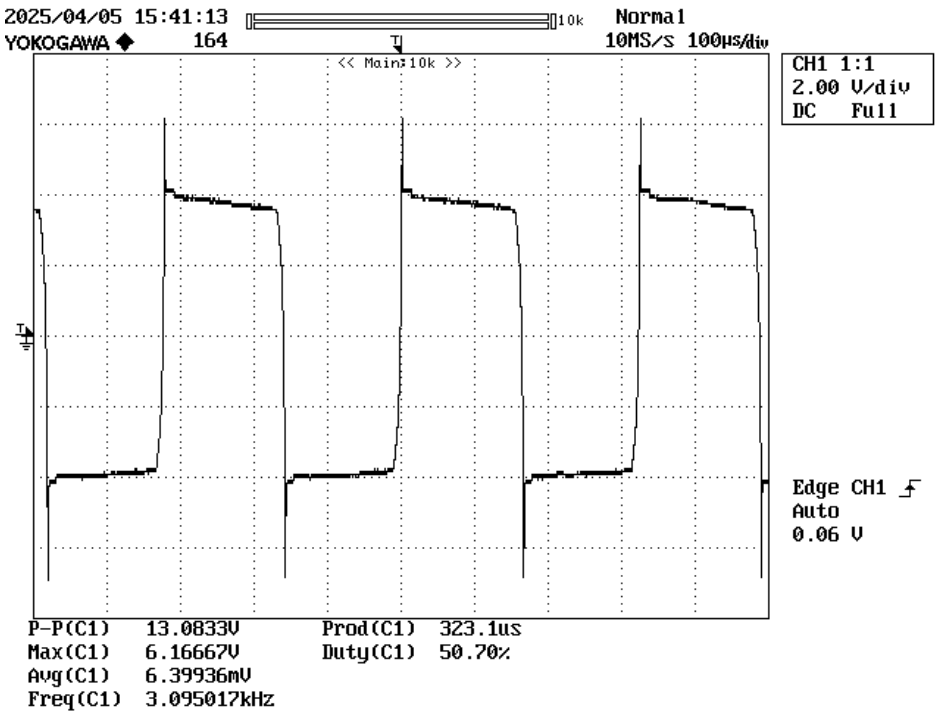

Figure 4.37: Inverter output voltage in loaded condition at 3 kHz.

4.4.1 Microcontroller based inverter output voltage in loaded condition at 10.40 kHz

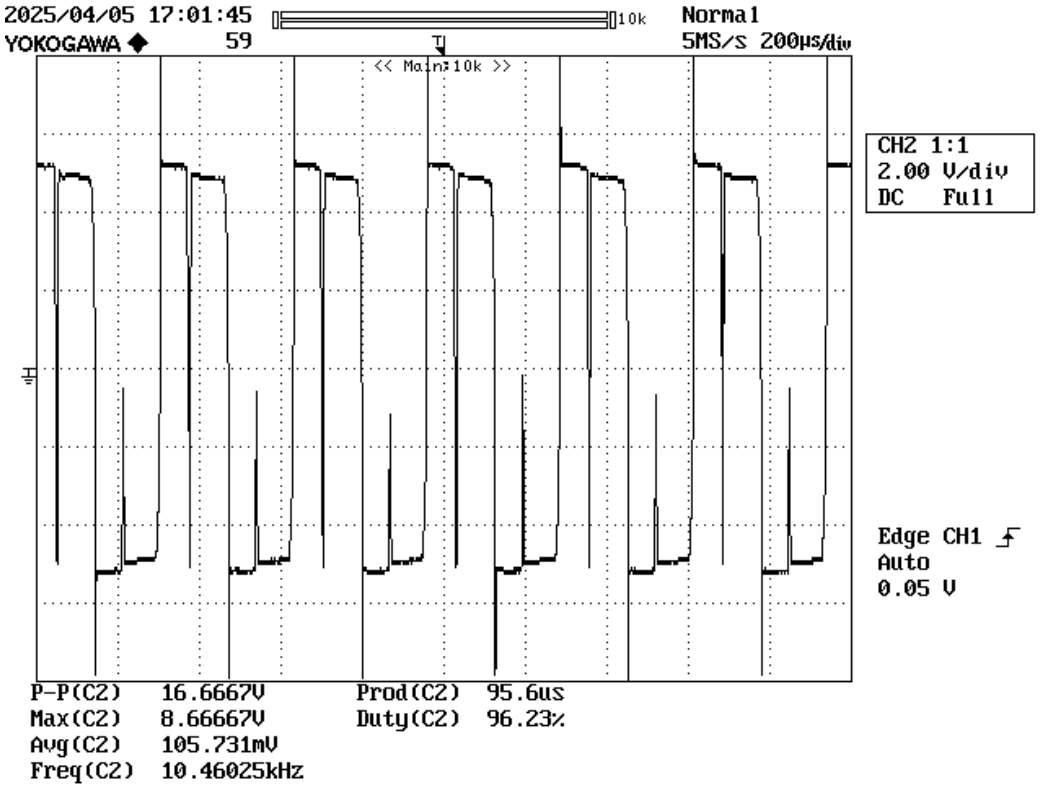

Figure 4.38: Inverter output voltage in loaded condition at 10.40 kHz.

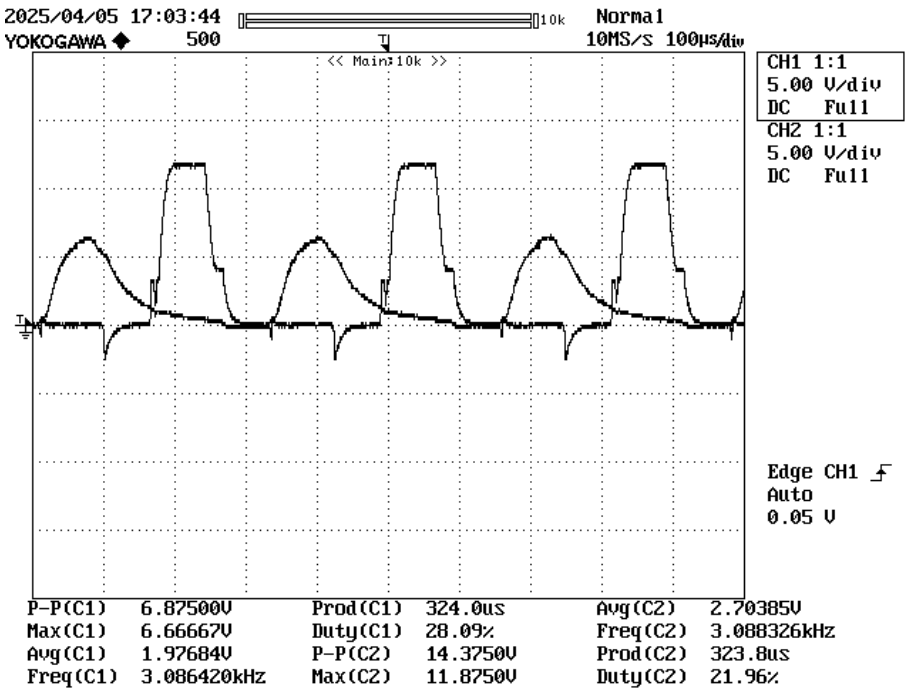

Figure 4.39: Driver output pulse voltages across Gate-Source while MOSFETs are not in proper function.

MOSFETs (IRFP460) are used as a switching device in the above mentioned inverter circuit due to its higher rating. All the experimental results and performance analysis has been investigated, different voltage wave shapes are captured using DSO as well. It has been seen that this inverter operates satisfactorily during loading condition in lower frequency (up to 10 kHz) where tungsten filament lamp consider as load. Related output wave shape of the voltages across load is shown in Fig 4.37 and 4.38. The MOSFETs tend to fail when the inverter is operated above 10 kHz under load conditions. The relevant gate-to-source voltage is shown in Fig 4.39, where it is evident that one of the MOSFETs has been damaged, this might have happened due to the delay function of the optocoupler. Hence, further study is required on this issue; this can be our future scope of work.

4.5 Summary

This chapter presents the design and implementation of a microcontroller based inverter using Arduino Uno, following a structured simulation-first approach before physical realization. The software simulation stage allows for early debugging and optimization, reducing hardware design errors. The final inverter prototype efficiently and reliably converts DC power into a stable AC output, operating effectively up to 10 kHz. Although the original target was to achieve very high-frequency operation, this remains a subject for future work.

Chapter-5

EXPERIMENTAL INVESTIGATIONS ON ACTIVATION ENERGIES AND ELECTRICAL CONDUCTIVITY IN VARIOUS FRUIT JUICES-LIQUIDS

5.1 Introduction

Foods carry electricity, especially liquid foods, and the charge carriers in food are ions rather than electrons as in metals. In most applications, the charges are carried by the ions as their mass travels along the electrical field. The electrical conductivity is determined by the ion concentration and mobility. Food ingredients and temperature do have an impact on ion mobility. Ions or molecules can hop electrons when exposed to strong electric fields. During processing of liquid food using ohmic heating, microwave heating, induction heating or pulsed electric fields, study of electrical characteristics are crucial. These characteristics can also be used to detect manufacturing conditions or assess food quality. When preparing food using ohmic heating, electrical conductivity can be utilized to track significant changes in the product [69]-[75]. The electrical conductivities of a few chosen liquids and fruit juices—apple, orange, and sugar cane were measured while they were being heated. A wide range of processing temperatures, from 20 to 50°C, was used to measure the various characteristic of different food samples reported here. All products have shown a linear rise in electrical conductivity as the temperature rises. Change in electrical conductance (G_S) is also studied with supply frequency at room temperature (20°C) and finally drawn and explain ac conductivity (σ_{ac}) variation with respect to angular frequency (ω). The electrical conductivity of the fruit juices like green coconut water, sugar cane juice, orange juices etc vary depending on the salt content in them [76], [77]. These juices basically having the salt in them show a finite conductivity and thereby a resistivity which is inverse of this conductivity. When current (I) passes through them, for a volume of liquid I^2R loss is present in the solution and its temperature rises, where R is resistance of food sample. Depending on the frequencies involved, there are two distinct ways to design ohmic heaters from the electrical perspective. They can be categorized as either high frequency or low frequency ohmic heaters based on this categorization. Literature survey reveals that high frequency operation is more effective than lower frequency ac supply for ohmic heating process of various liquid food materials as discussed earlier; during this processes high frequency ac reduces electrode corrosion [78],

[79]. Therefore it is necessary to study the variation of electrical conductivity or other parameters of the food material with frequency of any liquid food sample before going to develop the high frequency ohmic heater [80]-[82]. Hence considering various food sample composition like 0.1% KCl, 1% & 2% NaCl solution with distilled water, Coconut water, Sugar Cane Juice, Orange Juice etc; experimental analysis has been done that how the electrical parameters varies with the supply frequency. The electrical conductivity of liquid food materials changes with temperature due to the movement of ions within the liquid [83]-[86]. Higher temperature causes the ions in the liquid to move more freely, which raises the electrical conductivity. This is commonly observed in fruit juices, milk, honey solutions, and other liquid foods. Higher temperatures enhance the dissociation of salts, sugars, and acids, which increases the number of free ions in the liquid. Simultaneously, the viscosity of the liquid decreases, reducing resistance to ion movement, further boosting conductivity. Hence, this study was also conducted at different temperatures, and the activation energy responsible for ion movement was determined from the data of various materials. These findings, along with a comparative analysis, are reported in this chapter.

5.2 Materials and methods

Electrical characteristics are crucial when processing food using microwave, induction, and ohmic heating, among other methods [87]-[89]. These characteristics can also be used to detect manufacturing conditions or assess food quality. Researcher has just recently become interested in the electrical conductivity of liquid food, where liquid sample consider as parallel Resistance (R)-Capacitance (C) circuit. Information on food electrical conductivity is needed because of the recent focus on electrical resistance heating/ohmic heating used in pasteurization. An important factor in ohmic heating processes is electrical conductivity. Process design requires knowledge of a food's electrical conductivity under conditions of ohmic heating. Apart from temperature, ionic content, moisture mobility, physical structure, and heating procedure all have a significant impact on food's electrical conductivity. The electrical conductivity variations of liquid food material during conventional and Ohmic heating have been investigated by some researchers. When electrically treating items, higher temperature increases coincide with increased electrical conductivity. Measurements of a few basic characteristics at different temperatures are used to identify the electrical properties of liquid samples [90]. In order to analyze the DC conductivity (σ_{dc}) of the samples, their resistance is measured. For the investigation of AC conductivity and dielectric properties,

measurements are made of the capacitance (C_P) of liquid, electrical conductance (G_S), and dielectric loss angle (tan δ). To study complex impedance, the resistance (R_S), reactance (X), and impedance (Z) of liquid are measured. Various samples (KCl & NaCl) in different percentage were prepared using laboratory weighing scale machine shown in Fig 5.1 to make different solution with distilled water. Varying the concentration of different sample has been made to create different electrical conductivity. A digital conductivity meter with a conductivity cell having cell constant K=1 has been used to measure electrical conductivity shown in Fig 5.2. Electrical conductivity can be measured using conductivity or LCR meter. In this work electrical conductance of various liquid food samples were tested using experimental setup shown in Fig 5.3 from lower to higher frequencies. Via the conductivity cell, the sample is linked to an LCR meter bridge (Hioki-Model No. 3532-50). Here, a GPIB card is used to interface the LCR meter bridge with a personal computer (PC). Thus, a computer can be used to operate the LCR meter bridge. Capacitance and conductance measurements can be made in relation to the frequency of the liquid composition samples. The frequency range in which the measurements of various electrical parameters are done is 400Hz–140 kHz. This work was carried out at the Composite Materials Research Laboratory, UGC-MMTTC (Physics), University of North Bengal, West Bengal, India.

The relationship between dc electrical conductivity (σ) and temperature (T) of a liquid conductor can vary depending on the specific properties of the liquid. For many liquid conductors, particularly electrolytes, the relationship between conductivity and temperature can be described by an empirical equation known as the Arrhenius equation describes below:

$$\sigma = \sigma_0 . e^{-Ea/KT} \quad (5.1)$$

Where,

σ = Electrical conductivity

σ_0 = Pre-exponential factor

Ea = Activation energy

K = Universal gas constant, and

T = Absolute temperature (in Kelvin)

Activation energy (Ea) for conduction is a concept often used in physics and materials science, particularly in the context of electrical conductivity. It represents the minimum energy required for charge carriers (such as electrons or ions) to overcome barriers and move

through a material, thereby contributing to its conductivity. In the context of dc electrical conductivity, activation energy is typically associated with the mobility of charge carriers within a material. When an electric field is applied, charge carriers experience collisions with lattice defects, impurities, or other obstacles in the material. To move from one location to another, charge carriers must overcome these barriers, and the energy required to do so is the activation energy. The activation energy governs the temperature dependence of the conductivity. Higher activation energy implies that charge carriers require more energy to move through the material. This is an important parameter that influences the electrical properties and behavior of materials, and it is often determined experimentally through techniques such as conductivity measurements and temperature-dependent studies.

The Arrhenius equation is a simplified model and assumes that temperature affects the rate of reaction or conductivity through a single activation energy term. While this equation provides valuable insights into the temperature dependence of various processes, it may not fully capture the complexities of all systems. However, it serves as a foundational concept in understanding temperature-dependent phenomena in materials science. Here various material samples are heated at different temperatures from 20-48°C into the furnace chamber and measure electrical conductivity using digital conductivity meter at different temperature shown in Fig 5.4. It is reported that conductivity of different composition increases with temperature for all the composition (0.1% KCl, 1% & 2% NaCl solution with distilled water, Coconut water, Orange Juice, Sugar Cane Juice). The activation energy can be estimated by examining the temperature-dependent variations in conductivity, which provides insight into how the composition of the liquid affects ionic mobility.

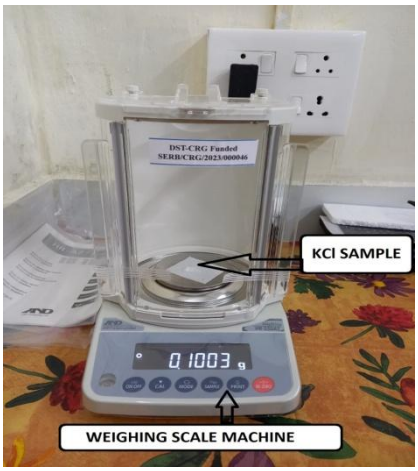

Figure 5.1: Weighing scale machine.

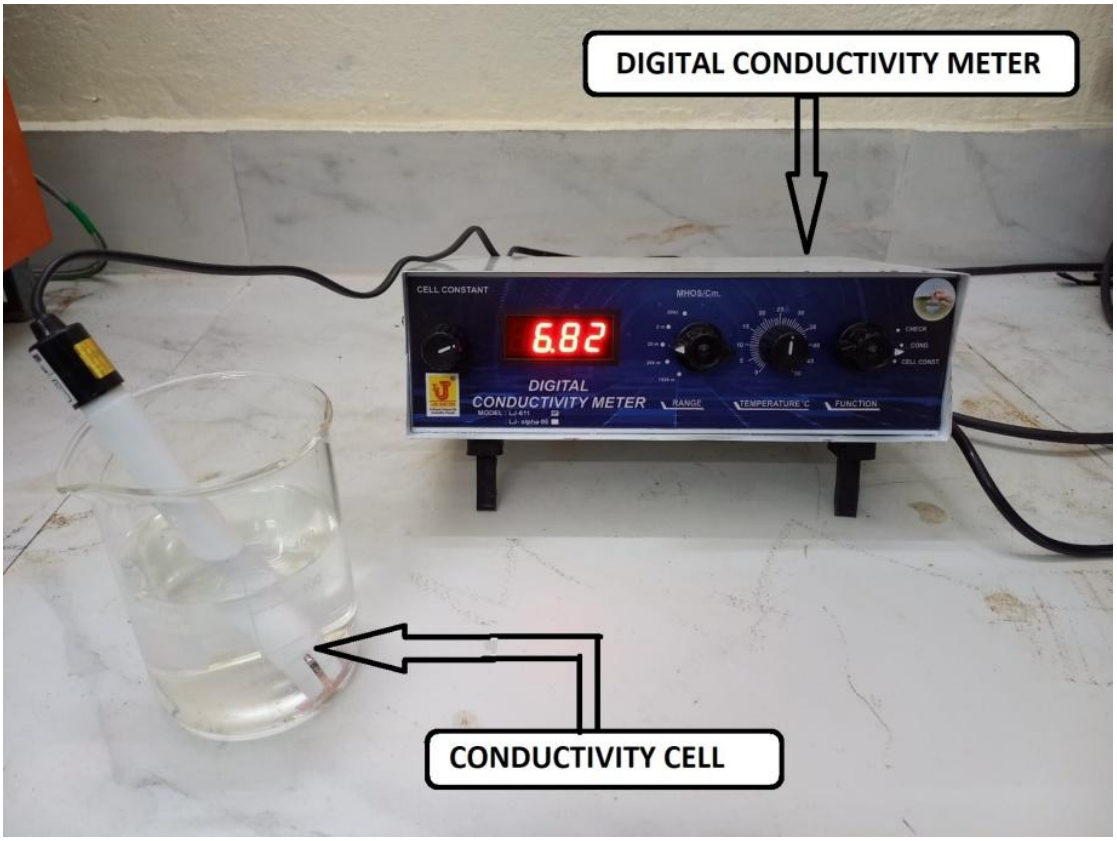

Figure 5.2: Digital conductivity meter.

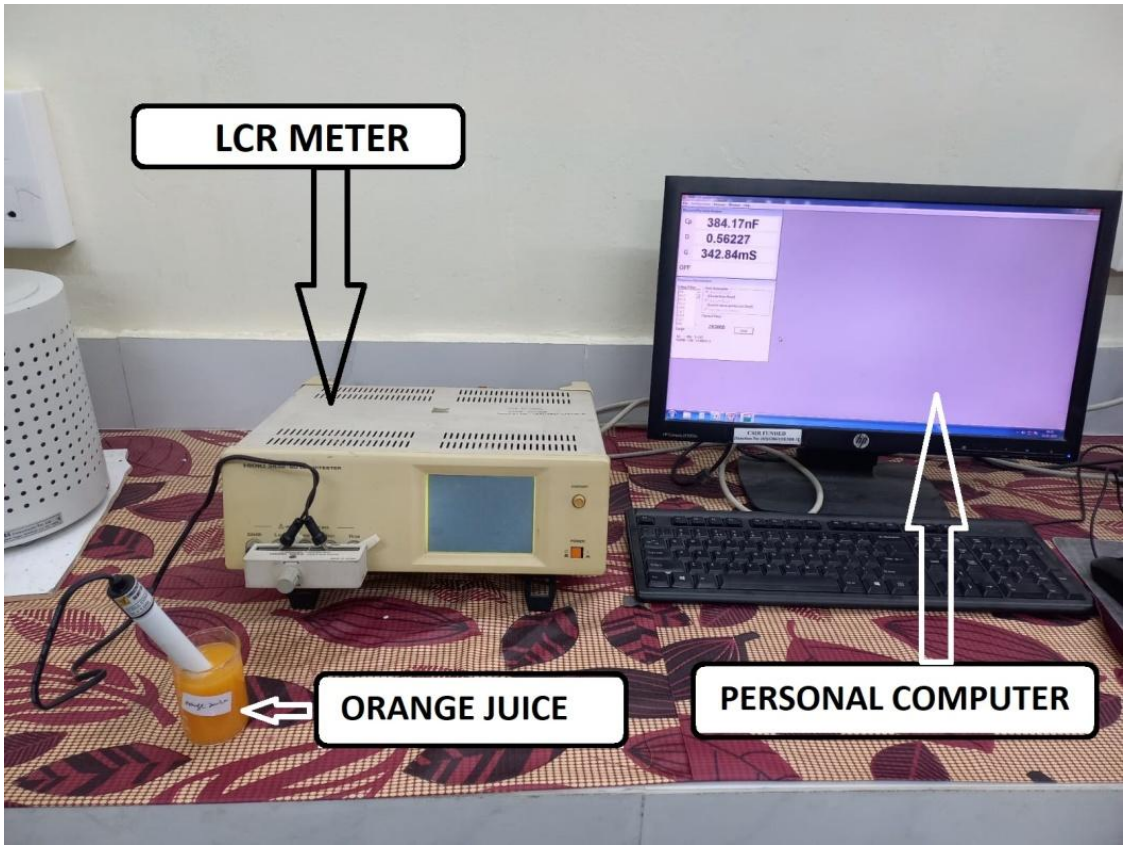

Figure 5.3: LCR Meter bridge with experimental setup.

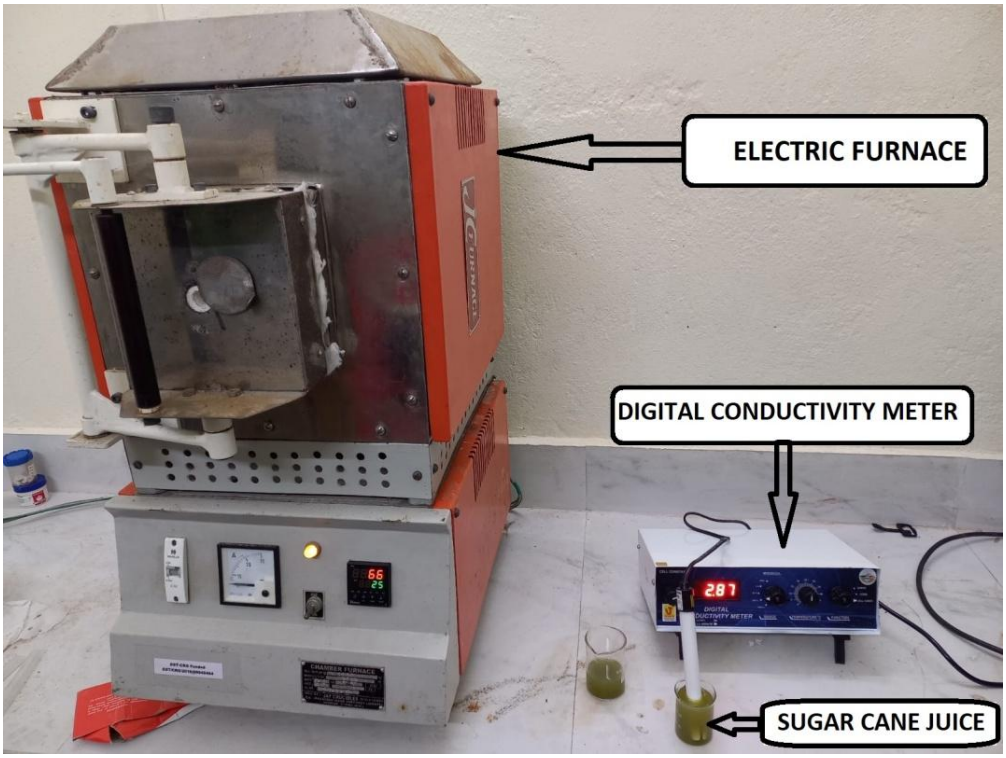

Figure 5.4: Furnace chamber and digital conductivity meter.

5.3 Results and discussion

DC conductivity measurement was done using digital conductivity meter at different temperature (20-48°C) for different composition reported here. The relation $\sigma_{dc} = (1/R)*(t/A)$ can be used to estimate the DC conductivity of all samples where, 'A' and't' cross-sectional area and thickness of the sample under test. The resistance of the liquid samples is denoted by R, while the thickness and cross section area of the samples are known from the conductivity cell's dimensions. Here, DC conductivity values are also derived from measurements of AC conductivity in the range of 400 Hz–140 kHz frequency. Another way to see the conduction phenomenon is with a complex impedance map, in which the x and y axes stand for the complex impedances Z' and Z'', respectively known as Cole-Cole plot. Resistivity variation is replicated by varying compositions of the radius of curvature. As the radius of curvature increases, the conductivity will decrease since the semi-circular plot's greater dispersion implies lower conductivity (high resistance). In the parallel RC circuit of liquid sample, the real (Z_{re}) and imaginary (Z_{im}) impedances can be connected to R as follows: $(Z_{re} - R/2)^2 + Z_{im}^2 = (R/2)^2$. This implies a half-circle in the complex plane with a radius of R/2, which can be confirmed by directly measuring R values with an electrometer.

5.3.1 DC conductivity measurement

The following are some methods for determining the DC conductivity of the prepared liquid samples:

1. Resistance measurements of the samples at different temperatures

2. from the complex impedance plots

3. Pollution of the frequency dependent conductivity to zero frequency.

Thermally activated nature is demonstrated by the reciprocal temperature dependent DC electrical conductivity of the current system, as seen in Fig 5.5. As the temperature rises, the DC conductivity rises as well, exhibiting a nonlinear shape. It is also observed that 2% NaCl solution with distilled water shows highest DC conductivity among these six compositions. Coconut water shows better DC conductivity than orange juice and sugar cane juice. Nature of the DC conductivity changes with temperature is also shown in Fig 5.5 for the entire liquid food conductor and it has been seen that lowest DC conductivity has been shown by 0.1% KCl solution with distilled water. 0.1% KCl, 1 and 2% NaCl solution with distilled water has been prepared to understand a comparative study with other liquid food materials as it is well known liquids food contains salt in them. Table 5.1 shows DC conductivity of different composition and their variation with temperature.

5.3.1.1 Variation of DC conductivity of different liquids with temperature

Temperature			Composition					
TEMP IN °C	**T IN KELVIN**	**1000/T**	**0.1% KCl CONDU-CTIVITY (mS)**	**1% NaCl CONDUCTIVITY (mS)**	**2% NaCl CONDUCTIVITY (mS)**	**COCONUT WATER CONDUCTIVITY (mS)**	**ORANGE JUICE CONDUCTIVITY (mS)**	**SUGAR CANE JUICE CONDUCTIVITY (mS)**
20	293	3.412969	1.6	10.3	17.1	6.82	2.49	2.38
30	303	3.300330	1.86	12.8	20.7	8.5	3.15	2.88
35	308	3.246753	2	13.6	21.13	8.86	3.48	3.15
40	313	3.194888	2.24	15	23.6	9.7	3.63	3.38
48	321	3.115264	2.46	16.62	25	10.25	3.91	3.72

Table 5.1: Variation of DC conductivity with temperature.

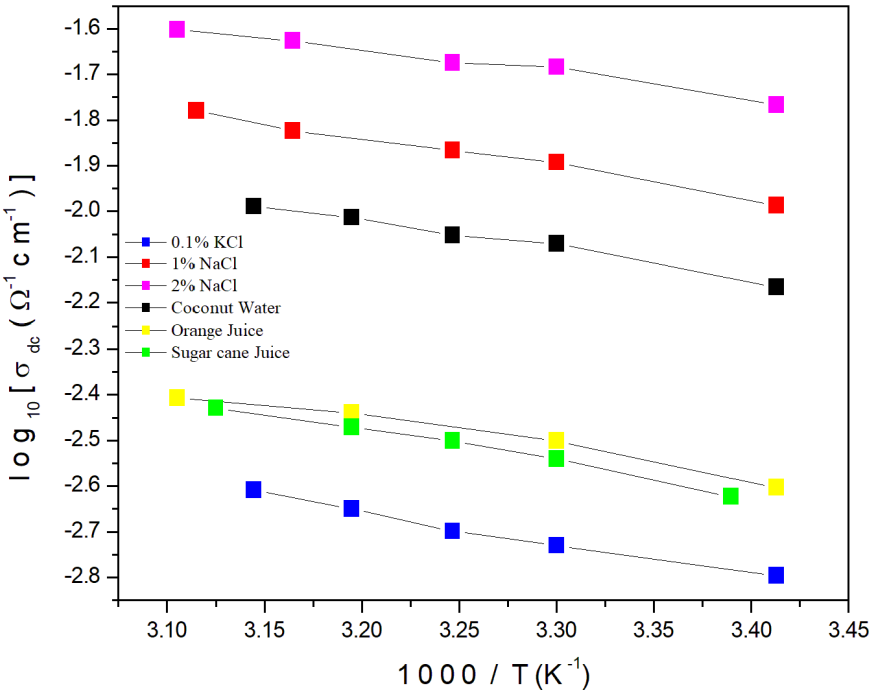

Figure 5.5: Temperature dependence of DC electrical conductivity.

In Fig 5.5 inverse of temperature is used i.e. 1/T, because this is the standard format used in Arrhenius equation (Equation 5.1) and multiplied by 1000 for easier plotting.

5.3.1.2 Activation energies (Ea) for different compositions

Composition	Slope (B)	Activation Energy (|Ea|)
0.1% KCl	-0.69409	0.13742982
1% NaCl	-0.66747	0.13215906
2% NaCl	-0.52461	0.10387278
Coconut Water	-0.65446	0.12958308
Orange Juice	-0.63803	0.12632994
Sugarcane Juice	-0.72683	0.14391234

Table 5.2: Activation energies (Ea) for different compositions.

From Fig 5.5 where all the curves are linearly fitted, values of slope (B) of all the curves are calculated and shown in tabular form. Activation energy (Ea) for all the compositions has been calculated from the slope shown in Table 5.2. The ease with which ions can move is influenced by the activation energy, as higher activation energy implies that more energy is needed to overcome the forces binding these ions in the liquid. This makes the ions less mobile and reduces the conductivity. Different liquid food materials (like milk, juice, or

broth) have different chemical compositions, which affect their ionic content and interactions. For example, a liquid with higher dissolved salts will generally have lower activation energy and higher conductivity, as ions can move more freely. Conversely, liquids with fewer ions (like distilled water or some juices) might have higher activation energy and lower conductivity. DC conductivity and activation energy for the samples consider here are plotted in the Fig 5.6. This illustrates that materials with lower activation energy will show a steeper increase in conductivity as temperature rises, as their ions are more easily mobilized. In summary, by studying the activation energy of liquid food materials, gain insights into how their ionic content, structure, and temperature affect their electrical conductivity.

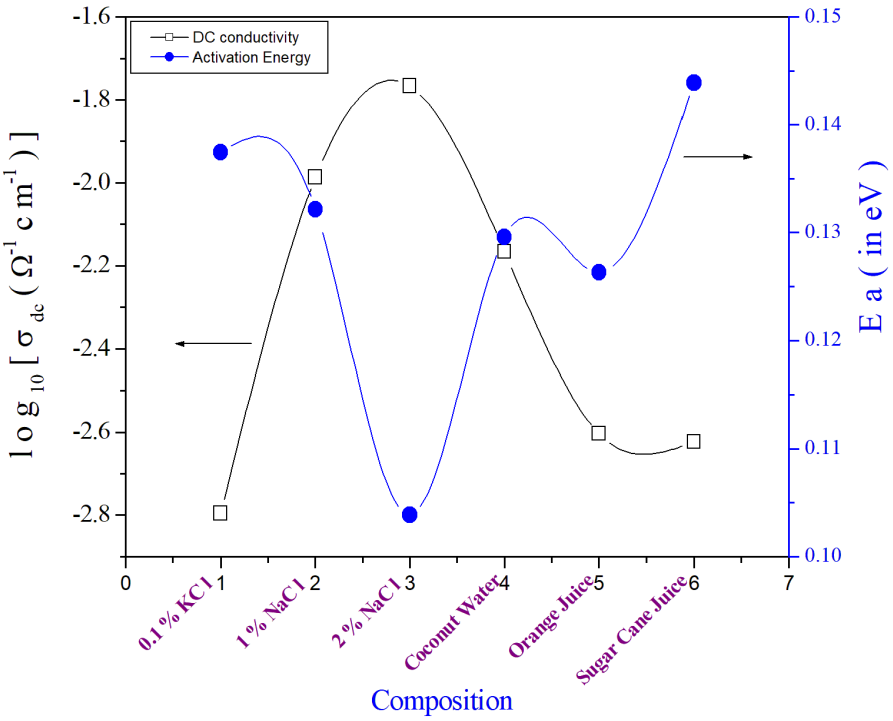

Figure 5.6: DC conductivity and Activation energy for different compositions.

5.3.2 AC conductivity measurement

Applying Cole-Cole plot analysis to a liquid conducting food material (such as a conductive food product, like a salty liquid or certain food pastes) can be an effective method for characterizing its electrical properties, including its conductivity, capacitance, and relaxation behaviors. Food materials that are conductive (like salty liquids, fermented foods, or certain juices) often exhibit ionic conductivity due to the presence of dissolved ions (e.g., Na+, K+, Cl-) and other charged species. The electrical impedance of these materials will depend on factors like: The concentration of ions, the structure of the material (e.g., viscosity, particle distribution) and temperature (which can affect ion mobility and relaxation times). Applying

an AC voltage across a sample of such a food material; the impedance measure will be influenced by resistive and capacitive components, leading to the characteristic features observed in a Cole-Cole plot. Therefore place the liquid food material in a suitable container and ensure that it is homogeneous and well-mixed. Use two electrodes to measure the impedance of the sample. These electrodes should be placed in contact with the sample i.e. conductivity cell and connected to an LCR meter as mentioned earlier impedance that can apply a range of frequencies. For food materials, anyone may use frequencies from 1 Hz to 10 MHz to cover the relevant electrical behaviors. Here food samples have been tested in the frequency range between 400 Hz to 140 kHz and Plot the impedance's real part (Z') versus its imaginary part (Z''), hence semicircular arc (distorted arc) will typically appear, reflecting the resistive and capacitive properties of the food material shown in Fig 5.7. Real axis (Z') represent the resistive component, which corresponds to the ionic conductivity of the food material. Imaginary axis (Z'') reflects the capacitive effects (related to the polarizability of the material), and at low frequencies, may observe a larger impedance contribution from these effects. The semicircular arc in the Cole-Cole plot is associated with the relaxation time of the material. The center of the semicircle indicates the characteristic time constant of the system, which gives insight into how quickly the ions in the conducting liquid can respond to changes in the applied frequency. The diameter of the arc relates to the resistance (or conductivity) of the material. The width of the arc in the Cole-Cole plot represents the distribution of relaxation times of the system. A wider arc may suggest a broader range of time constants, implying more complex relaxation processes within the food material, such as different ionic species or varying ion mobility.

Using the Cole-Cole model which can be mathematically expressed as a fractional model of the impedance which can be fitted the experimental data to obtain parameters like: Resistivity (ρ) which directly related to ionic conductivity. Capacitance (C), Relaxation time (ד): The time it takes for the ionic or dipolar response to reach equilibrium with the applied electric field Etc.

This model is often expressed as:

$$Z^*(\omega) = R_\infty + [(R_S - R_\infty)/ \{1 + (j\omega ד)^{1-\alpha}\}] \quad (5.2)$$

Where,

Z^* = complex impedance

R_S = Impedance at zero frequency (DC resistance)

R_∞ = Impedance at infinite frequency

ω = Angular frequency (ω=2 π f)

ד = Characteristic relaxation time

α= Cole-Cole parameter

j = √-1

The Cole-Cole plot of different composition shown in Fig 5.7 describe dc resistance, material's ionic content, capacitive properties, and relaxation behaviors for different composition that means this can be a powerful tool for studying the electrical conductivity and ionic behavior of liquid conducting food materials by analyzing the impedance spectra and fitting them with appropriate models.

5.3.2.1 Cole-Cole plot of different food samples

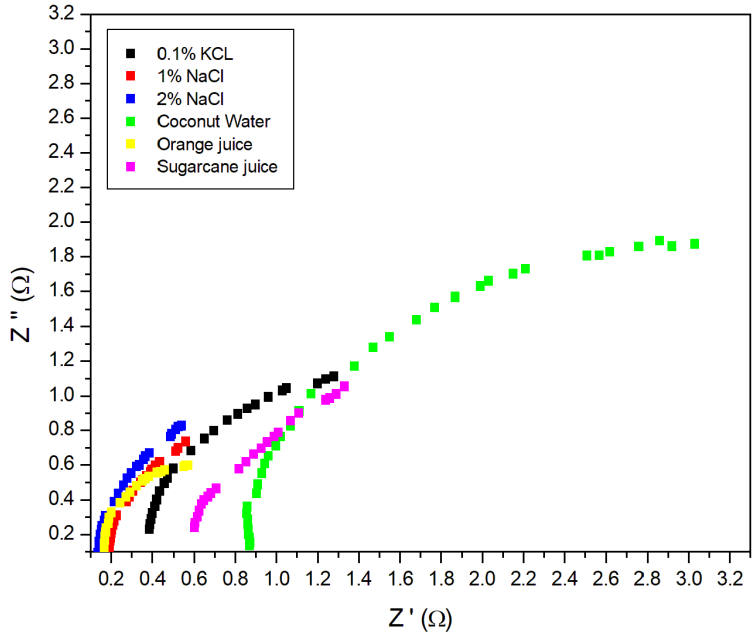

Figure 5.7: Cole-Cole plot of different food samples.

The Jonscher Power Law is widely used to describe the frequency-dependent electrical conductivity of liquid food materials, such as juices, milk, honey, and edible oils. These materials exhibit complex electrical behavior due to the presence of water, dissolved ions, proteins, fats, and sugars**,** which influence charge transport. The AC conductivity σ_{ac} of liquid

food materials follows the Jonscher equation. The following relation can be used to determine the frequency-dependent AC conductivity at a given frequency,

$$\sigma_{ac} = \sigma_{dc} + A.\omega^{s} \quad (5.3)$$

Where, A = Material-dependent constant, s = Frequency exponent (typically between 0 and 1) for various juices show high ionic conductivity due to water content and dissolved salts and s values typically between 0.7 and 1, indicating strong frequency dependence. Fig 5.8(a, b) to 5.13(a, b) shows how conductivity changes with frequency for the samples consider in this work. Nature of the graph for all the composition (0.1% KCl, 1% & 2% NaCl solution with distilled water, Coconut water, Orange Juice ,Sugar Cane Juice, etc.) looks like similar. The variation of ac conductivity (σ_{ac}) with respect to frequency is similar in nature, though their values differ.

5.3.2.2 Frequency dependent ac conductivity of different liquid compositions

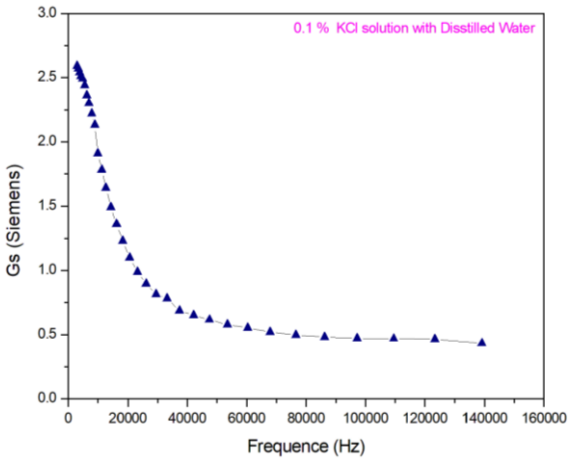

(a)

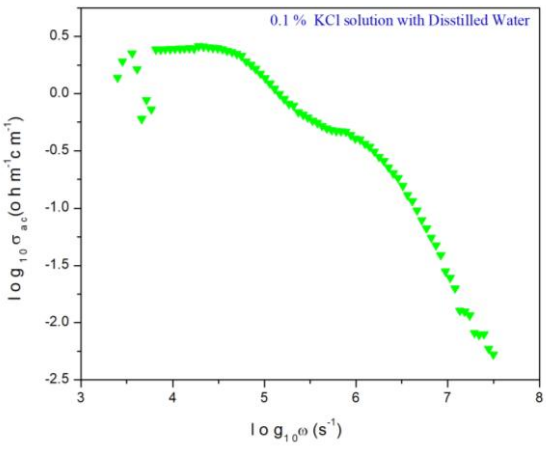

(b)

Figure 5.8(a, b): Frequency dependent ac conductivity of 0.1% KCl solution with distilled water.

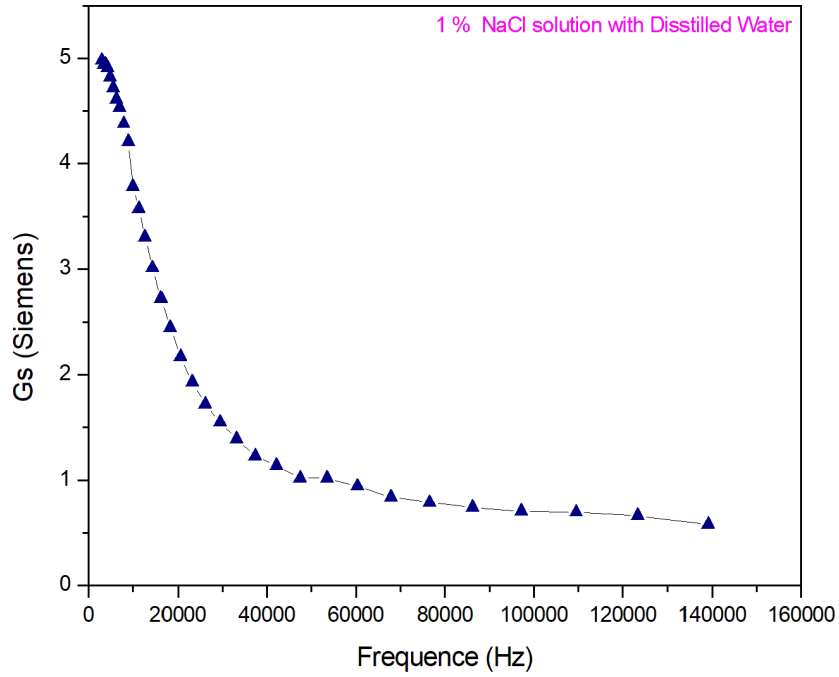

(a)

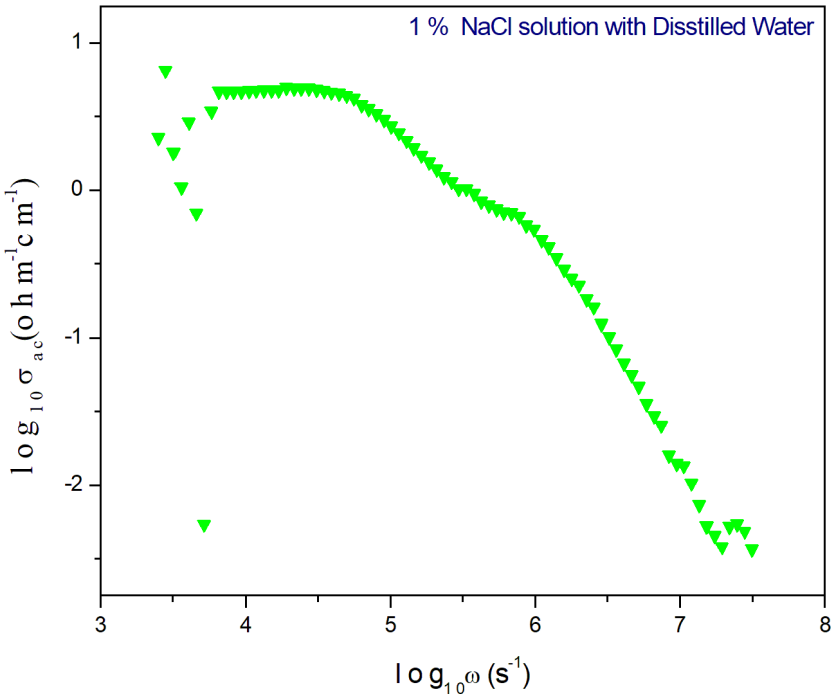

(b)

Figure 5.9(a, b): Frequency dependent ac conductivity of 1% NaCl solution with distilled water.

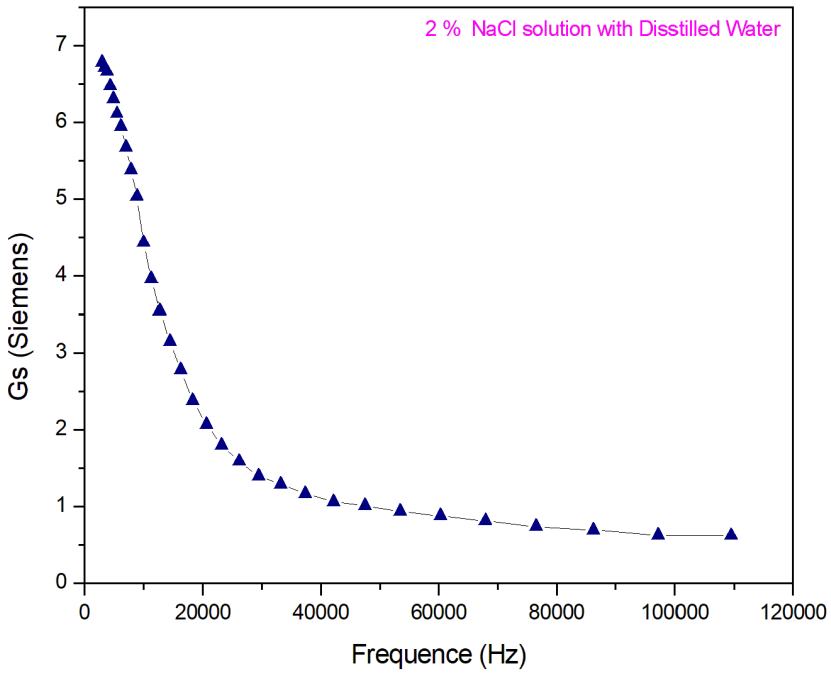

(a)

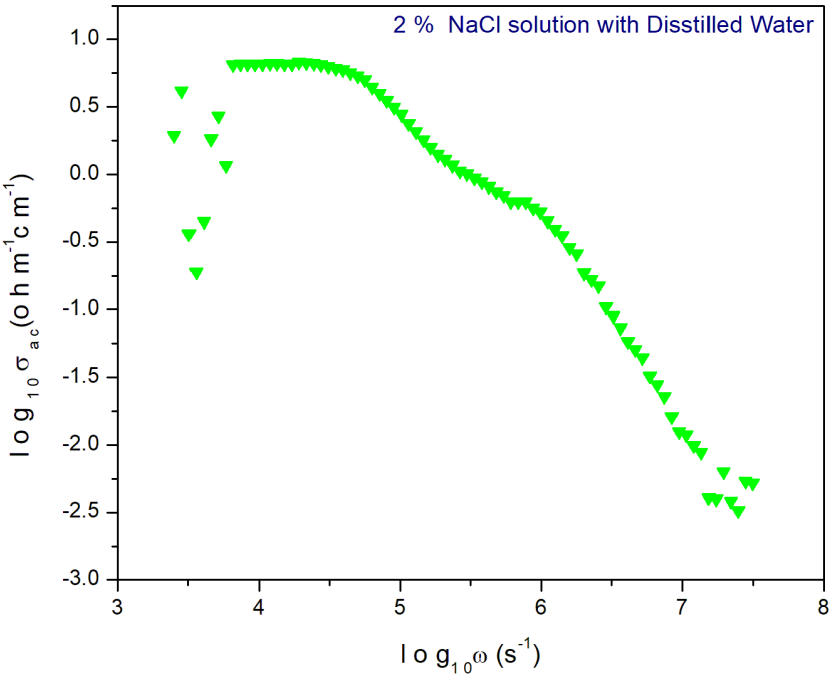

(b)

Figure 5.10(a, b): Frequency dependent ac conductivity of 2% NaCl solution with distilled water.

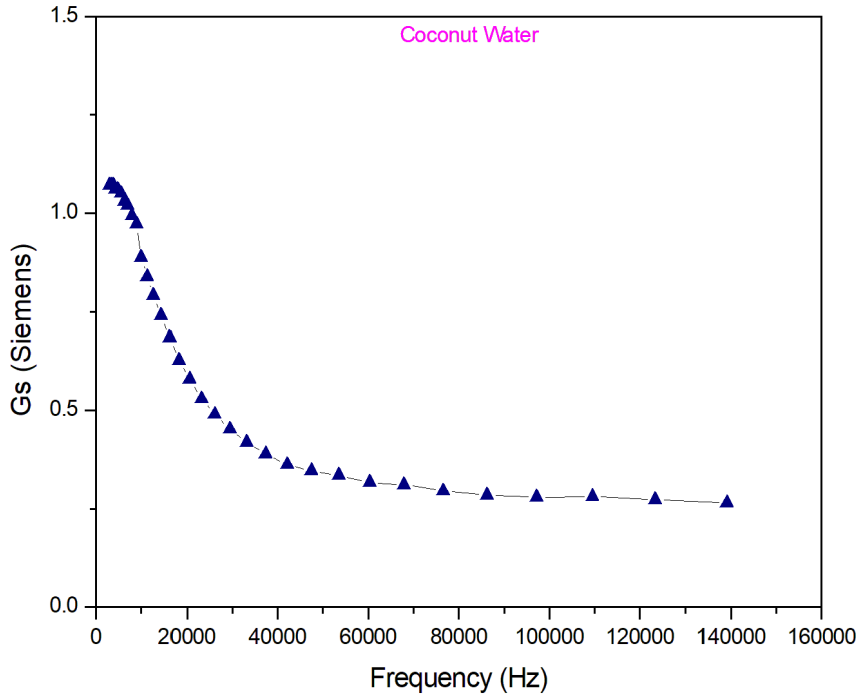

(a)

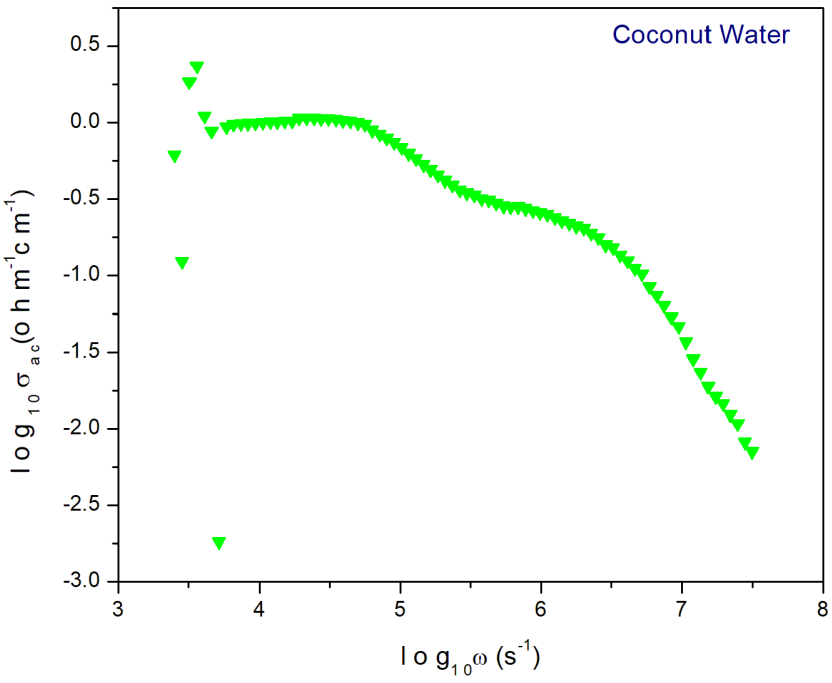

(b)

Figure 5.11(a, b): Frequency dependent ac conductivity of coconut water.

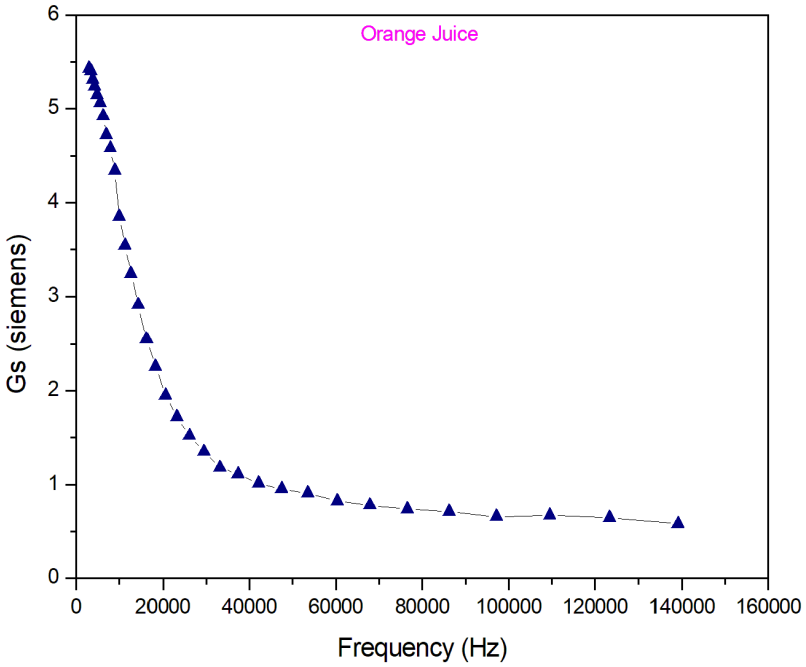

(a)

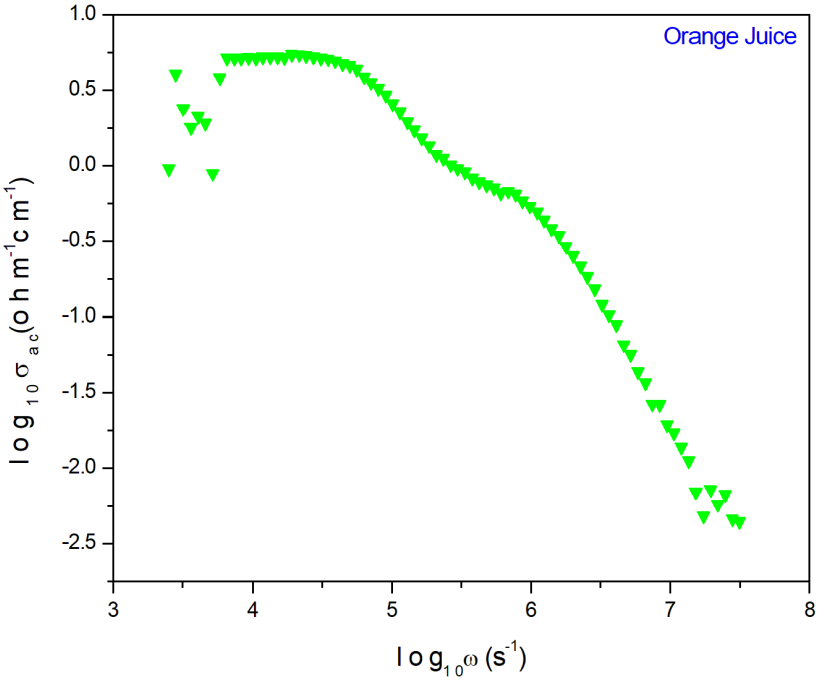

(b)

Figure 5.12(a, b): Frequency dependent ac conductivity of orange juice.

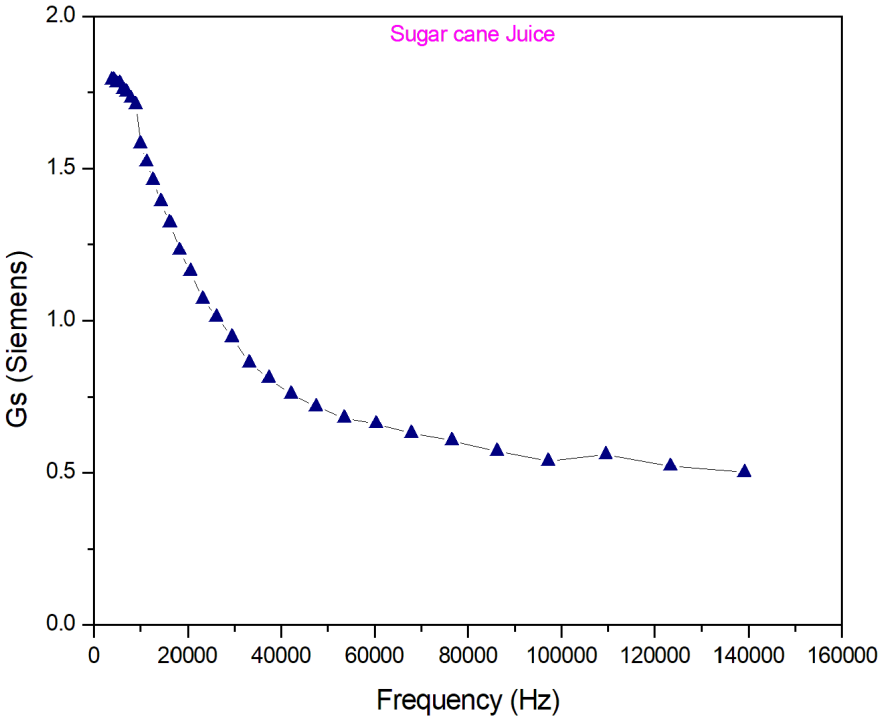

(a)

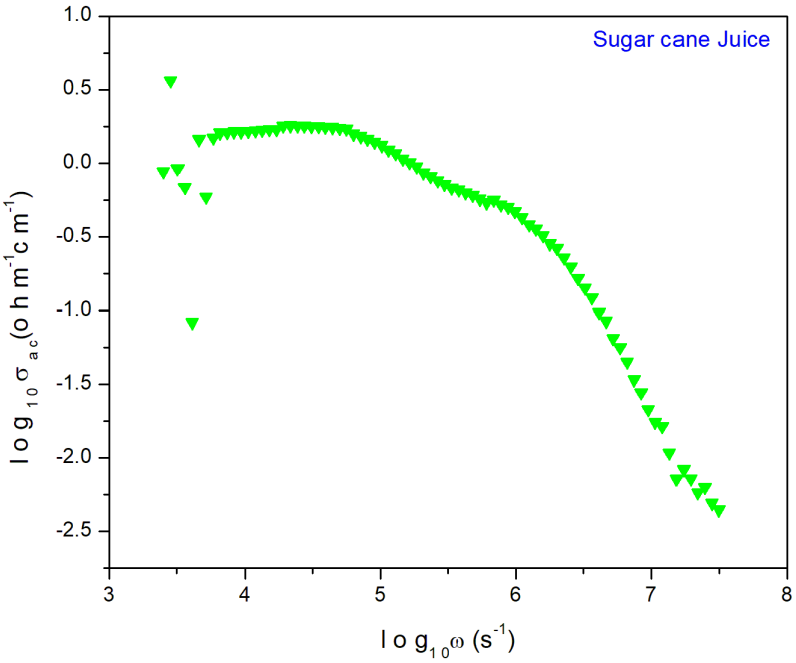

(b)

Figure 5.13(a, b): Frequency dependent ac conductivity of sugar cane juice.

Electrical conductivity of chosen liquid samples has been recorded for three different frequencies. Here it has been shown that as the frequency increases the ac conductivity gradually decreases though the changing pattern for all the composition are not same shown in Fig 5.14. Three frequency range has been consider; low (800 Hz), medium (100 kHz) and high (2 MHz) and noted the conductance for the samples mentioned above.

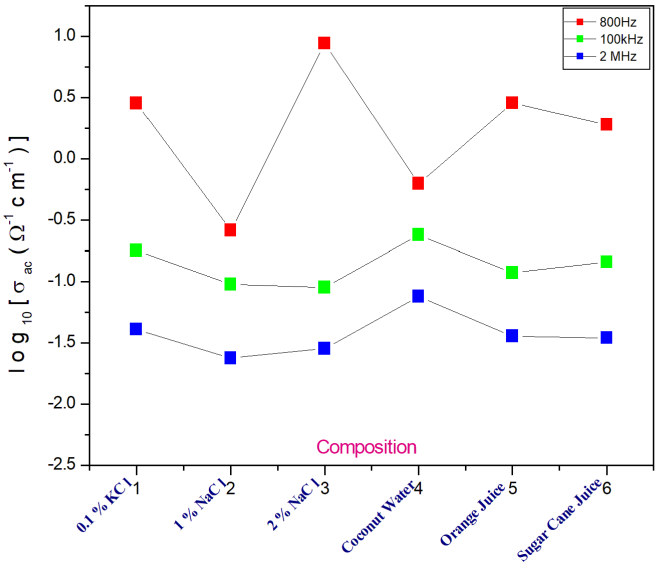

Figure 5.14: AC conductivity (σ_{ac}) for low, medium, and high frequencies for all compositions.

The primary reason for the differences of DC and AC resistances in the food material is the impact of frequency on ionic mobility. Ions travel more freely under DC or low-frequency which reduces resistance. The AC resistance is somewhat larger than the DC resistance as the frequency rises because the effective ionic mobility falls. Therefore the DC and AC resistance of different material consider here be mentioned like for 0.1% KCL solution DC resistance= 0.36 ohm and AC resistance= 1.1 ohm, for 1% NaCl solution DC resistance = 0.30 ohm and AC resistance = 0.59 ohm, for 2% NaCl solution DC resistance = 0.25 ohm and AC resistance = 0.55 ohm, for coconut water DC resistance = 0.19 ohm and AC resistance = 2.2 ohm, for orange juice DC resistance = 0.31 ohm and AC resistance = 0.61 ohm, for sugar cane juice DC resistance = 0.8 ohm and AC resistance = 1.1 ohm respectively.

Chemical changes may happen through electrolysis by applying a DC if alternating current is applied then chemical changes should not occur. As at increasing frequency the ohmic heated liquid visibly do not shows any change of color before and after. Only this observation has been made by the test.

A comparative study of electrical conductivity of chosen liquid samples has been recorded for three different frequencies. In Fig. 5.14, all the red points represent the conductance values of the different samples measured at 800 Hz. They are connected to show how much these values differ from one sample to another. In Fig 5.14 it has been observed that AC conductivity decreases with frequency it means resistance gets increased.

5.3.3 Graphical presentation of SEM-EDX results for green coconut water, electrodes after heat treatment

Scanning Electron Microscopy (SEM) and Energy Dispersive X-ray Spectroscopy (EDX) were performed on green coconut water to study metal ion migration into the heating medium and the formation of deposits on the electrode surfaces. Although other juices were included in the study, these specific analysis—including the "Element Line Scan" experiment—were conducted only for the green coconut water sample.

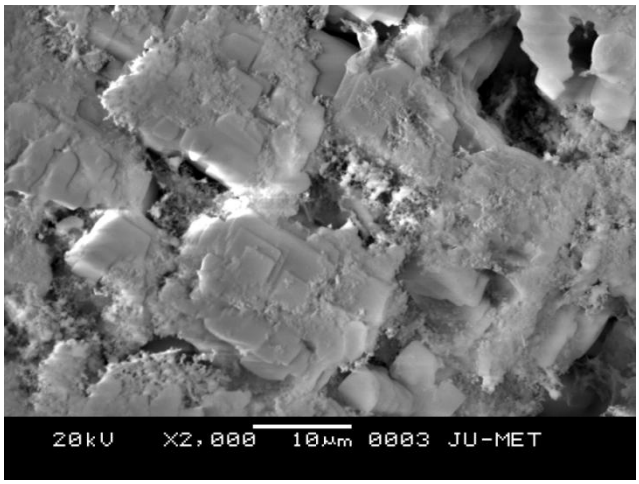

(a)

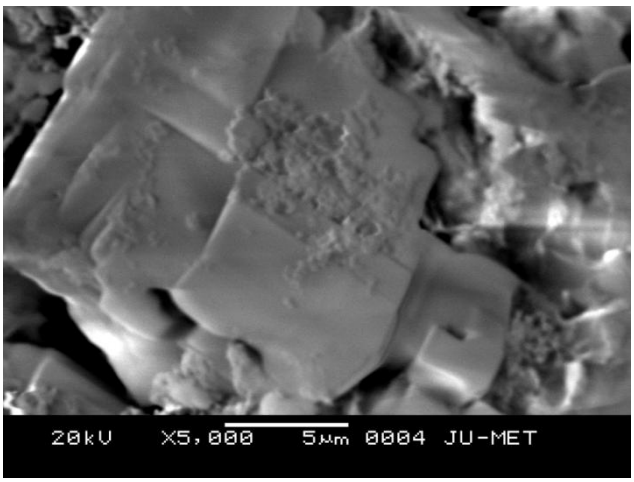

(b)

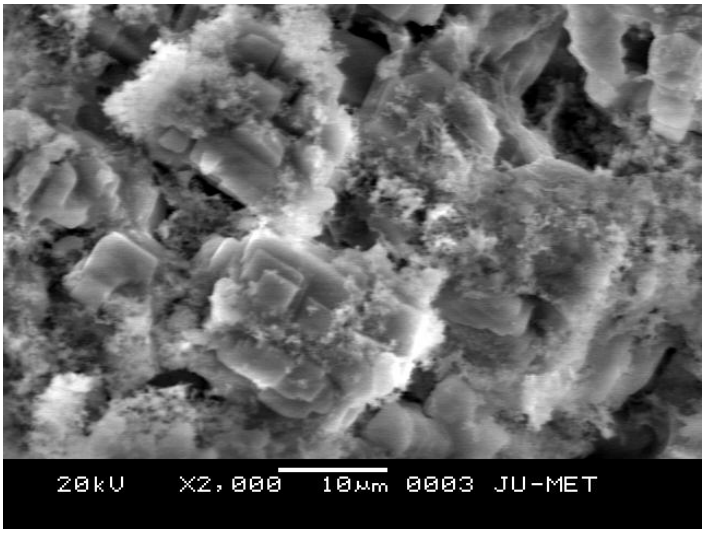

(c)

Figure 5.15(a, b, c): SEM micrograph of green coconut water.

5.3.3.1 EDX result of green coconut water (Titanium electrode)

Element	**Weight%**	**Atomic%**
O K	23.35	41.71
Mg K	3.01	3.53
Al K	0.26	0.27
Cl K	27.52	22.18
K K	36.54	26.70
Ca K	4.61	3.29
Ti K	3.09	1.84
Cr K	0.49	0.27
Co K	0.07	0.04
Ni K	0.06	0.03
Pt M	1.01	0.15
Totals	100.00	

Table 5.3: EDX result of green coconut water (Titanium electrode).

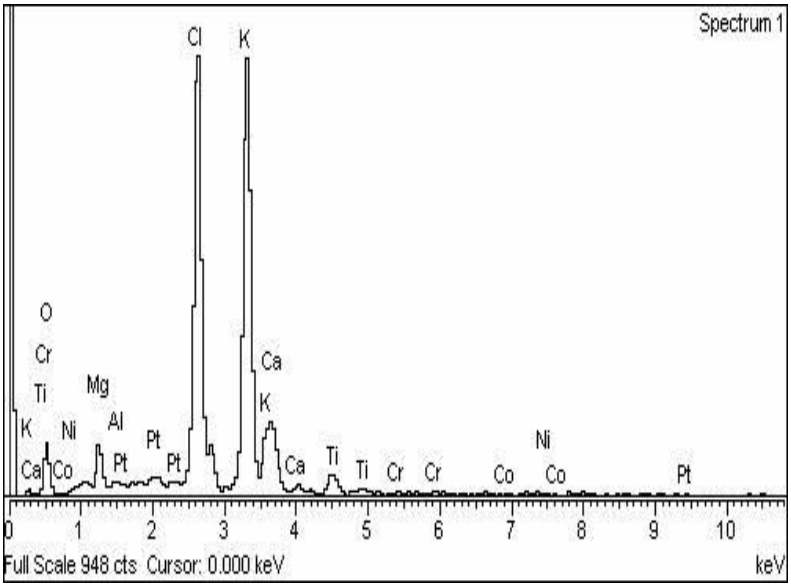

Figure 5.16: EDX result of green coconut water (Titanium electrode).

5.3.3.2 EDX result of green coconut water (Flat portion, Titanium electrode)

Element	**Weight%**	**Atomic%**
O K	17.82	33.26
Mg K	1.64	2.01
Al K	1.55	1.71
Cl K	37.06	31.22
K K	40.51	30.94
Ti K	0.97	0.61
Mn K	0.32	0.17
Fe K	0.03	0.02
Co K	0.11	0.05
Totals	100.00	

Table 5.4: EDX result of green coconut water (Flat portion, Titanium electrode)

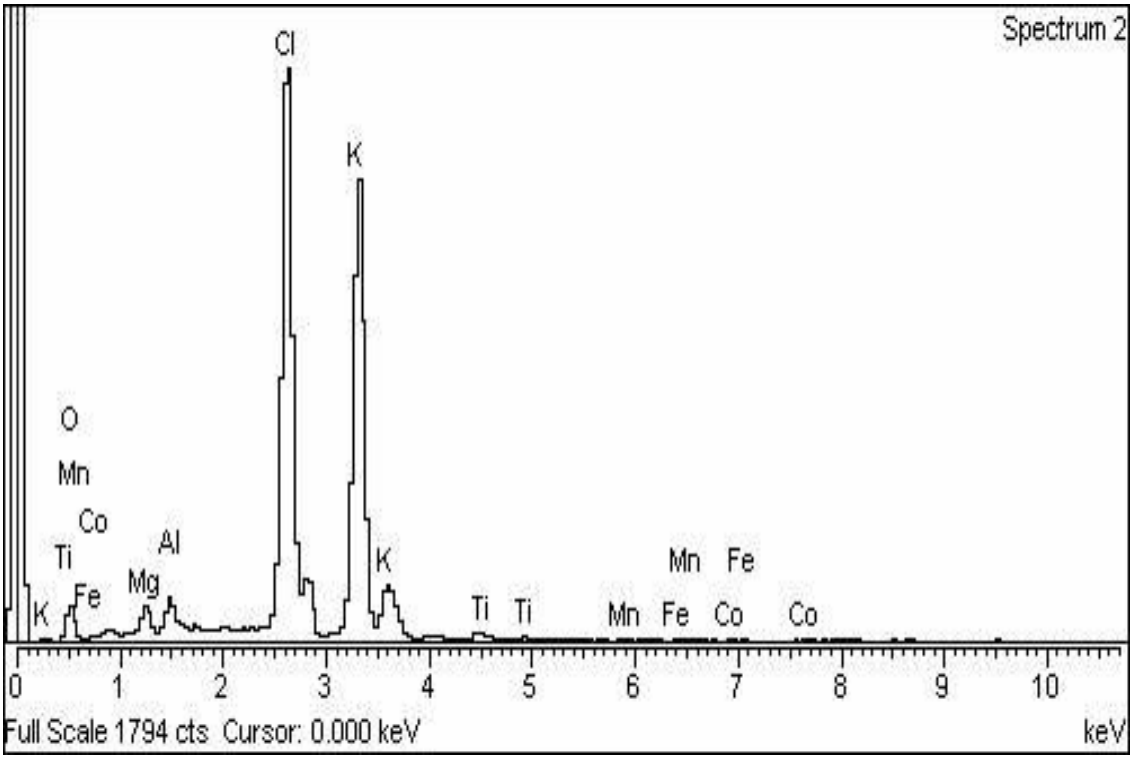

Figure 5.17: EDX result of green coconut water (Flat portion, Titanium electrode)

5.3.3.3 Chemical composition of green coconut water

Minerals	Concentration (mg 100 ml^{-1})
K	356-164
Cl	108-131
S	4-8
Ca	18-47
Na	4.1-48
Mg	7.8-15
P	6.3-21
Mn	0.08
Al	0.06
Zn	0.03
Fe	16-112
Cu	26-29.3

Table 5.5: Chemical Composition of green coconut water (Pradesh et al., 2012)

5.3.3.4 Element Line Scan (ELS) experiment on green coconut water

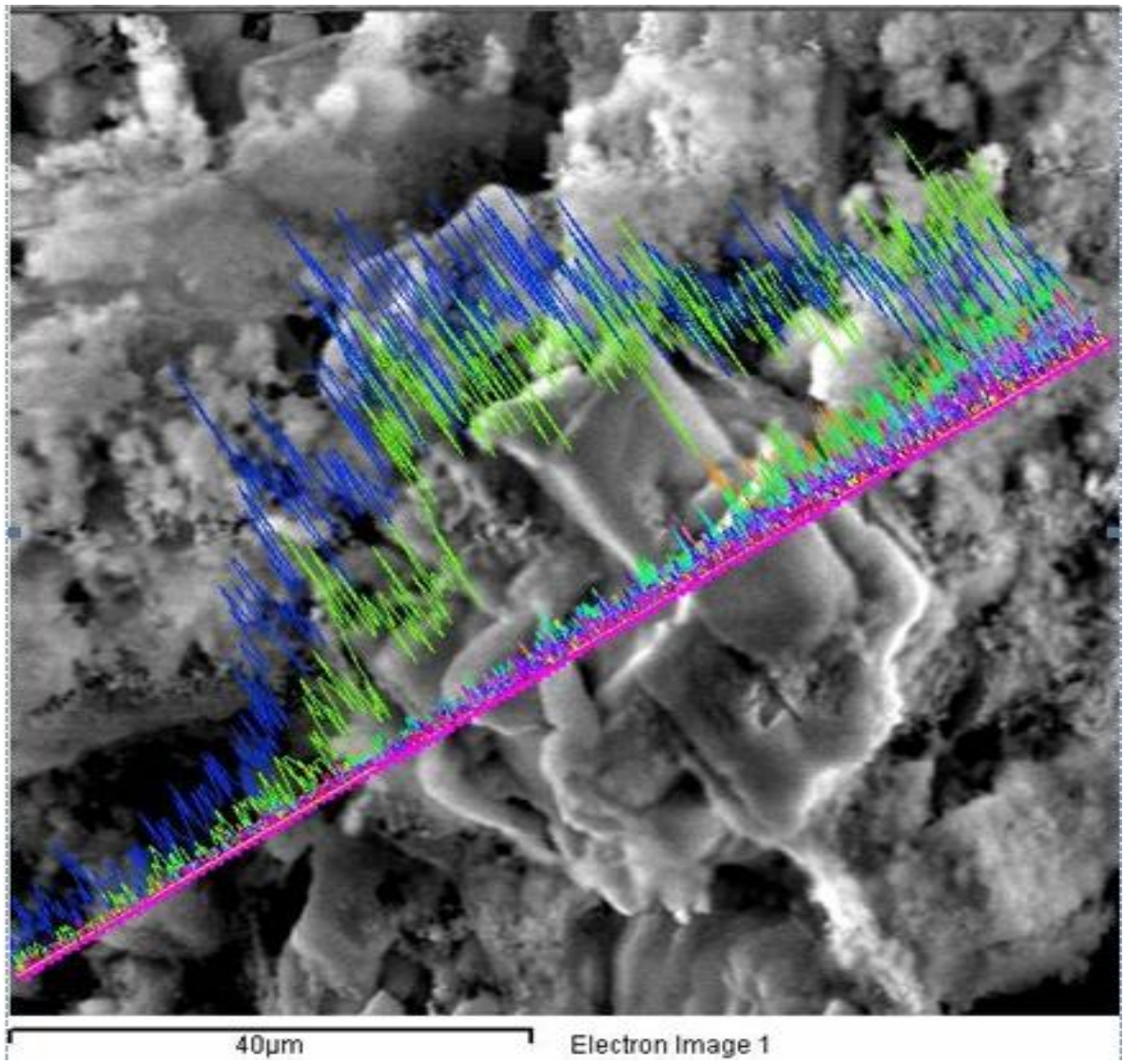

Figure 5.18: Identified elements deposited on the above-mentioned electrode surfaces

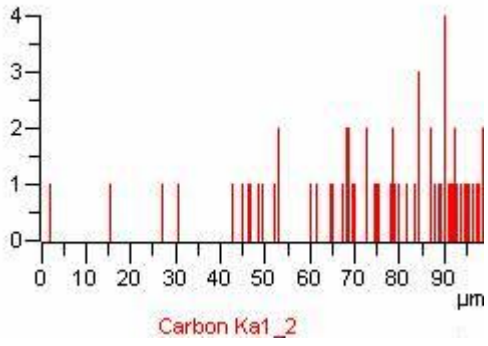

(a)

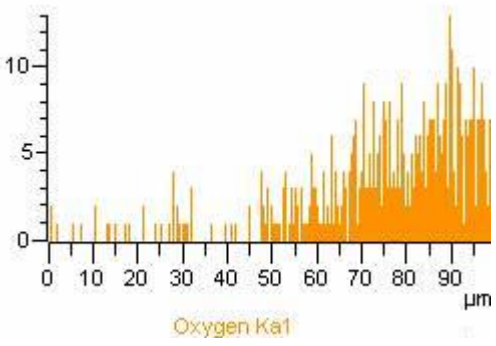

(b)

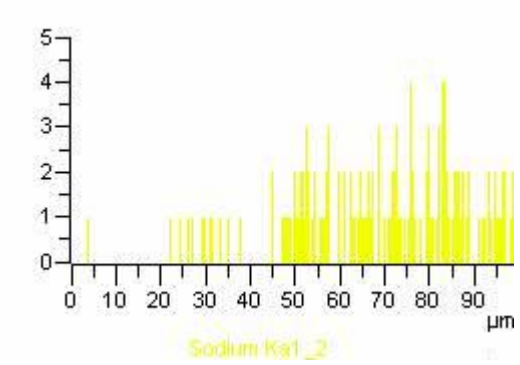
Sodium Ka1_2
µm

(c)

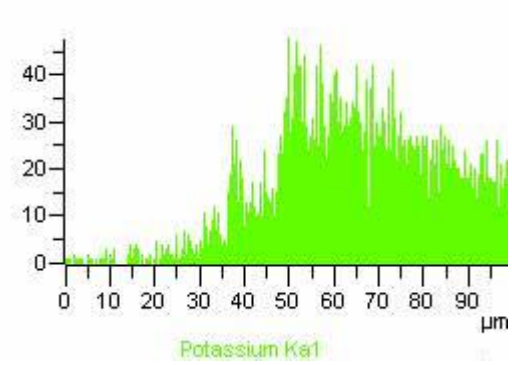
Potassium Ka1
µm

(d)

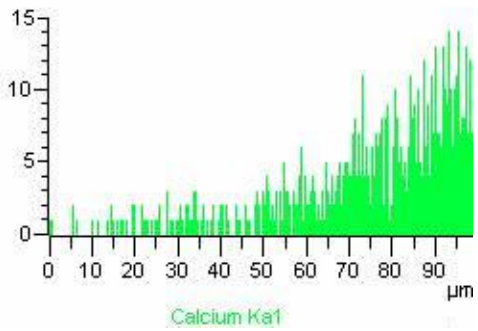
Calcium Ka1
µm

(e)

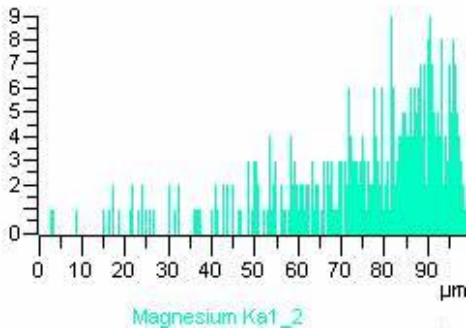
Magnesium Ka1_2
µm

(f)

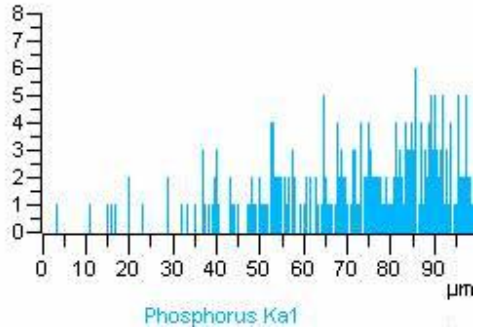
Phosphorus Ka1
µm

(g)

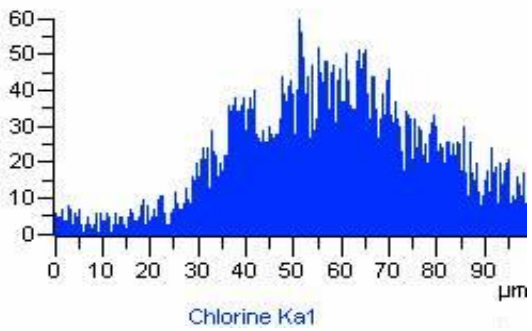
Chlorine Ka1
µm

(h)

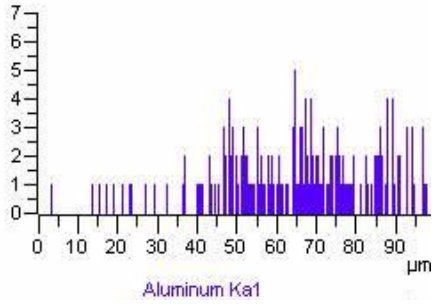
Aluminum Ka1
µm

(i)

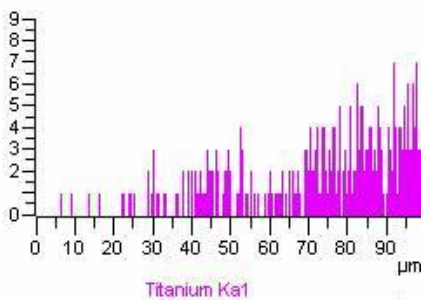
Titanium Ka1
µm

(j)

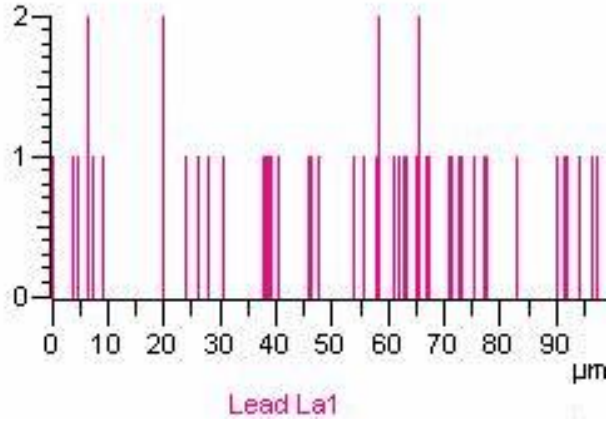

(k)

Fig 5.19(a, b, c, d, e, f, g, h, i, j, k): Elemental Line Scan of green coconut water (Titanium electrode).

5.4 Summary

Temperature and frequency has a significant impact on the tested samples' electrical conductivity which is increased with product temperature and decreases with higher frequencies. Electrical conductivities of the chosen liquid products are observed based on their temperatures and activation energy. An essential tool for designing and effectively running an ohmic heating process should be available in this database. Understanding electrical conductivity temperature relationships, in particular, will help determine the temperature change (ΔT) throughout a treatment, improved process control, and can give a tool for effective food treatment methods.

Chapter-6

DESIGN AND MODELING-SIMULATIONS OF THE HIGH FREQUENCY PUSH-PULL INVERTER SYSTEM

6.1 Introduction

High-frequency inverter systems have drawn a lot of interest lately because of their many uses in contemporary power electronics, such as ohmic heating, wireless power transfer, renewable energy systems, electric vehicles, and induction heating etc. These systems, which operate at frequencies significantly higher than the ordinary power grid (usually above 20 kHz), provide a number of benefits, including smaller passive components, larger power densities, and quicker dynamic response. But these advantages can have drawbacks, including component stress, switching losses, and electromagnetic interference (EMI) [91]-[93].

This chapter focuses on using MATLAB/Simulink to develop and model a high-frequency inverter system. A simulation-based method that allows for in-depth examination of the inverter's performance under varied operating circumstances and load kinds is what the goal is. Since the performance of crucial parts like MOSFETs, gate drivers, and optocouplers has a big impact on the system's overall efficiency and dependability, special attention is paid to understanding how they behave [94]-[95].

Before implementing hardware, designers can use this modeling technique to find possible problems including switching losses, gate drive delays, and heat effects. MATLAB/Simulink is a useful tool in the creation of high-frequency inverters because it offers a full platform for viewing circuit behavior, evaluating control schemes, and improving system parameters. High-frequency inverters, which frequently operate in challenging electrical conditions, need precise control over switching components. Failures may result if parasitic effects signal delays, and thermal restrictions are not taken into consideration during the design stage. Specifically, inappropriate switching may lead to device failure or system instability due to timing delays produced by optocouplers or incorrect gate drive signals. These dangers can be reduced by evaluating the circuit in a virtual setting using modeling and

simulation. In addition to aiding in design optimization, the modeling technique shortens development times by eliminating the need for intensive prototyping. It provides a flexible environment for iterative improvements, lowers development costs, and enables early detection of possible design problems. A review of inverter topologies acceptable for high-frequency operation opens this chapter, which is followed by the choice of relevant parts and design parameters. The modeling method using MATLAB/Simulink is then explored, including the creation of control strategies and performance simulation under many circumstances.

6.2 Materials and methods

The equivalent network of the experimental circuit shown in Fig. 6.1 includes the transformer for modeling, design, and calculation purposes. For no-load analysis, the series components R_S and L_S can be neglected. Capacitance appears during transient conditions due to MOSFET operation; however, it becomes negligible at steady state.

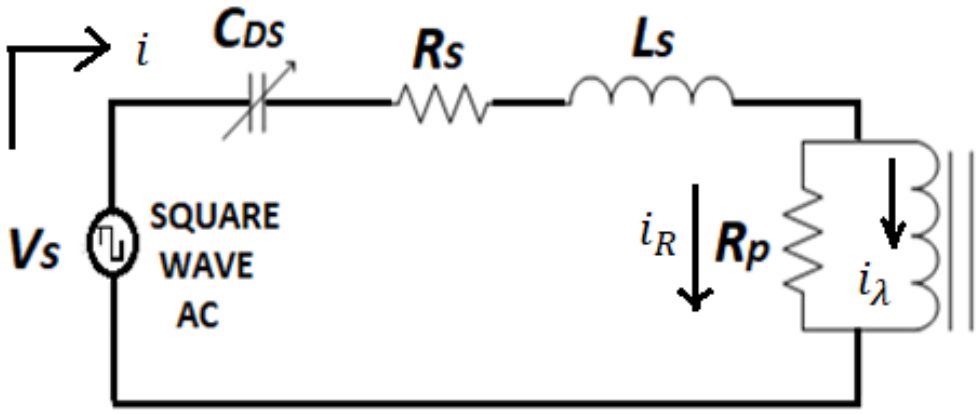

Figure 6.1: Equivalent circuit of push pull type MOSFET-inverter.

Let,

V_s = Square wave input

C_{DS} = Capacitance due to MOSFETs

= C_{eq} At transient condition

= 0 At steady state condition

Transformer equivalent circuit:

R_S = Series resistance due to transformer windings

L_S = Series inductance due to leakage flux

R_P = Parallel resistance due to core loss

KVL equation at transient state

$$V_S = V_C + V_{R_S} + V_{L_S} + V \tag{6.1}$$

Where,

V_C = Voltage across capacitance C_{DS}

V_{R_S} = Voltage across series resistance R_S

V_{L_S} = Voltage across series inductance L_S

V Is the voltage across parallel branch = Voltage across primary coil $= \frac{d\lambda}{dt}$

Here λ is the flux linkage.

Differentiating (6.1) with respect to time-

$$\frac{dV_S}{dt} = \frac{dV_C}{dt} + \frac{dV_{R_S}}{dt} + \frac{dV_{L_S}}{dt} + \frac{dV}{dt} \tag{6.2}$$

Capacitor voltage $V_C = \frac{1}{C_{DS}} \int i\, dt$ (6.3)

If i is the current flowing in the circuit, it will divide into two parts, i_R through R_P and i_λ through transformer winding, such that:

$$i = i_R + i_\lambda \tag{6.4}$$

Then,

$$i_R = \frac{V}{R_P} \tag{6.5}$$

And,

$$i_\lambda = a\lambda + b\lambda^7 \tag{6.6}$$

The last relation can be obtained from the experimental data (open circuit test of the transformer) as follows; Variation of flux linkages with respect to current passing through the primary coil shown in Fig 6.2.

6.2.1 Variation of flux linkages with respect to current

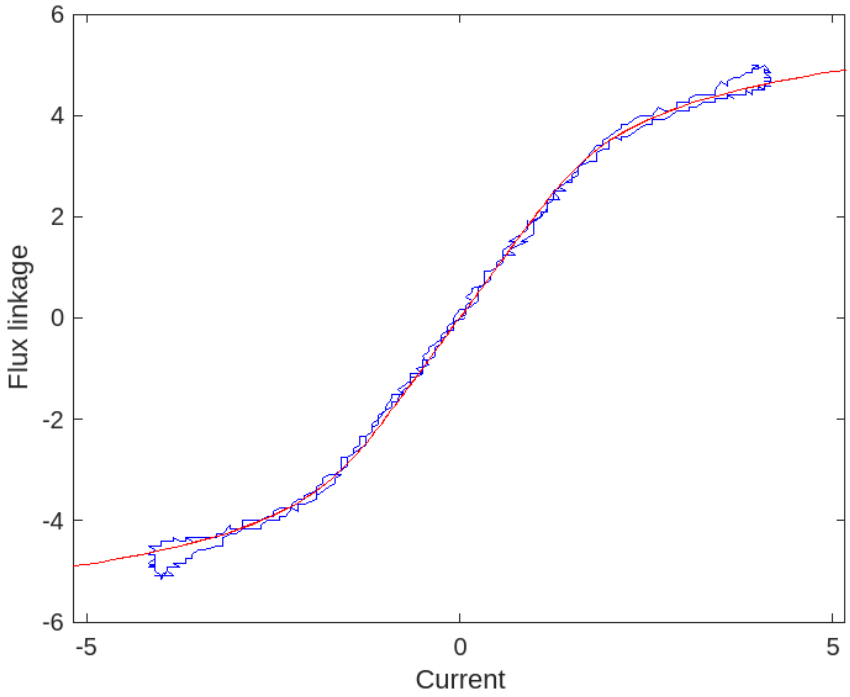

Figure 6.2: Variation of flux linkages with respect to current passing through the coil.

6.2.2 Modeling design of the system.

The blue curve is experimental and red curve is approximated with $a = 0.5$ and $b = 4 \times 10^{-5}$. The source voltage V_S needs to be calculated from Fourier series analysis. Equation (6.1) can be written as:

$$\frac{dV_S}{dt} = \frac{dV_C}{dt} + \frac{dV_{R_S}}{dt} + \frac{dV_{L_S}}{dt} + \frac{dV}{dt} \tag{6.7}$$

Or,

$$\frac{dV_S}{dt} = \frac{1}{C_{DS}} i + \frac{d}{dt}(iR_S) + \frac{d}{dt}\left(L_S \frac{di}{dt}\right) + \frac{d}{dt}\left(\frac{d\lambda}{dt}\right) \tag{6.8}$$

Or,

$$\frac{dV_S}{dt} = \frac{1}{C_{DS}} i + R_S \frac{di}{dt} + L_S \frac{d^2 i}{dt^2} + \frac{d^2 \lambda}{dt^2} \tag{6.9}$$

Or,

$$\frac{d^2 \lambda}{dt^2} = \frac{dV_S}{dt} - \frac{1}{C_{DS}} i - R_S \frac{di}{dt} - L_S \frac{d^2 i}{dt^2} \tag{6.10}$$

Now,

$$i = i_R + i_\lambda = \frac{V}{R_P} + (a\lambda + b\lambda^7) = \frac{1}{R_P}\left(\frac{d\lambda}{dt}\right) + (a\lambda + b\lambda^7) \tag{6.11}$$

Therefore current i can be written as equation (6.11), using this equation the modeling design of the system has been done in MATLAB. The entire block diagram is shown in Fig 6.3.

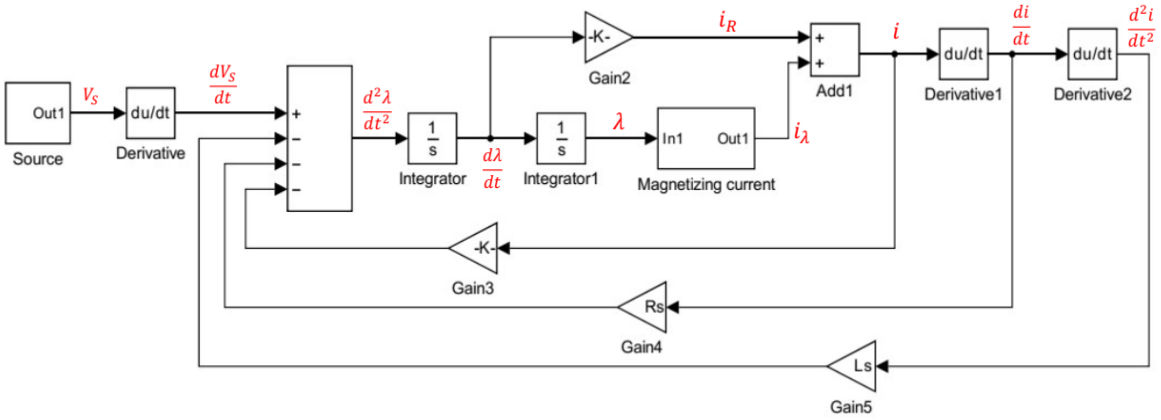

Figure 6.3: Modeling design of the system.

6.3 Results and discussion

The transformer model's performance and behavior were examined by obtaining simulation results in MATLAB at different operating frequencies considering effects of all the parameters of the circuit shown in Fig 6.1. The model included crucial characteristics like magnetizing inductance, leakage inductance, and winding resistance. Changes in the impedance characteristics were noted when the frequency changed, impacting the waveforms of voltage and current across the transformer. While parasitic components like capacitance and leakage inductance were increasingly noticeable at higher frequencies, the output stayed comparatively constant at lower frequencies. These models demonstrate the significance of frequency in transformer modeling and aid in the creation of precise designs for power electronics applications. Simulation results were obtained in MATLAB for the transformer model under various operating frequencies, shown in Fig 6.4 to 6.15. Fig 6.16(a, b) shows the practical inverter output voltage wave of ferrite core transformer these are almost similar in nature to the simulation results.

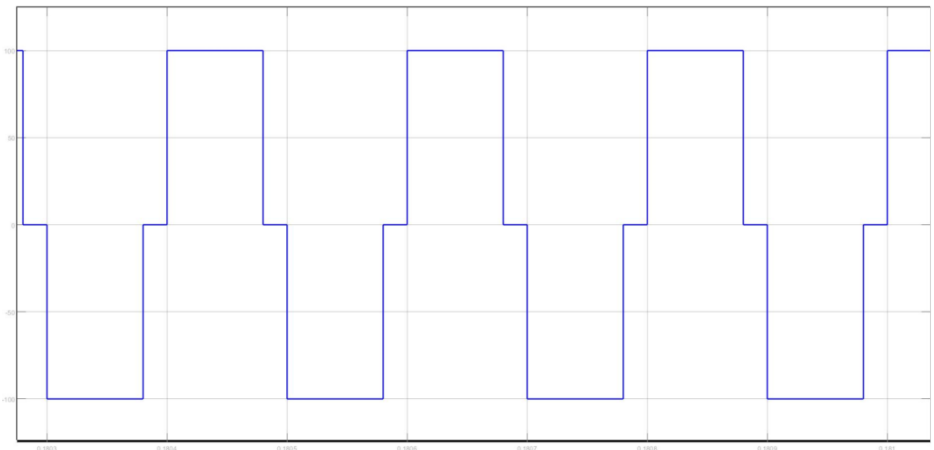

Figure 6.4: Square wave AC voltage (V_S) at 5kHz frequency.

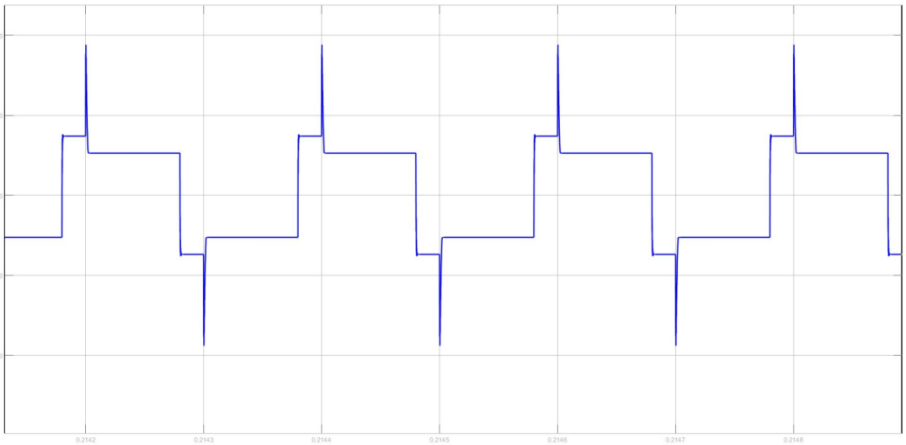

Figure 6.5: Secondary side voltage of the transformer at 5kHz frequency.

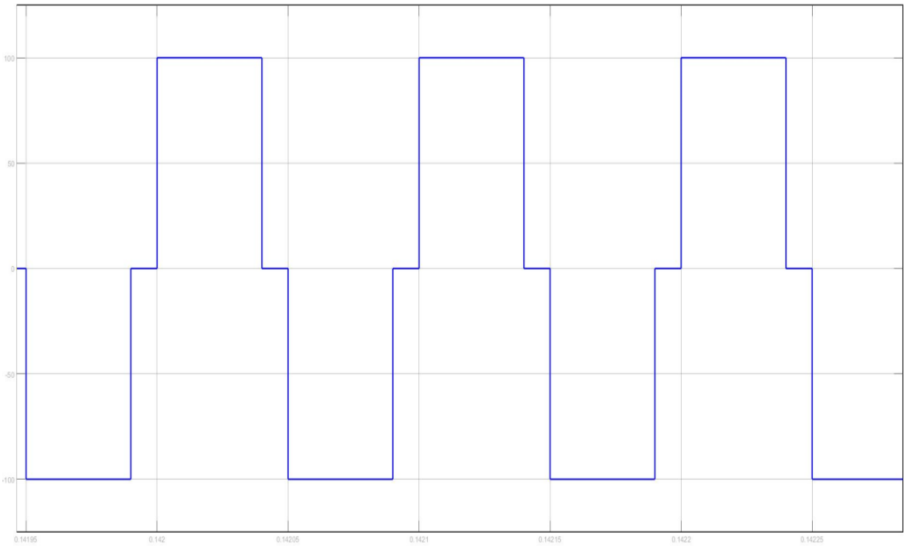

Figure 6.6: Square wave AC voltage (V_S) at 10kHz frequency.

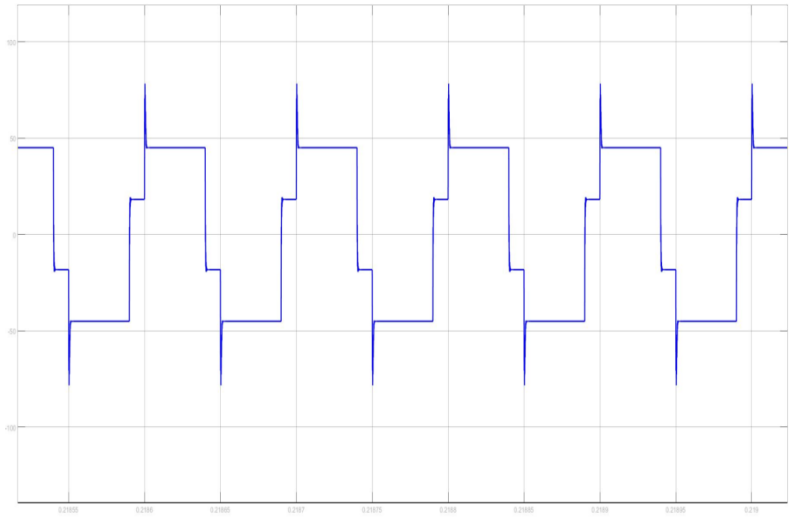

Figure 6.7: Secondary side voltage of the transformer at 10kHz frequency.

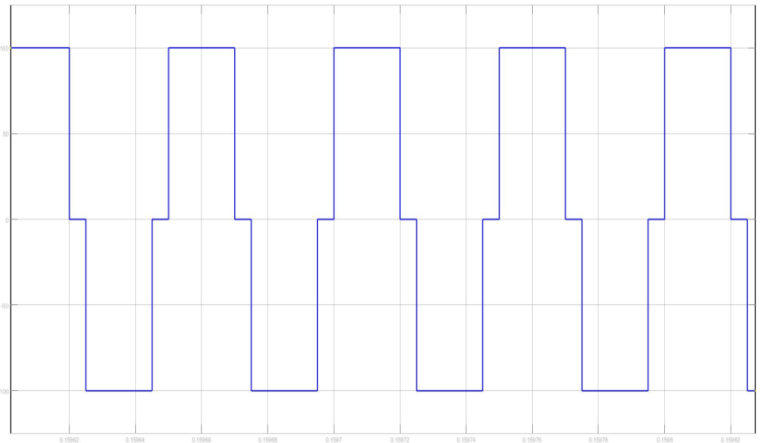

Figure 6.8: Square wave AC voltage (V_S) at 20kHz frequency.

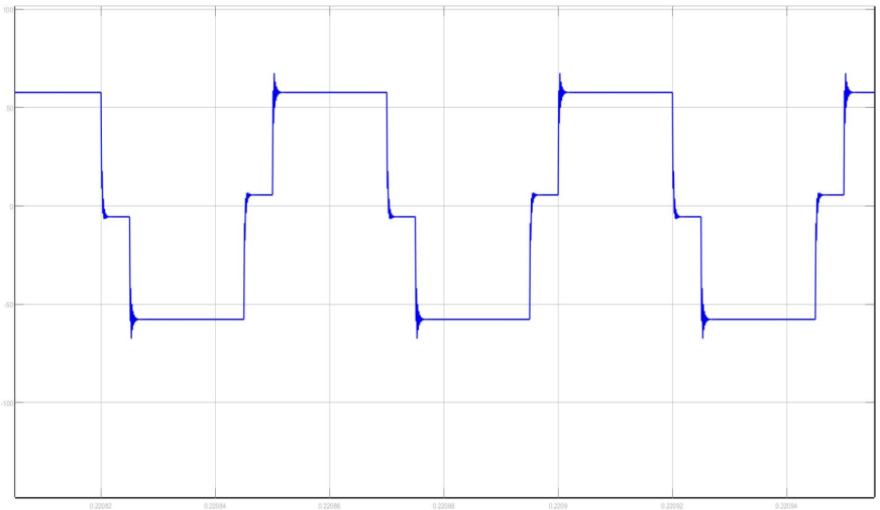

Figure 6.9: Secondary side voltage of the transformer at 20kHz frequency.

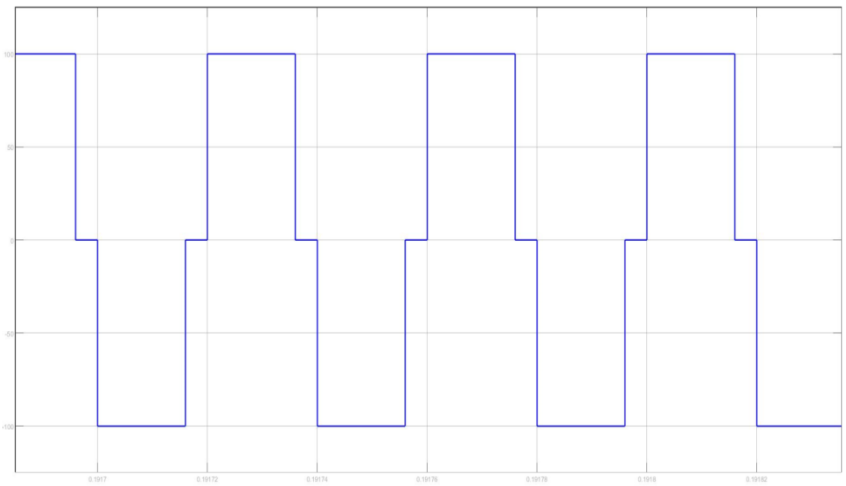

Figure 6.10: Square wave AC voltage (V_S) at 25kHz frequency.

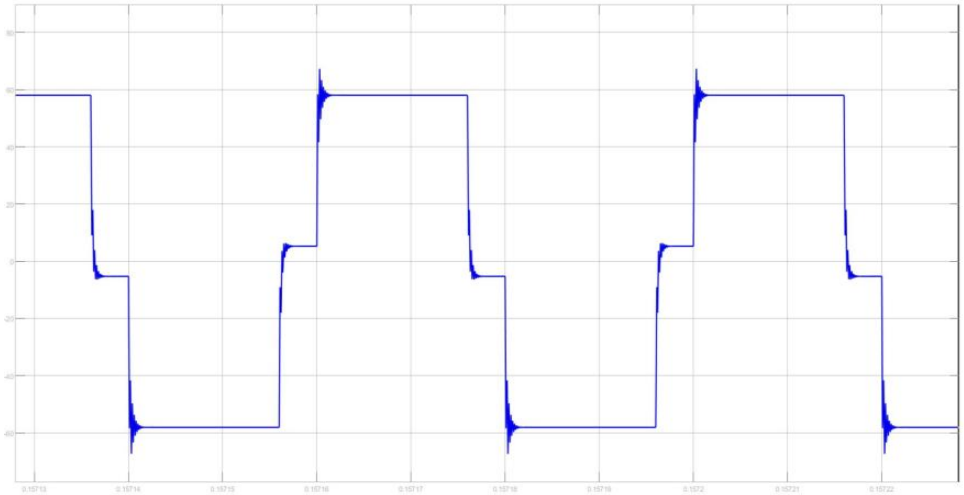

Figure 6.11: Secondary side voltage of the transformer at 25kHz frequency.

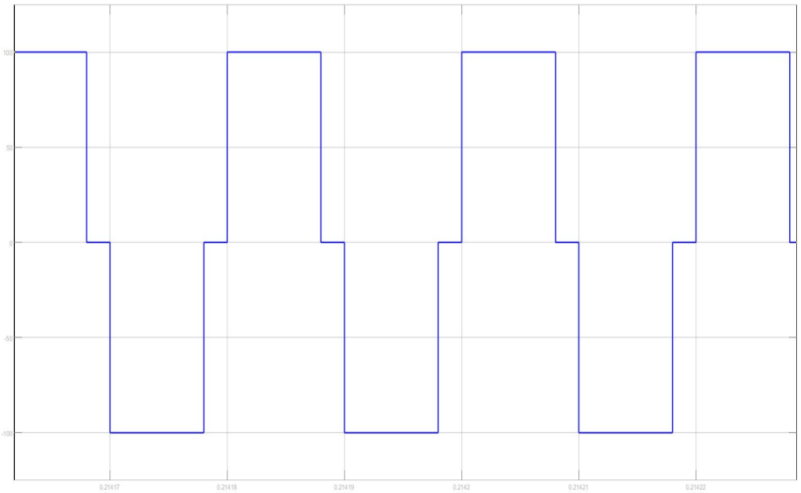

Figure 6.12: Square wave AC voltage (V_S) at 50kHz frequency.

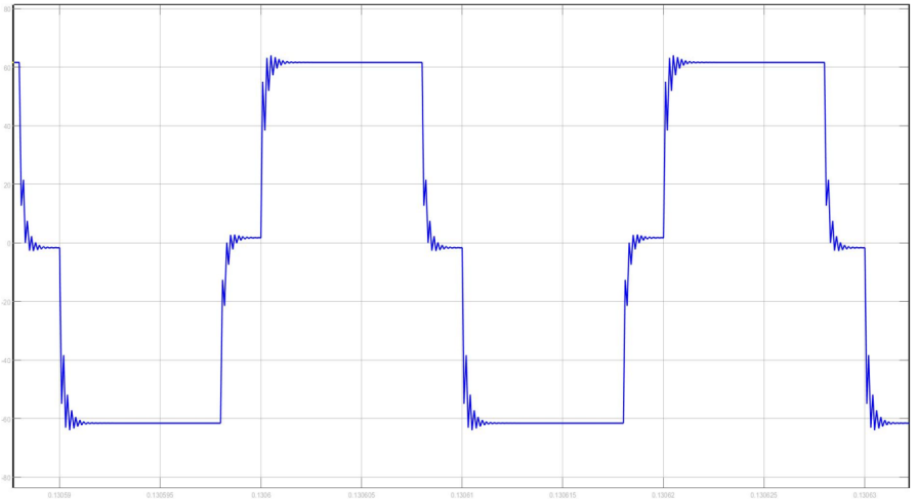

Figure 6.13: Secondary side voltage of the transformer at 50kHz frequency.

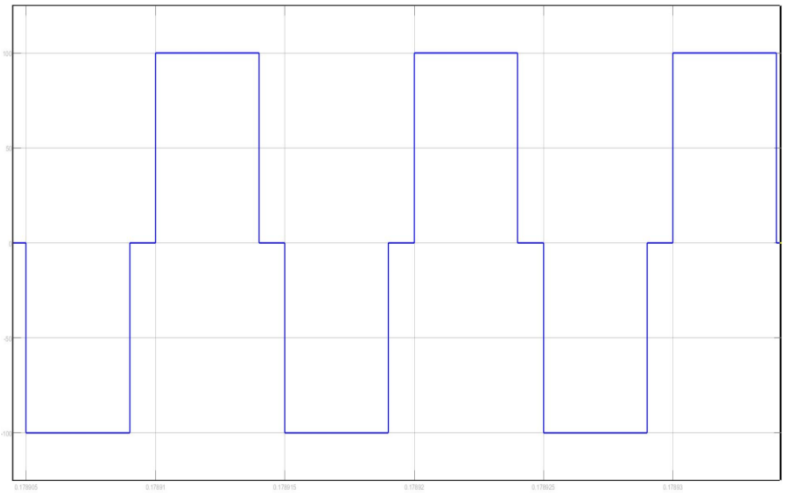

Figure 6.14: Square wave AC voltage (V_S) at 100kHz frequency.

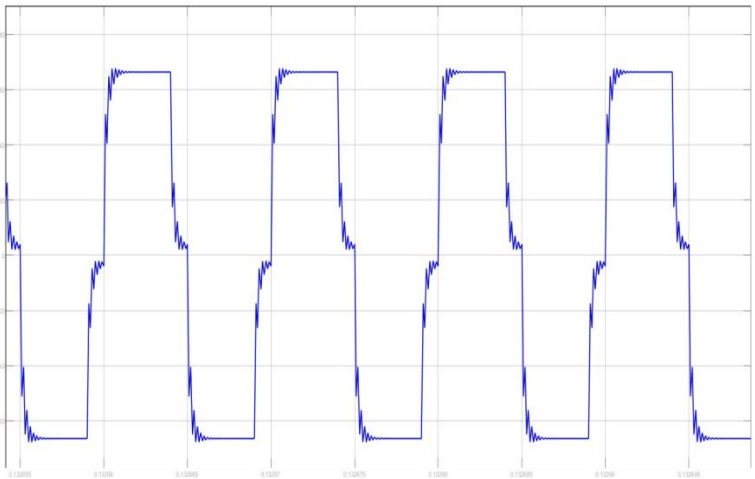

Figure 6.15: Secondary side voltage of the transformer at 100kHz frequency.

- **The output voltage of the real ferrite core transformer is presented below for comparison with the corresponding simulation results.**

(a)

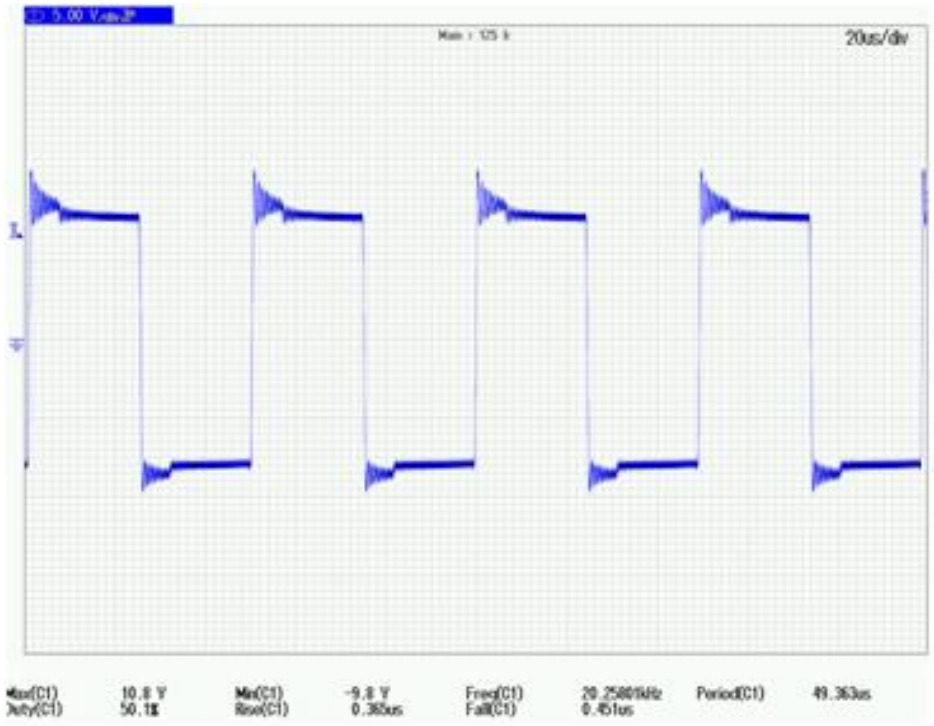

(b)

Figure 6.16(a, b): Secondary side voltage of the real transformer.

6.4 Summary

To assess the dynamic response of the transformer model, a MATLAB-based simulation was run over a variety of operating frequencies. Important components including capacitance due to MOSFETs, winding resistance and leakage inductance were incorporated in the model. The findings showed that the transformer's voltage-current behavior and impedance vary significantly with frequency. With little interference from parasitic components, the transformer operated steadily at lower frequencies. However, the effects of parasitic capacitance and leakage inductance become more noticeable at higher frequencies, influencing the impedance characteristics and waveform shape. In order to ensure accurate design and reliable performance—especially in high-frequency applications such as power electronics and switching converters results highlight the importance of accounting for frequency-dependent factors when modeling transformers.

In high-frequency operation using a ferrite-core transformer in a push–pull inverter, studying the effect of the all parasitic parameters including MOSFETs is essential for system design, selection of the components and elements into the inverter. Best optimized design could be done only with a rigorous simulation and observation of the results with these modeling techniques.

Chapter-7

CONCLUSIONS AND FUTURE SCOPE OF WORK

7.1 Conclusion

The use of optocouplers operated in the developed inverter for interfacing power and driver circuits initially seemed like a viable solution, but it presented significant challenges. At higher frequencies, the optocouplers introduced uneven delays and signal distortion, leading to MOSFET failures. Moreover, maintaining the precise dead-time required for safe switching of the MOSFETs became increasingly difficult. This resulted in cross-conduction, where both MOSFETs in the half-bridge configuration were inadvertently turned on simultaneously causing a short circuit and subsequent failure. These issues highlight the limitations of optocouplers in high-frequency applications.

It is observed that in the developed push-pull high frequency inverter operation there is no longer any discoloration by electrolysis and corrosion in the ohmic heated food-liquid conductor beyond 5 kHz, although frequency is increased and operated the inverter up to 20 kHz. It follows that this corrosion of electrodes can be totally eliminated if the frequency is raised even further.

Therefore, design and implementation of a microcontroller-based inverter using an Arduino Uno has been carried out, following a structured simulation-first approach prior to physical realization. The software simulation stage allows for early debugging and optimization, reducing hardware design errors. The final inverter prototype efficiently and reliably converts DC power into a stable AC output, operating effectively up to 10 kHz. Although the original target was to achieve very high-frequency operation, this remains a subject for future work.

Temperature and frequency have a significant impact on the ohmic heated food-liquid tested samples electrical conductivity which is increased with product temperature and decreases with higher frequencies. Electrical conductivities of the chosen liquid products are observed based on their temperatures and activation energy. An essential tool for designing and effectively running an ohmic heating process should be available in this database. Understanding electrical conductivity temperature relationships, in particular, will help determine the temperature change (ΔT) throughout a treatment, improved process control, and can give a tool for effective food treatment methods.

The transformer non-linear model is done by B-H magnetic hysteresis captured by DSO and then MATLAB-based simulation results was conducted across a range of operating frequencies to assess the dynamic response of the transformer model and MOSFET-applications. Important components including capacitance due to MOSFETs, winding resistance and leakage inductance of transformer were incorporated in the model. The findings showed that the transformer's voltage-current behavior and impedance vary significantly with frequency. With little interference from parasitic components, the transformer operated steadily at lower frequencies. However, the effects of parasitic capacitance and leakage inductance become more noticeable at higher frequencies, influencing the impedance characteristics and waveform shape. In order to ensure accurate design and reliable performance—especially in high-frequency applications such as power electronics and switching converters results highlight the importance of accounting for frequency-dependent factors when modeling transformers.

Based on the findings, it is concluded that ohmic heating overcomes the deficiency of traditional heating as it realizes material heating without temperature gradient, and the purpose of uniform heating throughout is achieved directly. It has advantages of rapid heating, no heating surface, easy control and environmentally friendly. It can achieve high temperature sterilization rapidly for liquid-solid mixing foods containing particles. So, the ohmic heating technology is considered to be one of the most potential heat treatment technologies in food processing. In high power and high frequency application an inverter has to be modified with protections and measurement scheme. The solutions having different concentration of salts like NaCL, Na_2SO_4, and KCL etc. were introduced in liquid solutions to achieve the conductivity for proper heating quickly. But a comparative study for various solution shows that corrosion of electrodes increases with the increase of concentration of salts in the solution. However, there should be a compromise between the increase in conductivity and decrease in corrosion and an appropriate concentration of the salts should be formulated. It may be mentioned here that this is the requirement for the sterilization of foods (liquid or semisolid) by ultra-high temperature with ohmic heating system.

This research investigates the various aspects of the theory, design and construction using ferrite core transformer instead of conventional transformer in a high frequency and high-power DC/AC push-pull type inverter. A comparison of the performance of various MOSFETs shows that the push pull inverter is a better one for high frequency ac source. Direct heating (ohmic heating) can achieve high temperature sterilization rapidly for liquid–

solid mixing foods containing particles like; orange juice, coconut water, milk etc by ohmic heater, but in doing so in laboratory it is found that the electrodes used for current flow through the liquid are getting corroded and thereby damaging itself as well as liquid conductor as a food contaminating that. To reduce/stop this corrosion of the electrodes a variable frequency ac power source using power inverter has been proposed. It is expected that if one increases the frequency in this kind of heating process the corrosion of the electrode can be completely eliminated and the liquid food conductor easily be sterilized using ultra-high temperature. One important point to mention here is that in this laboratory setup, attempts to increase the frequency beyond 20 kHz resulted in the destruction of the MOSFETs, despite forced cooling using a fan and heat sink. Therefore, it was not possible to operate above 20 kHz with this ferrite core transformer. It should be noted that the driver output is not responsible for the observed performance issues with the ferrite core transformer and inverter, as the gate drive output has been tested and found to be an almost perfect square wave. The driver circuit for the inverter source has been found to work very satisfactorily. Though this inverter works perfectly up to 20 kHz, electrode corrosion is reduced drastically at this frequency. Therefore, in the future, this high frequency power inverter will be a promising ohmic heater to sterilize the liquid food conductor at ultra-high temperature in food processing industry up to this range of frequency.

7.2 Scope of future work

The present work has established the potential of high frequency inverter in the system of liquid food ohmic heating. In high power and high-performance application of this drive circuit and high frequency inverter has to be modified with protections and measurement scheme. This has become a challenging task of future as high frequency involved. Microcontroller with high speed operation will be suitable for those protection and measurements. This may be another domain of prospective future work. To control the power during ohmic heating in the liquid foods, it has been observed that conductivity of the liquid foods increases non-linearly with the increase in temperature of the liquid. An ordinary power control scheme is not efficient, as the power must be cut off if the current through the liquid exceeds the system's capacity due to increased conductivity. And it is found that in these system conductivity increases three times when temperature goes to 100^0C and hence the current drawn is almost 3 times the initial value. To limit the current within the range, duty cycle should be controlled by using feedback loop with a temperature sensor or current

sensor. The gate control of the MOSFET/IGBT has been observed as an effective means for such experiment. Although feedback system has not been developed due to lack of time, but this may be the future scope of work. The high frequency ohmic heater is still under development for very high-power application using 3-phase power supply which may also be another area of future work.

REFERENCES

[1] Napp TA, Gambhir A, Hills TP, Florin N, Fennell PS. A review of the technologies, economics and policy instruments for decarbonising energy intensive manufacturing industries. Renewable Sustainable Energy Rev 2014;30:616–40.

[2] Lin B, Ouyang X. Electricity demand and conservation potential in the Chinese non-metallic mineral products industry. Energy Policy 2014;68:243–53.

[3] IEA. Tracking industrial energy efficiency and CO2 emissions: in support of the G8 plan of action. Paris, France; 2007.

[4] US Department of Energy Website available at ⟨https://www1.eere.energy.gov/manufacturing/tech_assistance/pdfs/proc_heat_sourcebook.pdf⟩.

[5] De Alwis AAP, Fryer PJ. The use of direct resistance heating in the food industry. J Food Eng 1990;11:3–27.

[6] Palaniappan S, Sastry Sk. Electrical conductivities of selected solid foods during ohmic heating. J Food Process Eng 1991;14:221–36.

[7] Amatore C, Berthou M, Hébert S. Fundamental principles of electrochemical ohmic heating of solutions. J Electroanal Chem 1998;457:191–203.

[8] Zell M, Lyng JG, Morgan DJ, Cronin DA. Development of rapid response thermocouple probes for use in a batch ohmic heating system. J Food Eng 2009;93:344–7.

[9] ⟨http://www.ctechinnovation.com/latest-articles/what-is-an-ohmic-heater. pdf⟩.

[10] Samaranayake CP, Sastry SK. Electrode and pH effects on electrochemical reactions during ohmic heating. J Electroanal Chem 2005;577:125–35.

[11] Castro I, Teixeira JA, Salengke S, Sastry SK, Vicente AA. Ohmic heating of strawberry products: electrical conductivity measurements and ascorbic acid degradation kinetics. Innovative Food Sci Emerg Technol 2004;5:27–36.

[12] Fryer PJ, de Alwis AAP, Koury E, Stapley AGF, Zhang L. Ohmic processing of solid-liquid mixtures: heat generation and convection effects. J Food Eng 1993;18:101–25.

[13] Murphy AB, Powell KJ, Morrow R. Thermal treatment of sewage sludge by ohmic heating. IEE Proc: Sci Meas Technol 1991;138:242–8.

[14] Zhu SM, Zareifard MR, Chen CR, Marcotte M, Grabowski S. Electrical con ductivity of particle–fluid mixtures in ohmic heating: measurement and simulation. Food Res Int 2010;43:1666–72.

[15] Jakób A, Bryjak J, Wójtowicz H, Illeová V, Annus J, Polakovič M. Inactivation kinetics of food enzymes during ohmic heating. Food Chem 2010;123:369–76.

[16] Tumpanuvatr T, Jittanit W. The temperature prediction of some botanical beverages, concentrated juices and purees of orange and pineapple during ohmic heating. J Food Eng 2012;113:226–33.

[17] Sun-Waterhouse, D.; Zhao, M.; Waterhouse, G.I.N. Protein Modification During Ingredient Preparation and Food Processing: Approaches to Improve Food Processability and Nutrition. *Food Bioprocess. Technol.* **2014**, *7*, 1853–1893.

[18] Indiarto, R.; Rezaharsamto, B. A Review on Ohmic Heating and Its Use in Food. *Int. J. Sci. Technol. Res.* **2020**, *9*, 485–490.

[19] Ramaswamy, H.S.; Marcotte, M.; Sastry, S.; Abdelrahim, K. (Eds.) *Ohmic Heating in Food Processing*; CRC Press: Boca Raton, FL, USA, 2014; ISBN 978-0-429-14996-2.

[20] Knirsch, M.C.; Alves Dos Santos, C.; Martins De Oliveira Soares Vicente, A.A.; Vessoni Penna, T.C. Ohmic Heating—A Review. *Trends Food Sci. Technol.* **2010**, *21*, 436–441.

[21] Assiry, A.; Sastry, S.K.; Samaranayake, C. Degradation Kinetics of Ascorbic Acid during Ohmic Heating with Stainless Steel Electrodes. *J. Appl. Electrochem.* **2003**, *33*, 187–196.

[22] Jaeger, H.; Roth, A.; Toepfl, S.; Holzhauser, T.; Engel, K.-H.; Knorr, D.; Vogel, R.F.; Bandick, N.; Kulling, S.; Heinz, V.; et al. Opinion on the Use of Ohmic Heating for the Treatment of Foods. *Trends Food Sci. Technol.* **2016**, *55*, 84–97.

[23] Guo, W.; Llave, Y.; Jin, Y.; Fukuoka, M.; Sakai, N. Mathematical Modeling of Ohmic Heating of Two-Component Foods with Non-Uniform Electric Properties at High Frequencies. *Innov. Food Sci. Emerg. Technol.* **2017**, *39*, 63–78.

[24] Alkanan, Z.T.; Altemimi, A.B.; Al-Hilphy, A.R.S.; Watson, D.G.; Pratap-Singh, A. Ohmic Heating in the Food Industry: Developments in Concepts and Applications during 2013–2020. *Appl. Sci.* **2021**, *11*, 2507.

[25] Halden, K. Changes in the Electrical Conductivity of Foods during Ohmic Heating. *Int. J. Food Sci. Technol.* **1990**, *25*, 9–25.

[26] Varghese, K.S.; Pandey, M.C.; Radhakrishna, K.; Bawa, A.S. Technology, Applications and Modelling of Ohmic Heating: A Review. *J. Food Sci. Technol.* **2014**, *51*, 2304–2317.

[27] Stancl, J.; Zitny, R. Milk Fouling at Direct Ohmic Heating. *J. Food Eng.* **2010**, *99*, 437–444.

[28] Kamonpatana, P.; Gavahian, M.; Sastry, S.K. Ohmic Heating for Food Processing: Methods and Procedures Related to Process Parameters. In *Emerging Food Processing Technologies*; Gavahian, M., Ed.; Methods and Protocols in Food Science; Springer: New York, NY, USA, 2022; pp. 181–193. ISBN 978-1-07-162135-6.

[29] Rocha, R.S.; Silva, R.; Ramos, G.L.P.; Cabral, L.A.; Pimentel, T.C.; Campelo, P.H.; Blumer Zacarchenco, P.; Freitas, M.Q.; Esmerino, E.A.; Silva, M.C.; et al. Ohmic Heating Treatment in High-Protein Vanilla Flavored Milk: Quality, Processing Factors, and Biological Activity. *Food Res. Int.* **2022**, *161*, 111827.

[30] Rosa, D.A.; Guimarães, J.D.T.; Cabral, L.A.; Silva, M.C.; Raices, R.S.L.; Ramos, G.L.P.A.; Pimentel, T.C.; Esmerino, E.A.; Cruz, A.G.D.; Freitas, M.Q.D. Effect of Ohmic Heating Temperature and Voltage on Liquid Whole Egg Processing. *Innov. Food Sci. Emerg. Technol.* **2023**, *89*, 103490.

[31] Cappato, L.P.; Ferreira, M.V.S.; Guimaraes, J.T.; Portela, J.B.; Costa, A.L.R.; Freitas, M.Q.; Cunha, R.L.; Oliveira, C.A.F.; Mercali, G.D.; Marzack, L.D.F.; et al. Ohmic Heating in Dairy Processing: Relevant Aspects for Safety and Quality. *Trends Food Sci. Technol.* **2017**, *62*, 104–112.

[32] Avelar, Z.; Vicente, A.A.; Saraiva, J.A.; Rodrigues, R.M. The Role of Emergent Processing Technologies in Tailoring Plant Protein Functionality: New Insights. *Trends Food Sci. Technol.* **2021**, *113*, 219–231.

[33] Avelar, Z.; Monge-Morera, M.; Delcour, J.A.; Saraiva, J.A.; Vicente, A.A.; Rodrigues, R.M. Ohmic Heating as an Innovative Strategy to Modulate Protein Fibrillation. *Innov. Food Sci. Emerg. Technol.* **2024**, *92*, 103587.

[34] Pereira, R.N.; Rodrigues, R.M.; Machado, L.; Ferreira, S.; Costa, J.; Villa, C.; Barreiros, M.P.; Mafra, I.; Teixeira, J.A.; Vicente, A.A. Influence of Ohmic Heating on the Structural and Immunoreactive Properties of Soybean Proteins. *LWT* **2021**, *148*, 111710.

[35] Moreira, T.C.P.; Pereira, R.N.; Vicente, A.A.; Da Cunha, R.L. Effect of Ohmic Heating on Functionality of Sodium Caseinate—A Relationship with Protein Gelation. *Food Res. Int.* **2019**, *116*, 628–636.

[36] Shimoyamada, M.; Itabashi, Y.; Sugimoto, I.; Kanauchi, M.; Ishida, M.; Tsuzuki, K.; Egusa, S.; Honda, Y. Characterization of Soymilk Prepared by Ohmic Heating and the Effects of Voltage Applied. *Food Sci. Technol. Res.* **2015**, *21*, 439–444.

[37] Wang, L.-J.; Li, D.; Tatsumi, E.; Liu, Z.-S.; Chen, X.D.; Li, L.-T. Application of Two-Stage Ohmic Heating to Tofu Processing. *Chem. Eng. Process. Process Intensif.* **2007**, *46*, 486–490.

[38] Li, X.; Ye, C.; Tian, Y.; Pan, S.; Wang, L. Effect of Ohmic Heating on Fundamental Properties of Protein in Soybean Milk. *J. Food Process Eng.* **2018**, *41*, e12660.

[39] Wang, X.; Wang, W.; Hu, X.; Zhu, X.; Wang, L.; Zhang, N.; Yu, D. Structural and Physical Properties of Soybean Protein Isolate Films with Ohmic Heating Treatment: Impacts of Electric Field. *Innov. Food Sci. Emerg. Technol.* **2022**, *82*, 103213.

[40] Samaranayake, Chaminda P., and Sudhir K. Sastry. "Electrode and pH effects on electrochemical reactions during ohmic heating." *Journal of Electroanalytical Chemistry* 577.1 (2005): 125-135.

[41] Bansal, Bipan, Xiao Dong Chen, and Sean XQ Lin. "Skim milk fouling during ohmic heating." (2005): 133.

[42] Bansal, Bipan, and Xiao Dong Chen. "A critical review of milk fouling in heat exchangers." *Comprehensive reviews in food science and food safety* 5.2 (2006): 27-33.

[43] Sakr, Mohamed, and Shuli Liu. "A comprehensive review on applications of ohmic heating (OH)." *Renewable and Sustainable Energy Reviews* 39 (2014): 262-269.

[44] Tola, Yetenayet Bekele, Navneet Singh Rattan, and Hosahalli S. Ramaswamy. "Electrodes in ohmic heating." *Ohmic heating in food processing* (2014): 141-155.

[45] Pataro, Gianpiero, et al. "Quantification of metal release from stainless steel electrodes during conventional and pulsed ohmic heating." *Innovative Food Science & Emerging Technologies* 21 (2014): 66-73.

[46] Mohan, Ned, Tore M. Undeland, and William P. Robbins. *Power electronics: converters, applications, and design*. John wiley & sons, 2003.

[47] Pathak, Abhijit D. "MOSFET/IGBT drivers theory and applications." *Application Note AN002* (2001).

[48] Sudhir K. Sastry, Q. Howard Zhang , David B. Min , Russ C. Hille, "Electrochemical Reaction During Ohmic Heating "Ohio State University 2003

[49] N. Nozturk, Analysis of switching losses of hard and soft switch ing in full bridge converter. J. Fac. Eng. Archit. Gazi Univ. 23(1), 25 (2008)

[50] N. Mohan, T.M. Undeland, W.P. Robbins, Power Electronics: Converters, Applications, and Design (Wiley, New York, 2003)

[51] Y. Li, F.C. Lee, D. Boroyevich, A three-phase soft-transition inverter with a novel control strategy for zero-current and near zero-voltage switching. IEEE Trans. Power Electron. 16(5), 710 723 (2001)

[52] https://www.alldatasheet.com/datasheet-pdf/pdf/8734/NSC/LM3524.html

[53] https://www.vishay.com/docs/83604/6n136.pdf

[54] https://www.ti.com/lit/ds/symlink/ne555.pdf

[55] https://www.alldatasheet.com/view.jsp?Searchword=2SK727

[56] https://www.alldatasheet.com/view.jsp?Searchword=irf840

[57] https://www.alldatasheet.com/datasheet-pdf/pdf/68529/IRF/IRFP460.html

[58] Standard Recommendations: Soft Ferrite Cores, A user's Guide by The International Magnetics Association.

[59] Lakshminarayanan.V, Anand.B, Balakrishnan. P.A.,"Analysisand Design of Ferrite Core Transformer for High Voltage, High Frequency Which Is Used In Ozonators", International Journal of Engineering and Applied Sciences,February 2013. Vol. 2, No.1, ISSN 2305-8269.

[60] Z Liu, GJJ Winands, K Yan, AJM Pemen, and EJM Van Heesch. A high-voltage pulse transformer with a modular ferrite core. Review of Scientific Instruments, 79(1), 2008.

[61] Hossein Babaie and Hassan Feshki Farahani. Analysis of thermal behavior of high frequency transformers using finite element method. Journal of Electromagnetic Analysis and Applications, 2010, 2010.

[62] Shuaichao Yue, Qingxin Yang, Yongjian Li, Changgeng Zhang, and Guizhi Xu. Core loss calculation of the soft ferrite cores in high frequency transformer under non-sinusoidal excitations. In 2017 20th International Conference on Electrical Machines and Systems (ICEMS), pages 1–5. IEEE, 2017.

[63] Krzysztof G´ orecki and Kalina Detka. Investigations of the influence of frequency on power losses in ferrite cores. In Journal of Physics: Conference Series, volume 1033, page 012004. IOP Publishing, 2018.

[64] Abraham Pressman. Switching power supply design. McGraw-Hill, Inc., 1997.

[65] Martin C Brown. Practical switching power supply design. Elsevier, 2012.

[66] Selami Balci, Ibrahim Sefa, and Necmi Altin. An investigation of ferrite and nanocrystalline core materials for medium-frequency power transformers. Journal of Electronic Materials, 45:3811–3821, 2016.

[67] G. Bal, N. Öztürk, E. Bekiroğlu, Investigation of switching losses for sinusoidal PWM zero current switching inverter and resonant link inverter. in 2009 35th Annual Conference of IEEE Industrial Electronics (IEEE, 2009). pp. 590–594

[68] Y. Li, F.C. Lee, D. Boroyevich, A three-phase soft-transition inverter with a novel control strategy for zero-current and near zero-voltage switching. IEEE Trans. Power Electron. 16(5), 710 723 (2001)

[69] Zhang, Q.H.; Chang, F.J.; Barbosa-Cánovas, G.V.; Swason, B.G. Engineering aspects of pulsed electric field pasteurization. J. Food Eng. 1995, 25, 261–291.

[70] Grahl, T.; Märkl, H. Killing of microorganisms by pulsed electric fields. Appl. Microbiol. Biotechnol. 1996, 45, 148–157.

[71] Barbosa-Cánovas, G.V.; Góngora-Nieto, M.M.; Pothakamury, U.R.; Swanson, B.G. Preservation of Foods with Pulsed Electric Fields: Academic Press: New York, NY, 1999.

[72] Evrendilek, G.A.; Jin, Z.T.; Ruhlman, K.T.; Qiu, X.; Zhang, Q.H.; Richter, E.R. Microbial safety and shelf-life of apple juice and cider processed by bench and pilot scale PEF systems. Innov. Food Sci. Emer. Technol. 2000, 1, 77–86.

[73] Yeom, H.W.; Streaker, C.B.; Zhang, Q.H.; Min, D.B. Effects on the quality of orange juice and comparison with heat pasteurization. J. Agricul. Food Chem. 2000, 48, 4597–4605.

[74] Alkanan ZT, Altemimi AB, Al-Hilphy ARS et al (2021) Ohmic heating in the food industry: Developments in concepts and applications during 2013–2020. Appl Sci 11:2507.

[75] Kaur N, Singh AK (2016) Ohmic heating: Concept and applications-a review. Crit Rev Food Sci Nutr 56:2338–2351.

[76] Zhang, Q.H.; Chang, F.J.; Barbosa-Cánovas, G.V.; Swason, B.G. Inactivation of microorgan isms in a Semisolid model food using high voltage pulsed electric fields. Leben.-Wiss.-Technol. 1994, 27, 538–543.

[77] Rodrigo, D.; Martínez, A.; Harte, F.; Barbosa-Cánovas, G.V.; Rodrigo, M. Study of inactivation of Lactobacillus plantarum in orange-carrot juice by means of pulsed electric fields: Compari son of inactivation kinetics models. J. Food Prot. 2001, 64 (2), 259–263.

[78] Gratz M, Schottroff F, Gall L et al (2021) Advantages of ohmic cooking in the kilohertz-range - part I: Impact of conductivity and frequency on the heating uniformity of potatoes. Innov Food Sci Emerg Technol 67:102595.

[79] Doan NK, Lai QD, Le TKP, Le NT (2021) Influences of AC frequency and electric field strength on changes in bioactive compounds in ohmic heating of pomelo juice. Innov Food Sci Emerg Technol 72:102754.

[80] Halden, K.; De Alwis, A.A.P.; Fryer, P.J. Change in electric conductivity of foods during ohmic heating. Int. J. Food Sci. Technol. 1990, 25, 9–25.

[81] Palaniappan, S.; Sastry, S.K. Electrical conductivity of selected juices: Influence of temperature, solids content, applied voltage, and particle size. J. Food Process. Eng. 1991, 14, 247–260.

[82] Yongsawatdigul, J.; Park, J.W.; Kolbe, E. Electric conductivity of pacific whiting surimi paste during ohmic heating. J. Food Sci. 1995, 60 (5), 922–925, 935.

[83] Marcotte, M.; Trigui, M.; Ramaswamy, H.S. Effect of salt and citric acid on electrical conduc tivities and ohmic heating of viscous liquids. J. Food Process. Preser. 2000, 24, 389–406.

[84] Henningsson, M., Östergren, K.; Dejmek, P. The electrical conductivity of milk – the effect of the dilution and temperature. Int. J. Food Prop. 2005, 8, 15–22.

[85] Ruhlman, K.T.; Jin, Z.T.; Zhang, Q.H. Physical properties of liquid foods for pulsed electric fields treatment. In Pulsed Electric Field in Food Processing: Fundamental Aspect and Appli cation; Barbosa- Cánovas, G.V.; Zhang, Q.W.; Eds.; Technomic Publishing: Pennsylvannia, 2001; 45–56.

[86] Raso, J.; Calderón, M.L.; Góngora-Nieto, M.M.; Barbosa-Cánovas, G.V.; Swason, B.G. Inactivation of Zygosaccharomyces bailii in fruit juices by heat, hydrostatic pressure and pulsed electric fields. J. Food Sci. 1998, 63 (6), 1042–1044.

[87] Dunn, J.E.; Pearlman, J.S. Methods and apparatus of extending the shelf-life of fluid food products. US Patent 4,695,472, Filed May 31, 1985; 1987.

[88] Nielen, M.; Deluyker, H.; Schukken, Y.H.; Brand, A. Electrical conductivity of milk: measure ment, modifiers, and meta analysis of mastitis detection performance. J. Dairy Sc. 1992, 75, 606–614.

[89] Bails, P.J.; Lee, J.G.M.; Parsons, A.R. An experimental investigation into the motion of a single drop in pulsed DC electric field. Trans IChemE 2000, 78, Part A. 499–505.

[90] Pethig, R. Dielectric and Electronic Properties of Biological Materials; John Wiley: New York, 1979.

[91] Ivanovic, Zeljko, and Mladen Knezic. "Modeling push–pull converter for efficiency improvement." *Electronics* 11.17 (2022): 2713.

[92] Trujillo, C. L., et al. "Modeling and control of a push–pull converter for photovoltaic microinverters operating in island mode." *Applied Energy* 88.8 (2011): 2824-2834.

[93] Shema, S. S., et al. "Simulation of push-pull inverter for photovoltaic applications via Multisim." *2011 5th International Power Engineering and Optimization Conference*. IEEE, 2011.

[94] Skandarnezhad, Atila, Abdolreza Rahmati, and Adib Abrishamifar. "Small signal modelling and implementation of push-pull based inverter with parasitics." *Tehnicki vjesnik-Tichnical Gazette* 22.6 (2015): 1457-1464.

[95] Glaser, John S., and Juan M. Rivas. "A 500 W push-pull dc-dc power converter with a 30 MHz switching frequency." *2010 Twenty-Fifth Annual IEEE Applied Power Electronics Conference and Exposition (APEC)*. IEEE, 2010.

Subrata Mandal
26/11/2025

Madhab Roy
26.11.25

Associate Professor
Electrical Engg. Dept.
Jadavpur University
Kolkata - 700 032